THÈSE DE DOCTORAT

Soutenue à Aix-Marseille Université
le 17 mars 2023 par

Michail Papadakis

Bio-inspired production of dihydrogen

Discipline
Science chimiques

École doctorale
ED250, Sciences Chimiques de Marseille

Laboratoire/Partenaires de recherche
Aix-Marseille Université
Institut de Sciences Moléculaires de Marseille

Composition du jury

Dr Élodie Anxolabéhère-Mallart Université Paris Cité-CNRS	Rapporteure
Dr Murielle Chavarot-Kerlidou Université De Grenoble-Alpes-CNRS	Rapporteure
Prof Athanassios G. Coutsolelos Université de Crète	Examinateur
Dr Christophe Léger Aix Marseille Université-CNRS	Président du jury
Dr Maylis Orio Aix Marseille Université-CNRS	Directrice de thèse
Dr Renaud Hardré Aix Marseille Université-CNRS	Co-directeur de thèse

THÈSE DE DOCTORAT

Soutenue à Aix-Marseille Université
le 17 mars 2023 par

Michail Papadakis

Bio-inspired production of dihydrogen

Discipline
Science chimiques

École doctorale
ED250, Sciences Chimiques de Marseille

Laboratoire/Partenaires de recherche
Aix-Marseille Université
Institut de Sciences Moléculaires de Marseille

Composition du jury

Dr Élodie Anxolabéhère-Mallart Université Paris Cité-CNRS	Rapporteure
Dr Murielle Chavarot-Kerlidou Université De Grenoble-Alpes-CNRS	Rapporteure
Prof Athanassios G. Coutsolelos Université de Crète	Examinateur
Dr Christophe Léger Aix Marseille Université-CNRS	Président du jury
Dr Frédéric Pitié Entreprise RENER	Membre Invité
Dr Maylis Orio Aix Marseille Université-CNRS	Directrice de thèse
Dr Renaud Hardré Aix Marseille Université-CNRS	Co-directeur de thèse

Affidavit

Je soussigné, Michail Papadakis, déclare par la présente que le travail présenté dans ce manuscrit est mon propre travail, réalisé sous la direction scientifique de Dr. Maylis Orio et Dr. Renaud Hardré, dans le respect des principes d'honnêteté, d'intégrité et de responsabilité inhérents à la mission de recherche. Les travaux de recherche et la rédaction de ce manuscrit ont été réalisés dans le respect à la fois de la charte nationale de déontologie des métiers de la recherche et de la charte d'Aix-Marseille Université relative à la lutte contre le plagiat.

Ce travail n'a pas été précédemment soumis en France ou à l'étranger dans une version identique ou similaire à un organisme examinateur.

Fait à Marseille le 13 décembre 2022



Cette œuvre est mise à disposition selon les termes de la Licence Creative Commons Attribution - Pas d'Utilisation Commerciale - Pas de Modification 4.0 International.

Affidavit

I, undersigned, Michail Papadakis, hereby declare that the work presented in this manuscript is my own work, carried out under the scientific direction of Dr. Maylis Orio and Dr. Renaud Hardré, in accordance with the principles of honesty, integrity and responsibility inherent to the research mission. The research work and the writing of this manuscript have been carried out in compliance with both the French national charter for Research Integrity and the Aix-Marseille University charter on the fight against plagiarism.

This work has not been submitted previously either in this country or in another country in the same or in a similar version to any other examination body.

Place Marseille, date 13 December 2022



Cette œuvre est mise à disposition selon les termes de la Licence Creative Commons Attribution - Pas d'Utilisation Commerciale - Pas de Modification 4.0 International.

Note:

The following doctoral dissertation consists of experimental work that took place from December 2019 to December 2022 in the BiosCiences group of iSm2 at the Saint Jérôme campus of Aix-Marseille University and is part of a CIFRE contract between RENER and the Centre National de la Recherche Scientifique (CNRS). Due to confidentiality reasons, the following chapters involve part of this research and do not include the main results of the industrial collaboration.

Publication list and participation to conferences

1) List of publication as part of the thesis project:

1. Michael Papadakis, Alexandre Barrozo, Tatiana Straistari, Nicolas Queyriaux, Anisa Putri, Jennifer Fize, Michel Giorgi, Marius Réglier, Julien Massin, Renaud Hardré and Maylis Orio, *"Ligand-based electronic effects on the electrocatalytic hydrogen production by thiosemicarbazone nickel complexes"*, Dalton Trans., 2020, *49*, 5064-5073.

2. Kalliopi Ladomenou, Michael Papadakis, Georgios Landrou, Michel Giorgi, Charalambos Drivas, Stella Kennou, Renaud Hardré, Julien Massin, Athanassios G. Coutsolelos and Maylis Orio, *"Nickel Complexes and Carbon Dots for Efficient Light-Driven Hydrogen Production"*, Eur. J. Inorg. Chem.. 2021, *30,* 3097-3103

2) Participation in conferences and summer schools during the period of the thesis:

1. Michael Papadakis, Anisa Putri, Tatiana Straistari, Alexandre Barrozo, Marius Réglier, Georgios Charalambidis, Julien Massin, Renaud Hardre, Athanassios G. Coutsolelos, Maylis Orio, *"Hydrogen evolution reactions catalyzed by Nickel bisthiosemicarbazone complexes"*, Journées de Chimie de Coordination 2020, 23-24 January 2020, Marseille, France. Poster presentation. (Best poster presentation award) International conference

2. Michael Papadakis, Anisa Putri, Tatiana Straistari, Alexandre Barrozo, Marius Réglier, Georgios Charalambidis, Julien Massin, Renaud Hardre, Athanassios G. Coutsolelos, Maylis Orio, *"Hydrogen evolution reactions catalyzed by Nickel bisthiosemicarbazone complexes"*, 5èmes Journées du GDR Solar Fuels, 27-29 September 2021 Saint Jacut de la Mer, France. Oral Presentation. (Best oral presentation award) International conference

3. Michael Papadakis, Anisa Putri, Tatiana Straistari, Alexandre Barrozo, Marius Réglier, Georgios Charalambidis, Julien Massin, Renaud Hardre, Athanassios G. Coutsolelos, Maylis Orio, *"Hydrogen evolution reactions catalyzed by Nickel bisthiosemicarbazone complexes"*, 2021 FrenchBIC meeting, 10-13 October 2021, Obernai, France. Oral Presentation. International conference

4. Michael Papadakis, Tatiana Straistari, Alexandre Barrozo, Renaud Hardré, Maylis Orio, *"How Nuclearity Impacts H_2 Production in Thiocarbohydrazone-based Complexes"*, 6èmes Journées du GDR Solar Fuels, 14-16 Novembre 2022, Fréjus, France. Poster Presentation. International conference

Acknowledgments

Before we go into the science of the last three years, I would like to express my gratitude to so many people that contributed to achieve everything that will be described in this manuscript. Arriving in Marseille in 2019 as an Erasmus intern, I had the opportunity to experience a unique city. Walking around the different neighbourhoods, the city changed styles and colors. From the salty breeze of the old port and the colorfulness of Le Panier to the incredible view of the Calanques, the city will always hold a special place in my heart. For this reason, I have to firstly thank Marseille itself for all the memories.

I want to thank the entire BiosCiences group that welcomed me from the start. Bruno was always happy to help with a smile, and Pierre could always find chemicals I was looking for. Julien, Michel, Olga, Mirreille, Medhi, Yolande, Thierry and Marius I thank you all for all the help in the laboratory. I want also to thank the head of RENER, my industrial employer, Jean-François Fardeau for trusting me on the industrial part of this thesis (stop asking me, it is confidential!).

I should mention here my previous academic supervisor professor Athanasios G. Coutsolelos and his team for the photocatalytic hydrogen production studies. However, most of all I want to thank him for opening his door to me 8 years ago and introducing me to science, which eventually evolved to be my great passion.

Three people deserve to be especially mentioned. The first two are my academic supervisors, Dr. Maylis Orio and Dr. Renaud Hardré. I greatly appreciate our scientific discussions, your constant support but also the trust and freedom you gave me to find my own footing as a researcher. Specifically for you Maylis, you can rest assured that I will not be lurking behind your office door every moment of the day anymore! Furthermore, I have to express my enormous gratitude to my “third supervisor” (as I like to call him), Dr. Frédéric Pitié for his help and support with the endless french bureaucracy. I would like to thank you for our discussions in and out of the workplace but most of all thank you for the (not always) great jokes - you cartoon.

So many students have come and left our team over these years: Quim, Raul, Hugo, Julie, Clarisse, Bernadette, Hamza and Elena just to name a few. I want also to thank all the students that worked with me over the last 3 years with a special mention to Léa my right hand through most of this period. In addition, I want also to thank all the current students of our group for the positive atmosphere that was created in our group.

How could I not mention the new family I found in Marseille? Alessia, Alex, Claudio, Iago, Robert, Rogelio and Stefani, I cannot thank you enough for the countless conversations, drinks, jokes, trips, memories, immeasurable support and help from the most trivial problem to the most important one.

I cannot forget my friends, Andreas, Antonis, Ifigenia, Kostas, Lefteris, Manos L., Manos O., Marva and Panagiotis for their constant support and cheerleading in my every endeavor.

Lastly, I want to express my gratitude to my family. They are the reason I have achieved anything in my life. My beloved father Emmanouil, who is no longer with us, my mother Sofia, my brother Kostas and his wife Peni, my grandparents Chrisoula and Mihalis. You are the reason any of this was made possible. I love you all.

Mike

Abstract

For the past two centuries, the consumption of fossil fuels has increased dramatically, leaving their reserves depleted. These problems have turned our interest towards developing catalytic systems that produce environmentally friendly fuel sources. Hydrogen is abundant and is considered an “ideal” fuel since its combustion only releases water vapors into the environment. In recent years, efforts have been made in developing new methods to generate hydrogen from renewable and sustainable resources, such as electrocatalytic and photocatalytic hydrogen evolution reactions (HER). Hydrogenases, the biological systems that naturally produce hydrogen, are a great inspiration for the design of metal-organic complexes that mimic their catalytic abilities.

In this work, we have synthesized, characterized and tested different series of nickel complexes based on thiocarbazone ligands for their ability to produce hydrogen from two different catalytic processes. The first part of this Ph.D. work describes the use of two new families based on bis-thiosemicarbazone ligands and investigates how appropriate ligand-tailoring can affect electrocatalytic performance for HER. The second part describes the use of a polynuclear nickel complex and how the incorporation of several metallic centers can affect electrocatalysis. In the last part of the manuscript, new photocatalytic systems were developed using carbon nanodots as light harvesters and the series of nickel-thiosemicarbazone complexes as catalytic centers for photo-producing hydrogen.

Keywords: nickel, hydrogen, electrochemistry, electrocatalysis, photocatalysis

Résumé

Au cours des deux derniers siècles, la consommation de combustibles fossiles a augmenté de façon spectaculaire contribuant à l'épuisement de leurs réserves. Ces problèmes nous ont amené à développer des systèmes catalytiques qui produisent des sources d'énergie respectueuses de l'environnement. L'hydrogène est abondant et est considéré comme un vecteur d'énergie idéal puisque sa combustion ne libère que des vapeurs d'eau dans l'environnement. Ces dernières années, de nombreux efforts ont été déployés pour mettre au point de nouvelles méthodes de production d'hydrogène à partir de ressources renouvelables et durables, telles que les réactions de production d'hydrogène par voies électrocatalytique et photocatalytique. Les hydrogénases, les systèmes biologiques produisant naturellement de hydrogène, sont une grande source d'inspiration pour la conception de complexes métallo-organiques imitant leur activité catalytique.

Dans ce travail, nous avons synthétisé, caractérisé et testé différentes séries de complexes de nickel basés sur des ligands thiocarbazone pour leur capacité à produire de l'hydrogène à partir de deux processus catalytiques différents. La première partie de ce travail de thèse décrit l'utilisation de deux nouvelles familles basées sur des ligands bis-thiosemicarbazone et étudie comment une modulation appropriée du ligand peut affecter les performances électrocatalytiques pour la production d'hydrogène. La deuxième partie décrit l'utilisation d'un complexe de nickel polynucléaire et comment l'incorporation de plusieurs centres métalliques peut affecter l'activité électrocatalitique du système. Dans la dernière partie du manuscrit, de nouveaux systèmes photocatalytiques ont été développés en utilisant des nanoparticules de carbone comme capteurs de lumière et la série de complexes nickel à ligands thiosemicarbazones comme centres catalytiques pour photoproduire de l'hydrogène.

Mots clés : nickel, hydrogène, électrochimie, électrocatalyse, photocatalyse

Περίληψη

Τους τελευταίους δύο αιώνες, η κατανάλωση ορυκτών καυσίμων έχει αυξηθεί δραματικά, με αποτέλεσμα να εξαντλούνται τα αποθέματά τους. Τα προβλήματα αυτά έχουν στρέψει το ενδιαφέρον μας προς την ανάπτυξη καταλυτικών συστημάτων που παράγουν φιλικές προς το περιβάλλον πηγές καυσίμων. Το υδρογόνο υπάρχει σε αφθονία γύρω μας και θεωρείται "ιδανικό" καύσιμο, καθώς η καύση του απελευθερώνει μόνο υδρατμούς στο περιβάλλον. Τα τελευταία χρόνια έχουν καταβληθεί προσπάθειες για την ανάπτυξη νέων μεθόδων παραγωγής υδρογόνου από ανανεώσιμες και βιώσιμες πηγές, όπως οι ηλεκτροκαταλυτικές και φωτοκαταλυτικές αντιδράσεις παραγωγής υδρογόνου. Οι υδρογενάσες, είναι βιολογικά συστήματα που υπάρχουν στη φύση και παράγουν υδρογόνο, ενώ αποτελούν μεγάλη έμπνευση για το σχεδιασμό μεταλλο-οργανικών συμπλόκων που μιμούνται τις καταλυτικές τους ιδιότητες.

Στην παρούσα εργασία, συνθέσαμε, χαρακτηρίσαμε και δοκιμάσαμε διαφορετικές σειρές συμπλόκων νικελίου με βάση υποκαταστάτες θειοκαρβαζόνης για την ιδιότητα τους να παράγουν υδρογόνο με δύο διαφορετικές καταλυτικές διεργασίες. Το πρώτο μέρος αυτής της διδακτορικής εργασίας περιγράφει τη χρήση δύο νέων οικογενειών που βασίζονται σε υποκαταστάτες διθειοσεμικαρβαζόνης και διερευνά τον τρόπο με τον οποίο η κατάλληλη προσαρμογή των υποκαταστατών μπορεί να επηρεάσει την ηλεκτροκαταλυτική απόδοση των αντιδράσεων παραγωγής υδρογόνου. Το δεύτερο μέρος περιγράφει τη χρήση ενός πολυπυρηνικού συμπλόκου νικελίου και πώς η ηλεκτροκατάλυση μπορεί να επηρεαστεί από την ενσωμάτωση πολλών μεταλλικών κέντρων. Στο τελευταίο μέρος της διατριβής αναπτύχθηκαν νέα φωτοκαταλυτικά συστήματα με τη χρήση νανοδομών άνθρακα ως φωτοσυλλέκτες και της σειράς συμπλόκων νικελίου-θειοσεμικαρβαζόνης ως καταλυτικών κέντρων για τη φωτοπαραγωγή υδρογόνου.

Λέξεις κλειδιά: νικέλιο, υδρογόνο, ηλεκτροχημεία, ηλεκτροκατάλυση, φωτοκατάλυση

Table of Contents

Affidavit 4
Affidavit 5
Publication list and participation to conferences 8
Abstract 11
Résumé 12
Περίληψη 13
Table of Contents 14
Chapter 1: Introduction 19
1.1 General Introduction 21
1.2 Hydrogenases 23
1.3 Biomimetic models of hydrogenases 26
1.4 Bioinspired models of hydrogenases 32
1.5 Electrocatalytic Hydrogen Evolution Reactions 39
1.6 Aim and scope of thesis 44
References 45
Chapter 2: Ligand chemical tailoring of thiosemicarbazone nickel complexes for electrocatalytic hydrogen production 53
2.1 Introduction 55
2.2 Results and Discussion 56
2.2.1 Synthesis and Characterization 56
2.2.2 Electrochemical Investigation 58
2.2.3 Electrocatalytic proton reduction 60
2.2.4 Mechanistic Investigations 64
2.3 Conclusions 71
2.4 Experimental section and supplementary data 72
2.4.1 Synthesis and Characterization 72
2.4.2 Electrochemistry 79
2.4.3 Foot-of-the-wave analysis (FOWA) 83
2.4.4 Overpotential and TOF calculations 86
References 88

Chapter 3: Ligand stereochemical tailoring of thiosemicarbazone nickel complexes for electrocatalytic hydrogen production 91
3.1 Introduction 93
3.2 Results and Discussion 94
3.2.1 Synthesis and Characterization 94
3.2.2 Electrochemical Investigation 96
3.2.3 Electrocatalytic proton reduction 98
3.2.4 Mechanistic Investigations 104
3.3 Conclusions 109
3.4 Experimental section and supplementary data 110
3.4.1 Synthesis and Characterization 110
3.4.2 Electrochemistry 119
3.4.3 Overpotential and TOF calculations 122
References 123
Chapter 4: Nuclearity influence on hydrogen evolution reaction with thiocarbohydrazone nickel complexes 125
4.1 Introduction 127
4.2 Results and Discussion 128
4.2.1 Synthesis and Characterization 128
4.2.2 Electrochemical Investigation 132
4.2.3 Electrocatalytic proton reduction 136
4.2.4 Mechanistic investigations 140
4.2.5 Benchmarking of performances 144
4.3 Conclusions 147
4.4 Experimental section and supplementary data 148
4.4.1 Synthesis and Characterization 148
4.4.2 Electrochemistry 151
4.4.3 Overpotential calculations 153
4.4.4 Kinetic analysis 153
References 155
Chapter 5: Light-driven hydrogen evolution with thiosemicarbazone complexes 157
5.1 General Introduction 159
5.2 Results and Discussion for the nickel series 165
5.2.1 Synthesis and Characterization 165
5.2.2 Photocatalytic hydrogen production 166
5.2.3 Mechanistic Investigation 171

5.3 Results and Discussion for the cobalt series 176
5.3.1 Synthesis and characterization 176
5.3.2 Photocatalytic hydrogen production 180
5.4 Conclusions 184
5.5 Experimental section and supplementary data 185
5.5.1 Synthesis and Characterization 185
5.5.2 Photocatalytic HER and Photophysical Measurements 188
References 189
Chapter 6: General conclusions and perspectives 193
Appendix 199
List of figures 215
List of Tables 225

Chapter 1: Introduction

1.1 General Introduction

As our society evolves and grows so do our energy demands. This growth is a problem that has become severe in our era. A big portion of the world is dependent on electricity for its daily life. Until now, our world produces electricity mainly through the consumption of fossil fuels such as coal, natural gas, and oil (Figure 1). Due to this uncontrollable use, our fossil fuel reserves are rapidly being depleted. Furthermore, their consumption produced an enormous amount of CO_2 and other greenhouse gases. For these reasons, we have turned our attention to alternative sources to produce electricity (like solar panels, wind turbines, etc.). Although these sources are more environmental-friendly they are not as efficient as fossil fuel combustion.

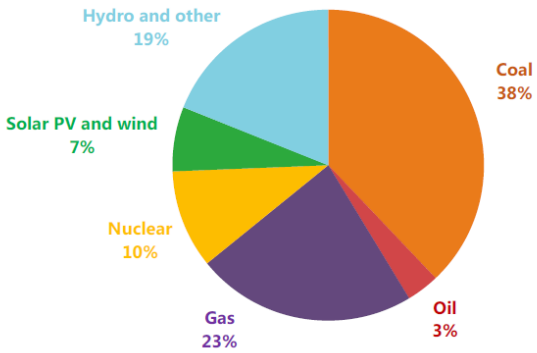

Figure 1. *Global electricity generation mix 2019.*[1,2]

One of the main issues with renewable energy sources is the storage of energy. The conversion of energy coming from the sun, the wind and other sources into electricity can only be beneficial while these generators are constantly running. If we manage to convert this energy into another more environmentally friendly fuel, most of our energy troubles could be tackled. All these characteristics are fulfilled by the most abundant element in the universe, hydrogen which, in its molecular form, can be used as fuel. Upon its combustion, only water vapors and heat are released.

$$\mathbf{2H_2 + O_2 \rightarrow 2H_2O\ (+heat)}$$

Our society already has the technology available to transition into a hydrogen-focused fuel industry. However, there is one major problem. Massive quantities of hydrogen have to be

generated. Until now most of the industrial hydrogen is produced by steam reforming of natural gas, oil reforming, or coal gasification. These processes are just as environmentally harmful as the consumption of fossil fuels since hydrogen is produced mainly by thermal processing of methane (CH_4) or by a water-gas shift reaction.[3]

$$\mathbf{CH_4 + 1/2O_2 \rightarrow CO + 2H_2\ (+heat)}$$

$$\mathbf{CO + H_2O \rightarrow CO_2 + H_2\ (+heat)}$$

Alkaline water electrolysis is yet another way to produce H_2 from water. This technology uses a cell consisting of two electrodes immersed in an alkaline electrolyte solution of KOH usually ranging from 20% to 30%. The two electrodes are separated by a diaphragm to keep the gas products apart. However, this technology also has flaws. The diaphragm does not prevent total cross-diffusion of H_2 and O_2, resulting in reformation of water in the cathode chamber and therefore reducing the efficiency of the system. Furthermore, the system must be able to withstand the big pressure needs of a small size device due to the dangerous nature of the explosive gases.[4]

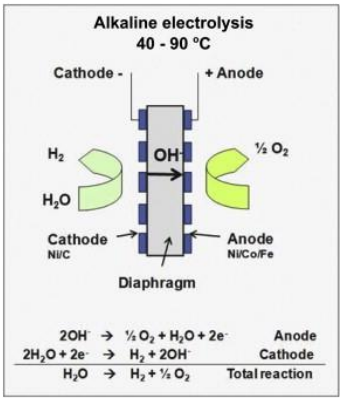

Figure 2. *Example of alkaline water electrolysis cell.*[4]

Another alternative is the use of the very rare and expensive platinum metal for this production. For these reasons, scientists have tried to find cost-efficient and green ways to produce hydrogen.

1.2 Hydrogenases

In nature, certain microorganisms produce hydrogen by employing a family of enzymes called hydrogenases. The scientific community has developed a greater interest in these enzymes over the years, as they might hold the keys to unlocking an effective way to provide the required amounts of hydrogen we seek to constantly produce.

Hydrogenases are a group of metalloenzymes that are found in bacteria, archaea and some eukarya. Their activity toward hydrogen production was firstly mentioned in 1931.[5] They catalyze one of the simplest molecular reactions, the splitting of molecular hydrogen into its building blocks, protons and electrons, but also the reverse reaction:

$$H_2 (\rightleftharpoons H^+ + H^-) \rightleftharpoons 2H^+ + 2e^-$$

This reaction takes place in the specialized metal center of these enzymes. Hydrogenases have been investigated as an alternative to platinum, because of their ability to work at the thermodynamic equilibrium and with high catalytic rates, whilst only containing first-row transition metals, iron and/or nickel, at the center of their active sites.[6] Hydrogenases are split into three categories according to the composition of the active site: [NiFe],[7] [FeFe][8] and [Fe]-only[9] hydrogenases (Figure 3).

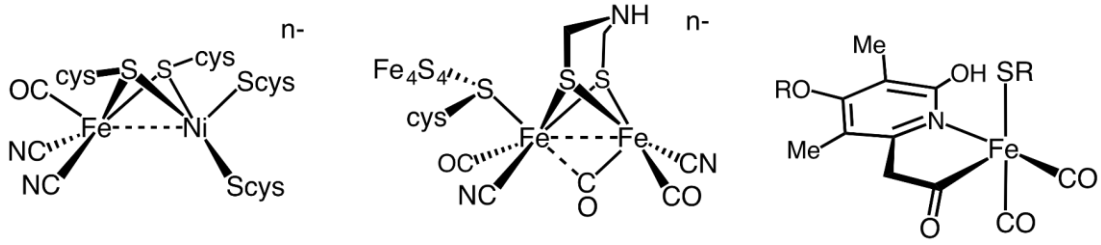

Figure 3. *Schematic views of the active sites of [NiFe] (left), [FeFe] (middle) and [Fe]-only (left) hydrogenases.*

Most of the known hydrogenases belong to the first two groups. Even though their structures and active site are different, [NiFe] and [FeFe] hydrogenases have some similarities. Both enzymes channel hydrogen and protons toward their active site to allow the production of molecular hydrogen or to release protons (Figure 4). Furthermore, both families feature three successive iron-sulfur clusters, which allow the flow of electrons. Their metallic centers also have similarities such as the presence of several thiolate ligands from cysteine or dithiolate co-factors and the organometallic nature of their active sites. It is also worth noting that the

presence of CN^- and CO ligands in the catalytic active site of an enzyme is without precedent in biology.

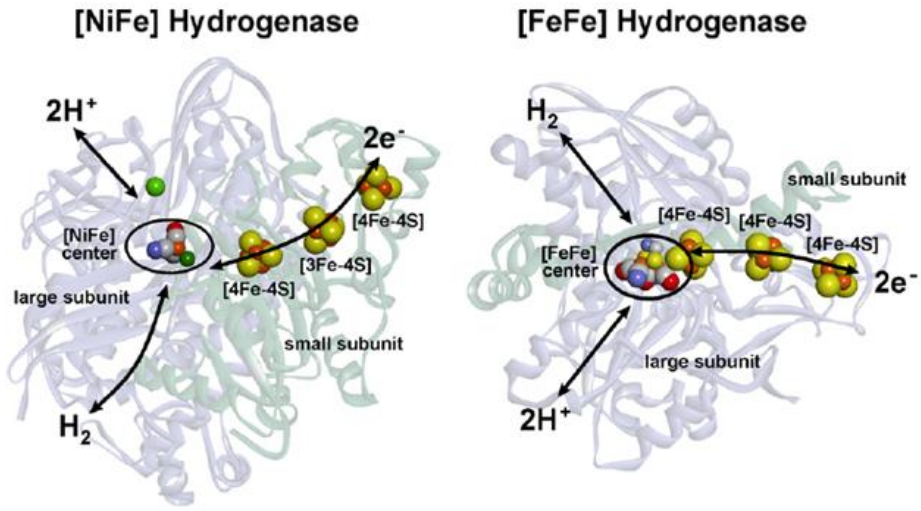

Figure 4. *Graphical representation of hydrogen splitting and production catalyzed at the metallic active sites of [NiFe] and [FeFe] hydrogenase.*[10]

[NiFe] and [FeFe] hydrogenases are able to catalyze the production of H_2 at very high rates (one molecule of hydrogenase produces between 1500 and 20000 molecules of H_2 per second at pH= 7 and T= 37ºC in water).[11,12] The third class of the family, [Fe] hydrogenases, are found only in archaea methanogens and employ the use of a hydride donor/acceptor substrate in order to perform the production or oxidation of H_2.[13]

Focusing further on the structural characteristics of [NiFe] hydrogenases active site, a small unit contains three aligned iron–sulphur clusters, a [4Fe-4S] cluster located 13 Å away from the active site, a distal [4Fe-4S] cluster close to the protein surface and a [3Fe-4S] sandwiched between the two [4Fe-4S] clusters.[7,14] Combined together, they form an electron transfer channel between a redox protein partner at the surface and the Ni-Fe active site, located deep within a large subunit of the enzyme. The presence of a Ni(III) ion is detected in the oxidized form of the cluster, existing in a distorted square pyramidal geometry. The four sulfurs coordinating to the cluster come from four cysteines, with two of them coordinating only to the nickel and the other two bridging the two metals. The Fe(II) is further coordinated by two CN ions and one CO ligand, as shown by FTIR spectroscopic studies. While the cyanide ions bind to the protein through hydrogen bonds, the carbon monoxide molecule is located in a hydrophobic cavity.

Several pathways have been proposed for the H_2 uptake of [NiFe] hydrogenases, but no agreement on a certain one has been reached by the scientific community.[15] One possibility starts from a Ni-SI form (Figure 5). A hydrogen molecule binds to the active site to produce a state name Ni-R. This form is inactive in EPR and three different structures have been proposed for it. H_2 binding to either nickel or iron, with a preference for the nickel metal. This preference is considered due to the hydrogen transport channel being connected to the nickel center instead of the iron.[16] Furthermore, exogenous CO, a competitive hydrogen inhibitor, can bind to iron[17–19] and lastly the H_2 binding to Ni(II) has been documented in 2012.[20] There is also a possibility that the cleavage of hydrogen molecules from proton abstraction by a cysteine terminal ligand coordinating to Ni happens at the Ni-R step of the catalytic cycle.[21,22] Next one electron removal gives rise to the paramagnetic Ni-C state.[23] ENDOR and HYSCORE spectroscopy showed that the Ni-C state contains a hydride bridging the two metal centers.[24–26] A second electron oxidation releases the bridging hydride as a proton and regenerates the starting Ni-R form to restart the catalytic cycle. All through the catalytic cycle, iron remains in its Fe(II) low-spin state, due to the high-field effects of CO and CN ligands. Meanwhile nickel alternates between Ni(II) and Ni(III) oxidation states. The production of molecular hydrogen is supposed to come from the same pathway in the reverse direction.

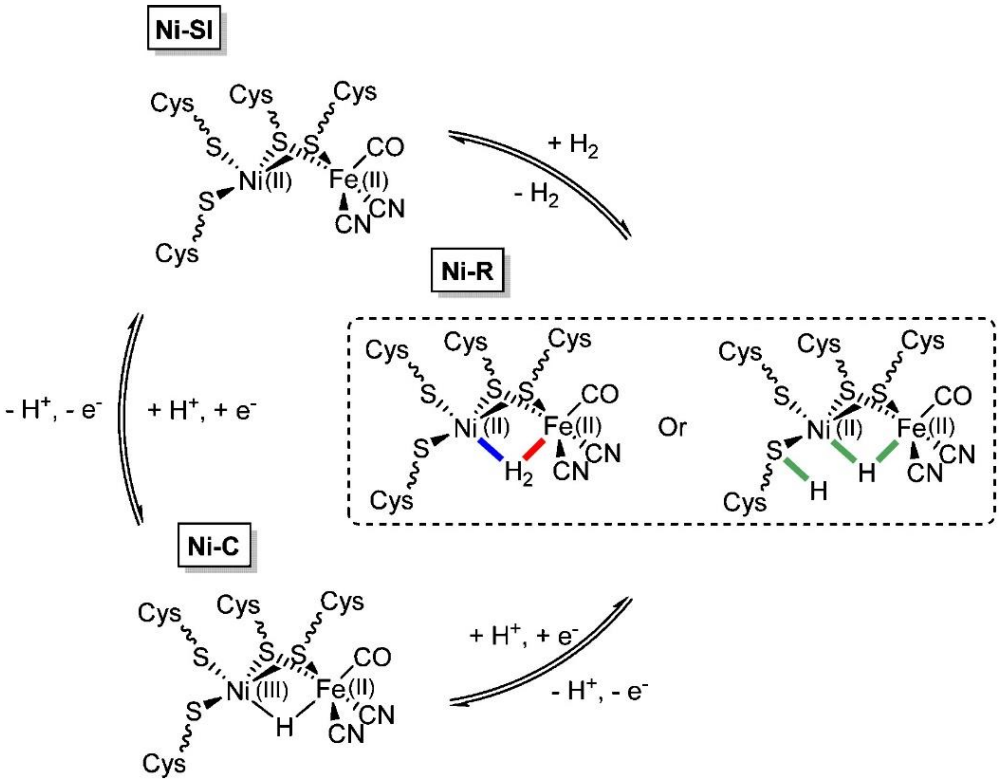

Figure 5. *The proposed catalytic mechanism for reversible hydrogen oxidation by the [NiFe] hydrogenase with the three proposed structures for the Ni-R state (red for Ni-H2 and blue for Fe-H2 binding).*[13]

Hydrogenases could be a promising replacement for platinum in the hydrogen production industry. Unfortunately, these enzymes are highly sensitive to oxygen, giving them a huge disadvantage for their potential bulk use in hydrogen production devices. As already mentioned, a lot of work has been put into decoding the catalytic mechanism of hydrogenases. Researchers all over the world have been trying to develop artificial hydrogenases to avoid the use of any biological organism to produce these enzymes. These investigations have given rise to organometallic compounds that can mimic both their structure and activity toward hydrogen production while providing air-stable catalysis and cost-effective ways to produce these compounds.

1.3 Biomimetic models of hydrogenases

Otto Schmitt firstly used the term “biomimetic” in the title of a publication in 1969.[27] This term was later implemented in Webster’s Dictionary in 1974 with the definition being the following: “*the study of the formation, structure, or function of biologically produced substances and materials (as enzymes or silk) and biological mechanisms and processes (as protein synthesis or photosynthesis) especially for the purpose of synthesizing similar products by artificial mechanisms which mimic natural ones.*”[28]

The scientific community has been trying to understand and copy the abilities of hydrogenases by synthesizing biomimetic models. Many compounds have been reported especially concerning the [NiFe] and [FeFe] hydrogenases. Developing these kinds of complexes is intriguing for a lot of reasons. Firstly, their structure is unlike any previously known compound. Furthermore, the active sites of hydrogenases include abundant and inexpensive metals (iron and nickel). They can reversibly work towards the production and/or the oxidation of molecular hydrogen. The results of such investigations can play a major role in unlocking an easy and inexpensive way to produce large amounts of hydrogen. In this part, we will mainly focus on biomimetic models for the [NiFe] hydrogenases.

In general, a lot of models of the active site of [NiFe] hydrogenases have been developed. Making complexes that are structurally almost identical to the active site of hydrogenase and also being able to replicate their activity has been a challenge, due to the cluster's complexity. A large amount of reported mimics,[15,29,30] while matching the sulphur coordination to nickel, the $Ni(\mu\text{-}SR)_2Fe$ core and the existence of the CN^- and CO ligands connected to iron, show little to no catalytic activity. (Figure 6)

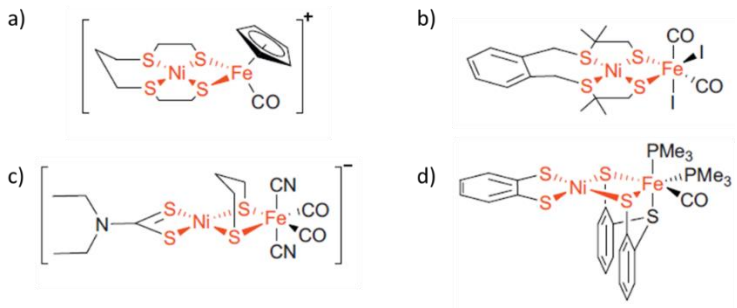

Figure 6. *Examples of structural mimics of the [NiFe] hydrogenase active site, with the [Ni(μ-SR)$_2$Fe] cores highlighted in red.*[31–34]

Ruthenium moieties have been also used to replace the [Fe(II)(CN)$_2$(CO)] fragment as there seems to be a lack of redox changes happening to iron during the catalytic activity of the enzymes. Therefore, the roles of CO and CN^- ligands can be either to regulate the electronic density at the Fe(II) center or maybe to stabilize some intermediates *i.e*. hydrogen derivatives or hydrides. The properties of Ru(II) make it an ideal replacement for iron as it can coordinate with both soft and hard effect ligands and it is also well known for its ability to work in hydrogenation or hydrogen transfer reactions.[13] Oudart and co-workers developed some Ni(II)-Ru(II) models that could work as hydrogen evolution catalysts (Figure 7).[35–37] with the best out of them reaching high turnover frequency (TOF) of 11.1 h^{-1} with a relatively low overpotential of 620 mV and an improved stability due to the bulky Cp* ligand (Figure 7c).[37]

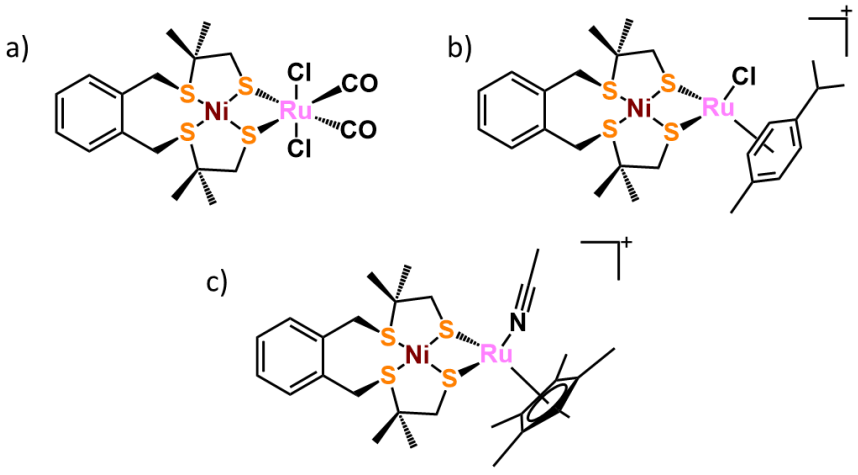

Figure 7. *Examples of structural mimics of the [NiFe] hydrogenase active site, with the Ni(II) and Ru(II) metallic centers.*[35–37]

The next step was to synthesize models containing only cheap first-row transition metals, which would be active toward hydrogen evolution reactions. Several of these complexes have been synthesized and studied, exhibiting catalytic activity (Figure 8).[38–40] Compounds containing the hydride bridging moiety were electrochemically active towards the production of H_2 from trifluoroacetic acid (TFA) in a solution of dichloromethane (Figure 8a-d).[38,39] Furthermore, in 2010 a Ni-Fe mimic (Figure 8e) was synthesized that could produce hydrogen with an overpotential of 730 mV in a solution of dimethylformamide (DMF) in the presence of TFA.

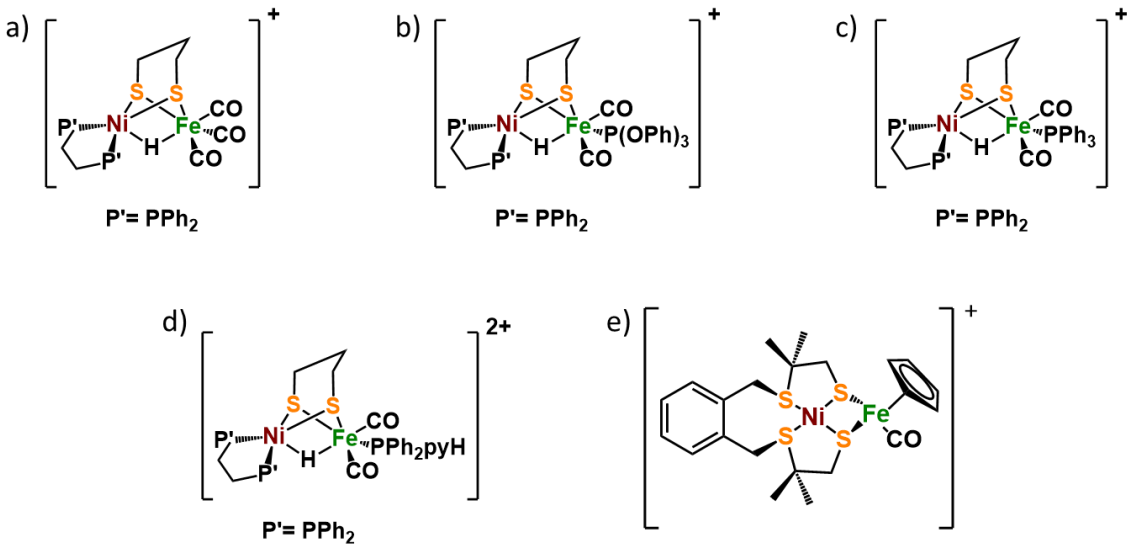

Figure 8. *Examples of catalytically active complexes containing nickel and iron as mimics of [NiFe] hydrogenase active site.*[38,39]

Additionally, some nickel manganese complexes have been synthesized as [NiFe] hydrogenase mimics (Figure 9). Complex 8a is similar to previously reported compounds either with an iron moiety (Figure 8e) or even a ruthenium one (Figure 7a). This complex is an active hydrogen-producing electrocatalyst requiring an overpotential of 860 mV in a DMF solution containing TFA.[41,42] Some neutral Ni-Mn complexes were also studied by Song *et al.* (Figure 9b) with a significantly lower overpotential of about 480 mV when changing to a solution of acetonitrile with acetic acid as the source of protons.[43]

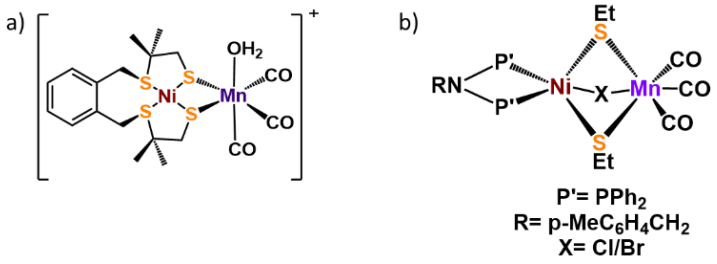

Figure 9. *Nickel and manganese containing complexes as mimics of [NiFe] hydrogenase active site.*[42,43]

Weber and coworkers made changes to the coordination sphere of nickel from four sulphur moieties to three with a thioether group and a CO ligand bridging the two metal centers.[40] It is very interesting to note that in the presence of fluoroboric acid (HBF_4) the terminal thiolate ligand is the one that gets protonated, a feature resembling the active site of the [NiFe] hydrogenases (Figure 10). Both unprotonated and protonated forms were proven active for HER by consuming TFA as the proton source in acetonitrile, with a low overpotential range of 540-570 mV.

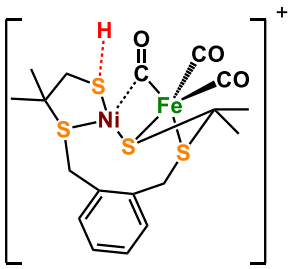

Figure 10. *[NiFe] hydrogenase mimic in both unprotonated and protonated forms (highlighted in red).*[40]

Ogo and coworkers have also reported on the use of binuclear nickel iron complexes that can both perform hydrogen evolution and hydrogen oxidation reactions (HER and HOR respectively) (Figure 11).[44,45] The novelty of their system is the employment of the ligands with triethylphosphite groups (-$P(OEt)_3$), later replaced with the bi-phosphine ligand (Figure 11b). Heterolytic hydrogen splitting occurs in the presence of a very strong base (methanolate), which catches one proton while a hydride is formed at the iron center in close proximity to the nickel one. This hydride can be then oxidized by methyl viologen at a low potential and a further proton removal completes the catalytic cycle and regenerates the starting catalyst. A disadvantage of the system is the use of a strong acid for the hydride species to produce hydrogen.

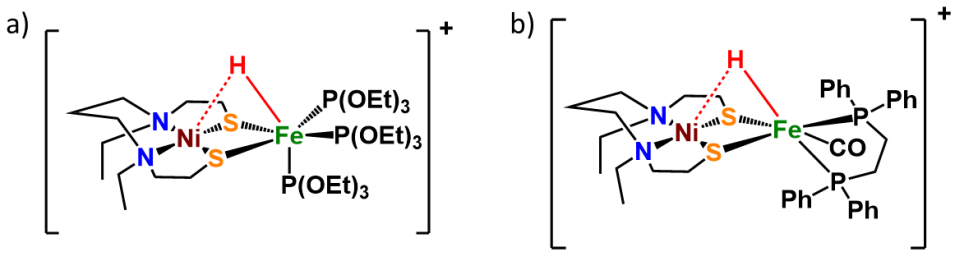

Figure 11. *Nickel iron complexes coordinating phosphorus-containing ligands to the iron center in their intermediate hydride form (hydride highlighted in red).*[44,45]

Although structurally almost identical, the comparison between the [NiFe] hydrogenase and these complexes should be made with caution, as there is not yet any consensus on the mechanism describing how the active site of hydrogenase works. One of the main concerns is the binding of the hydride intermediate, either being terminal on one of the two metals or a bridging ligand between nickel and iron. If an iron-bound hydride is needed for the activation of molecular hydrogen, it does not agree with the observed Ni-C state of the enzyme (Figure 5) which contains a hydride bridge between the two metals. The construction of such a ligand that can replicate the Ni(III)-Fe(II) metallic oxidation states of the Ni-C remains hard to accomplish. Therefore, Ogo's hydride derivatives (Figure 11) are more similar to the Ni-R state (Figure 4) of the proposed mechanism but fail to provide any definitive answer about the additional ligand in this state whether H_2 or H^- forms on the ligand and where it binds in the [Ni(ii)(-SR)$_2$Fe] core.

Two nickel-iron dinuclear complexes that represent the closest biomimetic model of the ligands at the iron center were reported by Manor and Rauchfuss in 2013.[46] The use of isocyanide ligands (Figure 12) protects the iron from chemical attacks due to their bulkiness, but also represent the CN^- anions found in the natural enzyme.

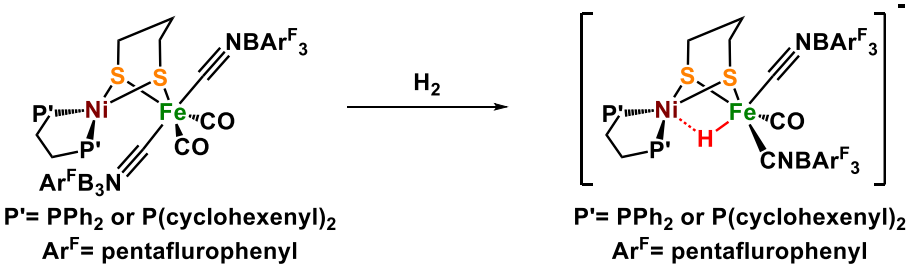

Figure 12. *Structure of Manor and Rauchfuss models without and with the bridging hydride.*

These compounds are able to split hydrogen heterolytically, transforming it into an intermediate with a hydride bridging the metals as shown by ^{1}H NMR and FTIR spectroscopies. These compounds show both hydrogen oxidation and production capabilities, with the former being performed in the presence of the strong diazabicycloun-decene (DBU) base and the latter in the presence of HCl. The similarities in structure and the existence of the hydride bridge make these molecules some of the closest models of Ni-C and Ni-R states of the [NiFe] hydrogenase. By comparing the overpotential (20 mV of difference) of the two compounds (very different pK_a of the diphosphine ligands), we can conclude that these models function through their iron center instead of the nickel one as observed in the active site of [NiFe] hydrogenases.

In 2016 Duboc and coworkers reported on the synthesis of a new biomimetic complex that actually displays reactivity at the nickel center (Figure 13).[47] Two intermediates of this compound were detected and characterized that reproduce structural and electronic features of the Ni-L and Ni-R states of the enzyme. Under electrocatalytic conditions, this mimic displays a TOF of 250 s^{-1} from mildly acidic acetonitrile solutions.

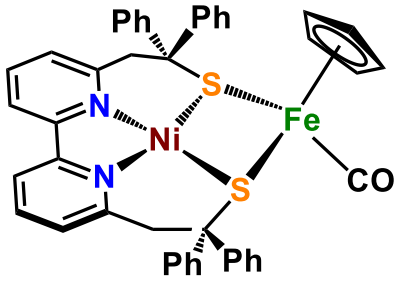

Figure 13. *Structure of the Duboc catalyst.*[47]

This huge amount of work provided some amazing results and lead to a new category of compounds. Although, there is one big issue as most of these systems are not able to work as effectively as the [NiFe] hydrogenases as their stability and performance (mostly very low TON values) leave things to be desired. Furthermore, the synthesis of these complexes is time consuming involving many reaction steps and does not represent a very cost-effective way to produce large amounts of catalysts. Looking at the [NiFe] hydrogenases, the last mimic's reactivity mainly involves redox chemistry at the nickel center. For these reasons, a transition to simple but catalytically active compounds employing only one metal was needed.

1.4 Bioinspired models of hydrogenases

As discussed in the previous part, hydrogenases are a major inspiration for the scientific community for their ability to both consume and produce hydrogen. While a lot of the models reported can very well work in both Hydrogen Oxidation Reaction (HOR) and Hydrogen Evolution Reaction (HER), the synthesis of these complexes holds a lot of difficulties. Their preparation requires a lot of synthetic steps and a lot of them have limited stability. For this reason, inspired by the active site of hydrogenases many compounds have been developed to work as catalysts toward hydrogen production but instead of prioritizing their structural similarities to the enzymes' metallic cluster, importance is given mostly to their catalytic performance and stability. Most of these complexes contain abundant first-row transition metals such as iron, nickel, cobalt and copper. One prominent example of such complexes is the iron porphyrin reported by Savéant and coworkers in 1996.[48] Iron(0) is electrochemically formed and in the presence of a weak acid Et_3NH^+, HER is observed with a turnover number (TON) of 22 for 1 hour of catalysis. A wide range of iron porphyrins has been inspired by Savéant's work (examples given in Figure 14). Dey and coworkers used a triazole moiety as a second-sphere proton transfer residue (Figure 14b), whereas Nocera and coworkers experimented with the influence of the second coordination sphere of the complexes (Figure 14c).

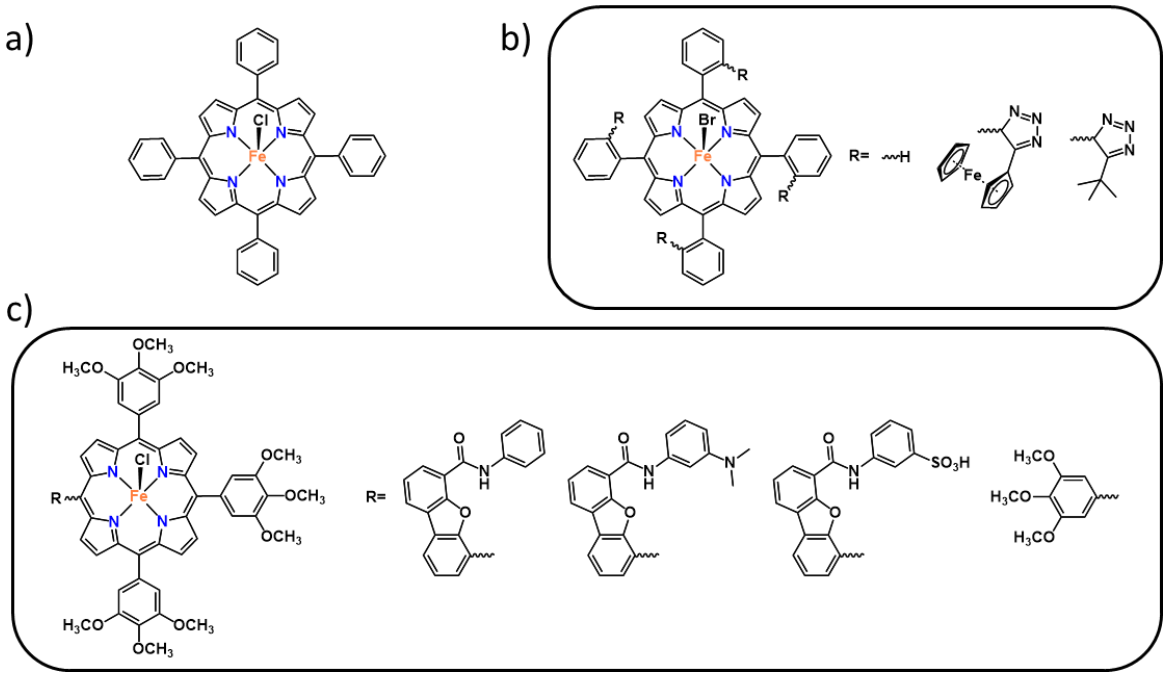

Figure 14. *Selected examples of iron porphyrin catalysts active for HER.*[48–50]

Artero and coworkers have reported on many cobalt complexes for electrocatalytic HER. One of the best is a cobaloxime (Figure 15a) reaching a TON of about 100 for 2.5 hours.[51] Another polypyridine cobalt complex was also investigated (Figure 15b) and presents the ability to change its catalytic mechanism depending on the strength of the acid used.[52] Other examples include cobalt complexes tested in acidic water solutions (pH= 2.2) for electrocatalytic hydrogen production.[53]

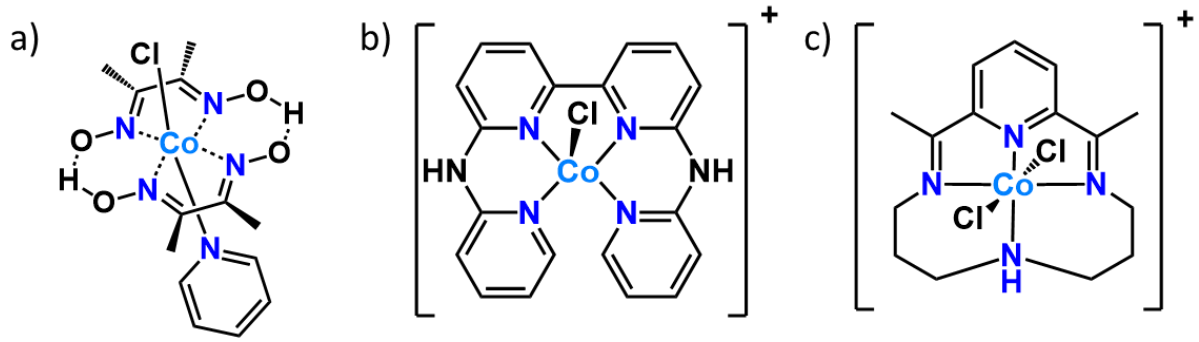

Figure 15. *Selected cobalt complexes reported as HER catalysts.*[51–53]

Copper has also been studied for the same kind of applications. The catalyst shown in Figure 16a was used in a phosphate buffer solution of pH= 2.5 with a relatively low overpotential of 420 mV.[54] A Cu(III) corrole has also been employed as a HER catalyst and was found to exhibit an incredible stability in the presence of TFA, something quite uncommon for corroles (Figure 16b).[55] Many polypyridine copper complexes have also been developed, and are able to work in mild conditions (phosphate buffer with pH= 7) to produce hydrogen reaching a TOF of 674 s^{-1} (Figure 16c).[56]

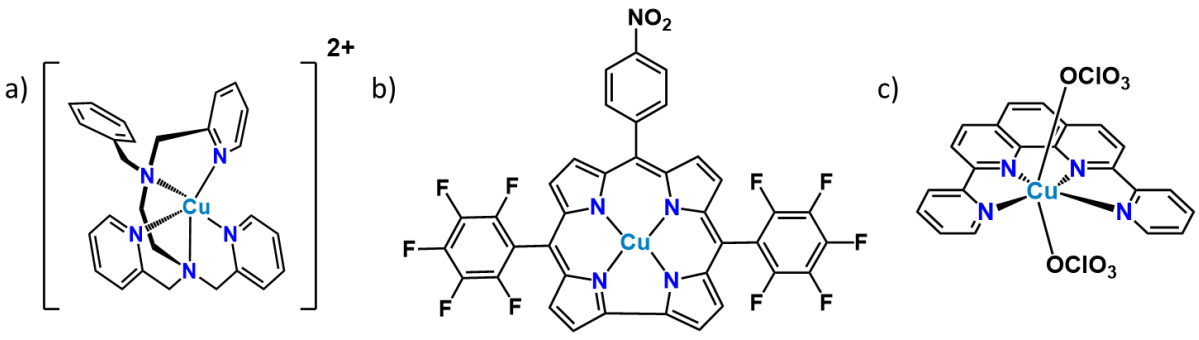

Figure 16. *Selected examples of copper catalysts active for HER.*[54–56]

Nickel plays a major role on the production or oxidation of hydrogen in the catalytic pathway of [NiFe] hydrogenases, by getting oxidized to Ni(III) in the Ni-C stage of the mechanism. For this reason, nickel holds a lot of scientific interest as the scientific community has been trying to unlock its catalytic potentials by employing a wide variety of ligands, tailored to match the electronic structures of the [NiFe] hydrogenases and their properties.

A big library of nickel square-planar complexes has been developed, all of them able to reduce protons into molecular hydrogen. The first generation is based on macrocyclic ligands with four nitrogen coordinating to a nickel moiety (Figure 17).[57,58] Complex 17a and 17b were among the first reported catalysts to produce hydrogen from water, although with low activity. It is also interesting to note that the protonation of these complexes also results in a Ni(III)-H species.[59,60]

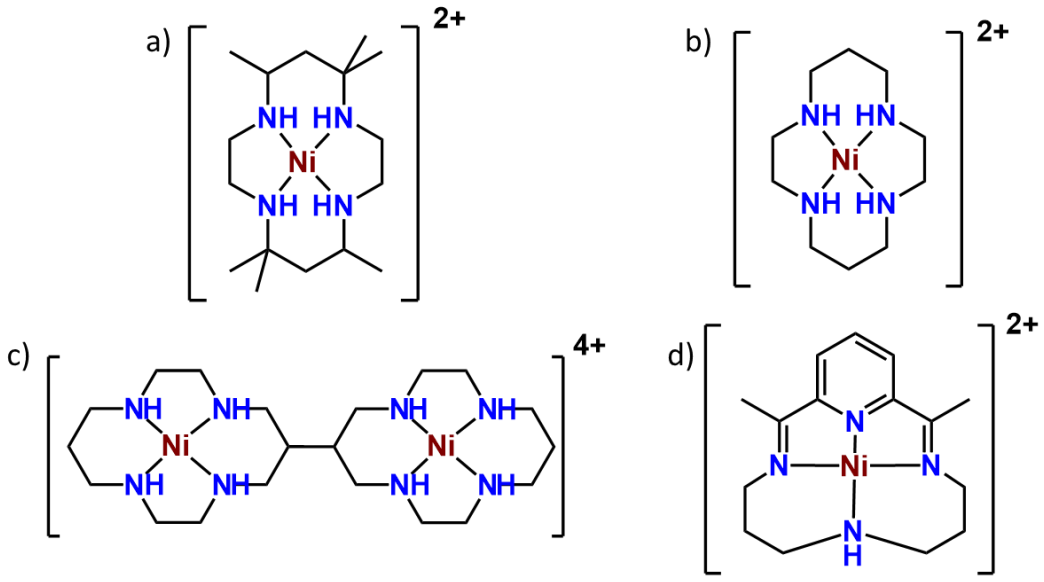

Figure 17. *Macrocyclic nickel complexes reported as HER catalysts.*[57–60]

The next generation of nickel complexes contained sulphur in the coordination sphere of the metal (Figure 18).[61–63] Although, these ligands were not tested as electrocatalysts they were proven to exchange a deuterium atom for a hydrogen one forming HD and HDO from D_2 and H_2O the same way hydrogenases do. [Ni(xbsms)] (Figure 18c), the precursor of many compounds discussed in Chapter 1.3, is also a member of this nickel-thiolate catalysts family and was shown to catalyze proton reduction in DMF, but with a low catalytic rate.[64]

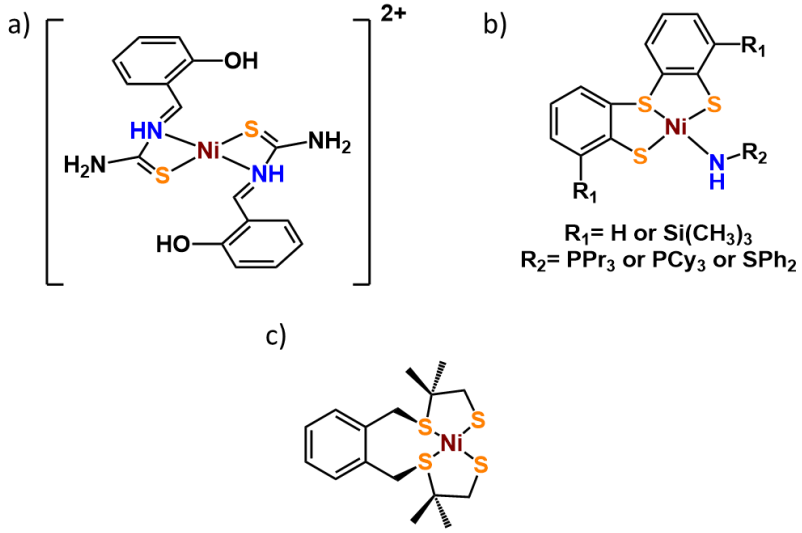

Figure 18. *Structures of complexes coordinating nickel with sulphur-containing ligands.*[61–64]

Next on the list of ligands were the implementation of phosphine containing groups (Figure 19). The first report on these complexes came from the group of Holm, which could produce hydrogen from the reduction of HCl.[65] Similar activity was exhibited by complex 19b which could produce HD or D_2 in the presence of DCl.[66] DuBois and his team also reported in a tetra phosphorous coordinated nickel complex able to both exchange H/D at a very slow rate in acetonitrile with a TOF of 0.5 s^{-1}.[67] The mechanism involves the heterolytic cleavage of hydrogen with the assistance of the amine which is eventually protonated and the hydride coordinates to the nickel center. The addition of extra amine residues resulted in the construction of way more active catalysts (Figure 19d).[68,69]

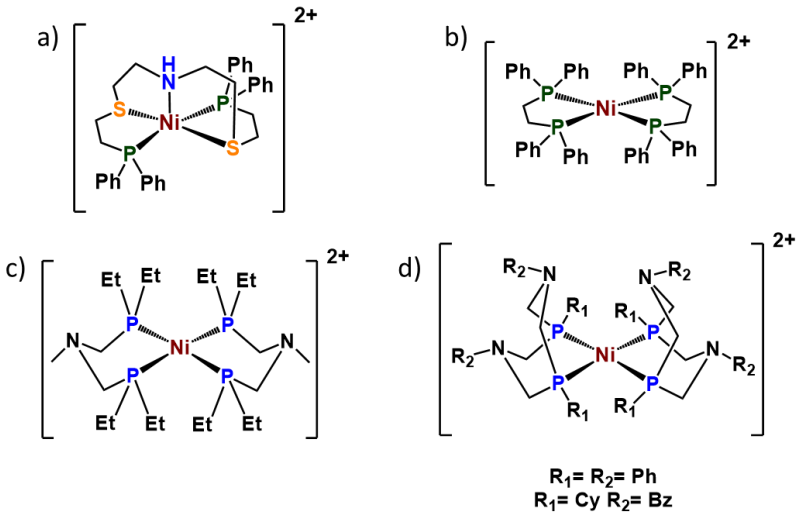

Figure 19. *Nickel complexes with phosphine ligands.*[65–69]

It is also worth noting that HOR catalysts are very rare with these complexes being only the second reports to do so after the ruthenium porphyrin that was reported by Collman and coworkers.[70]

DuBois and coworkers have also reported on the use of another nickel phosphine ligand for HER (Figure 20).[71] Their system, even up to this date, is one of the fastest producing systems in the electrocatalysis research field capable of reaching a TOF larger than 100.000 s^{-1}.

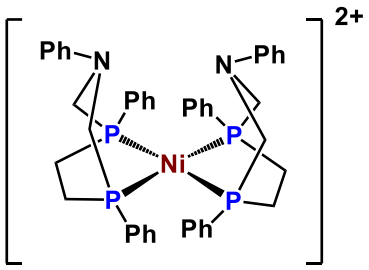

Figure 20. *Structure of the Dubois complex.*[71]

A series of metal complexes using redox active ligands like thiosemicarbazone has been investigated and their capability to behave as HER catalysts was evaluated, notably by Grapperhaus and coworkers. This group studied the catalytic activity of several of these complexes and first reported the use of a zinc complex (Figure 21a) and the metal-free ligand towards both HER and HOR.[72] Surprisingly, both molecules were shown to be active although with an overpotential of 756 mV and 1074 mV and a TOF of 1170 s^{-1} and 11700 s^{-1} for the zinc and metal-free compound, respectively.

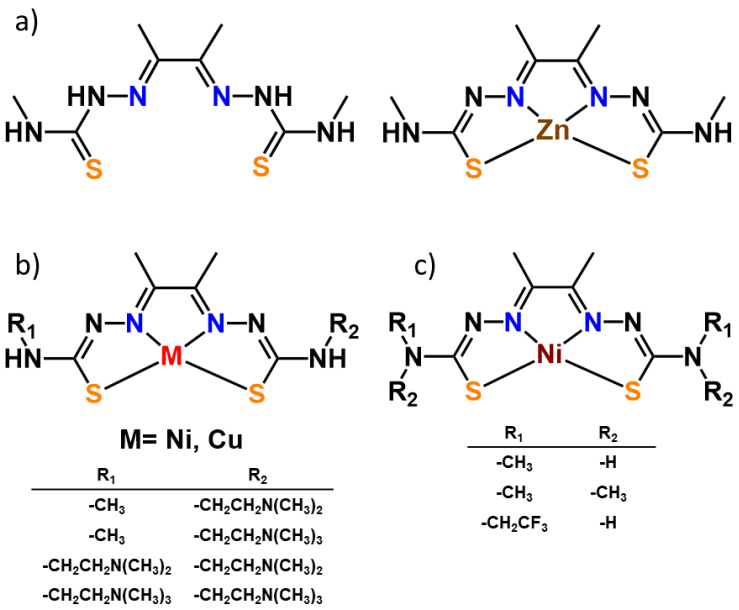

R_1	R_2
$-CH_3$	$-CH_2CH_2N(CH_3)_2$
$-CH_3$	$-CH_2CH_2N(CH_3)_3$
$-CH_2CH_2N(CH_3)_2$	$-CH_2CH_2N(CH_3)_2$
$-CH_2CH_2N(CH_3)_3$	$-CH_2CH_2N(CH_3)_3$

R_1	R_2
$-CH_3$	-H
$-CH_3$	$-CH_3$
$-CH_2CF_3$	-H

Figure 21. *First generation thiosemicarbazone-based catalysts for HER.*[72–75]

Further functionalization of the ligand and the use of different metals yielded also a family of metal-organic complexes that could electrocatalytically reduce protons to H_2.[73–75] Examples of these compounds are such as the complex families of 21b and 21c. These catalysts are obtained with relatively easy synthetic procedures and contain cheap first-row transition metals. Regarding their performances, the best nickel complex reaches a TOF of 7700 s^{-1} with an overpotential of 890 mV[73] and the best copper one has a 12000 s^{-1} TOF with a lower overpotential of 660 mV.[74] A few years later, the basic structure of the ligands changes from a bis-thiosemicabazone ligand to a thiosemicarbazone one with the inclusion of a 2-pyridinehydrazone moiety coordinating to the metal center (Figure 22). These complexes present either a ligand-assisted metal-centered reactivity or a ligand-centered mechanism depending on the nature of the metal center or the chemical substituents of the ligand.[76,77] These new complexes could all reduce protons from various proton sources with the palladium compound reaching a TOF of 8280 s^{-1} with an overpotential of 440 mV. When trying to see how further functionalization of the ligand would affect the catalysis, some very interesting results were obtained. The non-methylated form of the zinc complex works with a relatively high overpotential of 1.27 V but upon methylation while for the ligand alone, this value significantly drops to 0.57 V. For all these complexes, the proposed mechanism involves a ligand-centered reactivity that is independent of the nature of the metal center.

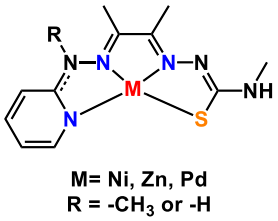

Figure 22. *Second-generation thiosemicarbazone-based catalystsfor HER.*[76,77]

In 2017 another nickel complex based on a thiosemicarbazone ligand was reported by Orio and coworkers. This compound proved to be a good catalyst for the production of hydrogen using TFA as the proton source.[78] The production capabilities of the catalyst reached a TON of 21 with an overpotential of 344 mV. The uncommon characteristic of this molecule is that it exhibits a metal-assisted ligand-centered reactivity. According to the revised mechanistic investigation based on Density-functional theory (DFT) calculations, the first two steps involve reduction and protonation steps both taking place on the ligand.[79] The reaction of the same ligand with cobalt also yielded another active electrocatalyst for HER that works in softer conditions, able to convert the protons from Et_3NH^+ into molecular hydrogen. Although this time the total production dropped, there was also a slight decrease in the overpotential requirements of the system.[80] Lastly, combining the bisthiosemicarbazone ligand with palladium, unfortunately, produced a very poorly active electrocatalyst. This was probably due to the presence of competitive mechanisms, one mediates limited H_2 production while the dominant one leads to deactivation of the catalyst through the formation of a Pd(0) species.[81]

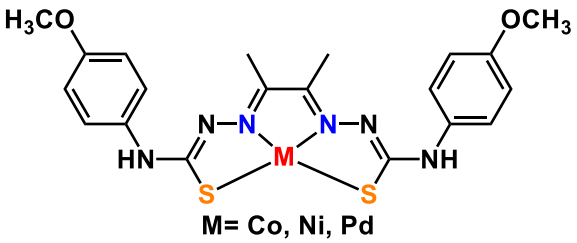

Figure 23. *Structures of the nickel, cobalt and palladium bisthiosemicarbazone catalysts active for HER.*[78–81]

The results reported by the groups of Grapperhaus and Orio suggest that the use of complexes based on thiosemicarbazone ligands show great promise in the development of easy-to-fabricate and cost-effective metal-organic compounds that can reduce efficiently protons into hydrogen. Further tailoring of the ligand can provide improved catalytic activity by tuning and controlling the electronic properties of the complexes.

1.5 Electrocatalytic Hydrogen Evolution Reactions

One of the most common ways to produce hydrogen is through water electrolysis. This reaction can be divided into two different half-cell reactions: hydrogen evolution reactions (HER) and oxygen evolution reactions (OER). HER is the reduction of water at the cathode to produce H_2, whereas OER is the oxidation of water on the anode to produce O_2 (Figure 24).

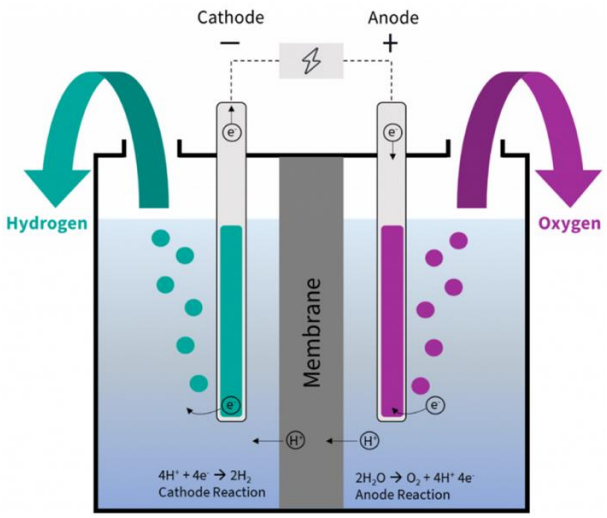

Figure 24. *Graphical representation of water electrolysis designed by International PtX Hub.*[82]

One of the main limiting factors for the use of water splitting as a way to produce hydrogen is the slow reaction kinetics due to high overpotential, a measure of the kinetic energy barriers. For this reason, it is essential to find catalysts that decrease the required overpotential mainly of HER toward efficient H_2 production.[83]

Water itself is a weak acid that can provide protons to a catalyst that later are combined with electrons to yield molecular hydrogen. Unfortunately, water is a very bad solvent for a lot of metal-organic compounds. In homogenous catalysis, water is most of the time replaced with an organic solvent (i.e. dichloromethane, acetonitrile, DMF, etc.) mixed with an acid to provide protons to the system (i.e. acetic acid, triethylammonium salts, trifluoroacetic acid, etc.)

Homogenous electrocatalytic HER consists of a simple three component-system: A source of protons (most commonly a weak acid), a solvent (organic or water depending on the catalyst) and of course, a catalyst. Finally, the system requires a controlled electron input provided by the use of a potentiostat.

To investigate the activity of a molecular HER catalyst, an electrochemical study has first to be performed and usually employs a three-electrode system using a working electrode as the cathode, a reference electrode and a counter electrode as the anode (Figure 25a). The redox behavior of a given compound is obtained from cyclic voltammetry (CV) by linearly varying the electrode potential between two limits at a specific rate while monitoring the current that develops in the electrochemical cell. CV relates the flow of electrons to chemical changes and in the present case; the resulting chemical change corresponds to the reduction of the compound under investigation (black line in Figure 25b).[84] CV is thus an invaluable tool to study electron transfer-initiated chemical reactions, which includes catalysis.

Upon substrate addition like introduction of a proton source, the recorded voltammogram can change if there is any reaction between the compound of interest and the substrate. In this case, one of these redox events – here the reduction – can become the trigger for electrocatalysis. Alternatively, the substrate can first interact with the catalyst in a chemical step. In the latter situation, one of the redox events of the substrate-catalyst adduct will trigger electrocatalysis. In the CV, this often manifests as an increase in current at the catalysis-initiating redox couple accompanied by a loss of reversibility of the redox couple, the exception being the total catalysis waveform (red line in Figure 25c).[85]

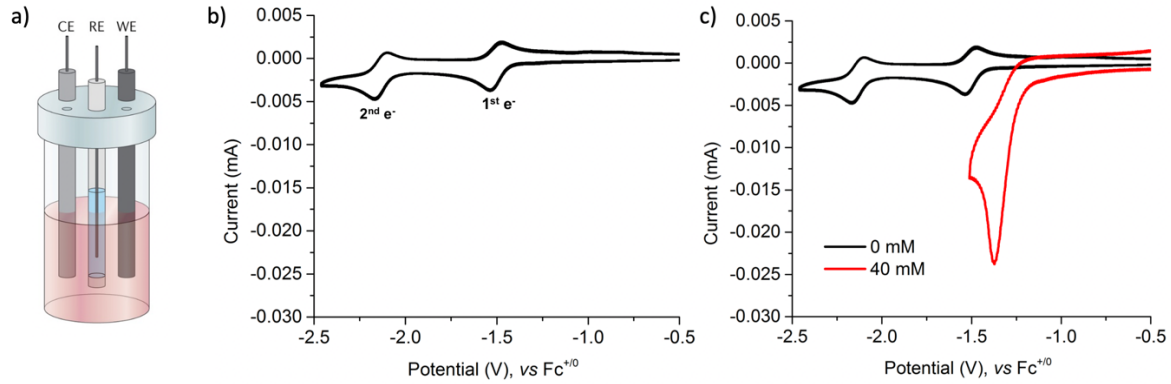

Figure 25. a) *Graphical representation of the electrochemical cell.*[86] b) *Example of cyclic voltammogram of a given complex.* c) *Example of an electrocatalytic voltammogram for the same complex in the presence of a proton source.*

The mid-wave potential of the catalytic reaction has to be calculated before any further analysis is carried out. It is calculated by measuring the average potential between the starting point of the catalytic wave and the point of maximum current achieved (green arrows in Figure 26).

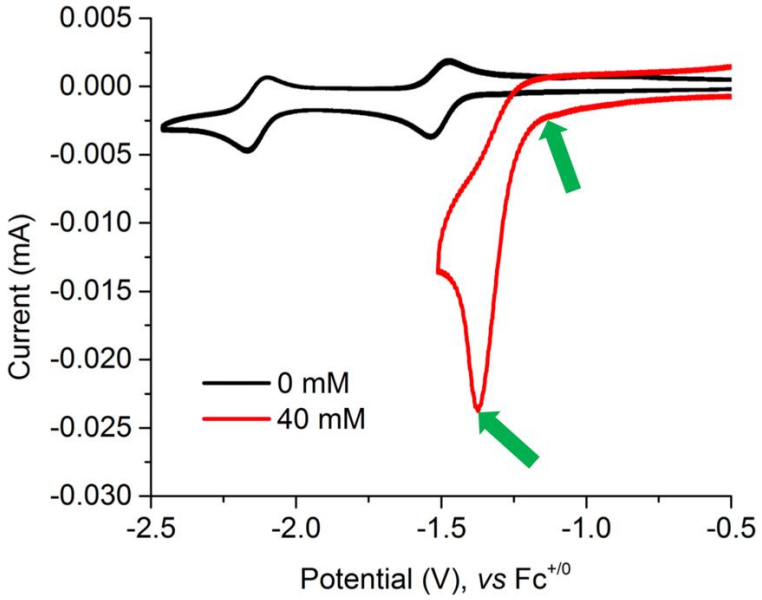

Figure 26. *Example of earliest event and maximum current of catalytic wave highlighted with green arrows.*

To support the actual formation of a catalytic product during the electrochemical measurements, one needs to perform gas analysis experiments to validate the evolution of hydrogen. Over a given period of time, we perform a bulk electrolysis experiment by applying a fixed potential that is obtained from the analysis of the voltammogram in catalytic conditions *i.e.* in presence of substrate. The recorded current is converted into the charge passing through the system while the evolved H_2 is quantified and analyzed for purity using gas chromatography. Such experiments enable verification of the stability of the catalyst upon cycling, which is a major criterion for future applications.

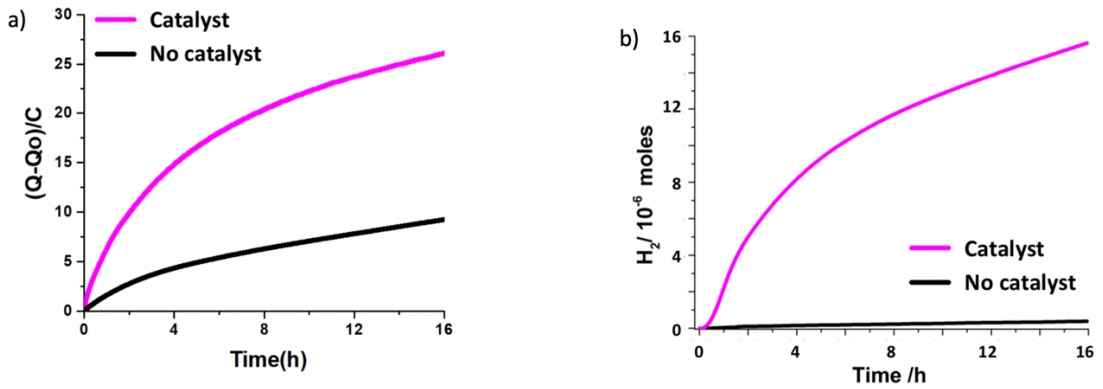

Figure 27. a) *Example of current recorded during electrolysis and converted into charge over time* b) *Example of evolved hydrogen measured over time by gas chromatography.*

Once hydrogen is proven to be detected, the catalyst can be described as active electrocatalytically and four main parameters can be extracted from the set of experimental measurements to evaluate the catalytic performances of the system under investigation.

One first important feature of the catalytic system is the overpotential (η) corresponding to the driving force of the reaction that we wish to be as small as possible since the electrochemical reduction of H^+ to H_2 proceeds at a low overpotential on a catalytic Pt. The overpotential corresponds to the difference between the applied potential at the working electrode and the equilibrium potential of the net redox reaction.[87] While different approaches have been developed over the years to evaluate the overpotential, the methodology developed by Fourmond and coworkers will be employed in this work.[41] They proposed to estimate the overpotential using the half-wave potential as reference potential and provided a simple method to measure it from cyclic voltammograms. Through the following equations, one can extract the overpotential of a catalytic reaction from cyclic voltammograms.

$$\eta = E_{cat/2} - E_{ref}$$

$$E_{ref} = E^0_{H^+/H_2} - \left(\frac{2.303 \times RT}{F}\right) \times pK_a + \varepsilon_D + \left(\frac{RT}{2F}\right) \times ln\left(2K_c^2 \times C_0 \times C^0_{H_2}\right)$$

These equations are going to be explained further in the following Chapters.

Another key factor to be drawn from hydrogen production measurements is the turnover number (TON) which shows how many catalytic cycles the system can has performed during the period of the reaction. This value is easily derived from the following equation:

$$TON = \frac{n_{hydrogen\ produced}}{n_{catalyst}}$$

where $n_{hydrogen\ produced}$ is the number of moles of H_2 that have been produced and $n_{\ catalyst}$ is the number of moles of catalyst that is used for a certain measurement. TON provides the efficiency of the system in production.

The faradaic efficiency or faradaic yield (FY) is another key parameter and corresponds to a percentage value providing insight into the selectivity of the catalyst for hydrogen production. The FY describes how many electrons provided to the system are used for the reaction of hydrogen evolution and it is calculated using the following formula:

$$FY\ (\%) = \frac{n_{hydrogen\ produced}}{n_{theoritical\ hydrogen\ produced}} * 100$$

$$n_{theoretical\ hydrogen\ produced} = \frac{Q}{2 * F}$$

where Q is the total charge that has passed through the system and F is the Faraday constant. The FY reflecting the selectivity of the reaction, it will show whether the hydrogen production is favored over all other processes happening inside the reactor.

The last observable of interest is the turnover frequency (TOF) which provides information on the speed of the catalysis. TOF can be calculated in more than one way with the most common one used for electrocatalytic HER provided by the following formula:

$$i_p = 0.4463 \times FA \times [cat] \times \sqrt{\frac{F\nu D}{RT}}$$

$$i_{cat} = nFA \times [cat] \times \sqrt{Dk[H^+]^2}$$

$$TOF = k_{obs} = 1.94 \times v \left[{}^{i_{cat}}\!/_{i_p} \right]^2$$

with i_p and i_{cat} being the peak currents without and with substrate, respectively. Their evaluation from cyclic voltammetry will be described in greater detail in the following Chapters.

All of these key parameters for catalysis, namely η, TON, FY, and TOF, characterize the system and give us a way to compare different systems with respect to their catalytic performances. The most common comparison being made is between catalysts studied in similar experimental conditions. However, what makes a “good” catalyst eventually? A “good” catalyst should need a very small amount of energy to work (small overpotential) and should produce a large amount of hydrogen (big TON) with quite a good speed (big TOF). The selectivity of the system is vital so a big faradaic yield is also important. Finding a catalyst that can fulfill or even balance all these criteria can provide one possible solution to one of the huge environmental problems we are currently facing.

1.6 Aim and scope of thesis

The study of [NiFe]-hydrogenases has shined light on the processes involving hydrogen production and oxidation. As many important features of these enzymes have been decoded, the research on designing efficient low-weight molecular catalysts that are able to perform HER and HOR, as effectively as the enzymes, has exploded.

The aim of this thesis is the synthesis, characterization and use of nickel complexes based on thiosemicarbazone ligands to achieve efficient hydrogen evolution. Chemical tailoring of the ligands was performed to investigate how different chemical groups affect the electrochemical properties of the complexes (Figure 28a) but also how the position of the methoxy group on the phenyl ring (Figure 28b) will affect the complexes' properties and therefore their catalytic performance, if any is present.

A trinuclear nickel complex has also been investigated for the same application and we evaluated whether the use of more than one active site will work and improve the activity toward hydrogen production (Figure 28c).

Lastly, a series of photocatalytic systems has been designed by employing nickel and cobalt complexes to investigate if these catalysts can also work in presence of metal-free photosensitizers to mediate the photoproduction of hydrogen (Figure 28d).

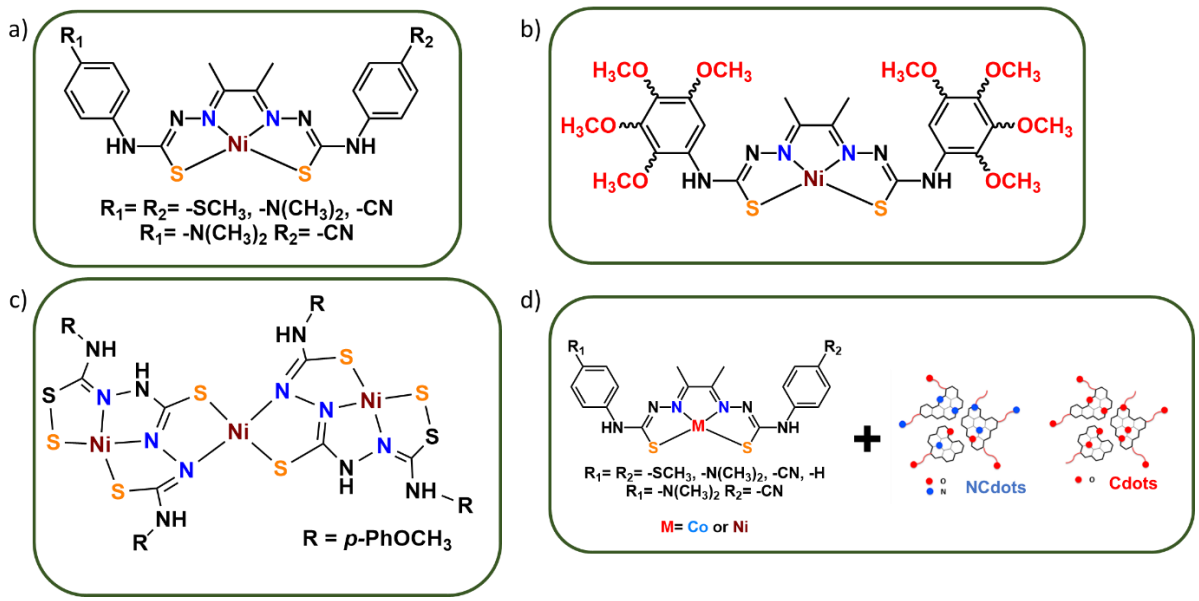

Figure 28. *Structure of complexes studied in this work.*

References

1. IEA – International Energy Agency. *IEA* https://www.iea.org.
2. Forum, W. E. How electrification can supercharge the energy transition. *The European Sting - Critical News & Insights on European Politics, Economy, Foreign Affairs, Business & Technology - europeansting.com* https://europeansting.com/2019/04/25/how-electrification-can-supercharge-the-energy-transition/ (2019).
3. Boretti, A. & Banik, B. K. Advances in Hydrogen Production from Natural Gas Reforming. *Adv Energy Sustain Res* **2**, 2100097 (2021).
4. Carmo, M., Fritz, D. L., Mergel, J. & Stolten, D. A comprehensive review on PEM water electrolysis. *International Journal of Hydrogen Energy* **38**, 4901–4934 (2013).
5. Stephenson, M. & Stickland, L. H. XXVII. HYDROGENASE: A BACTERIAL ENZYME ACTIVATING MOLECULAR HYDROGEN. I. THE PROPERTIES OF THE ENZYME.
6. Jones, A. K., Sillery, E., Albracht, S. P. J. & Armstrong, F. A. Direct comparison of the electrocatalytic oxidation of hydrogen by an enzyme and a platinum catalyst. *Chem. Commun.* 866–867 (2002).
7. Volbeda, A. *et al.* Crystal structure of the nickel–iron hydrogenase from Desulfovibrio gigas. *Nature* **373**, 580–587 (1995).
8. Nicolet, Y., Piras, C., Legrand, P., Hatchikian, C. E. & Fontecilla-Camps, J. C. Desulfovibrio desulfuricans iron hydrogenase: the structure shows unusual coordination to an active site Fe binuclear center. *Structure* **7**, 13–23 (1999).
9. X-ray Crystal Structure of the Fe-Only Hydrogenase (CpI) from Clostridium pasteurianum to 1.8 Angstrom Resolution | Science.
10. Lubitz, W., Ogata, H., Rüdiger, O. & Reijerse, E. Hydrogenases. *Chem. Rev.* **114**, 4081–4148 (2014).
11. Pershad, H. R. *et al.* Catalytic Electron Transport in *Chromatium vinosum* [NiFe]-Hydrogenase: Application of Voltammetry in Detecting Redox-Active Centers and Establishing That Hydrogen Oxidation Is Very Fast Even at Potentials Close to the Reversible H^+/H_2 Value. *Biochemistry* **38**, 8992–8999 (1999).
12. Madden, C. *et al.* Catalytic Turnover of [FeFe]-Hydrogenase Based on Single-Molecule Imaging. *J. Am. Chem. Soc.* **134**, 1577–1582 (2012).
13. Simmons, T. R., Berggren, G., Bacchi, M., Fontecave, M. & Artero, V. Mimicking hydrogenases: From biomimetics to artificial enzymes. *Coordination Chemistry Reviews* **270–271**, 127–150 (2014).
14. Volbeda, A. *et al.* Structure of the [NiFe] Hydrogenase Active Site: Evidence for Biologically Uncommon Fe Ligands. *J. Am. Chem. Soc.* **118**, 12989–12996 (1996).
15. Canaguier, S., Artero, V. & Fontecave, M. Modelling NiFe hydrogenases: nickel-based electrocatalysts for hydrogen production. *Dalton Trans.* 315–325 (2008).
16. Montet, Y. *et al.* Gas access to the active site of Ni-Fe hydrogenases probed by X-ray crystallography and molecular dynamics. *Nat Struct Mol Biol* **4**, 523–526 (1997).

17. Léger, C., Dementin, S., Bertrand, P., Rousset, M. & Guigliarelli, B. Inhibition and Aerobic Inactivation Kinetics of *Desulfovibrio fructosovorans* NiFe Hydrogenase Studied by Protein Film Voltammetry. *J. Am. Chem. Soc.* **126**, 12162–12172 (2004).
18. Leroux, F. *et al.* Experimental approaches to kinetics of gas diffusion in hydrogenase. *Proc. Natl. Acad. Sci. U.S.A.* **105**, 11188–11193 (2008).
19. Ogata, H. *et al.* Structural Studies of the Carbon Monoxide Complex of [NiFe]hydrogenase from *Desulfovibrio vulgaris* Miyazaki F: Suggestion for the Initial Activation Site for Dihydrogen. *J. Am. Chem. Soc.* **124**, 11628–11635 (2002).
20. Tsay, C. & Peters, J. C. Thermally stable N2 and H2 adducts of cationic nickel(ii). *Chem. Sci.* **3**, 1313 (2012).
21. Niu, S. & Hall, M. B. Modeling the Active Sites in Metalloenzymes 5. The Heterolytic Bond Cleavage of H_2 in the [NiFe] Hydrogenase of *Desulfovibrio gigas* by a Nucleophilic Addition Mechanism. *Inorg. Chem.* **40**, 6201–6203 (2001).
22. Krämer, T., Kampa, M., Lubitz, W., van Gastel, M. & Neese, F. Theoretical Spectroscopy of the Ni^{II} Intermediate States in the Catalytic Cycle and the Activation of [NiFe] Hydrogenases. *ChemBioChem* **14**, 1898–1905 (2013).
23. Whitehead, J. P., Gurbiel, R. J., Bagyinka, C., Hoffman, B. M. & Maroney, M. J. The hydrogen binding site in hydrogenase: 35-GHz ENDOR and XAS studies of the nickel-C (reduced and active form) and the Ni-L photoproduct. *J. Am. Chem. Soc.* **115**, 5629–5635 (1993).
24. Brecht, M., van Gastel, M., Buhrke, T., Friedrich, B. & Lubitz, W. Direct Detection of a Hydrogen Ligand in the [NiFe] Center of the Regulatory H_2-Sensing Hydrogenase from *Ralstonia e utropha* in Its Reduced State by HYSCORE and ENDOR Spectroscopy. *J. Am. Chem. Soc.* **125**, 13075–13083 (2003).
25. Foerster, S., Gastel, M. van, Brecht, M. & Lubitz, W. An orientation-selected ENDOR and HYSCORE study of the Ni-C active state of Desulfovibrio vulgaris Miyazaki F hydrogenase. *J Biol Inorg Chem* **10**, 51–62 (2005).
26. Pandelia, M.-E., Infossi, P., Stein, M., Giudici-Orticoni, M.-T. & Lubitz, W. Spectroscopic characterization of the key catalytic intermediate Ni–C in the O_2-tolerant [NiFe] hydrogenase I from Aquifex aeolicus: evidence of a weakly bound hydride. *Chem. Commun.* **48**, 823–825 (2012).
27. Vincent, J. F. V., Bogatyreva, O. A., Bogatyrev, N. R., Bowyer, A. & Pahl, A.-K. Biomimetics: its practice and theory. *J. R. Soc. Interface.* **3**, 471–482 (2006).
28. Harkness, J. M. In Appreciation**:** A Lifetime of Connections: Otto Herbert Schmitt, 1913 - 1998. *Physics in Perspective (PIP)* **4**, 456–490 (2002).
29. Lai, C.-H., Reibenspies, J. H. & Darensbourg, M. Y. Thiolate Bridged Nickel–Iron Complexes Containing both Iron(0) and Iron(II) Carbonyls. *Angew. Chem. Int. Ed. Engl.* **35**, 2390–2393 (1996).
30. Tard, C. & Pickett, C. J. Structural and Functional Analogues of the Active Sites of the [Fe]-, [NiFe]-, and [FeFe]-Hydrogenases. *Chem. Rev.* **109**, 2245–2274 (2009).
31. Zhu, W. *et al.* Modulation of the electronic structure and the Ni–Fe distance in heterobimetallic models for the active site in [NiFe]hydrogenase. *Proc. Natl. Acad. Sci. U.S.A.* **102**, 18280–18285 (2005).

32. Verhagen, J. A. W., Lutz, M., Spek, A. L. & Bouwman, E. Synthesis and Characterisation of New Nickel-Iron Complexes with an S_4 Coordination Environment around the Nickel Centre. *Eur. J. Inorg. Chem.* **2003**, 3968–3974 (2003).

33. Li, Z., Ohki, Y. & Tatsumi, K. Dithiolato-Bridged Dinuclear Iron−Nickel Complexes $[Fe(CO)_2(CN)_2(\mu\text{-}SCH_2Cl_2CH_2S)Ni(S_2CNR_2)]^-$ Modeling the Active Site of [NiFe] Hydrogenase. *J. Am. Chem. Soc.* **127**, 8950–8951 (2005).

34. Sellmann, D., Geipel, F., Lauderbach, F. & Heinemann, F. W. [(C6H4S2)Ni(μ-'S3')Fe(CO)(PMe3)2]: A Dinuclear [NiFe] Complex Modeling the [(RS)2Ni(μ-SR)2Fe(CO)(L)2] Core of [NiFe] Hydrogenase Centers. *Angew. Chem. Int. Ed.* **41**, 632–634 (2002).

35. Oudart, Y., Artero, V., Pécaut, J. & Fontecave, M. $[Ni(xbsms)Ru(CO)_2Cl_2]$: A Bioinspired Nickel−Ruthenium Functional Model of [NiFe] Hydrogenase. *Inorg. Chem.* **45**, 4334–4336 (2006).

36. Oudart, Y., Artero, V., Pécaut, J., Lebrun, C. & Fontecave, M. Dinuclear Nickel–Ruthenium Complexes as Functional Bio-Inspired Models of [NiFe] Hydrogenases. *Eur. J. Inorg. Chem.* **2007**, 2613–2626 (2007).

37. Canaguier, S., Fontecave, M. & Artero, V. Cp^{*-}-Ruthenium–Nickel-Based H_2-Evolving Electrocatalysts as Bio-inspired Models of NiFe Hydrogenases. *Eur. J. Inorg. Chem.* **2011**, 1094–1099 (2011).

38. Barton, B. E. & Rauchfuss, T. B. Hydride-Containing Models for the Active Site of the Nickel−Iron Hydrogenases. *J. Am. Chem. Soc.* **132**, 14877–14885 (2010).

39. Canaguier, S. *et al.* A structural and functional mimic of the active site of NiFe hydrogenases. *Chem. Commun.* **46**, 5876 (2010).

40. Weber, K. *et al.* A Functional [NiFe]-Hydrogenase Model Compound That Undergoes Biologically Relevant Reversible Thiolate Protonation. *J. Am. Chem. Soc.* **134**, 20745–20755 (2012).

41. Fourmond, V., Jacques, P.-A., Fontecave, M. & Artero, V. H_2 Evolution and Molecular Electrocatalysts: Determination of Overpotentials and Effect of Homoconjugation. *Inorg. Chem.* **49**, 10338–10347 (2010).

42. Fourmond, V. *et al.* A nickel–manganese catalyst as a biomimic of the active site of NiFe hydrogenases: a combined electrocatalytical and DFT mechanistic study. *Energy Environ. Sci.* **4**, 2417 (2011).

43. Song, L.-C., Li, J.-P., Xie, Z.-J. & Song, H.-B. Synthesis, Structural Characterization, and Electrochemical Properties of Dinuclear Ni/Mn Model Complexes for the Active Site of [NiFe]-Hydrogenases. *Inorg. Chem.* **52**, 11618–11626 (2013).

44. Ogo, S. *et al.* A Functional [NiFe]Hydrogenase Mimic That Catalyzes Electron and Hydride Transfer from H_2. *Science* **339**, 682–684 (2013).

45. Ogo, S. *et al.* [NiFe], [FeFe], and [Fe] hydrogenase models from isomers. *Sci. Adv.* **6**, eaaz8181 (2020).

46. Manor, B. C. & Rauchfuss, T. B. Hydrogen Activation by Biomimetic [NiFe]-Hydrogenase Model Containing Protected Cyanide Cofactors. *J. Am. Chem. Soc.* **135**, 11895–11900 (2013).

47. Brazzolotto, D. *et al.* Nickel-centred proton reduction catalysis in a model of [NiFe] hydrogenase. *Nature Chem* **8**, 1054–1060 (2016).
48. Bhugun, I., Lexa, D. & Savéant, J.-M. Homogeneous Catalysis of Electrochemical Hydrogen Evolution by Iron(0) Porphyrins. *J. Am. Chem. Soc.* **118**, 3982–3983 (1996).
49. Rana, A., Mondal, B., Sen, P., Dey, S. & Dey, A. Activating Fe(I) Porphyrins for the Hydrogen Evolution Reaction Using Second-Sphere Proton Transfer Residues. *Inorg. Chem.* **56**, 1783–1793 (2017).
50. Graham, D. J. & Nocera, D. G. Electrocatalytic H $_2$ Evolution by Proton-Gated Hangman Iron Porphyrins. *Organometallics* **33**, 4994–5001 (2014).
51. Razavet, M., Artero, V. & Fontecave, M. Proton Electroreduction Catalyzed by Cobaloximes: Functional Models for Hydrogenases.
52. Queyriaux, N. *et al.* Electrocatalytic Hydrogen Evolution with a Cobalt Complex Bearing Pendant Proton Relays: Acid Strength and Applied Potential Govern Mechanism and Stability. *J. Am. Chem. Soc.* **142**, 274–282 (2020).
53. McCrory, C. C. L., Uyeda, C. & Peters, J. C. Electrocatalytic Hydrogen Evolution in Acidic Water with Molecular Cobalt Tetraazamacrocycles. *J. Am. Chem. Soc.* **134**, 3164–3170 (2012).
54. Zhang, P., Wang, M., Yang, Y., Yao, T. & Sun, L. A Molecular Copper Catalyst for Electrochemical Water Reduction with a Large Hydrogen-Generation Rate Constant in Aqueous Solution. *Angew. Chem.* **126**, 14023–14027 (2014).
55. Lei, H. *et al.* Reactivity and Mechanism Studies of Hydrogen Evolution Catalyzed by Copper Corroles. *ACS Catal.* **5**, 5145–5153 (2015).
56. Xin, Z.-J. *et al.* Hydrogen production in a neutral aqueous solution with a water-soluble copper complex. *International Journal of Hydrogen Energy* **42**, 4202–4207 (2017).
57. Fisher, B. J. & Eisenberg, R. Electrocatalytic reduction of carbon dioxide by using macrocycles of nickel and cobalt. *J. Am. Chem. Soc.* **102**, 7361–7363 (1980).
58. Collin, J. P., Jouaiti, A. & Sauvage, J. P. Electrocatalytic properties of (tetraazacyclotetradecane)nickel(2+) and Ni2(biscyclam)4+ with respect to carbon dioxide and water reduction. *Inorg. Chem.* **27**, 1986–1990 (1988).
59. Efros, L. L., Thorp, H. H., Brudvig, G. W. & Crabtree, R. H. Towards a functional model of hydrogenase: electrocatalytic reduction of protons to dihydrogen by a nickel macrocyclic complex. *Inorg. Chem.* **31**, 1722–1724 (1992).
60. Kelly, C. A., Mulazzani, Q. G., Venturi, M., Blinn, E. L. & Rodgers, M. A. J. The Thermodynamics and Kinetics of CO2 and H+ Binding to Ni(cyclam)+ in Aqueous Solution. *J. Am. Chem. Soc.* **117**, 4911–4919 (1995).
61. Schulte, G., Luo, X.-L., Crabtree, R. H. & Zimmer, M. Functional Modeling of Ni,Fe Hydrogenases: A Nickel Complex in anN,O,S Environment. *Angew. Chem. Int. Ed. Engl.* **30**, 193–194 (1991).
62. Sellmann, D., Geipel, F. & Moll, M. [Ni(NHPnPr3)(`S3')], the First Nickel Thiolate Complex Modeling the Nickel Cysteinate Site and Reactivity of [NiFe] Hydrogenase. *Angewandte Chemie International Edition* **39**, 561–563 (2000).

63. Sellmann, D., Prakash, R. & Heinemann, F. W. Activation of H_2 and CO by Sulfur-Rich Nickel Model Complexes for [NiFe] Hydrogenases and CO Dehydrogenases. *Eur. J. Inorg. Chem.* **2004**, 1847–1858 (2004).

64. Verhagen, J. A. W., Ellis, D. D., Lutz, M., Spek, A. L. & Bouwman, E. Synthesis, characterisation and crystal structures of new nickel complexes in S4 coordination spheres; an unprecedented rearrangement during ligand synthesis. *J. Chem. Soc., Dalton Trans.* 1275–1280 (2002)

65. James, T. L., Cai, L., Muetterties, M. C. & Holm, R. H. Dihydrogen Evolution by Protonation Reactions of Nickel(I). *Inorg. Chem.* **35**, 4148–4161 (1996).

66. Henderson, R. A. Protonation mechanisms of Nickel Complexes Relevant to Industrial and Biological Catalysis. *Journal of Chemical Research* **2002**, 407–411 (2002).

67. Curtis, C. J. *et al.* $[Ni(Et_2PCH_2NMeCH_2PEt_2)_2]^{2+}$ as a Functional Model for Hydrogenases. *Inorg. Chem.* **42**, 216–227 (2003).

68. Wilson, A. D. *et al.* Hydrogen Oxidation and Production Using Nickel-Based Molecular Catalysts with Positioned Proton Relays. *J. Am. Chem. Soc.* **128**, 358–366 (2006).

69. Wilson, A. D. *et al.* Nature of hydrogen interactions with Ni(II) complexes containing cyclic phosphine ligands with pendant nitrogen bases. *Proc. Natl. Acad. Sci. U.S.A.* **104**, 6951–6956 (2007).

70. Collman, J. P. *et al.* Dihydrogen complexes of metalloporphyrins: characterization and catalytic hydrogen oxidation activity. *J. Am. Chem. Soc.* **114**, 5654–5664 (1992).

71. Helm, M. L., Stewart, M. P., Bullock, R. M., DuBois, M. R. & DuBois, D. L. A Synthetic Nickel Electrocatalyst with a Turnover Frequency Above 100,000 s^{-1} for H_2 Production. *Science* **333**, 863–866 (2011).

72. Haddad, A. Z., Garabato, B. D., Kozlowski, P. M., Buchanan, R. M. & Grapperhaus, C. A. Beyond Metal-Hydrides: Non-Transition-Metal and Metal-Free Ligand-Centered Electrocatalytic Hydrogen Evolution and Hydrogen Oxidation. *J. Am. Chem. Soc.* **138**, 7844–7847 (2016).

73. Calvary, C. A. *et al.* Synthesis, Characterization, and HER Activity of Pendant Diamine Derivatives of NiATSM. *Eur. J. Inorg. Chem.* **2019**, 3782–3790 (2019).

74. Calvary, C. A. *et al.* Copper bis(thiosemicarbazone) Complexes with Pendent Polyamines: Effects of Proton Relays and Charged Moieties on Electrocatalytic HER. *Eur. J. Inorg. Chem.* **2021**, 267–275 (2021).

75. Gupta, A. J. *et al.* Effect of Stacking Interactions on the Translation of Structurally Related Bis(thiosemicarbazonato)nickel(II) HER Catalysts to Modified Electrode Surfaces. *Inorg. Chem.* **58**, 12025–12039 (2019).

76. Cronin, S. P. *et al.* Utilizing Charge Effects and Minimizing Intramolecular Proton Rearrangement to Improve the Overpotential of a Thiosemicarbazonato Zinc HER Catalyst. *Inorg. Chem.* **58**, 12986–12997 (2019).

77. Phipps, C. A. *et al.* Ligand-Centered Hydrogen Evolution with Ni(II) and Pd(II)DMTH. *Inorg. Chem.* **61**, 9792–9800 (2022).

78. Straistari, T. *et al.* A Thiosemicarbazone-Nickel(II) Complex as Efficient Electrocatalyst for Hydrogen Evolution. *ChemCatChem* **9**, 2262–2268 (2017).

79. Barrozo, A. & Orio, M. Unraveling the catalytic mechanisms of H_2 production with thiosemicarbazone nickel complexes. *RSC Adv.* **11**, 5232–5238 (2021).
80. Straistari, T. *et al.* Hydrogen Evolution Reactions Catalyzed by a Bis(thiosemicarbazone) Cobalt Complex: An Experimental and Theoretical Study. *Chem. Eur. J.* **24**, 8779–8786 (2018).
81. Straistari, T. *et al.* Influence of the Metal Ion on the Electrocatalytic Hydrogen Production by a Thiosemicarbazone Palladium Complex. *Eur. J. Inorg. Chem.* **2018**, 2259–2266 (2018).
82. Water electrolysis explained – the basis for most Power-to-X processes. *PtX Hub* https://ptx-hub.org/water-electrolysis-explained/ (2021).
83. Wang, S., Lu, A. & Zhong, C.-J. Hydrogen production from water electrolysis: role of catalysts. *Nano Convergence* **8**, 4 (2021).
84. Elgrishi, N. *et al.* A Practical Beginner's Guide to Cyclic Voltammetry. *J. Chem. Educ.* **95**, 197–206 (2018).
85. Lee, K. J., McCarthy, B. D. & Dempsey, J. L. On decomposition, degradation, and voltammetric deviation: the electrochemist's field guide to identifying precatalyst transformation. *Chem. Soc. Rev.* **48**, 2927–2945 (2019).
86. Lee, K. J., Elgrishi, N., Kandemir, B. & Dempsey, J. L. Electrochemical and spectroscopic methods for evaluating molecular electrocatalysts. *Nat Rev Chem* **1**, 0039 (2017).
87. Nutting, J. E., Gerken, J. B., Stamoulis, A. G., Bruns, D. L. & Stahl, S. S. "How Should I Think about Voltage? What Is Overpotential?": Establishing an Organic Chemistry Intuition for Electrochemistry. *J. Org. Chem.* **86**, 15875–15885 (2021).

Chapter 2: Ligand chemical tailoring of thiosemicarbazone nickel complexes for electrocatalytic hydrogen production

2.1 Introduction

A nickel complex based on a thiosemicarbazone ligand bearing methoxy substituents, NiTSC-OCH_3, was previously reported in our lab.[1] The use of the NiTSC-OCH_3 complex provided an active hydrogen-producing electrocatalyst. In our pursuit of improving its catalytic performances, we investigated the substitution of the methoxy group of the phenyl ring with three different groups with various electronic properties (Figure 1). Based on their Hammett σ constants, we modified our parent thiosemicarbazone ligand and consequently, we synthesized three different symmetric ligands and an asymmetric one. Two electron-donating groups were employed, thiomethyl (-SCH_3) and dimethylamino (-$N(CH_3)_2$), and a cyano moiety (-CN) was used as an electron-withdrawing group. The asymmetric ligand was formed to investigate the effect of a possible push-pull effect on the electronic structure of the deriving complex by substituting the methoxy group with a -CN and a -$N(CH_3)_2$ moiety. This new family of complexes supposedly displays a wide range of electron-donating abilities. We evaluated their hydrogen evolution capabilities to determine the impact of these chemical changes to further understand how tailoring our ligands' electronic properties can affect the catalytic activity.

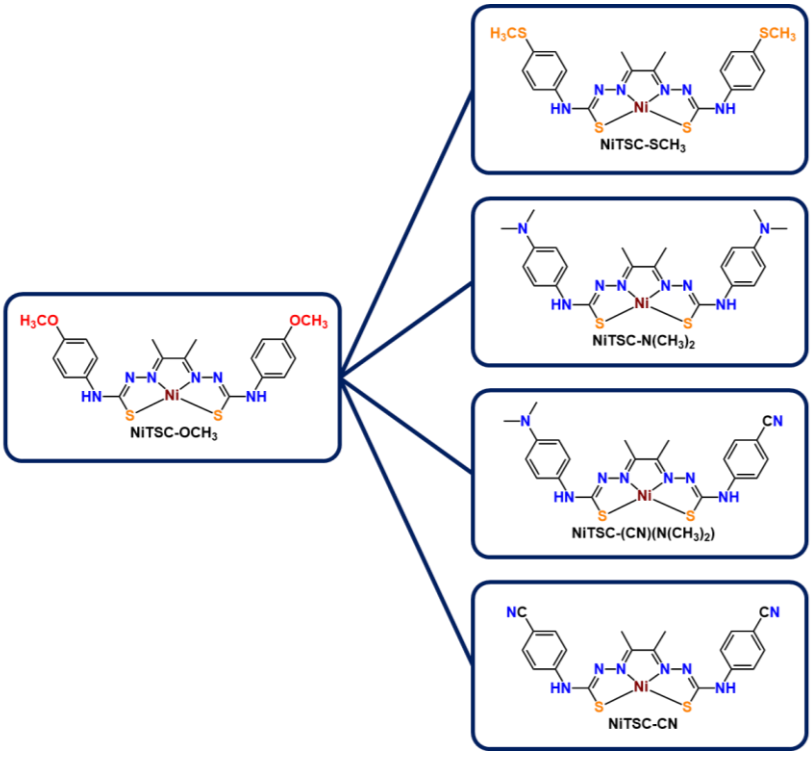

Figure 1. *Structures of NiTSC-R series derived from the parent NiTSC-OCH_3 complex.*

2.2 Results and Discussion

2.2.1 Synthesis and Characterization

The synthesis of the new family of ligands followed a slightly modified protocol for the parent bisemithiocarbazone ligand containing the methoxy group.[1] Upon the metalation reaction, the new complexes were characterized by NMR spectroscopy and HRMS ESI. Attempts were made to obtain suitable crystals for X-ray diffraction analysis for the NiTSC-R complexes, but we were successful for only two of these compounds. For the NiTSC-SCH_3 (Figure 2), slow evaporation of a THF solution provided us with crystals suitable for analysis, whereas for the NiTSC-CN complex, a vapor diffusion technique was used with DMF and ethanol as the solvents (see details in experimental section).

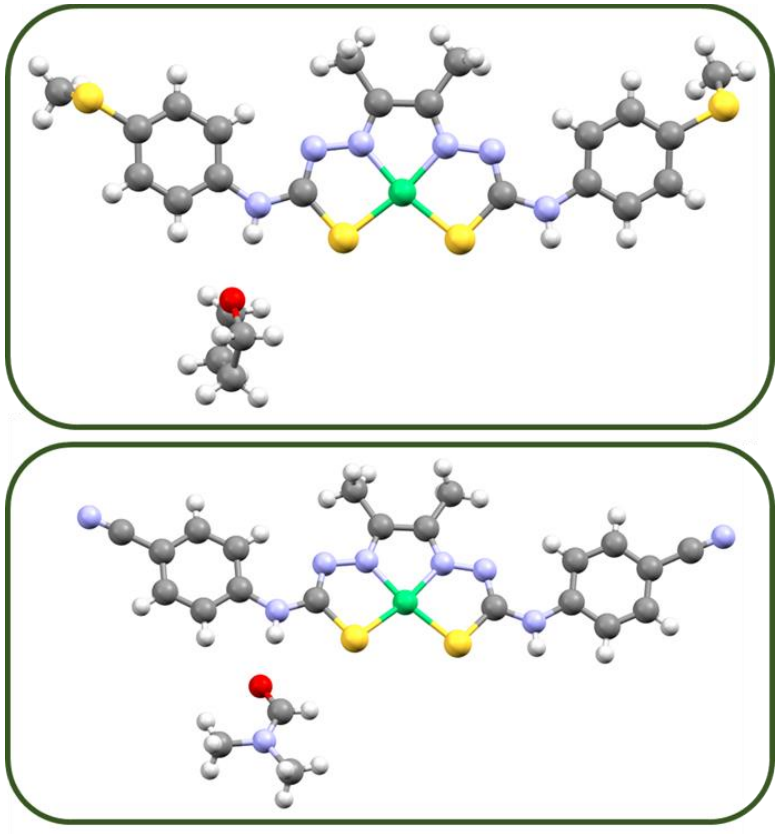

Figure 2. *X-ray crystal structure of NiTSC-SCH_3 (top) and NiTSC-CN (bottom) complexes.*

We also recorded the UV-vis spectra of the complexes in DMF. All complexes displayed an absorption band around 445-515 nm (Table 1). This absorption band is assigned to a d-d transition based on the previous computational analysis performed on the parent complex NiTSC-OCH_3.[1] The NiTSC-(CN)($N(CH_3)_2$ complex displays two absorption bands due to its asymmetric nature affecting the electron density distribution of the ligand upon excitation resulting in two high-energy absorption bands (Figure 3). The shift of the main absorption bands is attributed to the different electronic donating properties of the phenyl ring substituents ($-N(CH_3)_2$ > $-OCH_3$ > $-SCH_3$ > -CN). The strong electron-donating abilities of the $-N(CH_3)_2$ shift the band towards the red region, whereas the electron-withdrawing -CN shifts the band towards the blue region.

Table 1. *Selected spectral features from the electronic absorption spectra of NiTSC-R series in DMF.*

Complex	λ (nm)	ε ($M^{-1}*cm^{-1}$)
NiTSC-SCH₃	471	20715
	703	784
NiTSC-(CN)(N(CH₃)₂)	400/490	13816/9184
	735	771
NiTSC-N(CH₃)₂	514	16775
	716	2187
NiTSC-CN	445	23086
	750	2123

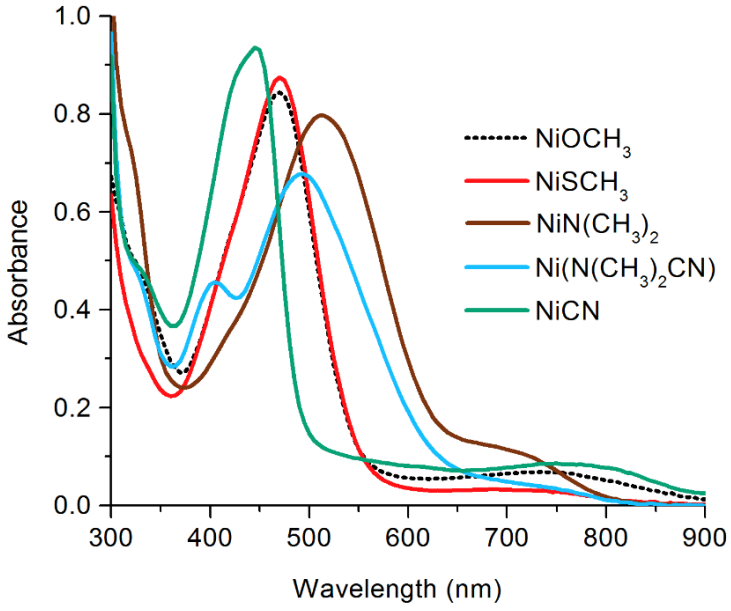

Figure 3. *UV-vis spectra of the NiTSC-R series including the NiTSC-OCH_3 reference complex.*

2.2.2 Electrochemical Investigation

Cyclic voltammograms were recorded in an inert atmosphere and at room temperature. The solutions were containing a supporting electrolyte tetrabutylammonium hexafluorophosphate (NBu_4PF_6) in DMF. A three-electrode system was used with the working electrode being a glassy carbon electrode. The redox behaviors of the complexes were investigated between +0.5 and -2.5 V vs $Fc^{+/0}$. We observed two quasi-reversible processes in the cathodic region from 0 to -2.5 V (Table 2 and Figure 4). Upon analysis, it is obvious that the substituents affect the electrochemical properties of the NiTSC-R series. Indeed the more positive the Hammett σ_{para} constant is, the less negative the potential of the first reduction wave becomes, proving that redox properties of the compounds can be tuned by tailoring the ligand.

Table 2. *Electrochemical data of NiTSC-R series (V vs. $Fc^{+/0}$).*

Complex	NiTSC-R / $[NiTSC-R]^-$	$[NiTSC-R]^-$ / $[NiTSC-R]^{2-}$
NiTSC-CN	-1.40	-1.99
NiTSC-(CN)(N(CH$_3$)$_2$)	-1.48	-2.09
NiTSC-OCH$_3$	-1.57	-2.20
NiTSC-SCH$_3$	-1.50	-2.13
NiTSC-N(CH$_3$)$_2$	-1.62	-2.11

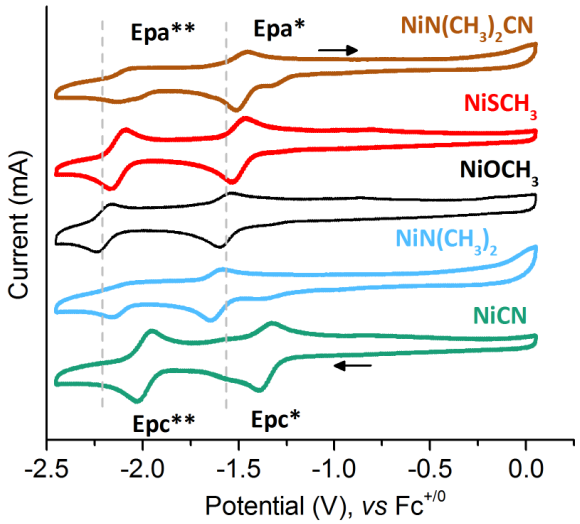

Figure 4. *Cyclic voltammograms of NiTSC-R series (V vs. $Fc^{+/0}$). Conditions: concentration 1 mM at a stationary 1.5 mm glassy carbon electrode in DMF (0.1 M NBu_4PF_6) using a 500 mV/s scan rate.*

The relative electron-donating abilities of the para substituents also match the trend of the first electrochemical process. This pattern provides some information about the electronic delocalization in the complexes. Indeed, these results suggest that electron-withdrawing groups tend to decrease the potential required for the reduction of the system since the metallic center of the complex becomes deprived of electronic density.

DFT computations were conducted on the series of complexes to confirm the above analysis and provide more insight into the nature of the species resulting from the two successive reduction events. The computated redox potentials confirm that the first reduction process remains ligand-based with a fair agreement between calculated values and experimental ones (Table 3). Regarding the second reduction process, the computational results confirm that the second reduction process is metal-centered. When analyzing the electronic structures of the one- and two-electron reduced species, we observed that the less negative redox potentials correspond to the complexes displaying less electronic density at the metal center. In the case of NiTSC-CN, the electronic density is driven away from the metal center while for NiTSC-$N(CH_3)_2$ having the most negative redox potential, we observe a subsequent localization of the spin density at the metal center. These data thus confirm that electron-withdrawing groups lead to a decrease of the reduction potential, which might affect the reactivity of the complexes if electrochemically induced.[2]

Table 3. *Calculated redox potentials of NiTSC-R series (V vs. $Fc^{+/0}$).*

Complex	NiTSC-R / $[NiTSC-R]^-$	$[NiTSC-R]^-$ / $[NiTSC-R]^{2-}$
NiTSC-CN	-1.21	-1.98
NiTSC-(CN)(N(CH₃)₂	-1.43	-2.09
NiTSC-OCH₃	-1.54	-2.28
NiTSC-SCH₃	-1.56	-2.20
NiTSC-N(CH₃)₂	-1.65	-2.26

2.2.3 Electrocatalytic proton reduction

To investigate the ability of this new family of complexes to reduce protons into hydrogen, we recorded their cyclic voltammograms in the presence of a proton source. In this study, we used trifluoroacetic acid (TFA, pK_a= 6.00 ± 0.03 in DMF).[3] The negative region was scanned after the addition of increased concentrations of TFA (Figures 5, 16 and 17). For all the complexes, we used identical experimental conditions but for the sake of clarity, we will focus most of our analysis on the NiTSC-SCH_3 complex that will be compared with the NiTSC-OCH_3 parent complex, as NiTSC-SCH_3 was identified as the catalyst providing the best results and outperforming all other “family member”.

The addition of acid to NiTSC-OCH_3 triggered the appearance of two proton-dependent waves with potential of -1.32 and -2.18 V vs $Fc^{+/0}$ (Figure 5a). The current increase of these peak-shaped waves was found to be proportional to the concentration of protons in the analysed solution. The peak potential gradually shifted from -2.18 to -2.39 V vs. $Fc^{+/0}$ for the second process, but the first one remained mostly unaffected by the different amounts of acid in the solution (Figures 5b and 5c). Recording a cyclic voltammogram with TFA, but in the absence of the complex, clearly indicates the role played by the metal complex in the current enhancement (Figure 5, black dashed line). The other complexes were also found to display the same behavior compared to the parent molecule NiTSC-OCH_3 (Figures 16 and 17).[1]

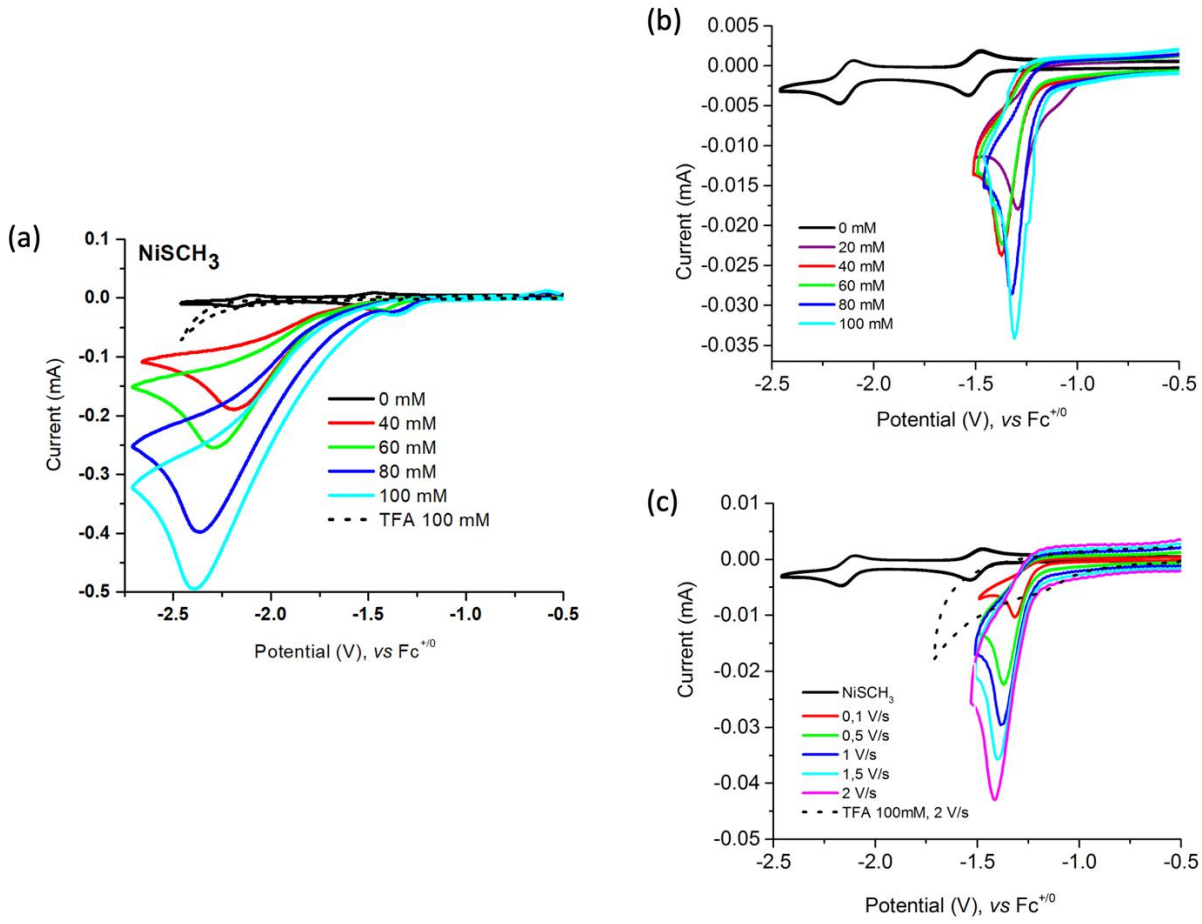

Figure 5. *Successive cyclic voltammograms recorded at a glassy carbon as working electrode of a 1 mM solution of NiTSC-SCH₃ complex in DMF (0.1 M NBu_4PF_6) in the presence of increasing amounts of TFA. The black dotted curve shows the CV of 100 mM TFA in the absence of complex under the same conditions. Scan rate: 500 mV/s.*

To verify that the signal observed is not corresponding to species being absorbed onto the surface of the working electrode, we performed a series of dip and rinse tests for all the complexes. After each measurement, the working electrode was removed from the solution and dipped into a fresh solution of DMF, containing electrolyte. For all the compounds, only the residual background signal was recorded from 0 to -2.5 V vs. $Fc^{+/0}$. Upon the addition of acid (60 mM TFA), sweeping the potential again in the cathodic region provided only the response of the blank acid (Figure 6). These control experiments proved that no absorbed species were formed onto the glassy carbon electrode during the electrocatalytic investigations. These data indicated that the signal was due to the dissolved NiTSC-R complexes and that, hence, we were investigating a homogenous catalytic system.

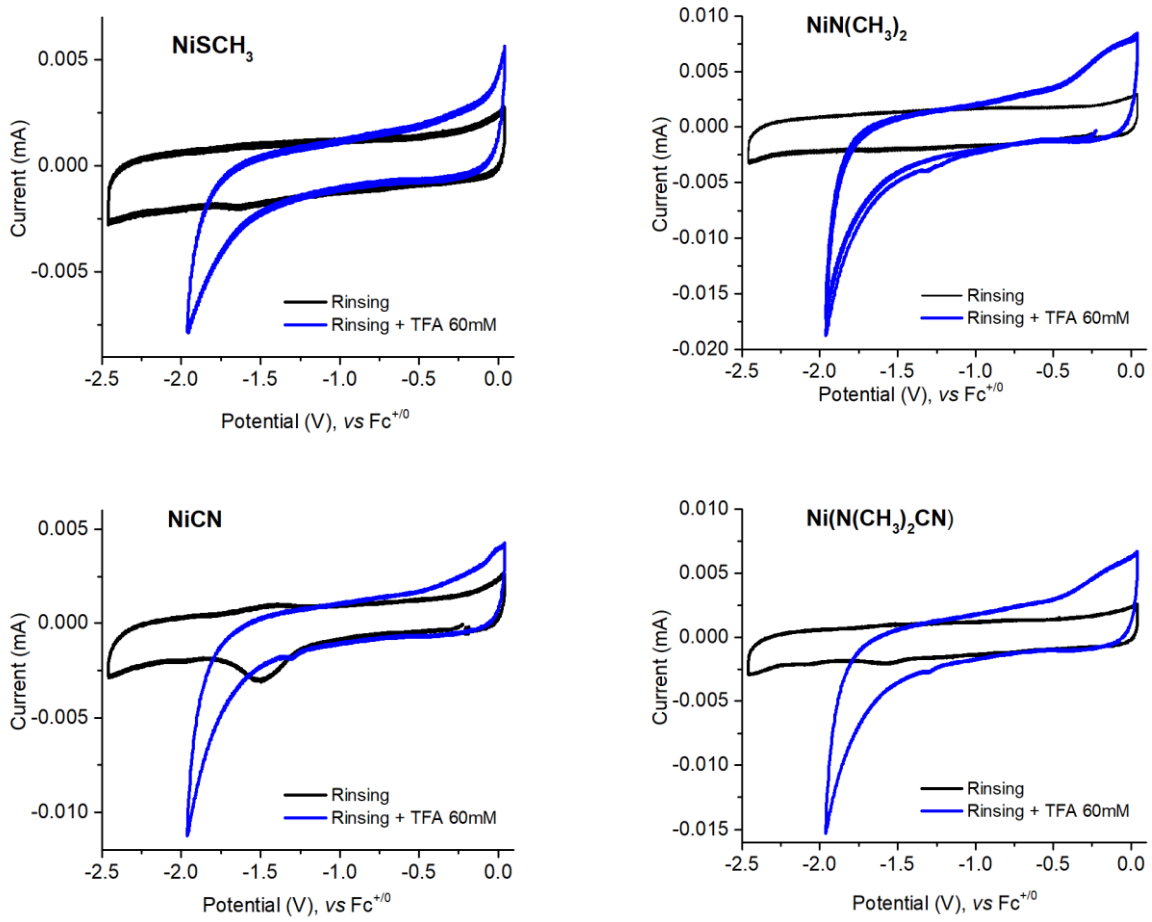

Figure 6. *Successive cyclic voltammograms recorded after electrocatalysis upon washing the glassy carbon electrode and immersion into a fresh solution of DMF (0.1 M NBu_4PF_6, black line) and in the presence of 60 mM of TFA (blue line). Scan rate: 500 mV/s.*

To confirm that the recorded electrochemical response upon the addition of the acid corresponds to hydrogen production, bulk electrolysis experiments were performed coupled with gas analysis. Solutions of 8 ml DMF (0.1M NBu_4PF_6) containing each time 1 mM of one of the NiTSC-R catalysts and 100 mM of TFA were prepared. We applied a fixed potential of -1.7 V vs. $Fc^{+/0}$ over 16 hours. The reaction was monitored by continuous in-line gas analysis. We used a mercury pool working electrode to make certain that any nanoparticles produced would be absorbed into mercury, maintaining the homogeneous nature of our catalytic systems.

During 16 hours, all of the new NiTSC-R complexes were active toward hydrogen evolution. The key parameters reporting on their catalytic performances are summarized in Table 4 and graphically illustrated in Figure 7. From these results, it became obvious that the NiTSC-SCH_3 complex outperforms the new catalytic family but also outperformed its predecessor, NiTSC-OCH_3, which displayed a faradaic efficiency of 80% and a TON of 21.[1]

Table 4. *HER parameters of the NiTSC-R series.*

Catalyst	Hammett Constant	Q (C)	Faradaic efficiency (%)	TON
NiTSC-SCH$_3$	0	61.075	94	37
NiTSC-(CN)(N(CH$_3$)$_2$)	-0.66/-0.83	26.169	86	14
NiTSC-N(CH$_3$)$_2$	-0.83	26.065	56	10
NiTSC-CN	0.66	18.617	63	8

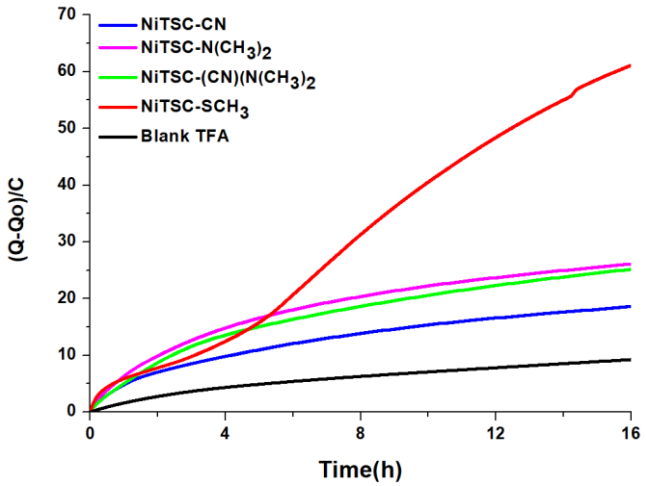

Figure 7. *Coulometry of the NiTSC-R series during bulk electrolysis experiments at -1.70 V vs. $Fc^{+/0}$ using a pool mercury working electrode. The electrolytic solution contains 0.1M NBu_4PF_6 in DMF, 100 mM TFA and/or 1 mM of NiTSC-R.*

These results support that chemical tailoring of the ligand can enhance the catalytic activity of the thiosemincarbazone complexes. However, so far it is not possible to consistently correlate the catalytic performances of the complexes with the electron-donating properties of their phenyl ring substituents.

2.2.4 Mechanistic Investigations

To get insight into the sequence of electrochemical (reduction) and chemical (protonation) events leading to hydrogen evolution with our series of complexes, we perform complementary experiments. To start with, UV-vis spectra were recorded in the absence and presence of TFA. NiTSC-CN and NiTSC-SCH_3 complexes displayed almost identical features upon the addition of acid (Figures 8a and 8b), indicating that their structure is unaffected by the presence of protons. On the other hand, the complexes containing the dimethylamino group displayed a small shift of their main absorption band towards the blue region (Figures 8c and 8d). These changes can be attributed to partial protonation of the dimethylamino group by TFA.

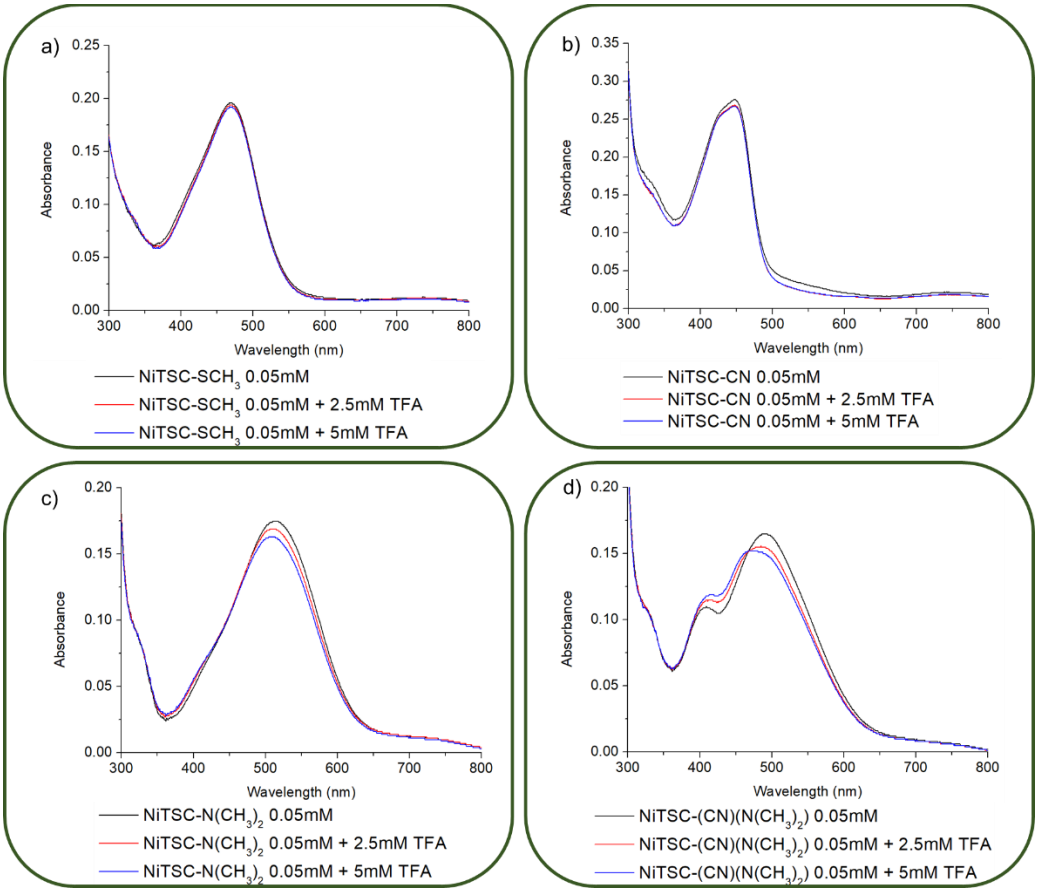

Figure 8. *UV-vis spectra of a) NiTSC-SCH_3, b) NiTSC-CN, c) NiTSC-$N(CH_3)_2$, d) NiTSC-$(CN)(N(CH_3)_2)$ in the absence and upon the addition of TFA.*

To further prove this assumption, a more “powerful” proton source was used, the triflic acid. Upon addition of this strong acid, the spectra of both NiTSC-N$(CH_3)_2$ and NiTSC-(CN)$(N(CH_3)_2)$ changed featuring a more obvious blue shift of the main transition (Figure 9). Although upon addition of a base, the triethylamine (Et_3N), to neutralize the acidic solution, the UV-vis spectra shift back to their initial shapes. These data support that although the dimethylamino group gets partially protonated; this process is reversible and is not destructive for the complex. From these data, we can also conclude that the mechanism of the reaction is not initiated by a chemical event like a protonation but is likely triggered by an electrochemical one in the form of a reduction process.

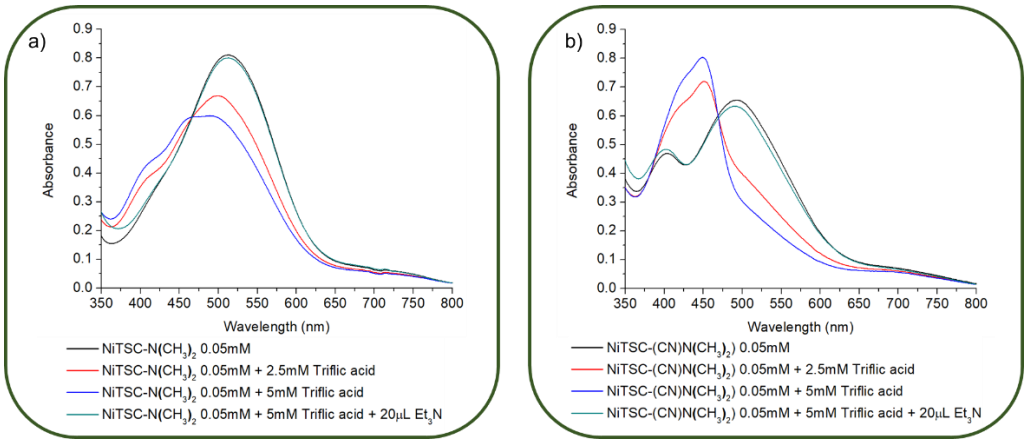

Figure 9. *UV-vis spectra of a) NiTSC-N$(CH_3)_2$, b) NiTSC-(CN)$(N(CH_3)_2)$ upon acidification and neutralization of the solution.*

Previous work in our team investigated the details of the hydrogen evolution catalytic process with our complexes using DFT calculations.[4] From the computations of redox potentials and pKa values, this study showed that two reaction mechanisms were possible (Figure 10). The first one involves a two-electron two-proton process while the second one is a two-electron three-proton process. The nitrogen atoms in close proximity to the nickel center are the focus of these processes. Both catalytic pathways start with a proton-coupled electron transfer (PCET) and involve protonating the distal nitrogen atom and reducing the ligand frame of the complex. From there, the two pathways part ways. The first one involves a second PCET process reducing the nickel center of the complex, with the protonation happening in the coordinating nitrogen atom. For the second mechanism, another PCET step occurs but with the protonation this time happening on the second symmetrical distal nitrogen atom (Figure 10, blue path). A third protonation process happens in either coordinating nitrogens and closes the catalytic cycle. From there, hydrogen is released and the complex goes back to its initial

form. Although both mechanisms happen at the same time, the one involving the two PCET steps and extra protonation was identified as the rate-limiting step of the catalytic cycle.

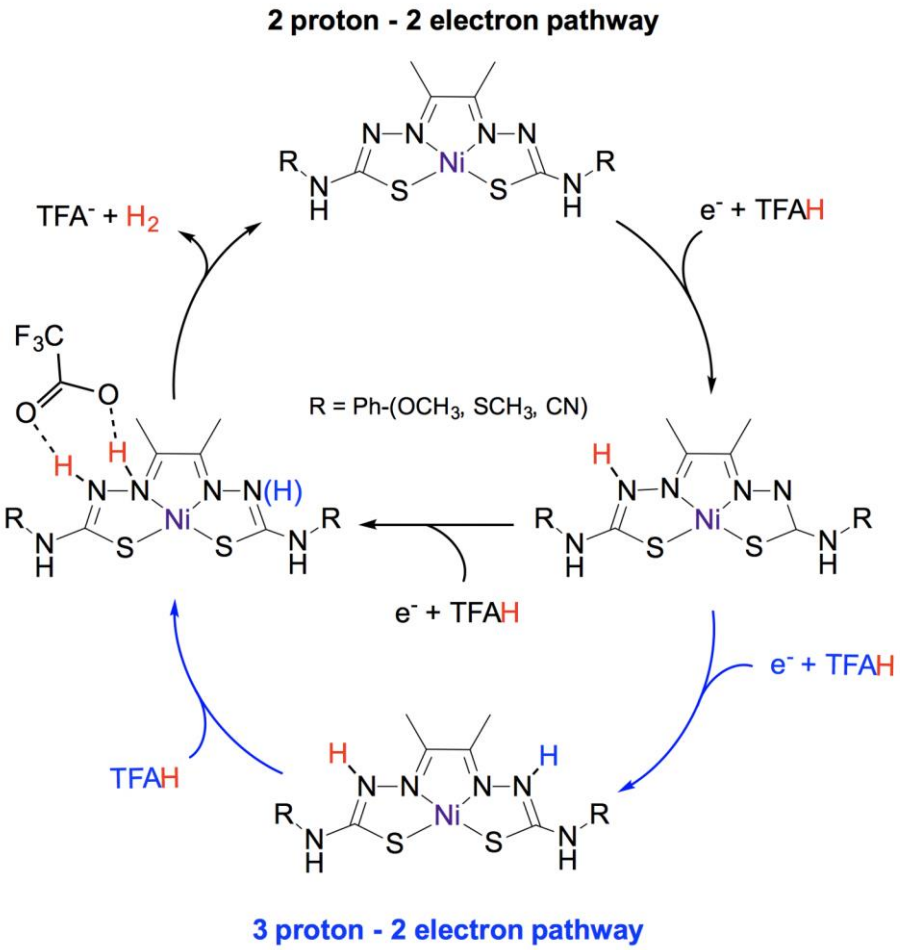

Figure 10. *Proposed DFT-computed catalytic mechanisms for hydrogen evolution with the NiTSC-R series.*[4]

To estimate the relevant HER rate constants from cyclic voltammetry measurements, the foot of the wave analysis (FOWA) was tentatively used.[5–7] Linearization of the catalytic wave was achieved by applying the equation corresponding to an ECEC mechanism with the second electron transfer being easier than the first one. The slope of the linear portion can extract helpful kinetic information.[6] The rate-determining step (RDS) of the catalytic reaction must be studied. As the electron transfers are fast and non-limiting, the kinetic bottleneck is connected to either of the protonation steps (k_1 for the first protonation step and k_2 for the second). Our results show a less negative mid-wave potential for this series of complexes than the redox potential triggering the catalytic wave, suggesting that the second protonation is

more likely the RDS and preventing any unambiguous determination of the rate constant from FOWA.

To overcome this limitation, the TOF values were thus determined from the bulk electrolysis experiments as previously reported.[8,9] For heterolytic processes, the following equation was used:

$$\mathrm{TOF} = \frac{{i_{\mathrm{el}}}^2 \left(1 + \exp\left[\frac{F}{RT}(E_{\mathrm{appl}} - E_{1/2})\right]\right)}{F^2 A^2 D_{\mathrm{cat}} [\mathrm{Cat}]^2}$$

where *F* is the Faraday constant, *A* the surface area of the working electrode, D_{cat} the diffusion coefficient, *[Cat]* the concentration of the catalyst, E_{appl} the applied potential during electrolyses, $E_{1/2}$ the mid-wave potential for the catalytic wave and i_{el} the current density during bulk electrolysis (see experimental section for details). The maximal turnover frequencies (TOF_{max}) of the series of complexes were then evaluated using the following relation:

$$\mathrm{TOF} = \frac{\mathrm{TOF}_{\mathrm{max}}}{1 + \exp\left[\frac{F}{RT}(E_{\mathrm{appl}} - E_{1/2})\right]}$$

TOF_{max} values of 115.9, 18.8, 14.3 and 10.2 s^{-1} were thus obtained for NiTSC-SCH_3; NiTSC-(CN)($N(CH_3)_2$); NiTSC-$N(CH_3)_2$ and NiTSC-CN, respectively. When comparing these values with the parent complex NiTSC-OCH_3 (TOF_{max}= 89.7 s^{-1}), our results show a slight improvement of the catalytic performances of only the NiTSC-SCH_3 complex (Table 5).

Table 5. *Calculated TOF values for the NiTSC-R series.*

Complex	D_{cat} (cm^2*s^{-1})	i_{el} (A)	F.Y. (%)	$E_{1/2}$ (V vs. $Fc^{+/0}$)	TOF
NiTSC-SCH₃	$4.50.10^{-6}$	$2.71.10^{-3}$	94	-1.32	115.9
NiTSC-(CN)(N(CH₃)₂)	$4.50.10^{-6}$	$1.44.10^{-3}$	86	-1.28	18.8
NiTSC-N(CH₃)₂	$7.80.10^{-6}$	$1.29.10^{-3}$	56	-1.31	14.3
NiTSC-CN	$8.43.10^{-6}$	$1.10.10^{-3}$	63	-1.27	10.2

The overpotential values of the complexes were determined following the protocol previously reported in the literature.[3] This parameter is calculated as the difference between the mid-wave catalytic potential ($E_{1/2}^{cat}$) and the theoretical half-wave potential ($E_{1/2}^{T}$) such as:

$$\eta = E_{1/2}^{cat} - E_{1/2}^{T}$$

When comparing the calculated overpotential values, our results highlight the dependence of the driving force of the reaction with the electronic properties of the ligand, the lowest overpotential being obtained for the most electron-withdrawing group, -CN (Table 6).

Table 6. *Calculated mid-wave potentials and overpotentials (V vs. $Fc^{+/0}$) for NiTSC-R series.*

Complex	$E_{1/2}$	Overpotential (η)
NiTSC-SCH₃	-1.32	0.334
NiTSC-(CN)(N(CH₃)₂)	-1.28	0.324
NiTSC-N(CH₃)₂	-1.31	0.294
NiTSC-CN	-1.27	0.284
NiTSC-OCH₃	-1.33	0.344

Taking into account the mid-wave potentials of both the series and the reference complex with values of -1.32, -1.33, -1.31, -1.28 and -1.27 V vs. $Fc^{+/0}$ for NiTSC-SCH_3, NiTSC-OCH_3, NiTSC-(CN)($N(CH_3)_2$), NiTSC-$N(CH_3)_2$ and NiTSC-CN respectively, and using the equilibrium potential of H^+/H_2 couple (-0.986 V vs. $Fc^{+/0}$) with 1 M of TFA, catalytic Tafel plots were derived (Figure 11), showing the relationship between the turnover frequency of H_2 evolution and the overpotential (η).[5]

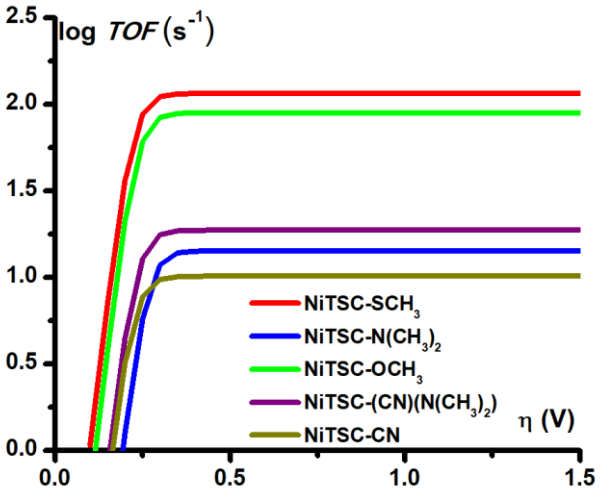

Figure 11. *Catalytic Tafel plots: Comparison of performances for HER catalyzed by the series of NiTSC-R complexes in DMF in presence of 1 M TFA.*

Focusing on the best performing catalyst of the new series, NiTSC-SCH_3 (red trace, Figure 12), we observe that this complex displays a good catalytic activity (log(TOF) > 1) for low overpotential values. It compares well with benchmark molecular catalysts of the literature, like cobaloximes[10] (blue trace, Figure 12) or nickel bisdiphosphine catalysts[11,12] (orange trace, Figure 12) as far as the overpotential requirements are concerned. Interestingly, NiTSC-SCH_3 features similar catalytic performances when compared to NiTSC-OCH_3. However, when looking at other HER parameters (faradaic yield and turnover number) it is clear that the thiomethyl containing catalyst is improved with respect to the parent methoxy containing complex as it displays an increased long-term stability and production. Taken together, these results support the fact that substitution of the phenyl group of the ligand influences the electronic and redox properties of the system, which directly affect its catalytic behavior. However, it seems unclear whether there is an actual relationship between the catalytic observables and the electronic properties of the phenyl ring substituent within the NiTSC-R series of complexes. While the overpotential increases when going from the cyano substituent to the dimethylamino one, matching the relative electron-donating ability of the para-substituents, the TOF_{max} values seem to go in the opposite direction with smaller values being obtained for the more electron-withdrawing substituents (Figure 11).

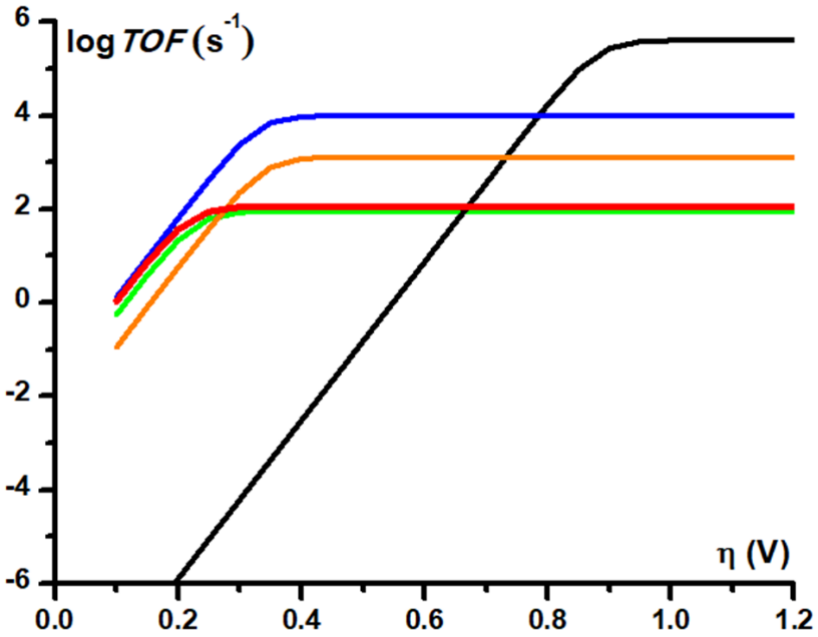

Figure 12. *Catalytic Tafel plots: comparison of performances for HER catalysed by NiTSC-SCH_3 in DMF in the presence of 1 M TFA (red line) and NiTSC-OCH_3[1] in DMF in the presence of 1 M TFA (green line) with other catalysts reported in the literature. Black: Fe^{II}TPP, DMF, Et_3NH^+,[5,13] blue: $[Co^{II}(dmgH)_2py]$, DMF, Et_3NH^+,[5,14] orange: $[Ni^{II}(P_2PhN_2C_6H_4X)_2]^{2+}$, X = $CH_2P(O)(OEt)_2$, MeCN, $DMFH^+$.*[5,11]

2.3 Conclusions

A new family of nickel catalysts based on a series of thiosemicarbazone ligands was prepared to expand upon the original methoxy containing ligand. The new series was investigated for their ability to produce hydrogen through electrocatalytic means. Our approach was focused on the electronic properties of the catalysts based on the different Hammett Sigma constants of the chemical groups placed at the para position of the phenyl rings of the ligand. Although the substitution of the methoxy moieties slightly altered their electrochemical properties there was a big difference in their catalytic performance for HER. The new NiTSC-SCH_3 complex was crowned as the new best electrocatalyst, outperforming both the new series and the parent NiTSC-OCH_3 complex. Detailed analysis of the electrocatalytic data allowed benchmarking of their performance and through catalytic Tafel plots, it is obvious that the NiTSC-SCH_3 can be compared with benchmarked molecular catalysts regarding the overpotential requirement.

Our study confirms that the chemical nature of para substituents of the thiosemicarbazone ligands play an important role in the catalytic performances of the resulting complexes. Further work will be necessary to decipher the connection between the electron donating ability of the phenyl ring substituent and their HER capabilities as no clear connection was drawn from our experimental investigations. Further functionalizations on the ligand can pave the way to better understand which part of our complex needs to be improved and in what way to push our catalysis to even greater heights.

2.4 Experimental section and supplementary data

2.4.1 Synthesis and Characterization

General synthetic protocol of ligands

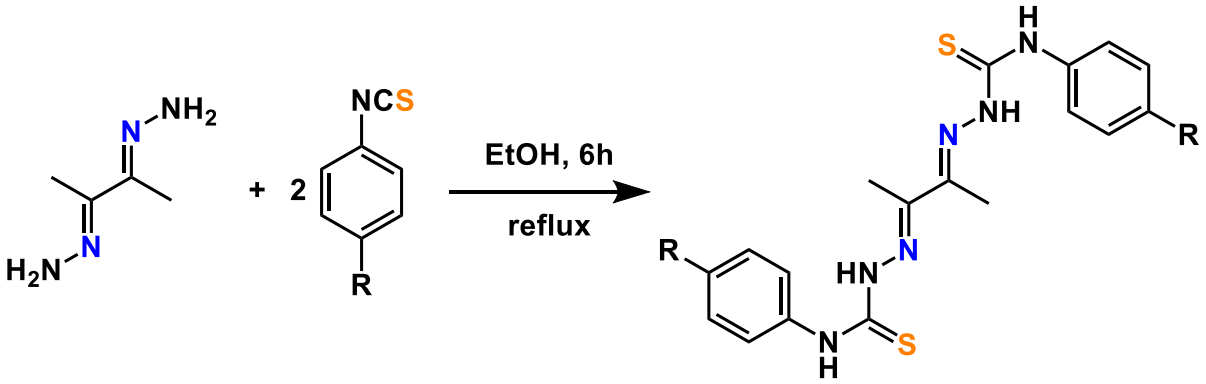

R= -SCH_3, -CN, -$N(CH_3)_2$

In a solution of ethanol, 1 equivalent of butan-2,3-dihydrazone and 2 equivalents of the corresponding isothiocyanate are added. The mixture is heated at reflux for 6 hours. After that time, it is allowed to cool down to room temperature and then an ice bath is used to cool it down to 0 °C. A yellow precipitate is formed. The solid obtained after filtration is washed with two portions of ethanol and used without any further purification.

Synthetic protocol of assymetric ligands

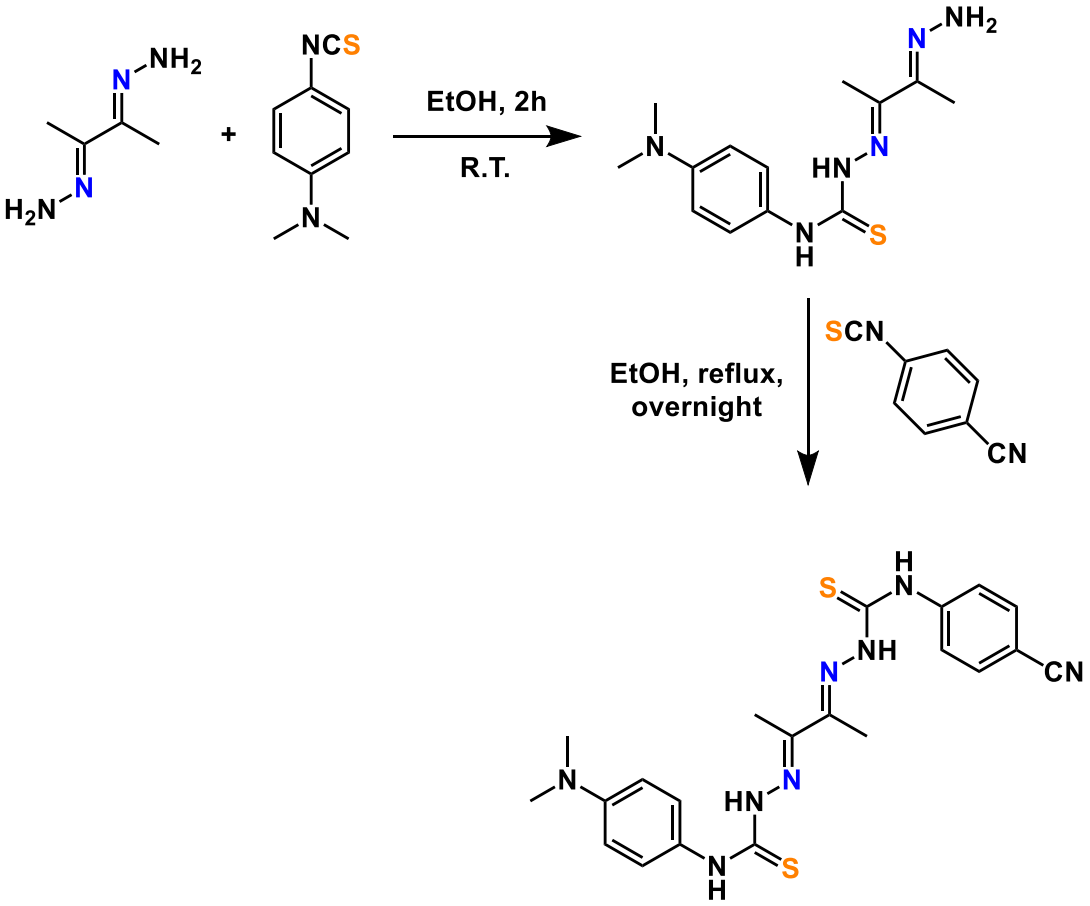

In a solution of ethanol, 1 equivalent of butan-2,3-dihydrazone and 1 equivalent of 4-dimethylaminophenyl isothiocyanate are added. The reaction is stirred at room temperature for 2 hours and then 1 equivalent of 4-cyanophenyl isothiocyanate is added. Then the reaction is refluxed overnight. Next, the reaction is cooled to 0°C by using an ice bath. A yellow solid precipitates and is filtered and washed with two portions of ethanol. The solid obtained after filtration is washed with two portions of ethanol and used without any further purification.

General synthetic protocol of nickel complexes

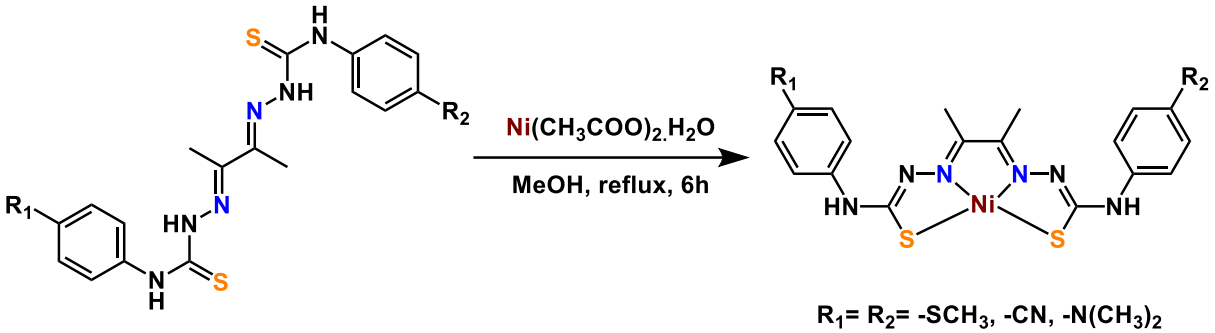

In a solution of methanol 1 equivalent of the corresponding ligand is added with 1.2 equivalents of $Ni(CH_3COO)_2{\cdot}4H_2O$. The mixture is refluxed. After 6 hours, the reaction is cooled to 0°C with a water bath and water is added. The mixture is filtered and washed with cold water and cold methanol. An alumina liquid chromatography column is prepared to purify the desired compound.

*2,3-di(4-(methylmercaptophenylthiosemicarbazone) butane nickel (II) (*NiTSC-SCH_3)

From 2,3-di(4-(methylmercaptophenylthiosemicarbazone) butane (0.084 mmol, 40 mg) in 3 ml methanol and $Ni(CH_3COO)_2(H_2O)_4$ (0.096 mmol, 24 mg) in solution in 2 ml methanol. Alumina column with dichloromethane/cyclohexane 7:3. A dark brown solid (36 mg, 80 %) was obtained.

^{1}H NMR (400 MHz, DMSO-*d6*, TMS): δ = 10.03 (s, 2H; NH), 7.57 (d, J = 8.83 Hz, 4H; o-CH), 7.22 (d, J = 8.84 Hz, 4H; m-CH), 2.45 (s, 6H; -SCH_3), 2.08 (s, 6H; -CH_3).

HR ESI-MS: $[M+H]^+$ calculated for $C_{20}H_{23}N_6S_4Ni$: 533.0215, observed: 533.0211.

*2,3-di(4-(dimethylaminophenylthiosemicarbazone) butane nickel (II) (*NiTSC-$N(CH_3)_2$)

From 2,3-di(4-(dimethylaminophenylthiosemicarbazone) butane (0.085 mmol, 40 mg) in 3 ml methanol and $Ni(CH_3COO)_2(H_2O)_4$ (0.102 mmol, 26 mg) in solution in 2 ml methanol. Alumina column with dichloromethane/cyclohexane 6:4. A dark brown solid (28 mg, 63 %) was obtained after filtration and washing with two portions of methanol.

^{1}H NMR (400 MHz, DMSO-*d6*, TMS): δ = 9.74 (s, 2H; NH), 7.43 (d, J = 8.50 Hz, 4H; o-CH), 6.67 (d, J = 9.22 Hz, 4H; m-CH), 2.85 (s, 12H; -$N(CH_3)_2$), 2.04 (s, 6H; -CH_3).

HR ESI-MS: $[M+H]^+$ calculated for $C_{22}H_{29}N_8S_2Ni$: 527.1305, observed: 527.1297.

*2,3-di(4-(cyanophenylthiosemicarbazone) butane nickel (II) (*NiTSC-CN)

From 2,3-di(4-(cyanophenylthiosemicarbazone) butane (0.092 mmol, 40 mg) in 3 ml methanol and $Ni(CH_3COO)_2(H_2O)_4$ (0.105 mmol, 28 mg) in solution in 2 ml methanol. Alumina column with dichloromethane/ethanol 2%. A dark brown solid (24 mg, 52 %) was obtained after filtration and washing with two portions of methanol.

^{1}H NMR (400 MHz, DMSO-*d6*, TMS): δ = 10.42 (s, 2H; NH), 7.78-7.72 (m, 8H; -CH), 2.12 (s, 6H; $-CH_3$).

HR ESI-MS: $[M+H]^+$ calculated for $C_{20}H_{17}N_8S_3Ni$: 491.0366, observed: 491.0358.

*2-(4-(dimethylaminophenylthiosemicarbazone), 3-(4-(cyanophenylthiosemicarbazone) butane nickel (II) (*NiTSC-N$(CH_3)_2$CN)

From 2-(4-(dimethylaminophenylthiosemicarbazone), 3-(4-(cyanophenylthiosemicarbazone) butane (0.088 mmol, 40 mg) in 3 ml methanol and $Ni(CH_3COO)_2(H_2O)_4$ (0.106 mmol, 26 mg) in solution in 2 ml methanol. Alumina column with dichloromethane/cyclohexane 8:2. A dark brown solid (34 mg, 75 %) was obtained after filtration and washing with two portions of methanol.

^{1}H NMR (400 MHz, DMSO-*d6*, TMS): δ = 10.30 (s, 1H; NH-CN), 9.92 (s, 1H; NH-$N(CH_3)_2$), 7.75 (dd, J = 8.75 Hz, 4H; o-CH), 7.43 (broad d, J = 5.12 Hz, 2H; m-CH-CN), 6.67 (d, J = 9.24 Hz, 2H; m-CH-$N(CH_3)_2$), 2.85 (s, 6H; -$N(CH_3)_2$), 2.11 (s, 3H; -CH_3-$N(CH_3)_2$), 2.05 (s, 3H; -CH_3-CN).

HR ESI-MS: $[M+H]^+$ calculated for $C_{21}H_{23}N_8S_2Ni$: 509.0835, observed: 509.0833.

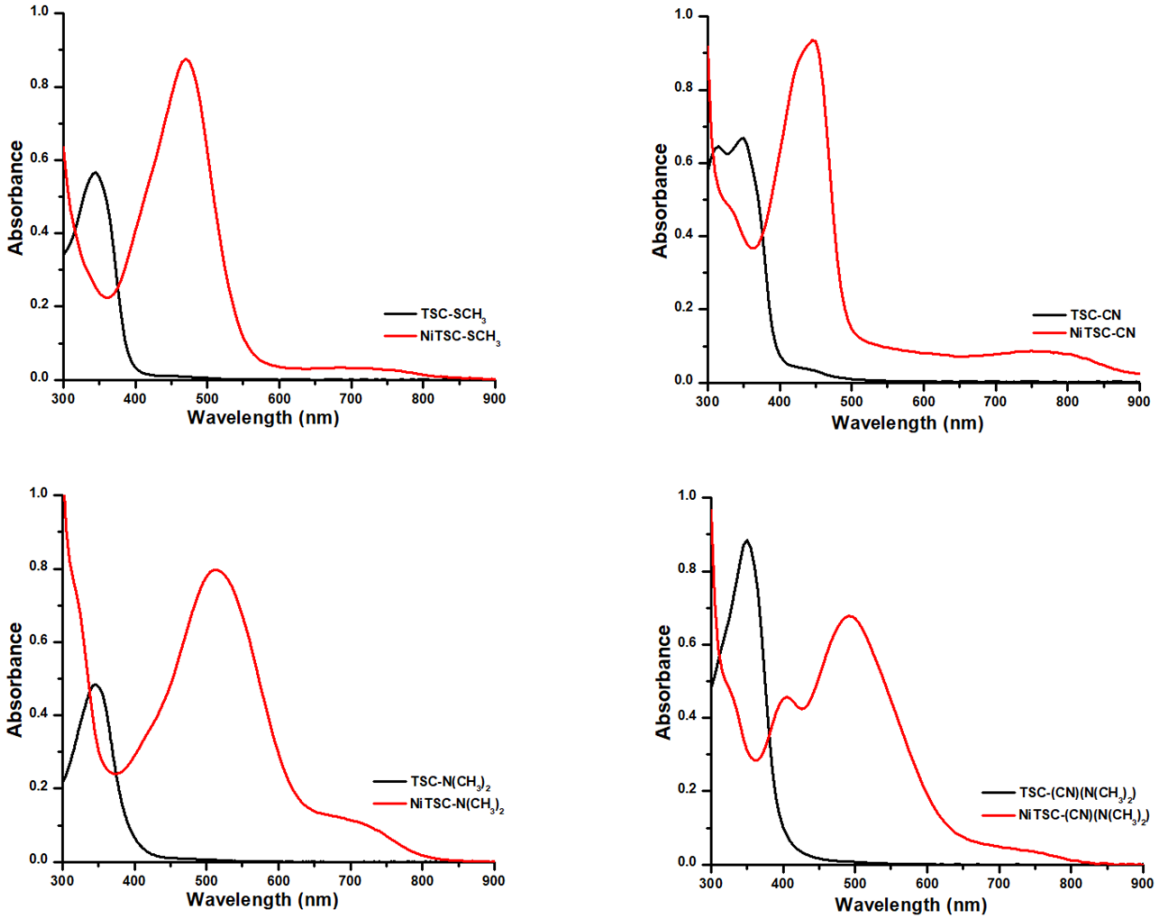

Figure 13. *Electronic absorption spectra of each ligand and NiTSC-R complex in DMF.*

Table 7. *Crystallographic data, details of data collection and structure refinement parameters for NiTSC-SCH₃.*

Identification code	$NiSCH_3$
Empirical formula	$C_{44}H_{52}N_{12}Ni_2OS_8$
Formula weight	1138.87
Temperature/K	295
Crystal system	triclinic
Space group	P-1
a/Å	9.9569(2)
b/Å	16.3128(4)
c/ Å	16.4216(4)
α/°	78.440(2)
β/°	87.160(2)
γ/°	86.818(2)
Volume/ $Å^3$	2607.13(11)
Z	2
ρ_{calc} g/cm^3	1.451
μ/mm^{-1}	4.269
Crystal size/mm^3	0.38 x 0.12 x 0.12
Radiation	Cu Kα 9 (λ= 1.54184)
2Θ range for data collection/°	5.498 to 140.344
Index ranges	$-12 \leq h \leq 12$, $-19 \leq k \leq 19$, $-19 \leq l \leq 19$
Reflections collected	37322
Independent reflections	9758 [R_{int}= 0.0401]
Data/restraints/parameters	9758/48/612
Goodness-of-fit on F^2	1.028
Final R indexes [$I \geq 2\sigma(I)$]	R_1 = 0.0652, wR_2= 0.1780
Final R indexes [all data]	R_1 = 0.0886, wR_2= 0.2011
Largest diff. peak/hole / e $Å^{-3}$	0.71/-0.53

Table 8. *Crystallographic data, details of data collection and structure refinement parameters for NiTSC-CN.*

Identification code	NiCN
Empirical formula	$C_{23}H_{23}N_9NiOS_2$
Formula weight	564.33
Temperature/K	295
Crystal system	triclinic
Space group	P-1
a/Å	7.1855(4)
b/Å	11.6933(5)
c/ Å	16.0032(5)
α/°	89.907(3)
β/°	88.694(3)
γ/°	73.541(4)
Volume/ $Å^3$	1289.17(10)
Z	2
ρ_{calc} g/cm^3	1.454
μ/mm^{-1}	2.892
Crystal size/mm^3	0.14 x 0.08 x 0.03
Radiation	Cu Kα 9 (λ= 1.54184)
2Θ range for data collection/°	5.524 to 165.754
Index ranges	$-9 \leq h \leq 8$, $-14 \leq k \leq 13$, $-19 \leq l \leq 19$
Reflections collected	22000
Independent reflections	5045 [R_{int}= 0.0559]
Data/restraints/parameters	5045/0/329
Goodness-of-fit on F^2	1.035
Final R indexes [$I \geq 2\sigma(I)$]	R_1 = 0.0436, wR_2= 0.1112
Final R indexes [all data]	R_1 = 0.0575, wR_2= 0.1221
Largest diff. peak/hole / e $Å^{-3}$	0.38/-0.42

2.4.2 Electrochemistry

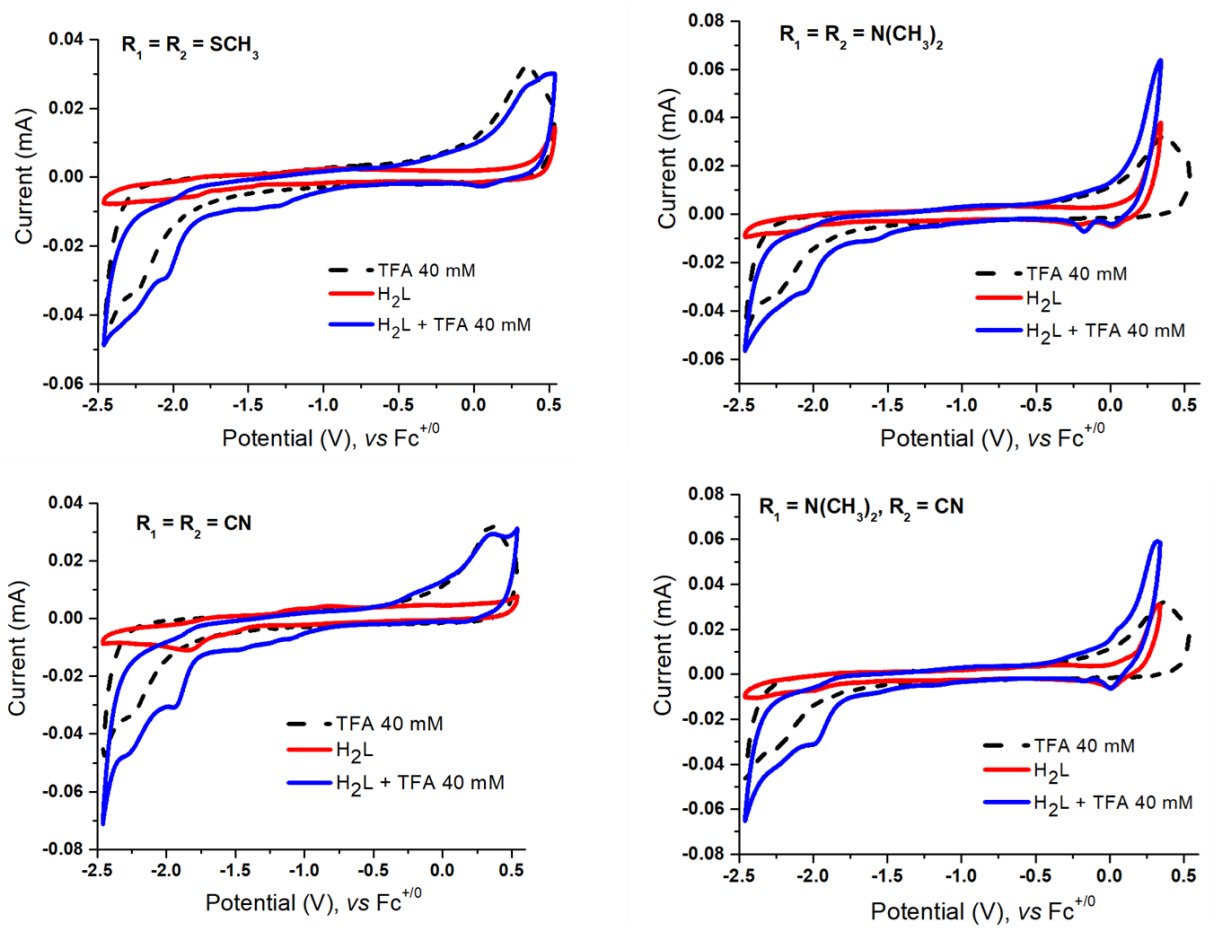

Figure 14. *Cyclic voltammograms of 1 mM of ligand (red line) recorded at a stationary glassy carbon electrode in DMF with 0.1 M NBu_4PF_6 as supporting electrolyte. The cyclic voltammograms of 40 mM of TFA solution in the absence (dotted black line) and in the presence of 1 mM ligand (blue line) are also shown. Scan rate: 500 mV/s.*

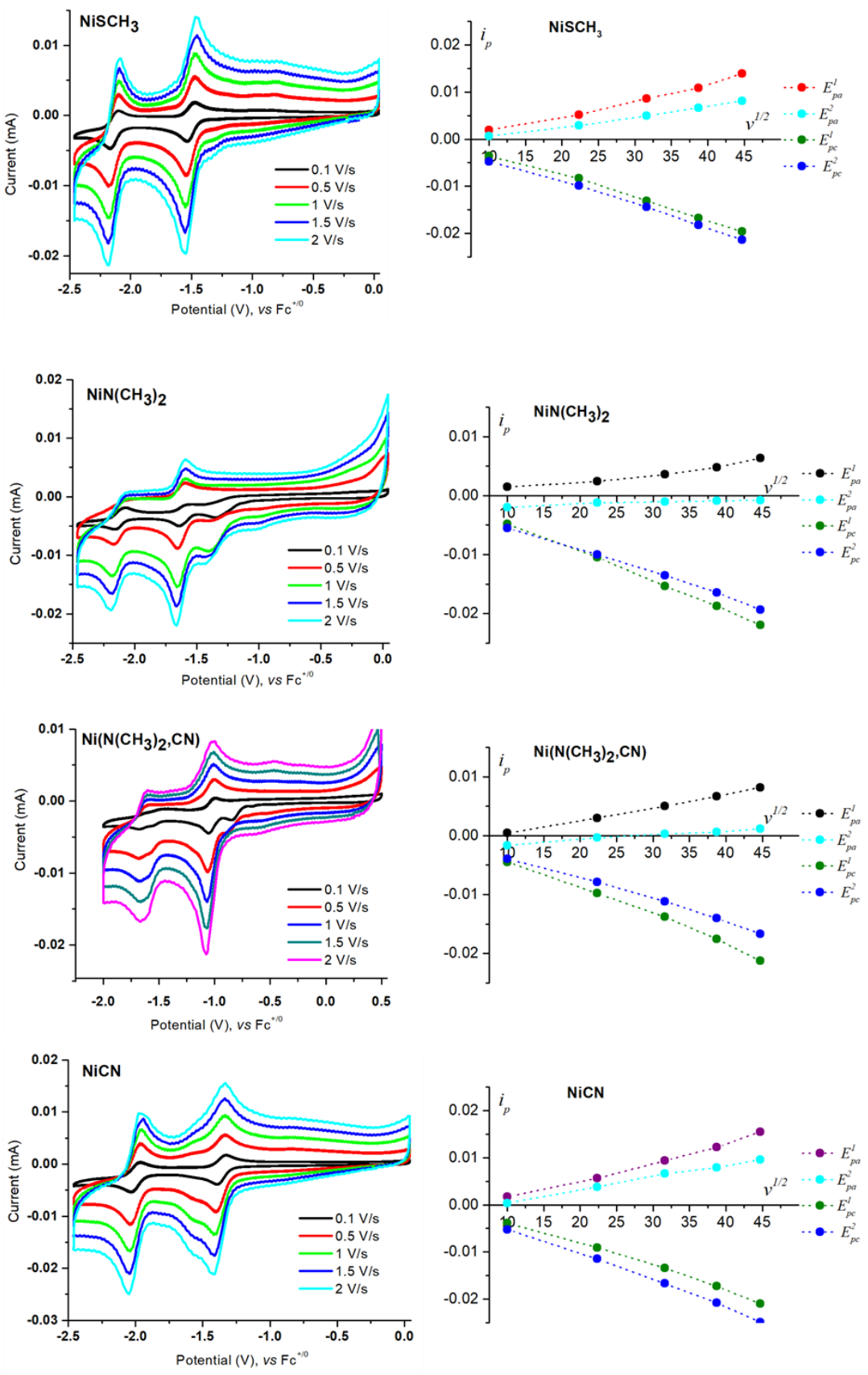

Figure 15. *Cyclic voltammograms of NiTSC-R at a stationary glassy carbon electrode at different scan rates (v) in DMF with 0.1 M NBu_4PF_6 as supporting electrolyte (left) and linear plot of ip vs. $v^{1/2}$ for anodic and cathodic waves of both processes (right).*

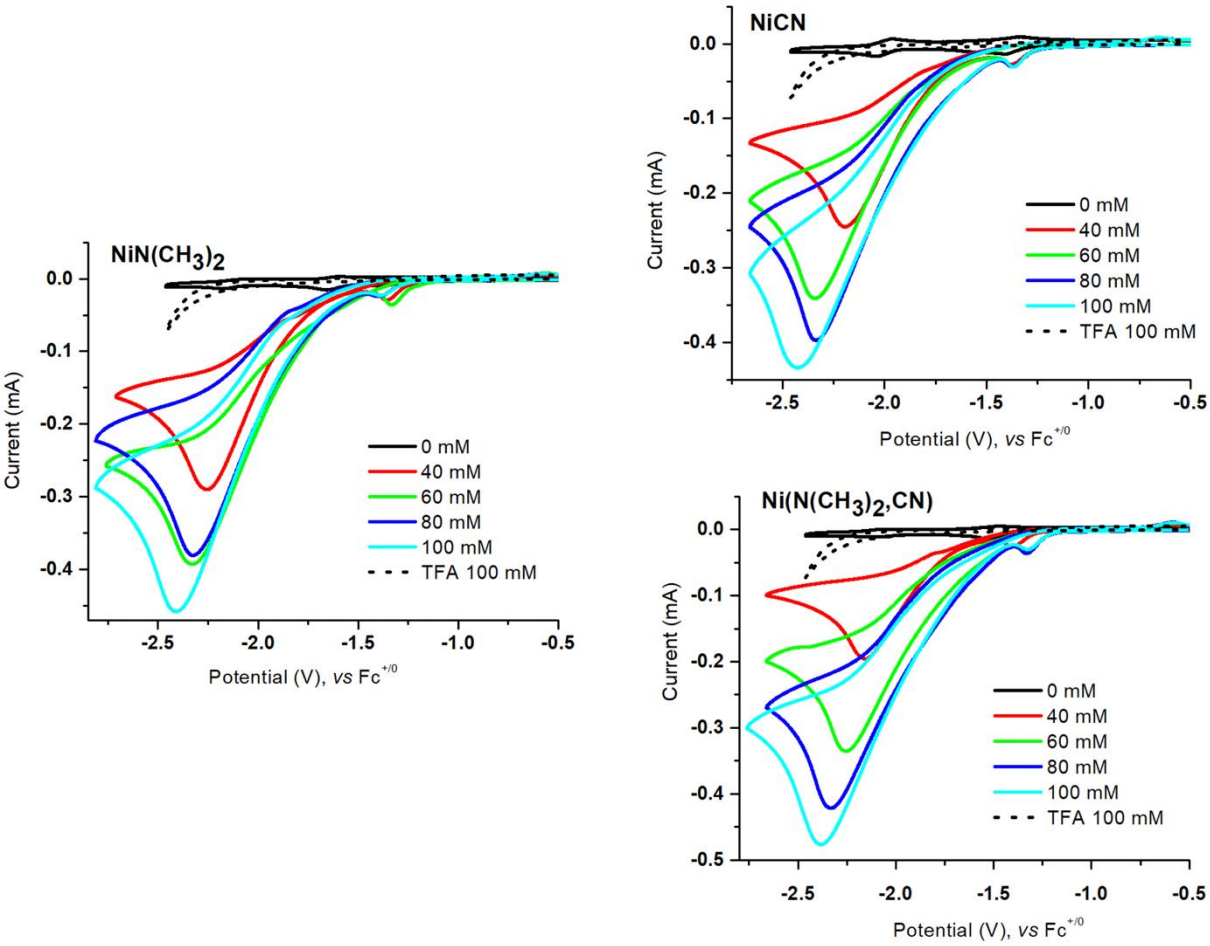

Figure 16. *Successive cyclic voltammograms recorded at a glassy carbon as working electrode of a 1 mM solution of NiTSC-R complex in DMF (0.1 M NBu_4PF_6) in the presence of increasing amounts of TFA. The black dotted curve shows the CV of 100 mM TFA in the absence of complex under the same conditions. Scan rate: 500 mV/s.*

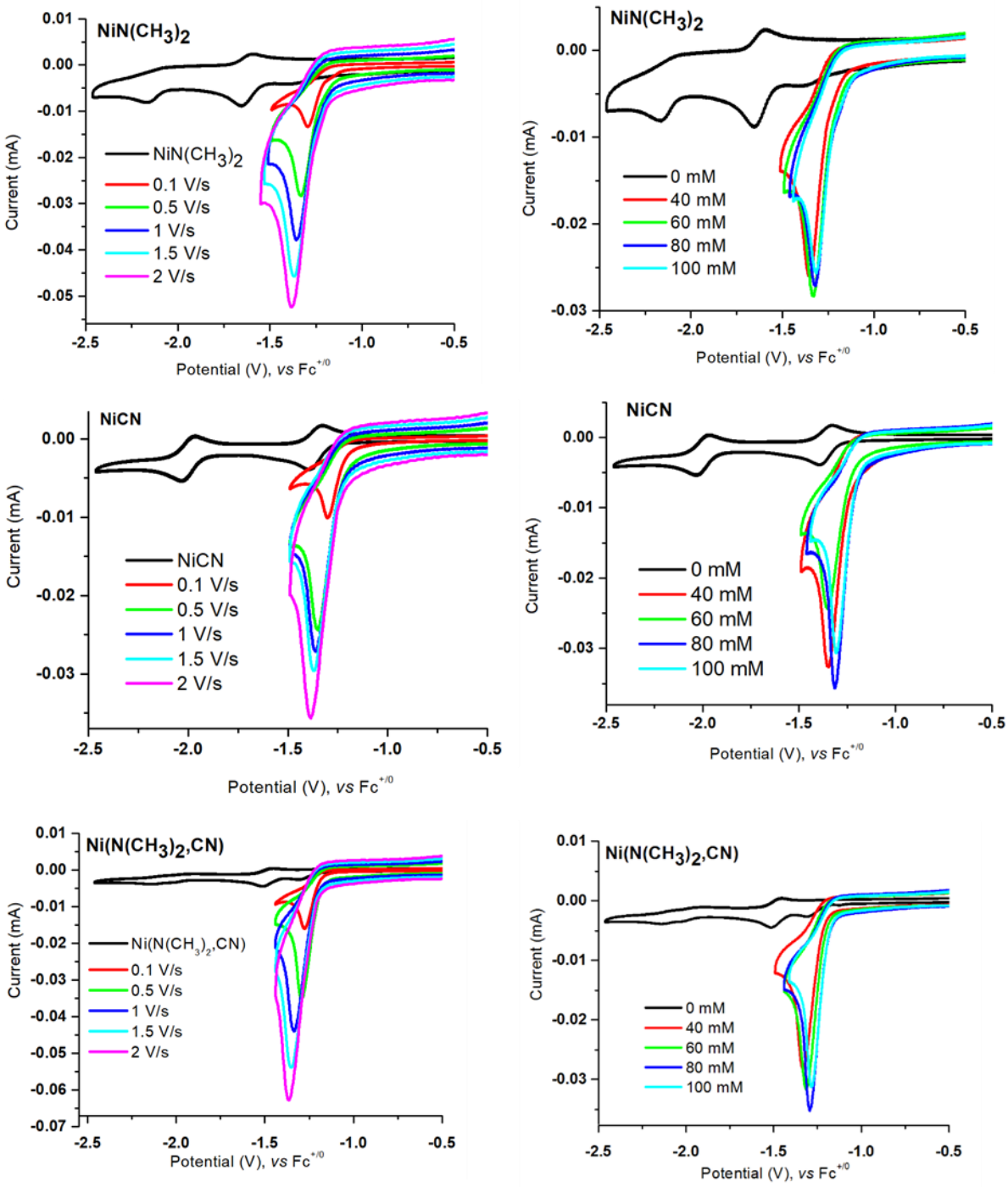

Figure 17. *Successive cyclic voltammograms recorded at a glassy carbon as working electrode of a 1 mM solution of NiTSC-R series in DMF (0.1 M NBu_4PF_6) with 60 mM TFA at five different scan rates (left) and increasing concentration of TFA at 500 mV/s scan rates (right).*

2.4.3 Foot-of-the-wave analysis (FOWA)

As previously discussed in the results section, an ECEC mechanism with the rate determining step being the second reduction was considered. For such multi electron and proton process the expression of the current is given by the following equations:

$$i = \frac{i_{pl}}{1+e^{\left[\frac{RT}{F}(E-E_C^0)\right]}} \quad (1)$$

$$i_{pl} = 2FS[\mathrm{Cat}]\sqrt{D_{cat}}\frac{1}{\frac{1}{\sqrt{k_1[H^+]}}+\frac{1}{\sqrt{k_2[H^+]}}} \quad (2)$$

where i_{pl} the catalytic plateau current, *R* the gas constant, *T* the temperature, *F* the Faraday constant, E_c^0 the standard potential of the catalytic process, *S* the active surface of the electrode, *[Cat]* the concentration of the catalyst, D_{cat} the diffusion coefficient of catalyst, $[H^+]$ the concentration of acid, k_1 the first protonation rate constant and k_2 the second protonation rate constant.

Dividing *i* by the current i_p^0 associated with a reversible one-electron transfer under diffusion control (Randles-Sevcik equation (3)) allows simplification of redundant constants.

$$i_p^0 = 0.446FS[Cat]\sqrt{\frac{Fv D_{cat}}{RT}} \quad (3)$$

$$\frac{i}{i_p^0} = \frac{\mathrm{i}_{pl}}{\mathrm{i}_p^0} \times \frac{1}{1+e^{\left[\frac{F}{RT}(E-E_C^0)\right]}} \quad (4)$$

Plotting the catalytic enhancement ($i_{cat}/i_p{}^0$) as a function of $\frac{1}{1+e^{\left[\frac{F}{RT}(E-E_C^0)\right]}}$ near the foot of the catalytic wave, gives a linear curve the slope of which allows further determination of relevant rate constants (Figure 18). From this point, two situations must be considered :

- $k_1 << k_2$, if the first protonation step is the rate-determining one,
- $k_2 << k_1$, if the second protonation step is the rate-determining one.

In the case where $k_1 << k_2$, E_c^0 is equaling the potential of the redox couple which triggers the catalytic process (equation (5)). In addition, the expression of the plateau current is also simplified in equation (6). Thus k_1 values were thus extracted from the slopes of the linearization plots. Multiple scan rates have been investigated (spanning from 0.5 to 2 V/s) and revealed a clear independence of the rate constant determined (Table 9).

$$E_c^0 = \mathrm{E}^0_{(Ni^{II}L/Ni^{II}L^{\cdot-})} \quad (5)$$

$$i_{pl} = 2FS[\mathrm{Cat}]\sqrt{D_{cat}}\sqrt{k_1[H^+]} \quad (6)$$

When k_1 >> k_2, the value of the catalytic potential must be comprised between $\mathrm{E}^0_{(Ni^{II}L/Ni^{II}L^{\cdot-})}$ (lower limit) and the graphically-determined $E_{1/2}$ (higher limit). In principle, only the minimum value that can be reached by k_2 can be calculated thanks to equation (7), using the previously determined k_1 and considering the graphically-determined value of the catalytic potential $E_{1/2}$ as equalling E_c^0, respectively.

$$E_c^0 = \mathrm{E}^0_{(Ni^{II}L/Ni^{II}L^{\cdot-})} + \frac{RT}{F}\ln\left(\sqrt{\frac{k_1}{k_2}}\right) \quad (7)$$

Consequently, the value of the catalytic potential cannot be unambiguously determined preventing direct extraction of the k_2 value from FOWA and no accurate evaluation of the TOF values can be performed.

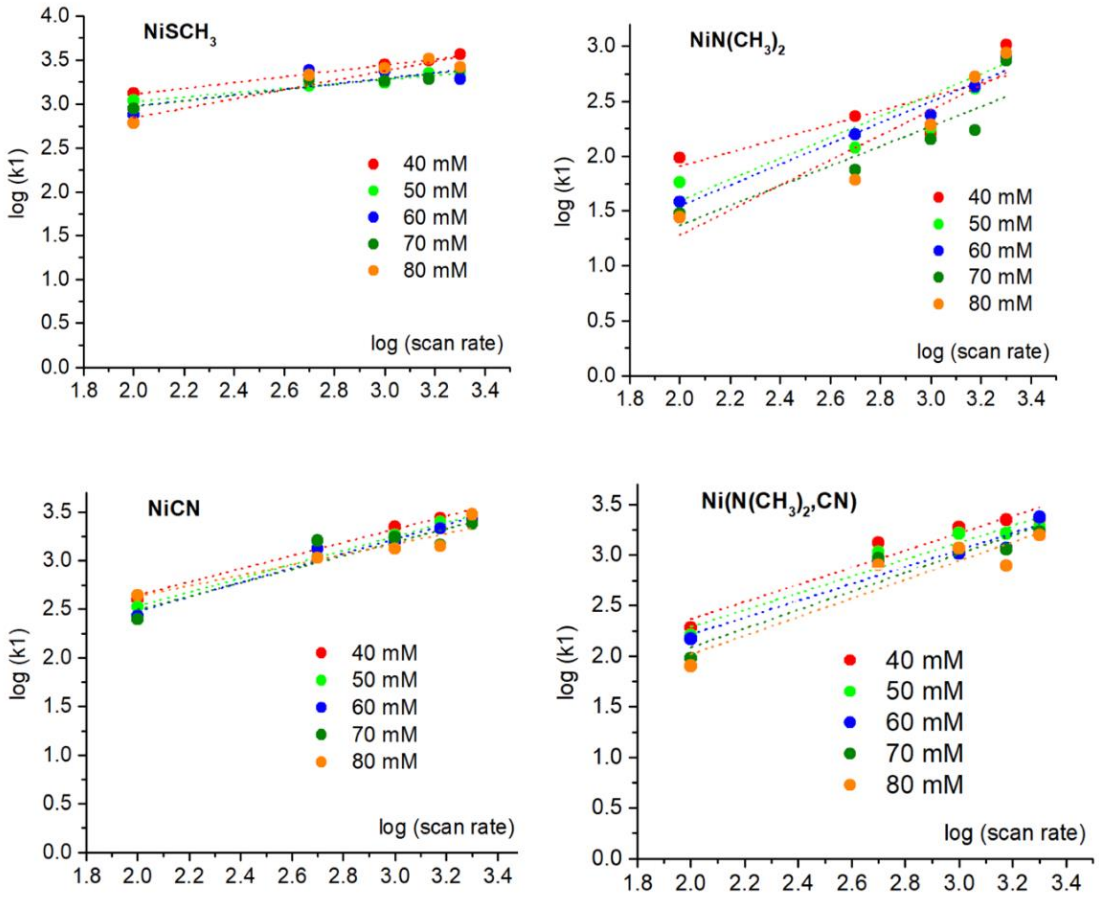

Figure 18. *Log(k_1) values obtained through FOWA for NiTSC-R complexes.*

Table 9. *k_1 calculations using different concentrations of TFA at 4 different scan rates.*

NiTSC-SCH_3			**k_1**		
v (V/s)	**40 mM**	**50 mM**	**60 mM**	**70 mM**	**80 mM**
0.5	2052.67	1581.35	2412.18	1874.32	2126.08
1	2829.57	1719.88	2381.55	1834.45	2561.88
1.5	3115.97	2261.95	1906.86	1920.63	3287.39
2	3662.72	2264.61	1933.42	2552.03	2611.35
NiTSC-$N(CH_3)_2$			**k_1**		
v (V/s)	**40 mM**	**50 mM**	**60 mM**	**70 mM**	**80 mM**
0.5	231.27	119.67	158.57	75.06	60.6
1	161.11	179.56	238.75	142.72	191.9
1.5	414.34	413.28	430.19	173.12	523.43
2	1039.92	1900.56	805.87	743.80	865
NiTSC-$(CN)(N(CH_3)_2)$			**k_1**		
v (V/s)	**40 mM**	**50 mM**	**60 mM**	**70 mM**	**80 mM**
0.5	1320.41	1063.73	870.14	931.86	795.46
1	1887.08	1632.08	1041.31	1153.50	1166.01
1.5	2218.10	1630.74	1162.93	1139.21	779.45
2	2289.52	1897.87	2362.53	1708.15	1576.31
NiTSC-CN			**k_1**		
v (V/s)	**40 mM**	**50 mM**	**60 mM**	**70 mM**	**80 mM**
0.5	1615.57	1101.11	1336.36	1620.57	1071.96
1	2226.91	1829.16	1573.89	1732.60	1325.10
1.5	2734.09	2496.50	2131.68	1451.80	1413.13
2	2944.09	2702.22	2630.99	2397.19	2976.48

2.4.4 Overpotential and TOF calculations

The overpotential values were determined following the protocol described by Fourmond et coworkers.[3] This parameter is calculated as the difference between the mid-wave catalytic potential ($E_{1/2}^{cat}$) and the theoretical half-wave potential ($E_{1/2}^{T}$) such as:

$$\eta = E_{1/2}^{cat} - E_{1/2}^{T} \quad (8)$$

The value of $E_{1/2}^{T}$ depends on the standard potential for the reduction of protons in DMF (E_{H^+/H_2}^{0}), the pKα of the proton source, the total concentration of the acid (C_0), the concentration of dissolved hydrogen ($C_{H_2}^{0}$), and the difference in diffusion coefficients between the acid and H_2 (ε_D). When homoconjugation is negligible as for the case of trifluoroacetic acid in DMF, the theoretical half-wave potential, $E_{1/2}^{T}$, can be calculated using the following equation:

$$E_{1/2}^{T} = E_{H^+/H_2}^{0} - \left(2.303 \times RT/F\right) \times pK_a + \varepsilon_D - \left(RT/2F\right) \times ln\left(C_0/C_{H_2}^{0}\right) \quad (9)$$

The relevant values of E_{H^+/H_2}^{0} (-0.62 V), pK_a (6.00 ± 0.3), ε_D (0.04 ± 0.005 V) and $C_{H_2}^{\circ}$ (1.9.10-3 M), were obtained from literature. (2,3) We used R = 8.31 J.K^{-1}.mol^{-1}, T = 298 K, F = 96500 C.mol^{-1} and C_0 = 0.1 M.

TOF values were extracted from the electrolysis data following the approach previously reported by Saveant and co-workers. Equations 10-13 were used to for the calculations under the assumption that the electron transfer to the catalyst is fast and the Nernst law is obeyed.

$$TOF = \frac{i_{el}^2\left(1+exp\left[\frac{F}{RT}\left(E_{appl}-E_{1/2}\right)\right]\right)}{F^2A^2D_{cat}[Cat]^2} \quad (10)$$

$$i_{el} = \frac{Q_{el}F.Y.}{t} \quad (11)$$

$$i_p = 0.446FA[Cat]\sqrt{\frac{FvD_{cat}}{RT}} \quad (12)$$

$$TOF = \frac{TOF_{max}}{1+exp\left[\frac{F}{RT}\left(E_{appl}-E_{1/2}\right)\right]} \quad (13)$$

Where i_{el} is the current during electrolysis, TOF_{max} is the maximum turnover frequency obtained from cyclic voltammetry, F is Faraday's constant, A is the surface area of the mercury-pool working electrode, D_{cat} is the diffusion coefficient, *[Cat]* is the concentration of the catalyst, E_{appl} is the applied potential during electrolysis, $E_{1/2}$ is the half-wave potential for the catalytic wave,

Q_{el} is the charge passed during the electrolysis, *F.Y.* is the Faradaic yield, and *t* is the electrolysis time. The charge increased linearly in the early stage of electrolysis and became non-linear after about 20 to 30 min due to catalyst degradation and/or substrate consumption. For this reason, the *TOF* values were calculated using the amount of charge passed during the initial twenty minutes of electrolysis. The most important values calculated from this analysis are summarized in Tables 5 and 6.

References

1. Straistari, T. *et al.* A Thiosemicarbazone-Nickel(II) Complex as Efficient Electrocatalyst for Hydrogen Evolution. *ChemCatChem* **9**, 2262–2268 (2017).
2. Papadakis, M. *et al.* Ligand-based electronic effects on the electrocatalytic hydrogen production by thiosemicarbazone nickel complexes. *Dalton Trans.* **49**, 5064–5073 (2020).
3. Fourmond, V., Jacques, P.-A., Fontecave, M. & Artero, V. H_2 Evolution and Molecular Electrocatalysts: Determination of Overpotentials and Effect of Homoconjugation. *Inorg. Chem.* **49**, 10338–10347 (2010).
4. Barrozo, A. & Orio, M. Unraveling the catalytic mechanisms of H_2 production with thiosemicarbazone nickel complexes. *RSC Adv.* **11**, 5232–5238 (2021).
5. Artero, V. & Saveant, J.-M. Toward the rational benchmarking of homogeneous H_2-evolving catalysts. *Energy Environ. Sci.* **7**, 3808–3814 (2014).
6. Costentin, C. & Savéant, J.-M. Multielectron, Multistep Molecular Catalysis of Electrochemical Reactions: Benchmarking of Homogeneous Catalysts. *CHEMELECTROCHEM* **1**, 1226–1236 (2014).
7. Rountree, E. S., McCarthy, B. D., Eisenhart, T. T. & Dempsey, J. L. Evaluation of Homogeneous Electrocatalysts by Cyclic Voltammetry. *Inorg. Chem.* **53**, 9983–10002 (2014).
8. Roy, S. *et al.* Molecular Cobalt Complexes with Pendant Amines for Selective Electrocatalytic Reduction of Carbon Dioxide to Formic Acid. *J. Am. Chem. Soc.* **139**, 3685–3696 (2017).
9. Queyriaux, N. *et al.* Electrocatalytic Hydrogen Evolution with a Cobalt Complex Bearing Pendant Proton Relays: Acid Strength and Applied Potential Govern Mechanism and Stability. *J. Am. Chem. Soc.* **142**, 274–282 (2020).
10. Razavet, M., Artero, V. & Fontecave, M. Proton Electroreduction Catalyzed by Cobaloximes: Functional Models for Hydrogenases.
11. Galan, B. R. *et al.* Electrocatalytic Oxidation of Formate by $[Ni(P^{R}_2N^{R'}_2)_2(CH_3CN)]^{2+}$ Complexes. *J. Am. Chem. Soc.* **133**, 12767–12779 (2011).
12. Wilson, A. D. *et al.* Hydrogen Oxidation and Production Using Nickel-Based Molecular Catalysts with Positioned Proton Relays. *J. Am. Chem. Soc.* **128**, 358–366 (2006).
13. Bhugun, I., Lexa, D. & Savéant, J.-M. Homogeneous Catalysis of Electrochemical Hydrogen Evolution by Iron(0) Porphyrins. *J. Am. Chem. Soc.* **118**, 3982–3983 (1996).
14. Coutard, N., Kaeffer, N. & Artero, V. Molecular engineered nanomaterials for catalytic hydrogen evolution and oxidation. *Chem. Commun.* **52**, 13728–13748 (2016).

Chapter 3: Ligand stereochemical tailoring of thiosemicarbazone nickel complexes for electrocatalytic hydrogen production

3.1 Introduction

With the aim to broaden our research scope following the chemical changes made on the thiosemicarbazone ligand-based nickel complexes discussed in Chapter 2, we decided to investigate if the position of the substituent group was more important than its chemical nature. This assumption has already been discussed in the literature in the context of photocatalytic hydrogen evolution.[1] For this reason, we prepared a series of nickel thiosemicarbazone complexes based on the original para substituted ligand placing the methoxy group into different positions on the phenyl ring and considering multiple combinations of these positions (Figure 1). The -OCH_3 group is known to act as an electron donor in the para position. By just shifting it to the meta position, its electronic nature changes into an electron acceptor. Pushing -OCH_3 into the ortho position, it acts once again as an electron donor. To complete this new family of complexes, we wished also to validate the necessity of any substituted group on the ring and we prepared a ligand having a non-functionalized phenyl moiety. This investigation focuses on how different structures of almost chemically identical compounds can affect their catalytic performances toward electrocatalytic hydrogen evolution.

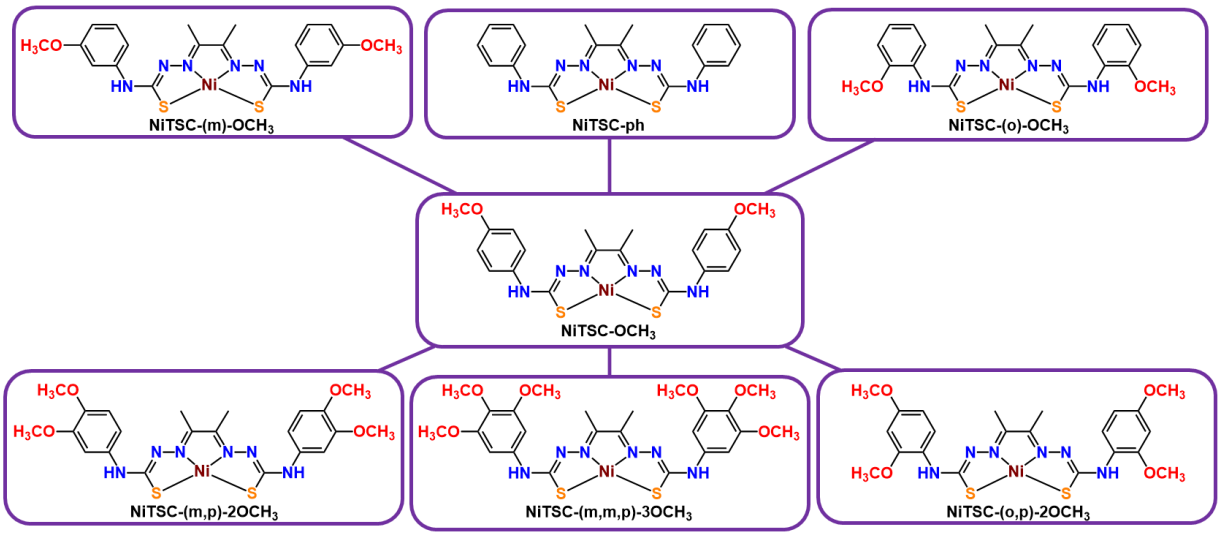

Figure 1. *Structures of NiTSC-(x)-OCH_3 and NiTSC-ph series derived from the parent complex NiTSC-OCH_3.*

3.2 Results and Discussion

3.2.1 Synthesis and Characterization

The synthesis of the new ligands followed the same protocol that was discussed in the previous Chapter.[2,3] Upon the metalation reaction, the new complexes were purified and characterized by NMR spectroscopy, HRMS ESI and UV-vis spectroscopy. We were able to obtain suitable crystals by slow evaporation of different solvents (see details in experimental section). The crystal structures of all the new nickel complexes were solved by X-ray diffraction analysis (Figure 2).

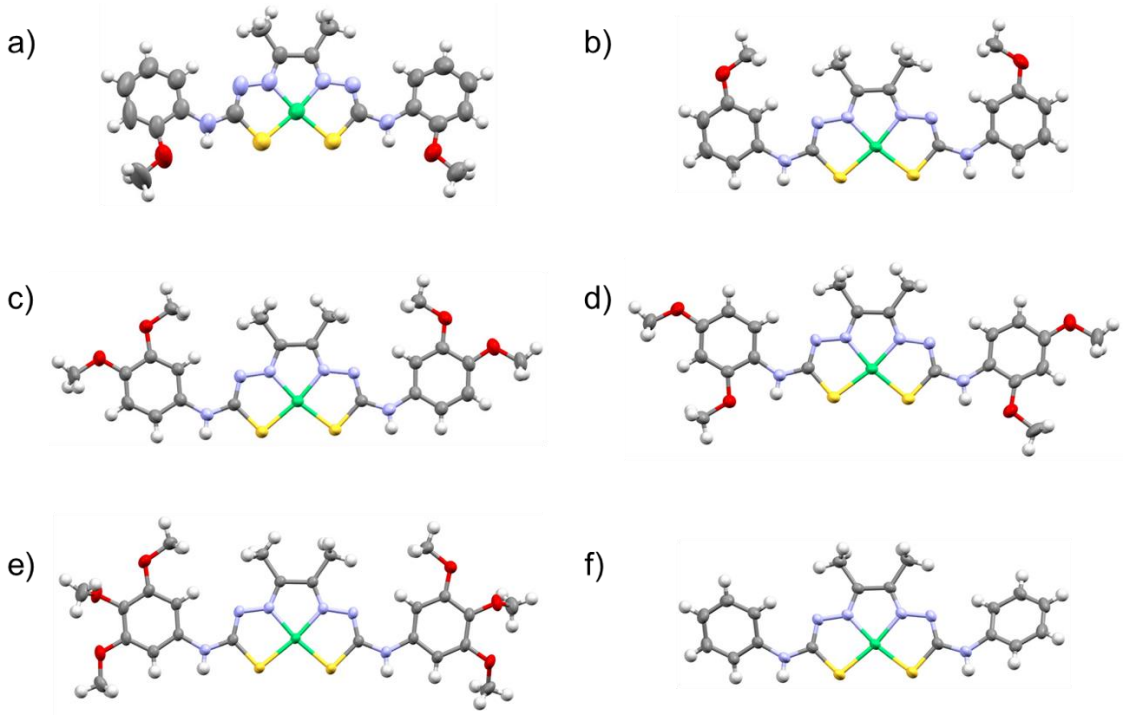

Figure 2. *X-ray crystal structures of nickel complexes: a) NiTSC-(o)-OCH_3 b) NiTSC-(m)-OCH_3 c) NiTSC-(m,p)-$2OCH_3$ d) NiTSC-(o,p)-$2OCH_3$ e) NiTSC-(m,m,p)-$3OCH_3$ f) NiTSC-ph.*

We also recorded the UV-vis spectra of the complexes in DMF (Figure 3). All complexes displayed a main absorption band around 450-480 nm (Table 1). This absorption band was attributed to a d-d transition based on the previous computational analysis performed

on the parent complex NiTSC-OCH_3.[2] A second absorption band is located in the UV region around 271-275 nm and is assigned to the absorption of the ligand.

Table 1. *Selected spectral features from the electronic absorption spectra of NiTSC-(x)-OCH_3 series in DMF.*

Catalyst	λ (nm)	ε ($M^{-1}s^{-1}$)
NiTSC-(o)-OCH_3	271	36903
	452	19226
NiTSC-(m)-OCH_3	273	38631
	457	20748
NiTSC-(m,p)-2OCH_3	272	34738
	480	15819
NiTSC-(o,p)-2OCH_3	274	41682
	464	20601
NiTSC-(m,m,p)-3OCH_3	272	51727
	474	22824
NiTSC-ph	272	35200
	455	21700

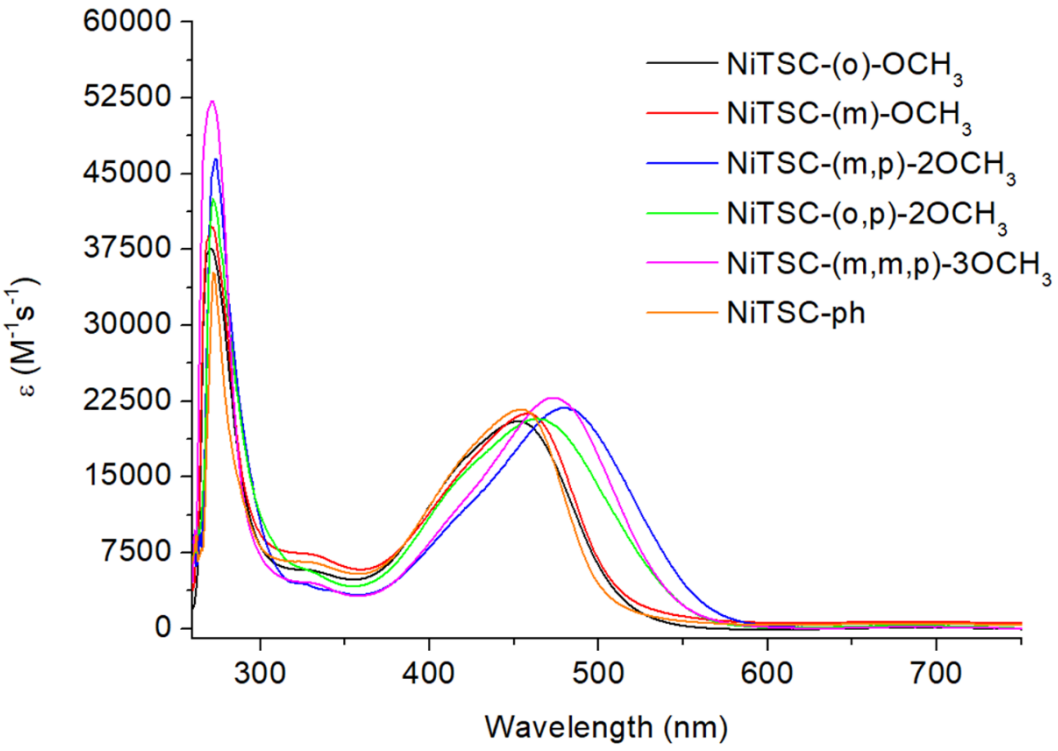

Figure 3. *UV-vis spectra of the the NiTSC-(x)-OCH_3 series in DMF.*

3.2.2 Electrochemical Investigation

Cyclic voltammograms were recorded under nitrogen atmosphere at room temperature. The solutions contained as supporting electrolyte the tetrabutylammonium hexafluorophosphate (NBu_4PF_6) in DMF. A three-electrode system was used with the working electrode being a glassy carbon electrode. The redox behaviors of the complexes were investigated. Following the results presented in Chapter 2, their electrochemical response remained similar to the NiTSC-OCH_3 complex. We observed two quasi-reversible processes when scanning the cathodic region from 0 to -2.75 V vs $Fc^{+/0}$ (Table 2). Upon comparison of the two reduction peaks within the complex family, we can observe that they are weakly affected by either the shift, combination, or total absence of the methoxy group in all investigated positions (Figure 4).

Table 2. *Electrochemical data of NiTSC-(x)-OCH_3 series (V vs. $Fc^{+/0}$) including the parent complex NiTSC-OCH_3.*

Complex	NiTSC-(x)-OCH_3 / [NiTSC-(x)-OCH_3]$^-$	[NiTSC-(x)-OCH_3]$^-$ / [NiTSC-(x)-OCH_3]$^{2-}$
NiTSC-(o)-OCH_3	-1.52	-2.19
NiTSC-(m)-OCH_3	-1.55	-2.20
NiTSC-(m,p)-2OCH_3	-1.61	-2.25
NiTSC-(o,p)-2OCH_3	-1.56	-2.21
NiTSC-(m,m,p)-3OCH_3	-1.54	-2.20
NiTSC-ph	-1.55	-2.20
NiTSC-OCH_3	-1.57	-2.20

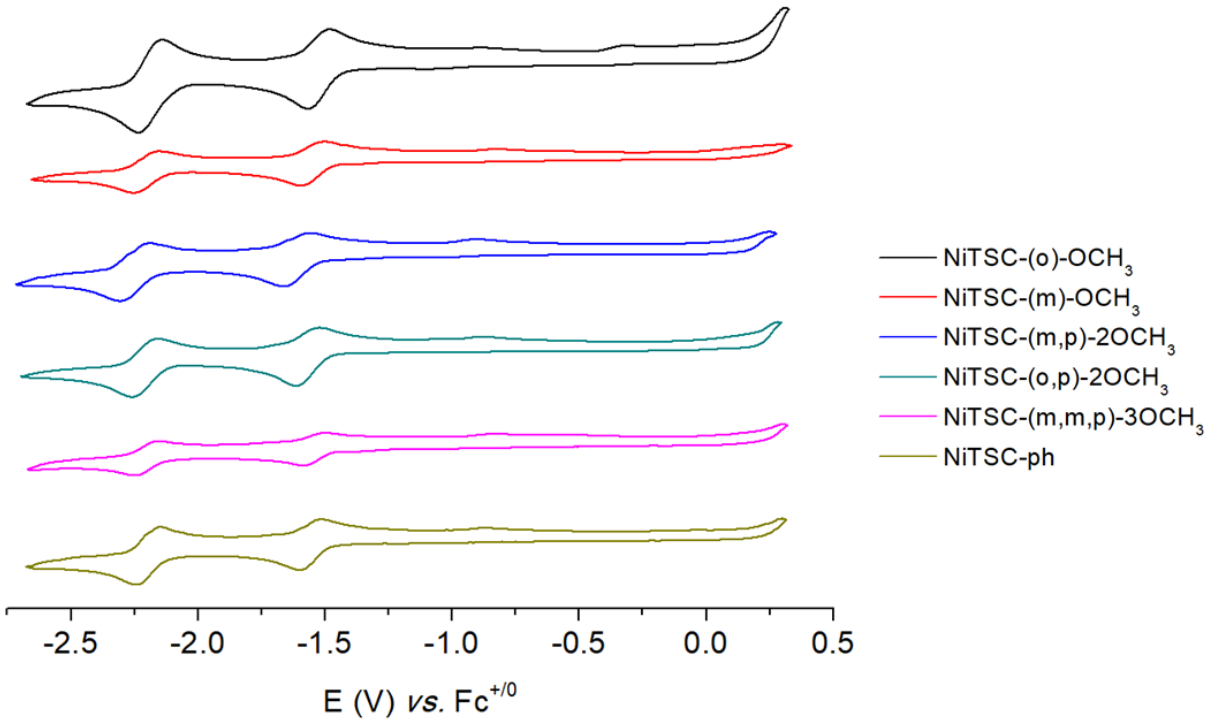

Figure 4. *Cyclic voltammograms of NiTSC-(x)-OCH_3 series. Conditions: concentration 1 mM at a stationary 1 mm glassy carbon electrode in DMF (0.1 M NBu_4PF_6) using a 500 mV/s scan rate.*

In theory, an electron donating group should shift the reduction potentials to more negative values as it displaces the electronic density of the complex toward the metal, making electron transfer harder in an already electron rich environment. On the contrary, an electron withdrawing group should drive away the density from the metal and facilitate the reduction process leading to a decrease of the redox potential. Looking at our results, the bigger change in redox potential is only about 40 mV and comes from the NiTSC-(m,p)-$2OCH_3$ complex having the most negative redox potential. This complex bears substituents that behave as an acceptor and a donor group and thus shows that the electronic properties of the ligand do not cancel each other out. Consequently, no clear rational can be made regarding the substitution effects on the electrochemical behavior of the complexes.

DFT computations were also performed on this family of complexes to confirm the above analysis and provide more insight into the nature of the species resulting from the two successive reduction events. The computed redox potentials confirm that the first reduction process remains ligand-based with a fair agreement between calculated values and experimental ones (Table 3). Regarding the second reduction process, the computational results confirm that the second reduction process is metal-centered, as observed in the case of the chemical substitution study.

Table 3. *Calculated redox potentials of NiTSC-(x)-OCH_3 series (V vs. $Fc^{+/0}$).*

Complex	NiTSC-(x)-OCH_3 / [NiTSC-(x)-OCH_3]$^-$	[NiTSC-(x)-OCH_3]$^-$ / [NiTSC-(x)-OCH_3]$^{2-}$
NiTSC-(o)-OCH_3	-1.55	-2.18
NiTSC-(m)-OCH_3	-1.50	-2.17
NiTSC-(m,p)-2OCH_3	-1.64	-2.06
NiTSC-(o,p)-2OCH_3	-1.58	-2.29
NiTSC-(m,m,p)-3OCH_3	-1.44	-2.22
NiTSC-ph	-1.43	-2.17
NiTSC-OCH_3	-1.54	-2.28

3.2.3 Electrocatalytic proton reduction

To investigate the ability of the complex family to mediate electrocatalytic hydrogen evolution, we recorded their cyclic voltammograms in the presence of a proton source using trifluoroacetic acid (TFA, pK_a= 6.00 ± 0.03 in DMF).[4] The negative region was scanned after the addition of increased concentrations of TFA (Figures 5 and 12). For all the complexes, we used identical experimental conditions.

The addition of acid to the NiTSC-(x)-OCH_3 series triggered the appearance of two proton-dependent waves. The current increase of these peak-shaped waves was found to be proportional to the amount of proton source added in each solution. The first wave displays the same peak potential for all complexes at around -1.5 V vs. $Fc^{/+0}$. The peak potential of the second wave is observed between -2.11 and -2.28 V vs. $Fc^{+/0}$ and is slowly shifted to more negative potential values upon successive addition of TFA (Figure 12). For instance, the peak potential of NiTSC-(o)-OCH_3 is found at -2.14 V vs. $Fc^{+/0}$ in presence of 20 mM of TFA and it is displaced at -2.38 V vs. $Fc^{+/0}$ with 100 mM of TFA. For the first process, the potential value remained mostly unaffected upon the gradual addition of the proton source (Figure 5). To prove the role played by the nickel complex in the observed current enhancement, we recorded the cyclic voltammogram of TFA only was also recorded (Figure 12, black dashed line).

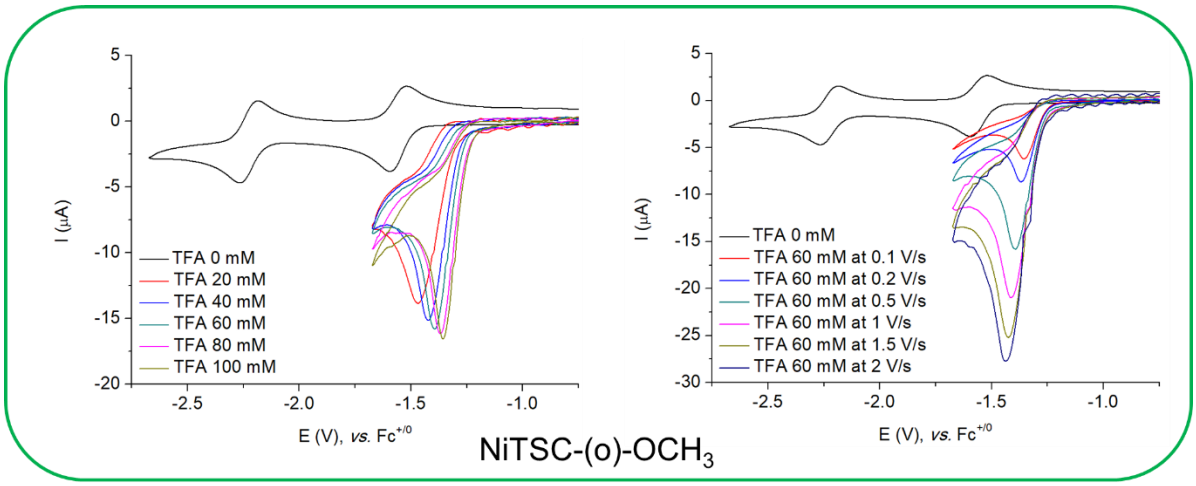

NiTSC-(o)-OCH_3

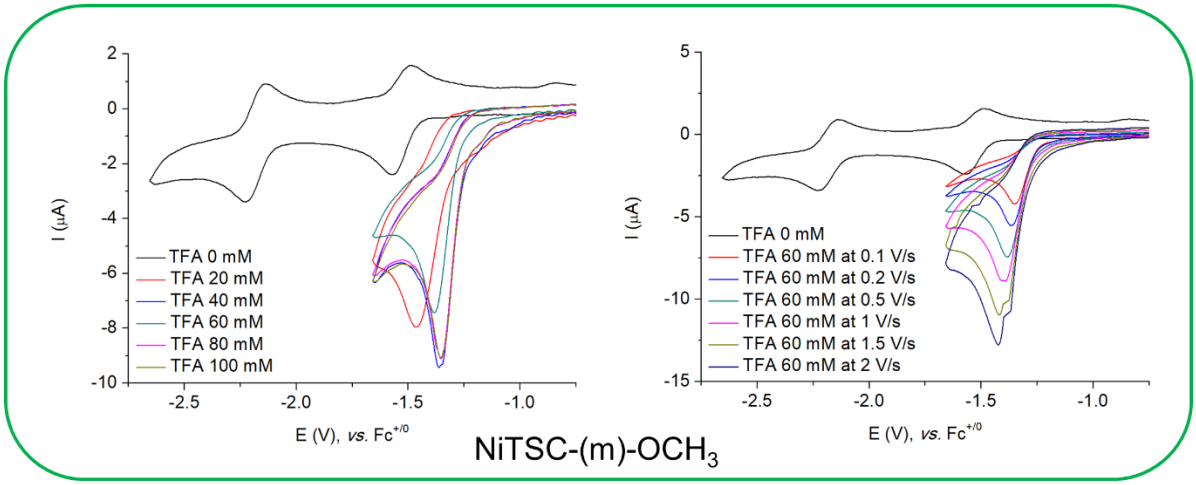

NiTSC-(m)-OCH_3

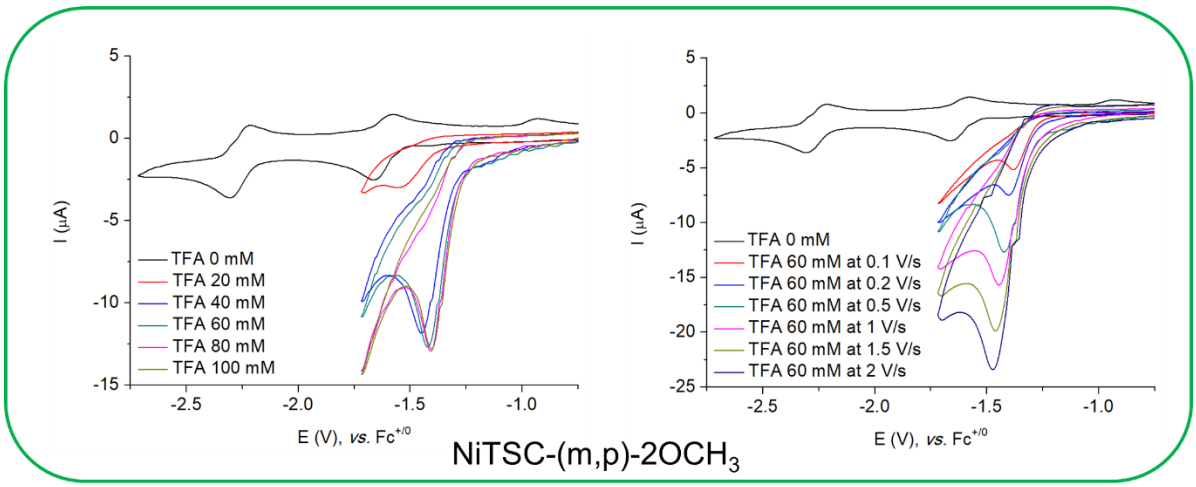

NiTSC-(m,p)-$2OCH_3$

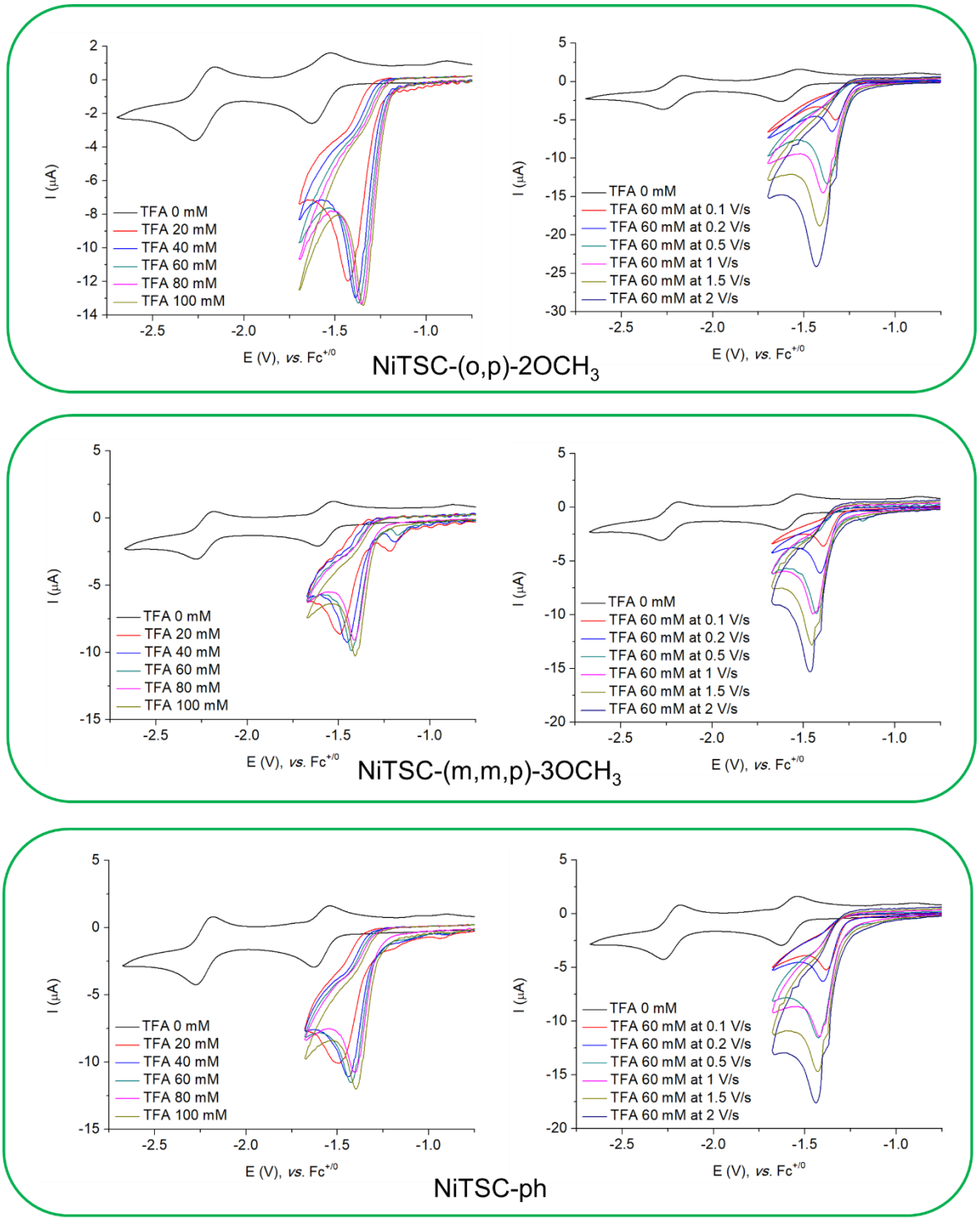

Figure 5. *Successive cyclic voltammograms recorded at a glassy carbon as working electrode of a 1 mM solution of NiTSC-(x)-OCH₃ series in DMF (0.1 M NBu₄PF₆) with increasing concentration of TFA at 500 mV/s scan rates (left) and 60 mM TFA at five different scan rates (right).*

To verify that the signal observed is not connected with species being absorbed onto the surface of the working electrode, we performed a series of dip and rinse tests for all the complexes. After each measurement, the working electrode was removed from the solution and dipped into a fresh solution of DMF (0.1 M NBu_4PF_6). For all the series, only the residual background signal was recorded when scanning toward the negative region (black lines Figure 6). Upon addition of 100 mM TFA, sweeping the potential again provided only the response of acid (blue lines Figure 6). These control experiments allow us to confirm that no species are absorbed onto the glassy carbon electrode during the electrocatalytic experiments. This investigation proves that the signal was due to the dissolved NiTSC-(x)-OCH_3 complexes and that, hence, we were investigating a homogenous system.

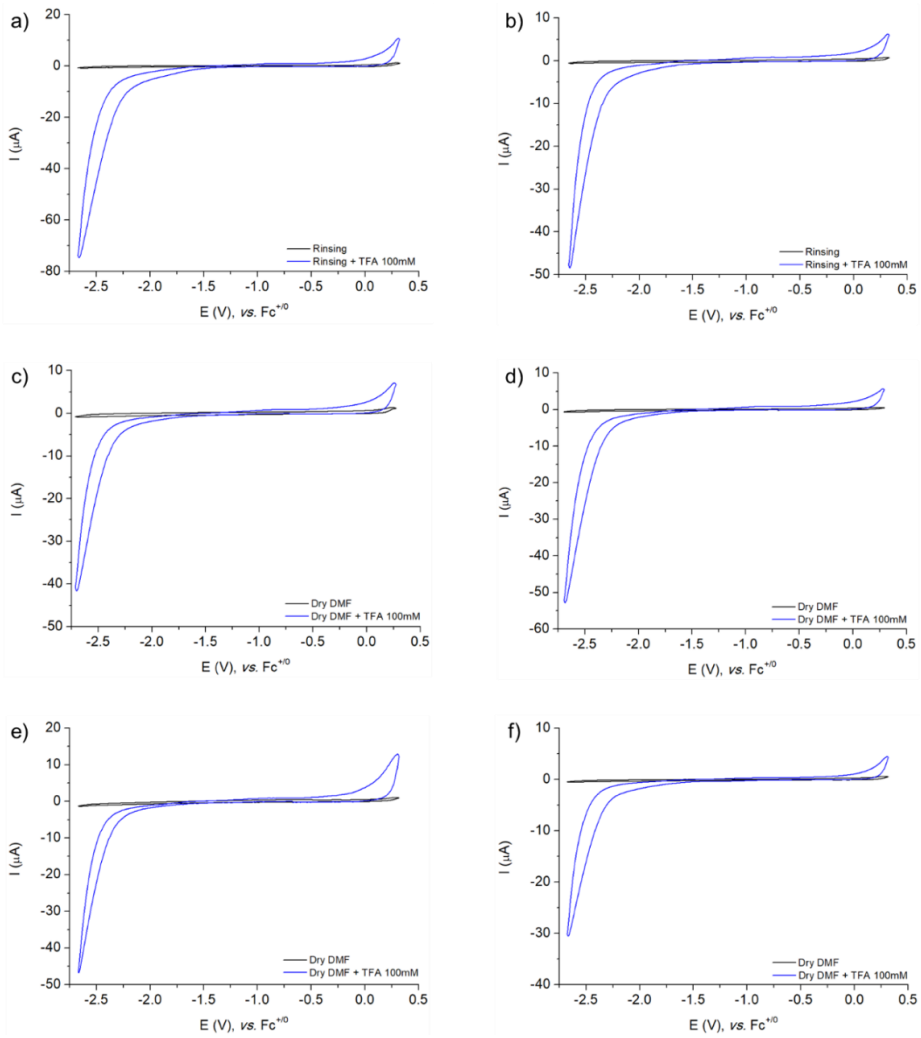

Figure 6. *Successive cyclic voltammograms recorded after electrocatalysis upon washing the glassy carbon electrode and immersion into a fresh solution of DMF (0.1 M NBu_4PF_6, black line) and in the presence of 100 mM of TFA (blue line) of: a) NiTSC-(o)-OCH_3 b) NiTSC-(m)-OCH_3 c) NiTSC-(m,p)-$2OCH_3$ d) NiTSC-(o,p)-$2OCH_3$ e) NiTSC-(m,m,p)-$3OCH_3$ f) NiTSC-ph. Scan rate: 500 mV/s.*

To confirm that the recorded electrochemical responses presented in Figures 5 and 12 correspond to hydrogen production, bulk electrolysis experiments were performed coupled with gas analysis. Solutions of 8 ml DMF (0.1 M NBu_4PF_6) containing 1 mM of each of the NiTSC-(x)-OCH_3 complex and 100 mM of TFA were prepared. We applied a fixed potential of -1.7 V vs. $Fc^{+/0}$ over 16 hours. The reaction was monitored by continuous in-line gas analysis. We used a mercury pool working electrode to make certain that any nanoparticles produced would be absorbed into mercury, maintaining the homogeneous nature of our systems.

During 16 hours, all complexes showed to be active toward hydrogen evolution. The results of their performances are summarized in Table 4 and the charge evolution over time is graphically presented in Figure 7. From these measurements, lots of information can be extracted.

Firstly, looking at the supposedly "outcast" complex of the group, namely NiTSC-ph, we can observe that it reached a turnover number of 20 similar to that of the reference complex NiTSC-OCH_3 (TON= 21),[2] but its faradaic yield (FY) dropped of about 10% in magnitude compared to the parent catalyst (71.6% and 80% for NiTSC-ph and NiTSC-OCH_3, respectively). These data prove that the methoxy substituent is providing a positive effect on catalysis, rendering it necessary to achieve greater performance.

Table 4. *HER parameters of the NiTSC-(x)-OCH_3 series.*

Catalyst	Q (C)	Faradaic efficiency (%)	TON
NiTSC-(o)-OCH_3	82.887	90.5	44
NiTSC-(m)-OCH_3	56.025	92.8	34
NiTSC-(m,p)-2OCH_3	25.897	64.1	11
NiTSC-(o,p)-2OCH_3	27.879	66.7	12
NiTSC-(m,m,p)-3OCH_3	52.214	96.3	32
NiTSC-ph	41.592	71.6	20

Secondly, we can observe that the combination of positions on the phenyl ring affects the catalysis in two different ways. The two double-substituted complexes NiTSC-(m,p)-2OCH_3 and NiTSC-(o,p)-2OCH_3 performed very similarly with each other and presented the worst HER parameters of the series both in terms of TON and FY values. On the other hand, the performances of the triple-substituted complex NiTSC-(m,m,p)-3OCH_3 came with great surprise. It surpassed the original mono-substituted NiTSC-OCH_3 in hydrogen production

(TON= 32) and displayed the best faradaic efficiency (FY= 96.3%) while still not being the best catalyst in these series.

Finally, the best results to be discussed concern the mono methoxy-bearing complexes. Both NiTSC-(o)-OCH_3 and NiTSC-(m)-OCH_3 significantly outperformed the parent complex with a TON of 44 and 34, respectively. Although the hydrogen production of the ortho substituted nickel catalyst was unmatched, the meta analog had a slightly better faradaic efficiency (90.5% and 92.8% for NiTSC-(o)-OCH_3 and NiTSC-(m)-OCH_3, respectively). We can thus conclude that when the methoxy group is at the meta position of the ligand, it can use the electrons given to the system to mediate hydrogen evolution in a more efficient manner. That is also supported by the fact that the NiTSC-(m,m,p)-$3OCH_3$ catalyst, bearing two meta -OCH_3 moieties, displays by far the biggest faradaic efficiency of the family.

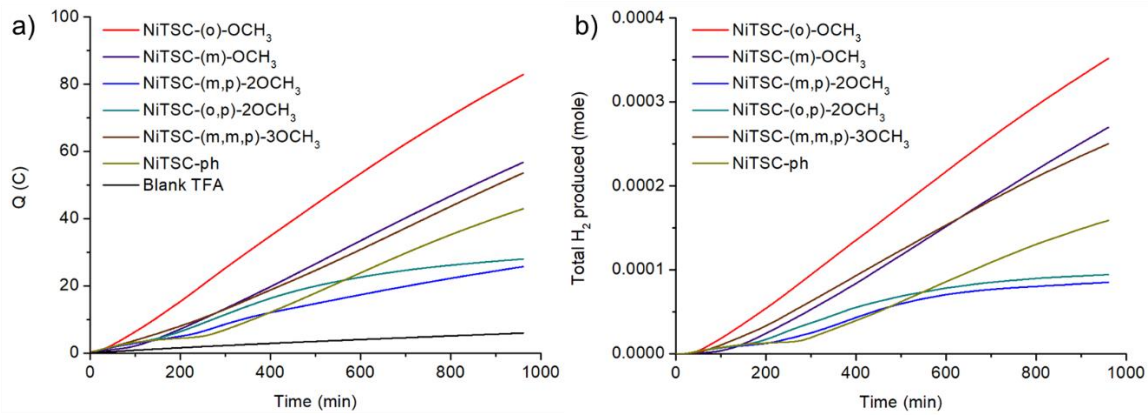

Figure 7. *a) Coulometry and b) total H_2 production of the NiTSC-(x)-OCH_3 series during bulk electrolysis experiments at -1.70 V vs. $Fc^{+/0}$ using a pool mercury working electrode. The electrolytic solution contains 0.1 M NBu_4PF_6 in DMF, 100 mM TFA and 1 mM of NiTSC-(x)-OCH_3.*

To summarize, it is clear that the chemical nature of the substituted group in the phenyl ring of the ligand seems to be not as important as its position since the best catalyst of the position series NiTSC-(o)-OCH_3 is more efficient in H_2 production (TON= 44) than the best performing catalyst of the chemical substitution series (NiTSC-SCH_3 with TON= 37).

3.2.4 Mechanistic Investigations

To investigate the sequence of events leading to hydrogen production with our new family of complexes, we recorded the UV-vis spectra of every complex in the absence and presence of TFA (Figure 8). For all the series, it is clear that upon the addition of up to 100 equivalents of the acid, no shift happened to the main absorption bands of the spectra. These experiments rule out a chemical (protonation) event as the first step of the catalytic process.

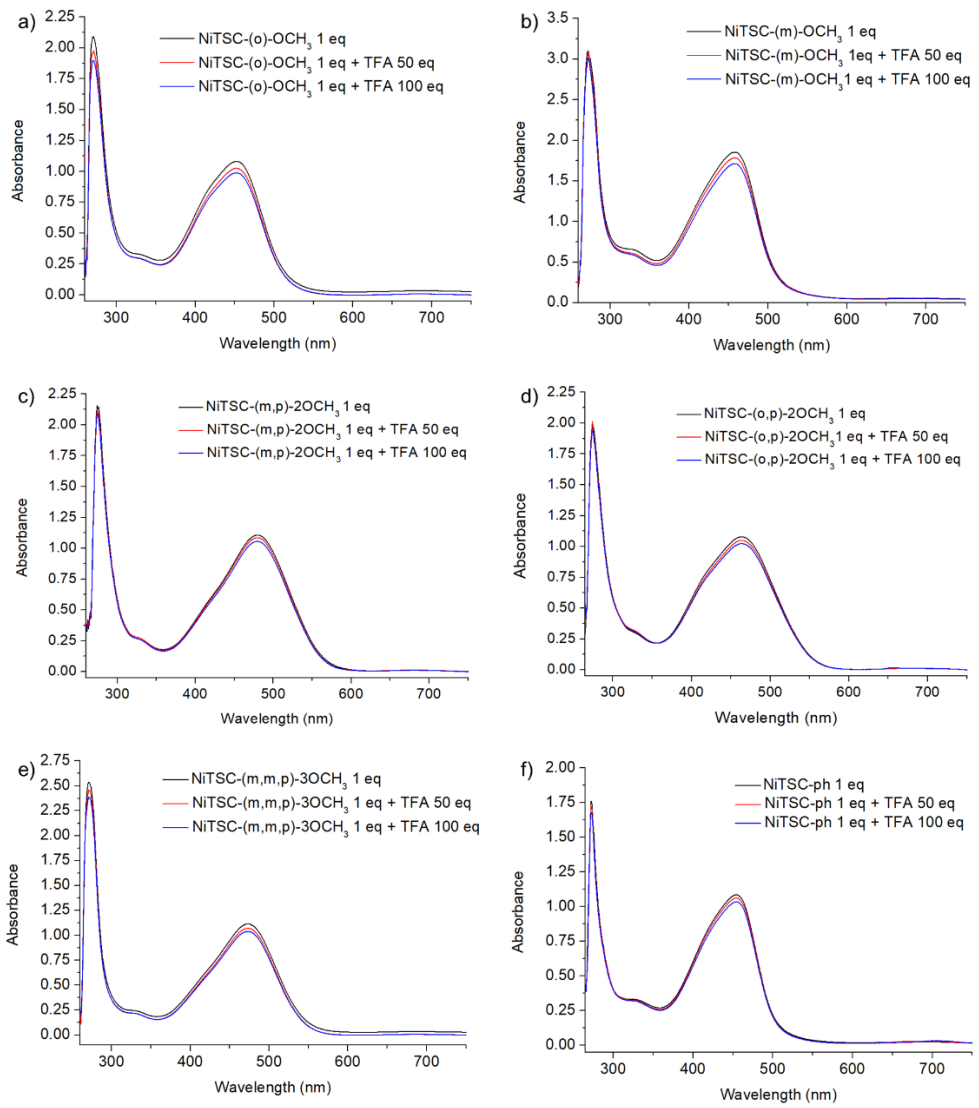

Figure 8. *UV-vis spectra of: a) NiTSC-(o)-OCH_3 b) NiTSC-(m)-OCH_3 c) NiTSC-(m,p)-$2OCH_3$ d) NiTSC-(o,p)-$2OCH_3$ e) NiTSC-(m,m,p)-$3OCH_3$ f) NiTSC-ph, in the absence and upon the addition of TFA.*

Based on our findings with the chemical substitution series in Chapter 2, the catalytic process of these compounds should follow a similar catalytic pathway with an ECEC mechanism.[5] DFT mechanistic investigations are currently being performed by our group to validate this hypothesis and prove that the stereochemical changes of the ligands do not affect their hydrogen evolution mechanism.

To further investigate our series of catalysts, we calculated the TOF values using the data obtained from bulk electrolysis experiments. We followed the same approach we employed in Chapter 2 and used the following equation:[6,7]

$$\mathrm{TOF} = \frac{{i_{\mathrm{el}}}^2 \left(1 + \exp\left[\frac{F}{RT}(E_{\mathrm{appl}} - E_{1/2})\right]\right)}{F^2 A^2 D_{\mathrm{cat}} [\mathrm{Cat}]^2}$$

where F is Faraday constant, A the surface area of the working electrode, D_{cat} the diffusion coefficient, *[Cat]* the concentration of the catalyst, E_{appl} the applied potential during electrolyses, $E_{1/2}$ the mid-wave potential for the catalytic wave and i_{el} the current density during bulk electrolysis (see experimental section of Chapter 2 for details). The maximal turnover frequencies (TOF_{max}) of the series of complexes were then evaluated using the following relation:

$$\mathrm{TOF} = \frac{\mathrm{TOF}_{\mathrm{max}}}{1 + \exp\left[\frac{F}{RT}(E_{\mathrm{appl}} - E_{1/2})\right]}$$

The results of this analysis are summarized in Table 5. Although the best performing catalyst for producing hydrogen was found to be the ortho substituted complex, the NiTSC-(m,m,p)-3OCH_3 complex has by far the fastest catalytic response reaching a TOF equal to 421.3 s^{-1}, a value 1.5 times larger than that of NiTSC-(o)-OCH_3 (TOF= 283.5 s^{-1}). Looking at the catalysis rate values, it is very interesting to observe that almost all the members of the new family outperformed the reference complex NiTSC-OCH_3 (TOF= 89.7 s^{-1}) with exception of the double substituted complexes NiTSC-(m,p)-2OCH_3 and NiTSC-(o,p)-2OCH_2

Table 5. *Calculated TOF values for the NiTSC-(x)-OCH_3 complex family.*

Complex	D_{cat} (cm^2/s)	i_{el} (A)	F.Y. (%)	$E_{1/2}$ (V vs. $Fc^{+/0}$)	TOF (s^{-1})
NiTSC-(o)-OCH_3	$2.47*10^{-6}$	$1.20*10^{-3}$	90.5	-1.260	283.5
NiTSC-(m)-OCH_3	$0.58*10^{-6}$	$0.53*10^{-3}$	92.8	-1.216	237.5
NiTSC-(m,p)-OCH_3	$1.12*10^{-6}$	$0.45*10^{-3}$	64.1	-1.283	85.7
NiTSC-(o,p)-OCH_3	$1.12*10^{-6}$	$0.43*10^{-3}$	66.7	-1.244	80.2
NiTSC-(m,m,p)-OCH_3	$0.73*10^{-6}$	$0.80*10^{-3}$	96.3	-1.301	421.3
NiTSC-ph	$1.1*10^{-6}$	$0.57*10^{-3}$	71.6	-1.283	140.1

The overpotential values of the complex series were determined following the previously reported protocol[4] and were calculated as the difference between the mid-wave catalytic potential ($E_{1/2}^{cat}$) and the theoretical half-wave potential ($E_{1/2}^{T}$) such as:

$$\eta = E_{1/2}^{cat} - E_{1/2}^{T}$$

When comparing the calculated overpotential values, our results highlight the dependence of the driving force of the reaction with the ligand electronic properties (Table 6). All calculated overpotential values are improved compared to that of the parent complex NiTSC-OCH_3 (η= 0.344). Interestingly, the lowest overpotential is obtained for the catalyst with the most electron-withdrawing group, NiTSC-(m)-OCH_3 which is consistent with our previous observations with the chemical substitution series for which the lowest overpotential was obtained with the NiTSC-CN catalyst.

Table 6. *Calculated mid-wave potential and overpotential (V vs. $Fc^{+/0}$) for the NiTSC-(x)-OCH_3 family.*

Complex	$E_{1/2}$	Overpotential (η)
NiTSC-(o)-OCH_3	-1.260	0.274
NiTSC-(m)-OCH_3	-1.216	0.230
NiTSC-(m,p)-OCH_3	-1.283	0.297
NiTSC-(o,p)-OCH_3	-1.244	0.258
NiTSC-(m,m,p)-OCH_3	-1.301	0.315
NiTSC-ph	-1.283	0.297

Taking into account the mid-wave potentials of both the series and the reference complex (Table 6) and using the equilibrium potential of H^+/H_2 couple (-0.986 V vs. $Fc^{+/0}$) with 1 M of TFA, catalytic Tafel plots were derived (Figure 9), showing the relationship between the turnover frequency of H_2 evolution and the overpotential (η).

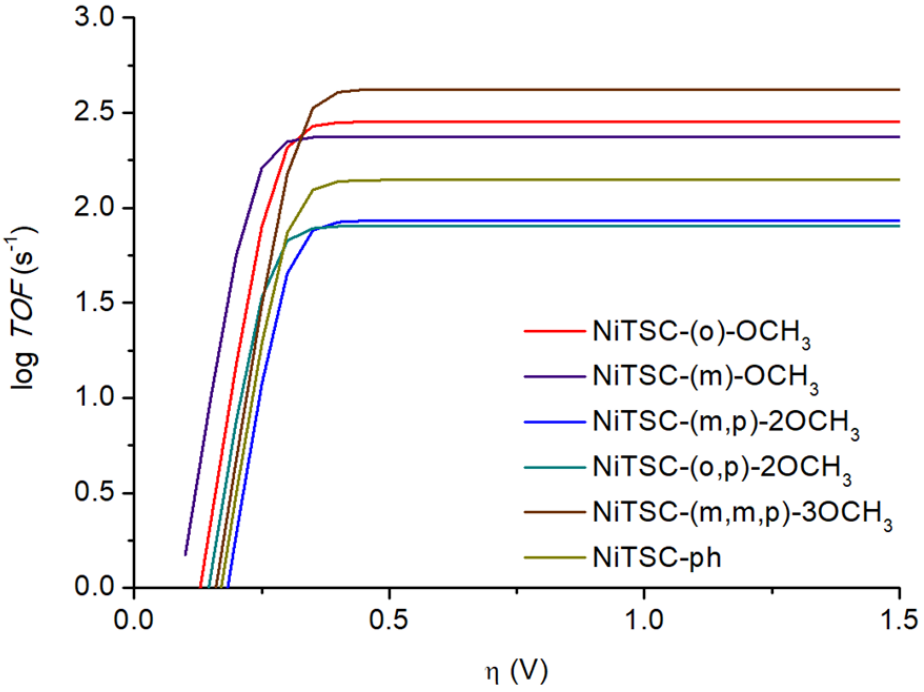

Figure 9. *Catalytic Tafel plots: comparison of performances for HER catalyzed by NiTSC-(x)-OCH_3 series in DMF in presence of 1 M TFA.*

Focusing on the best performing catalysts of this family, NiTSC-(o)-OCH_3, NiTSC-(m)-OCH_3 and NiTSC-(m,m,p)-3OCH_3 (red, purple and brown traces respectively, Figure 9 and 10), we observe that these complex displays significant catalytic activity (log(TOF) > 1) for low overpotential values. They can easily be compared well with benchmark molecular catalysts of the literature, like cobaloximes[8] (blue trace, Figure 10) or nickel bisdiphosphine catalysts[9,10] (orange trace, Figure 10) as far as the overpotential requirements are concerned. Interestingly, all the complexes outperform their parent complex NiTSC-OCH_3. Upon carefully analysing all these data, we can now confirm that the position of the methoxy group on the benzyl ring of the ligand has an important effect on the catalytic performances of the bisthiosemicarbazone-based complexes. Additionally, these results also support that the position of the ligand substituent has a greater effect on the catalysis parameters (TON, TOF, FY, η) than its chemical nature.

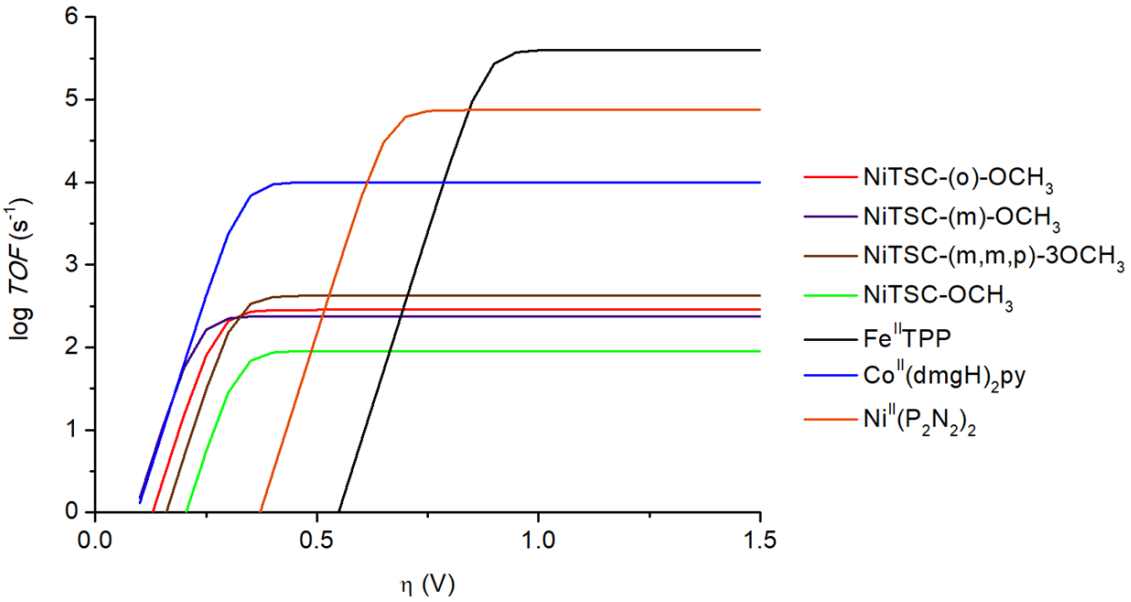

Figure 10. *Catalytic Tafel plots: comparison of performances for HER catalysed by NiTSC-(o)-OCH₃, NiTSC-(m)-OCH₃ and NiTSC-(m,m,p)-3OCH₃ in DMF in the presence of 1 M TFA (red, purple and brown line respectively) and NiTSC-OCH₃*[2] *in DMF in the presence of 1 M TFA (green line) with other catalysts reported in the literature. Black: Fe^{II}TPP, DMF, Et_3NH^+,*[11,12] *blue: $[Co^{II}(dmgH)_2py]$, DMF, Et_3NH^+,*[11,13] *orange: $[Ni^{II}(P_2PhN_2C_6H_4X)_2]^{2+}$, X = $CH_2P(O)(OEt)_2$, MeCN, $DMFH^+$.*[9,11]

3.3 Conclusions

A new series of nickel catalysts based on thiosemicarbazone ligands was prepared to expand upon the original para substituted methoxy-containing ligand. We investigated the new series for its ability to evolve hydrogen via electrocatalysis. Our approach was to test different positions of the methoxy group (ortho, meta, para) and evaluate the importance of its presence within the complex considering the unsubstituted complex NiTSC-ph. Although this mainly stereochemical difference did not affect the electrochemical characteristics of the complexes, we observed significant differences in their HER performance. The NiTSC-(o)-OCH_3 complex outperformed all the other family members in total H_2 produced with a TON of 44 and was identified as the second fastest producing catalyst reaching a TOF of 283.5 s^{-1}. The NiTSC-(m,m,p)-$3OCH_3$ complex surpassed every expectation with very good production (TON= 32), the best faradaic yield of 96.3% and the largest catalysis rate (TOF= 421.3 s^{-1}). The NiTSC-(m)-OCH_3 complex was found to be the catalyst displaying the lower driving force (η = 0.230) with a catalysis rate and HER parameters comparable to those of NiTSC-(m)-OCH_3. Detailed analysis of the electrocatalytic data allowed benchmarking of their performances and catalytic Tafel plots showed that the NiTSC-(o)-OCH_3, NiTSC-(m)-OCH_3 and NiTSC-(m,m,p)-$3OCH_3$ can compare with benchmarked molecular catalysts when focusing on the overpotential requirements.

Our study confirms the theory that the position of the substituent group is significantly more important than its chemical nature, as the new series overshadows the previous chemical substitution study presented in Chapter 2. Our results suggest that the next step to better improve HER performances with our catalysis would consist in combining both approaches. For instance, the use of the -SCH_3 group in a different position through the preparation of either the NiTSC-(o)-SCH_3, the NiTSC-(m)-SCH_3 or even the NiTSC-(m,m,p)-$3SCH_3$) complexes could provide new electrocatalysts with enhanced producing capabilities, pushing our system at the level of benchmarked molecular catalysts reported in the literature.

3.4 Experimental section and supplementary data

3.4.1 Synthesis and Characterization

The synthesis of the complexes follows the same protocol as discussed in Chapter 2.

General synthetic protocol of ligands

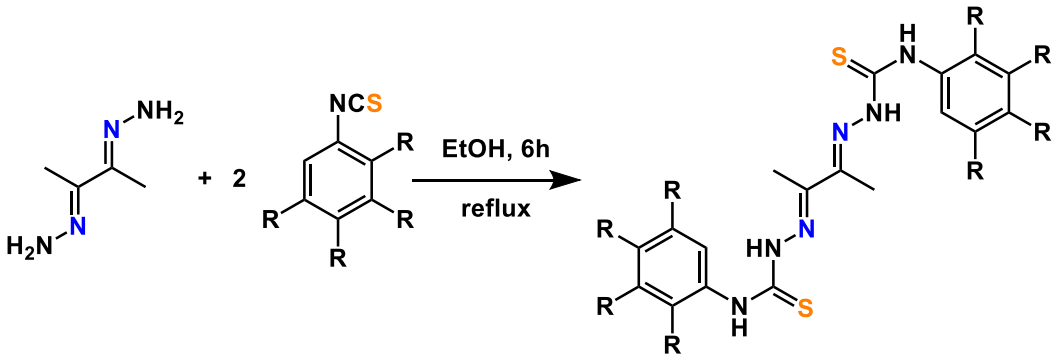

In a solution of ethanol, 1 equivalent of butan-2,3-dihydrazone and 2 equivalents of the corresponding isothiocyanate are added. The mixture is heated at reflux for 6 hours. After that time, it is allowed to cool down to room temperature and then an ice bath is used to cool it down to 0 °C. A yellow precipitate is formed. The solid obtained after filtration is washed with two portions of ethanol and used without any further purification.

General synthetic protocol of nickel complexes

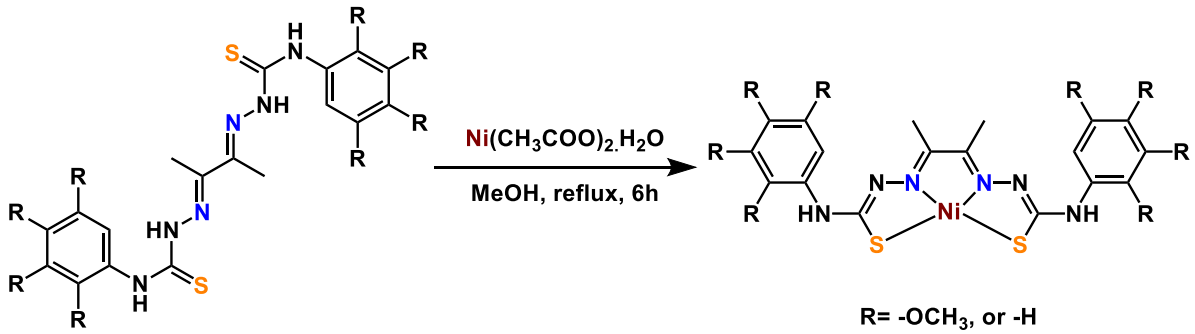

In a solution of methanol, 1 equivalent of the corresponding ligand is added with 1.2 equivalents of $Ni(CH_3COO)_2{\cdot}4H_2O$. The mixture is refluxed. After 6 hours, the reaction is cooled to 0°C with a water bath and water is added. The mixture is filtered and washed with cold water and cold methanol. A neutral alumina (Al_2O_3) liquid chromatography column is prepared to purify the desired compound.

*2,3-di(2-(methoxyphenylthiosemicarbazone)butane nickel (II) (*NiTSC-(o)-OCH_3)

From 2,3-di(2-(methoxyphenylthiosemicarbazone) butane (0.112 mmol, 50 mg) in 3 ml methanol and $Ni(CH_3COO)_2(H_2O)_4$ (0.135 mmol, 34 mg) in solution in 2 ml methanol. Alumina column with dichloromethane/cyclohexane 5:5. A dark brown solid (52 mg, 92 %) was obtained.

^{1}H NMR (400 MHz, DMSO-*d6*, TMS): δ = 8.65 (s, 2H; NH), 7.70 (d, J= 7.56 Hz, 2H; o-CH), 7.11-7.02 (m, 4H; m-CH), 6.94-6.91 (m, 2H; p-CH), 3.83 (s, 6H; O-CH_3), 1.99 (s, 6H; CH_3).

HR ESI-MS: $[M+H]^+$ calculated for $C_{20}H_{22}N_6O_2S_2Ni$: 501.0672, observed: 501.0671.

*2,3-di(3-(methoxyphenylthiosemicarbazone)butane nickel (II) (*NiTSC-(m)-OCH_3)

From 2,3-di(3-(methoxyphenylthiosemicarbazone) butane (0.112 mmol, 50 mg) in 3 ml methanol and $Ni(CH_3COO)_2(H_2O)_4$ (0.135 mmol, 34 mg) in solution in 2 ml methanol. Alumina column with dichloromethane/cyclohexane 7:3. A dark yellow solid (49 mg, 87 %) was obtained.

^{1}H NMR (400 MHz, DMSO-*d6*, TMS): δ = 10.00 (s, 2H; NH), 7.42 (t, J= 2.11 Hz, 2H; m-CH), 7.20 (t, J= 8.11 Hz, 2H; o(1)-CH), 7.20 (t, J= 8.09 Hz, 2H; o(5)-CH), 6.60-6.58 (m, 2H; p-CH), 3.78 (s, 6H; O-CH_3), 2.09 (s, 6H; CH_3).

HR ESI-MS: $[M+H]^+$ calculated for $C_{20}H_{22}N_6O_2S_2Ni$: 501.0672, observed: 501.0670.

*2,3-di(3,4-(dimethoxyphenylthiosemicarbazone)butane nickel (II) (*NiTSC-(m,p)-2OCH_3)

From 2,3-di(3,4-(dimethoxyphenylthiosemicarbazone) butane (0.099 mmol, 50 mg) in 3 ml methanol and $Ni(CH_3COO)_2(H_2O)_4$ (0.119 mmol, 30 mg) in solution in 2 ml methanol. Alumina column with dichloromethane/cyclohexane 9:1. A dark orange solid (43 mg, 77 %) was obtained.

^{1}H NMR (400 MHz, DMSO-*d6*, TMS): δ = 9.88 (s, 2H; NH), 7.49 (broad d, J = 1.53 Hz, 2H; o(1)-CH), 7.23 (dd, J_1= 8.76 Hz, J_2= 2.40 Hz, 2H; m-CH), 6.87 (d, J = 1.52 Hz, 2H; o(5)-CH), 3.73 (s, 6H; m-O-CH_3), 3.71 (s, 6H; p-O-CH_3), 2.08 (s, 6H; CH_3).

HR ESI-MS: $[M+H]^+$ calculated for $C_{22}H_{26}N_6O_4S_2Ni$: 561.0883, observed: 561.0886.

*2,3-di(2,4-(dimethoxyphenylthiosemicarbazone)butane nickel (II) (*NiTSC-(o,p)-2OCH_3)

From 2,3-di(2,4-(dimethoxyphenylthiosemicarbazone) butane (0.099 mmol, 50 mg) in 3 ml methanol and $Ni(CH_3COO)_2(H_2O)_4$ (0.119 mmol, 30 mg) in solution in 2 ml methanol. Alumina column with dichloromethane/cyclohexane 8:2. A dark brown solid (47 mg, 84 %) was obtained.

^{1}H NMR (400 MHz, DMSO-*d6*, TMS): δ = 8.67 (s, 2H; NH), 7.60 (broad d, J = 2.65 Hz, 2H; o-CH), 6.58 (d, J = 7.80 Hz, 2H; m(3)-CH), 6.58 (dd, J_1= 8.82 Hz, J_2= 2.65 Hz, 2H; m(5)-CH), 3.80 (s, 6H; o-O-CH_3), 3.74 (s, 6H; p-O-CH_3), 1.94 (s, 6H; CH_3).

HR ESI-MS: $[M+H]^+$ calculated for $C_{22}H_{26}N_6O_4S_2Ni$: 559.0738, observed: 559.0739.

*2,3-di(3,4,3'-(trimethoxyphenylthiosemicarbazone)butane nickel (II) (*NiTSC-(m,m,p)-3OCH_3)

From 2,3-di(3,4,3'-(trimethoxyphenylthiosemicarbazone) butane (0.089 mmol, 50 mg) in 3 ml methanol and $Ni(CH_3COO)_2(H_2O)_4$ (0.106 mmol, 27 mg) in solution in 2 ml methanol. Alumina column with dichloromethane. A dark orange solid (38 mg, 68 %) was obtained.

^{1}H NMR (400 MHz, DMSO-*d6*, TMS): δ = 9.88 (s, 2H; NH), 7.08 (s, 4H; o-CH), 3.72 (s, 12H; m-O-CH_3), 3.60 (s, 6H; p-O-CH_3), 2.12 (s, 6H; CH_3).

HR ESI-MS: $[M+H]^+$ calculated for $C_{24}H_{30}N_6O_6S_2Ni$: 619.0949, observed: 619.0950.

*2,3-di(phenylthiosemicarbazone)butane nickel (II) (*NiTSC-ph)

From 2,3-di(phenylthiosemicarbazone) butane (0.130 mmol, 50 mg) in 3 ml methanol and $Ni(CH_3COO)_2(H_2O)_4$ (0.156 mmol, 39 mg) in solution in 2 ml methanol. Alumina column with dichloromethane/cyclohexane 6:4. A dark brown solid (39 mg, 68 %) was obtained.

^{1}H NMR (300 MHz, DMSO-*d6*, TMS): δ = 10.00 (s, 2H; NH), 7.60 (d, J= 7.65 Hz, 4H; o-CH), 7.29 (t, J= 7.99 Hz, 4H; m-CH), 7.00 (t, J= 7.35 Hz, 2H; p-CH), 2.08 (s, 6H; CH_3).

HR ESI-MS: $[M+H]^+$ calculated for $C_{18}H_{18}N_6S_2Ni$: 439.0315, observed: 440.0388.

Crystals suitable for X-ray diffraction analysis were obtained from slow evaporation of the following solutions: a THF solution for the NiTSC-(o)-OCH_3 and NiTSC-ph, a DMF/EtOH solution for the NiTSC-(m)-OCH_3 and a THF/Cyclohexane solution for the NiTSC-(m,p)-$2OCH_3$, NiTSC-(o,p)-$2OCH_3$ and NiTSC-(m,m,p)-$3OCH_3$. Details of data collection and structure refinement parameters are listed in Tables 7-12.

Table 7. *Crystallographic data, details of data collection and structure refinement parameters for NiTSC-(o)-OCH_3.*

Identification code	niooch3thf
Empirical formula	$C_{80}H_{88}N_{24}Ni_4O_8S_8$
Formula weight	2005.06
Temperature/K	295
Crystal system	monoclinic
Space group	$P2_1$
a/Å	14.4569(9)
b/Å	14.7236(5)
c/ Å	23.5508(8)
α/°	90
β/°	905.414(4)
γ/°	90
Volume/ Å^3	4990(4)
Z	2
ρ_{calc} g/cm^3	1.334
μ/mm^{-1}	0.971
Crystal size/mm^3	0.26 x 0.08 x 0.03
Radiation	Mo Kα (λ= 0.71073)
2Θ range for data collection/°	4.214 to 58.72
Index ranges	-10 ≤ h ≤ 18, -19 ≤ k ≤ 19, -32 ≤ l ≤ 32
Reflections collected	50299
Independent reflections	22899 [R_{int}= 0.0500, R_{sigma}= 0.0837]
Data/restraints/parameters	22899/37/1118
Goodness-of-fit on F^2	0.964
Final R indexes [I≥2σ (I)]	R_1 = 0.0567, wR_2= 0.1061
Final R indexes [all data]	R_1 = 0.1186, wR_2= 0.1308
Largest diff. peak/hole / e Å^{-3}	0.44/-0.28

Table 8. *Crystallographic data, details of data collection and structure refinement parameters for NiTSC-(m)-OCH_3.*

Identification code	Nimoch3
Empirical formula	$C_{23}H_{29}N_7NiO_3S_2$
Formula weight	574.36
Temperature/K	295
Crystal system	monoclinic
Space group	$P2_1/n$
a/Å	9.4084(2)
b/Å	8.1911(2)
c/ Å	33.8729(7)
α/°	90
β/°	90.333(2)
γ/°	90
Volume/ Å^3	2610.38(10)
Z	4
ρ_{calc} g/cm^3	1.461
μ/mm^{-1}	2.898
Crystal size/mm^3	0.28 x 0.14 x 0.03
Radiation	Cu Kα (λ= 1.54184)
2Θ range for data collection/°	9.742 to 140.912
Index ranges	$-11 \le h \le 8$, $-9 \le k \le 9$, $-41 \le l \le 36$
Reflections collected	10788
Independent reflections	4855 [R_{int}= 0.647, R_{sigma}= 0.0389]
Data/restraints/parameters	4855/0/331
Goodness-of-fit on F^2	1.094
Final R indexes [I≥2σ (I)]	R_1 = 0.0572, wR_2= 0.1508
Final R indexes [all data]	R_1 = 0.0622, wR_2= 0.1535
Largest diff. peak/hole / e Å^{-3}	0.66/-0.35

Table 9. *Crystallographic data, details of data collection and structure refinement parameters for NiTSC-(m,p)-2OCH₃.*

Identification code	Nimp2och3
Empirical formula	$C_{22}H_{28}N_6NiO_5S_2$
Formula weight	579.33
Temperature/K	295
Crystal system	Triclinic
Space group	P-1
a/Å	7.3626(4)
b/Å	9.2464(7)
c/ Å	19.0277(13)
α/°	102.393(6)
β/°	90.090(5)
γ/°	97.539(6)
Volume/ Å³	1253.65(15)
Z	2
ρ_{calc} g/cm³	1.535
μ/mm^{-1}	3.072
Crystal size/mm³	0.16 x 0.03 x 0.02
Radiation	Cu Kα (λ= 1.54184)
2Θ range for data collection/°	4.758 to 144.722
Index ranges	-9 ≤ h ≤ 8, -11 ≤ k ≤ 11, -23 ≤ l ≤ 23
Reflections collected	7775
Independent reflections	7775 [R_{sigma}= 0.0616]
Data/restraints/parameters	7775/0/332
Goodness-of-fit on F^2	0.961
Final R indexes [I≥2σ (I)]	R_1 = 0.0613, wR_2= 0.1723
Final R indexes [all data]	R_1 = 0.0903, wR_2= 0.1849
Largest diff. peak/hole / e Å^{-3}	0.78/-0.68

Table 10. *Crystallographic data, details of data collection and structure refinement parameters for NiTSC-(o,p)-2OCH₃.*

Identification code	Niop2och3
Empirical formula	$C_{22}H_{26}N_6NiO_4S_2$
Formula weight	561.32
Temperature/K	295
Crystal system	triclinic
Space group	P-1
a/Å	7.4733(6)
b/Å	8.6415(4)
c/ Å	20.1328(19)
α/°	90.344(5)
β/°	91.846(7)
γ/°	106.979(5)
Volume/ Å³	1242.71(17)
Z	2
ρ_{calc} g/cm³	1.500
μ/mm^{-1}	3.050
Crystal size/mm³	0.2 x 0.05 x 0.02
Radiation	Cu Kα (λ= 1.54184)
2Θ range for data collection/°	4.392 to 140.724
Index ranges	-9 ≤ h ≤ 9, -10 ≤ k ≤ 10, -19 ≤ l ≤ 24
Reflections collected	6132
Independent reflections	6132 [R_{sigma}= 0.0364]
Data/restraints/parameters	6132/0/323
Goodness-of-fit on F^2	1.049
Final R indexes [I≥2σ (I)]	R_1 = 0.0537, wR_2= 0.1519
Final R indexes [all data]	R_1 = 0.0669, wR_2= 0.1576
Largest diff. peak/hole / e Å^{-3}	0.43/-0.60

Table 11. *Crystallographic data, details of data collection and structure refinement parameters for NiTSC-(m,m,p)-3OCH₃.*

Identification code	NimmpTHFCy
Empirical formula	$C_{24}H_{32}N_6NiO_7S_2$
Formula weight	639.38
Temperature/K	295
Crystal system	monoclinic
Space group	I2/a
a/Å	20.5967(2)
b/Å	8.19530(9)
c/ Å	34.8277(4)
α/°	90
β/°	105.5619(12)
γ/°	90
Volume/ Å³	5663.25(11)
Z	8
ρ_{calc} g/cm³	1.500
μ/mm^{-1}	2.832
Crystal size/mm³	0.28 x 0.02 x 0.02
Radiation	Cu Kα (λ= 1.54184)
2Θ range for data collection/°	5.268 to 147.77
Index ranges	-25 ≤ h ≤ 24, -10 ≤ k ≤ 10, -36 ≤ l ≤ 43
Reflections collected	21480
Independent reflections	5685 [R_{int}= 0.0422, R_{sigma}= 0.0616]
Data/restraints/parameters	5685/0/372
Goodness-of-fit on F^2	1.033
Final R indexes [I≥2σ (I)]	R_1 = 0.0416, wR_2= 0.1068
Final R indexes [all data]	R_1 = 0.0486, wR_2= 0.1148
Largest diff. peak/hole / e Å^{-3}	0.46/-0.38

Table 12. *Crystallographic data, details of data collection and structure refinement parameters for NiTSC-ph.*

Identification code	nitscph
Empirical formula	$C_{18}H_{18}N_6NiS_2$
Formula weight	441.21
Temperature/K	295
Crystal system	triclinic
Space group	P-1
a/Å	8.9912(2)
b/Å	9.3850(2)
c/ Å	11.6134(3)
α/°	74.972(2)
β/°	88.950(2)
γ/°	83.043(2)
Volume/ Å^3	939.40(4)
Z	2
ρ_{calc} g/cm^3	1.560
μ/mm^{-1}	1.271
Crystal size/mm^3	0.22 x 0.08 x 0.03
Radiation	Mo Kα (λ= 0.71073)
2Θ range for data collection/°	6.498 to 57.922
Index ranges	-12 ≤ h ≤ 11, -12 ≤ k ≤ 12, -15 ≤ l ≤ 15
Reflections collected	37738
Independent reflections	4560 [R_{int}= 0.0288, R_{sigma}= 0.0180]
Data/restraints/parameters	4560/0/246
Goodness-of-fit on F^2	1.111
Final R indexes [I≥2σ (I)]	R_1 = 0.0311, wR_2= 0.0752
Final R indexes [all data]	R_1 = 0.0399, wR_2= 0.0792
Largest diff. peak/hole / e Å^{-3}	0.31/-0.22

3.4.2 Electrochemistry

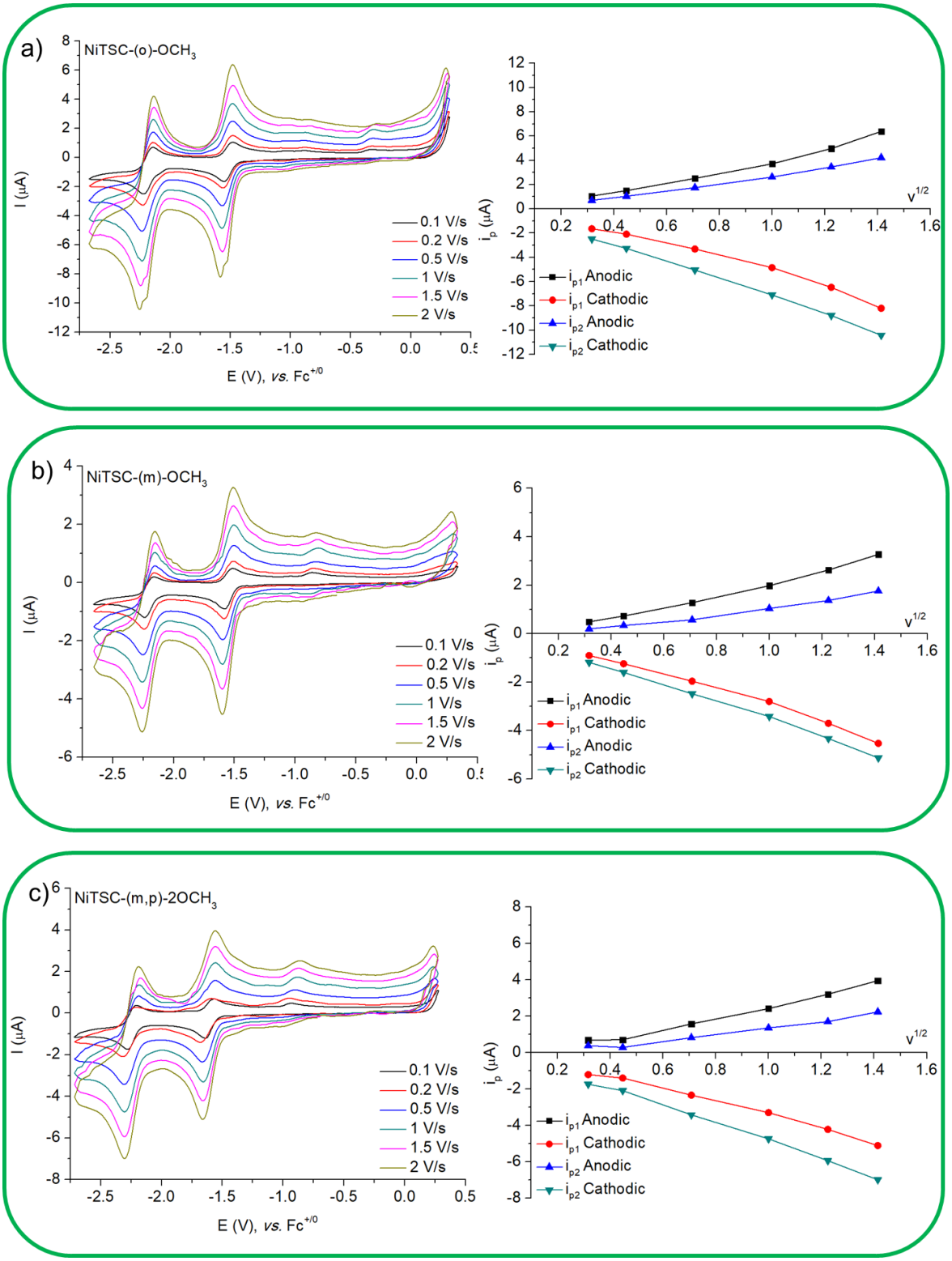

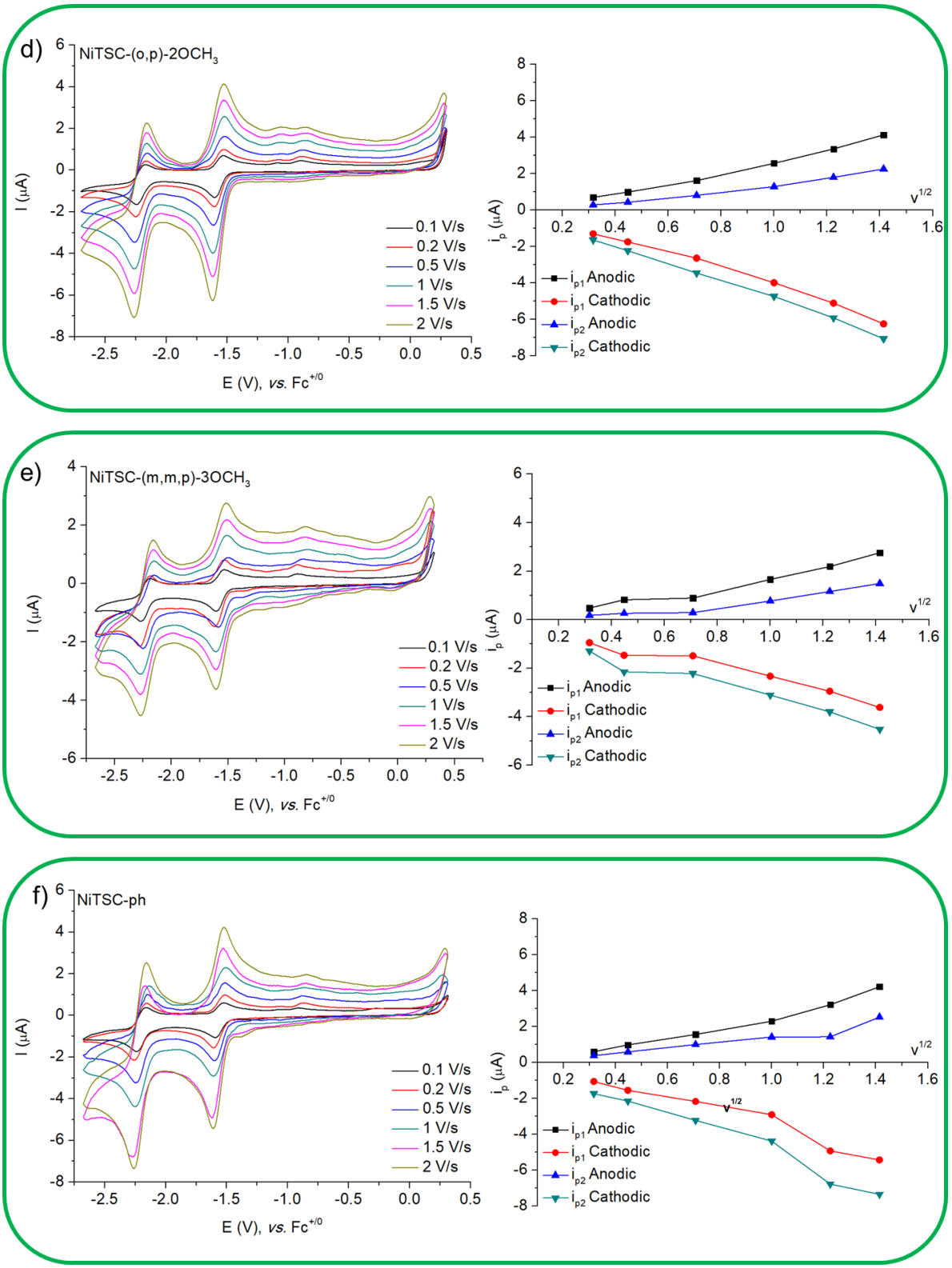

Figure 11. *Cyclic voltammograms of: a) NiTSC-(o)-OCH_3, b) NiTSC-(m)-OCH_3, c) NiTSC-(m,p)-$2OCH_3$, d) NiTSC-(o,p)-$2OCH_3$, a) NiTSC-(m,m,p)-$3OCH_3$ and a) NiTSC-ph at a stationary glassy carbon electrode at different scan rates (v) in DMF with 0.1 M NBu_4PF_6 as supporting electrolyte (left) and linear plots of ip vs. $v^{1/2}$ for anodic and cathodic waves of both processes (right).*

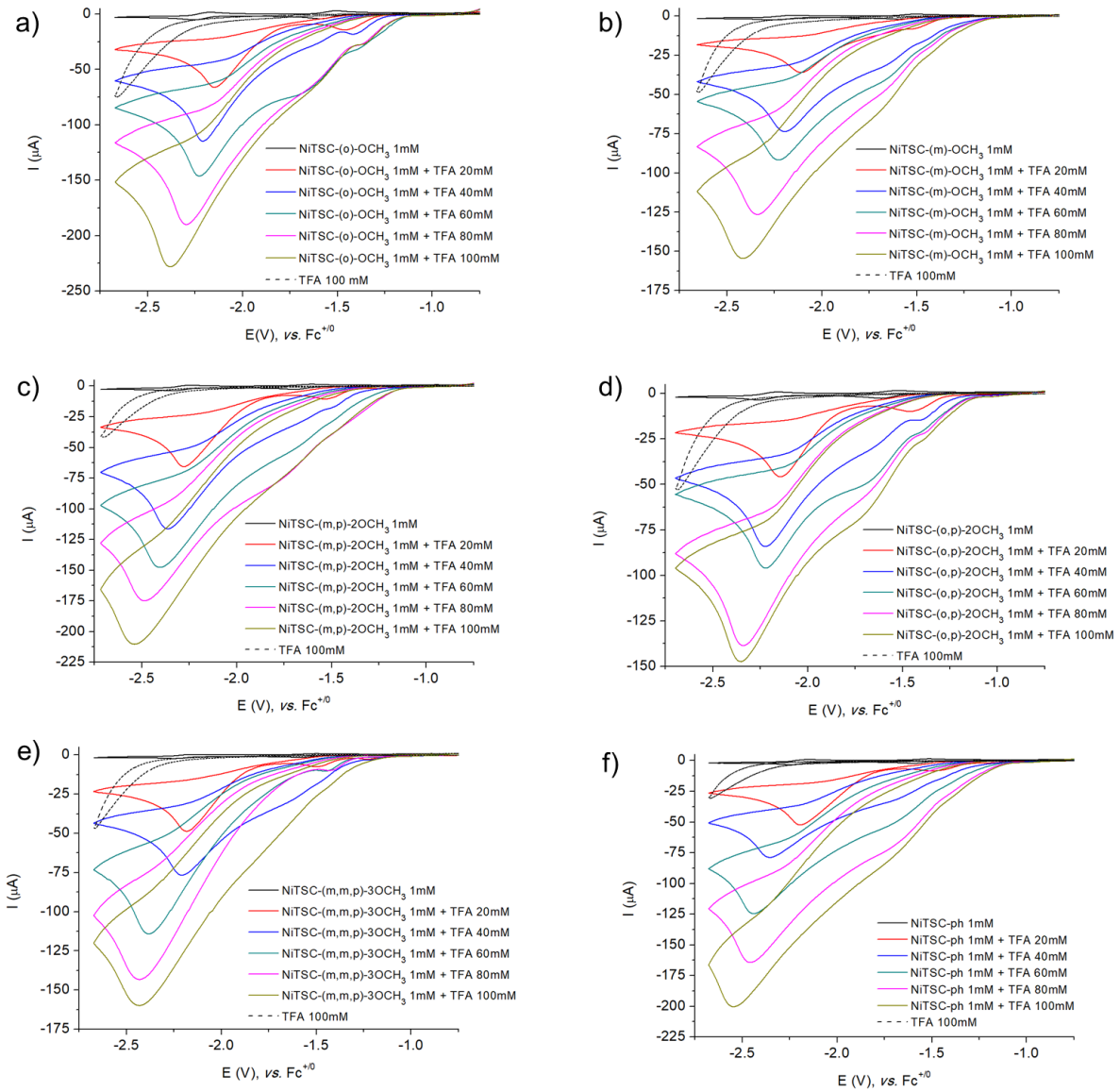

Figure 12. *Successive cyclic voltammograms recorded at a glassy carbon as working electrode of a DMF solution (0.1 M NBu_4PF_6) with 1 mM of: a) NiTSC-(o)-OCH_3 b) NiTSC-(m)-OCH_3 c) NiTSC-(m,p)-$2OCH_3$ d) NiTSC-(o,p)-$2OCH_3$ e) NiTSC-(m,m,p)-$3OCH_3$ f) NiTSC-ph in the presence of increasing amounts of TFA. Scan rate: 500 mV/s.*

3.4.3 Overpotential and TOF calculations

The calculated overpotential and TOF values for all the complexes were obtained following the same protocols that were presented in the previous chapters (see experimental section of Chapter 2 for the detailed analysis and formulas used).

References

1. Lucarini, F. *et al.* Rationalizing Photo-Triggered Hydrogen Evolution Using Polypyridine Cobalt Complexes: Substituent Effects on Hexadentate Chelating Ligands. *ChemSusChem* **14**, 1874–1885 (2021).
2. Straistari, T. *et al.* A Thiosemicarbazone-Nickel(II) Complex as Efficient Electrocatalyst for Hydrogen Evolution. *ChemCatChem* **9**, 2262–2268 (2017).
3. Papadakis, M. *et al.* Ligand-based electronic effects on the electrocatalytic hydrogen production by thiosemicarbazone nickel complexes. *Dalton Trans.* **49**, 5064–5073 (2020).
4. Fourmond, V., Jacques, P.-A., Fontecave, M. & Artero, V. H_2 Evolution and Molecular Electrocatalysts: Determination of Overpotentials and Effect of Homoconjugation. *Inorg. Chem.* **49**, 10338–10347 (2010).
5. Barrozo, A. & Orio, M. Unraveling the catalytic mechanisms of H_2 production with thiosemicarbazone nickel complexes. *RSC Adv.* **11**, 5232–5238 (2021).
6. Roy, S. *et al.* Molecular Cobalt Complexes with Pendant Amines for Selective Electrocatalytic Reduction of Carbon Dioxide to Formic Acid. *J. Am. Chem. Soc.* **139**, 3685–3696 (2017).
7. Queyriaux, N. *et al.* Electrocatalytic Hydrogen Evolution with a Cobalt Complex Bearing Pendant Proton Relays: Acid Strength and Applied Potential Govern Mechanism and Stability. *J. Am. Chem. Soc.* **142**, 274–282 (2020).
8. Razavet, M., Artero, V. & Fontecave, M. Proton Electroreduction Catalyzed by Cobaloximes: Functional Models for Hydrogenases.
9. Galan, B. R. *et al.* Electrocatalytic Oxidation of Formate by $[Ni(P^{R}_2N^{R'}_2)_2(CH_3CN)]^{2+}$ Complexes. *J. Am. Chem. Soc.* **133**, 12767–12779 (2011).
10. Wilson, A. D. *et al.* Hydrogen Oxidation and Production Using Nickel-Based Molecular Catalysts with Positioned Proton Relays. *J. Am. Chem. Soc.* **128**, 358–366 (2006).
11. Artero, V. & Saveant, J.-M. Toward the rational benchmarking of homogeneous H_2-evolving catalysts. *Energy Environ. Sci.* **7**, 3808–3814 (2014).
12. Bhugun, I., Lexa, D. & Savéant, J.-M. Homogeneous Catalysis of Electrochemical Hydrogen Evolution by Iron(0) Porphyrins. *J. Am. Chem. Soc.* **118**, 3982–3983 (1996).
13. Coutard, N., Kaeffer, N. & Artero, V. Molecular engineered nanomaterials for catalytic hydrogen evolution and oxidation. *Chem. Commun.* **52**, 13728–13748 (2016).

Chapter 4: Nuclearity influence on hydrogen evolution reaction with thiocarbohydrazone nickel complexes

4.1 Introduction

In this study, we designed and investigated the structure, properties and reactivity toward the electrocatalytic hydrogen evolution of a trinuclear nickel complex with a redox-active ligand. This complex is based on a non-innocent ligand, the thiocarbohydrazone (Figure 1). Our goal with this study was to probe the possibility to improve the catalytic performances for hydrogen production by increasing the number of active sites within the transition metal complex. To do so, the new catalyst, once obtained, was investigated by comparison with its mononuclear nickel counterpart, NiTSC-OCH_3.[1] As both complexes were derived from structurally similar ligands, their comparison can directly inform on the influence of having multiple metallic centers with respect to the key parameters for catalysis: the overpotential and the TOF. Our results pointed at an improved catalytic activity of the trinuclear complex showed but with the main drawback of an underwhelming stability and a larger overpotential requirement.

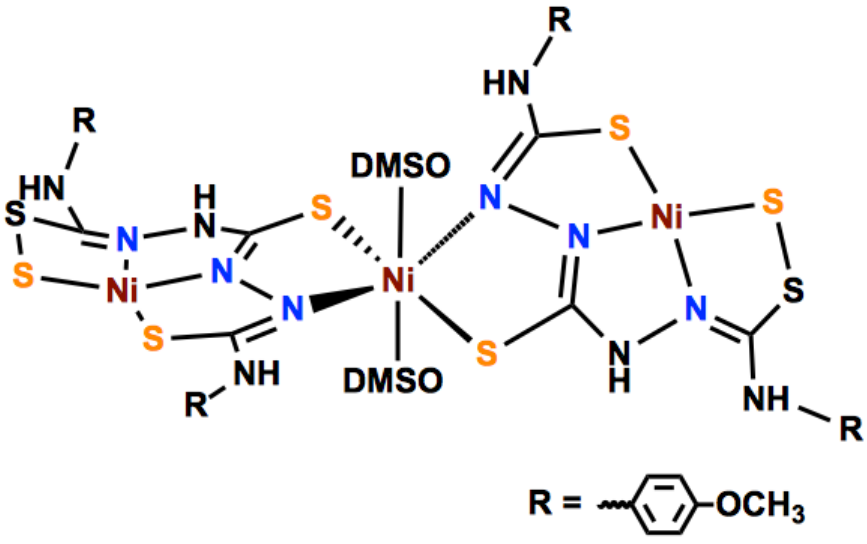

Figure 1. *Structure of the trinuclear nickel thiocarbohydrazone complex (Ni_3L_2).*

4.2 Results and Discussion

4.2.1 Synthesis and Characterization

The ligand (H_6L) was prepared by the condensation reaction of thiocarbohydrazide and the 1-isothiocyanato-4-methoxy-benzene. The reaction was performed in ethanol at reflux for 2 hours. After it was purified by recrystallization, the ligand was mixed with nickel nitrate and sodium hydrosulfide to yield the targeted trinuclear nickel complex, Ni_3L_2 (Figure 2).

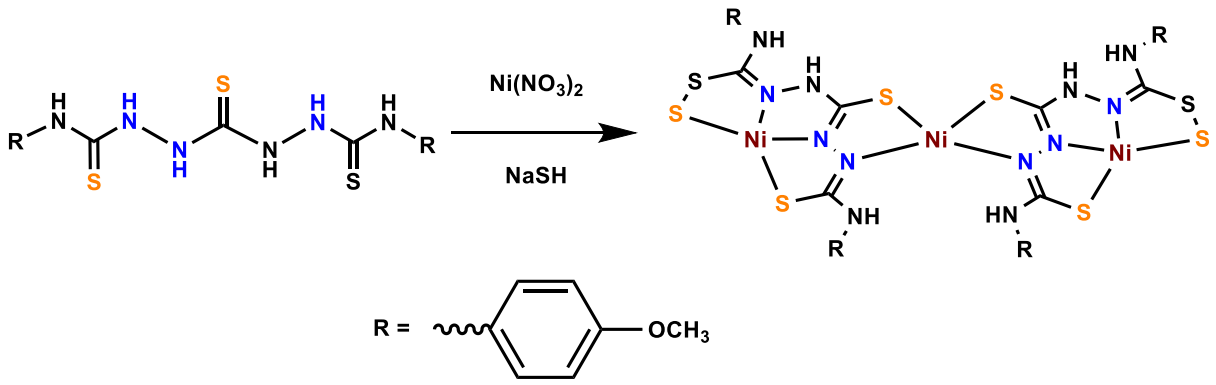

Figure 2. *Schematic representation of the synthetic protocol yielding Ni_3L_2.*

The complex was recrystallized and washed with methanol. No further purification was required and the resulting product precipitated as a brown powder. Both ligand and complex were characterized by NMR spectroscopy and ESI mass spectrometry. These data support the existence of a diamagnetic trinuclear structure. 2D-NMR experiments based on the DOSY sequence provide a unique diffusion coefficient of $1.10*10^{-10}$ m^2/s, which supports the existence of a single species in solution, ruling out possible decomposition of the trinuclear complex into lower nuclearity compounds (Figure 3).

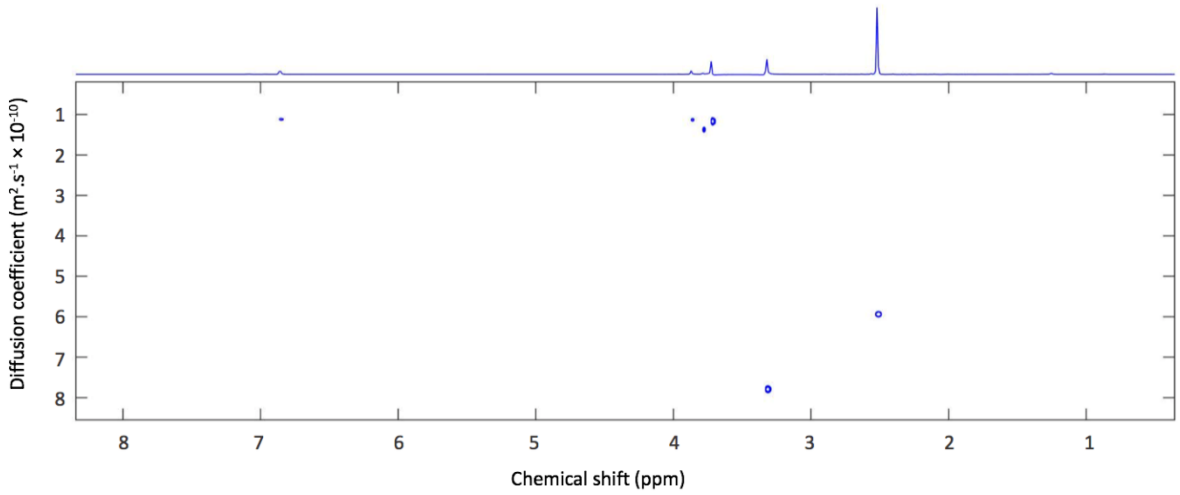

Figure 3. *2D DOSY Spectrum for Ni_3L_2 in DMF at 298 K processed using DOSY Toolbox.*

Suitable crystals were obtained by slow evaporation of a DMSO and ethanol solution and allowed to solve the solid-state structure of the complex by X-ray crystallography analysis (Figure 4). The crystal of the complex shows two DMSO molecules coordinating to the central nickel. Although the NMR data showed a diamagnetic compound in solution, with all three nickels likely having a square planar or distorted square planar geometry, the crystal structure raised some questions about the local geometry of the central nickel which was found to be octahedral in the solid state.

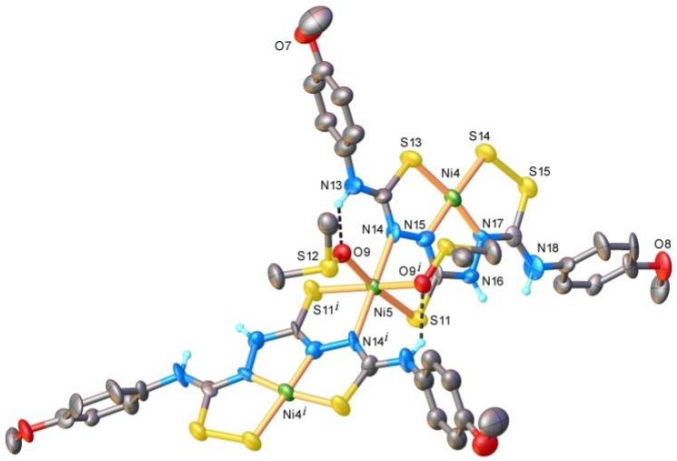

Figure 4. *X-ray molecular structure of **Ni_3L_2** with selected atom labelling and thermal ellipsoids at 40% level. Non-relevant H-atoms are omitted for clarity. Symmetry code: [i] [1]2 − x, y, 1.5 − z. Selected bonds (Å) and angles (°): Ni4-S13 2.133(3), Ni4-S14 2.145(3), Ni4-N15 1.843(8), Ni4-N17 1.786(9), Ni5-S11 2.392(3), Ni5-O9 2.131(6), Ni5-N14 2.137(9); N15-Ni4-S13 85.7(3), N17-Ni4-S14 92.8(3), N15-Ni4-S14 176.5(4), N17-Ni4-S13 1···69.7(3), N14-Ni5-S11 85.2(3), N14-Ni5-O9 90.4(3), $O9^1$-Ni5-O9 85.0(4), O9-Ni5-S11 172.1(2). H bond parameters: N13-H···O9 [N13-H 0.86 Å, H···O9 2.02 Å, N13···O9 2.73(1) Å, ∠N13HO9 138.7°.*

To address this question, the magnetic properties of the compound in solid state were investigated using Superconducting Quantum Interference Device (SQUID) measurements. Figure 5 shows the temperature dependence of the product between the susceptibility with the temperature, χT, at different fields of 0.1, 1 and 4 Tesla. At room temperature, χT is 1.254 emu.K.mol^{-1} and does not show any significant temperature dependence when cooling down to about 10 K. Then, it decreases at higher fields due to the thermal saturation of the ground state. The dashed line represents the best fit for a paramagnetic center of spin S= 1 and g_{iso}= 2, in agreement with having only one high-spin Ni^{II} ion (S= 1) present in the complex. This is expected, as the latter displays an octahedral coordination sphere in the solid-state structure while the two-other external Ni^{II} ions are square planar and compatible with a low-spin configuration (S= 0). Therefore, the magnetic behavior of Ni_3L_2 is ascribed to the central high-spin Ni^{II} ion in an octahedral environment. The possible inter-trimer interactions are found to be weak and mostly hidden by the static field effect.

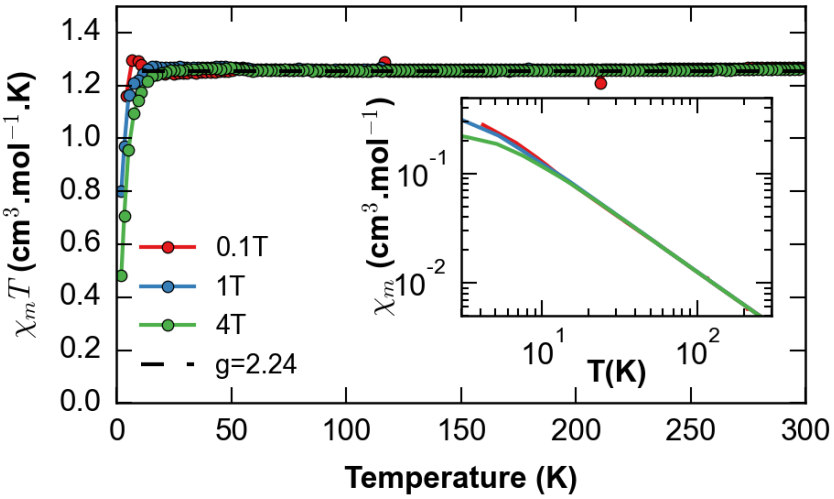

Figure 5. *Temperature dependence of the magnetic susceptibility for Ni_3L_2. The inset is the temperature dependence of the susceptibility in log scale showing the expected Curie behavior for any field at T>10K.*

The electronic properties of both the ligand and the complex were investigated by UV-vis spectroscopy and the spectra recorded in DMF are presented in Figure 6. The evolution of the spectra upon ligand metalation allowed us to confirm the nickel binding to the ligand. The ligand displays two main absorption bands centered at 270 and 325 nm while the nickel complex displays two main electronic transitions found at 268 and 363 nm and two weaker broad bands around 518 and 895 nm (Table 1).

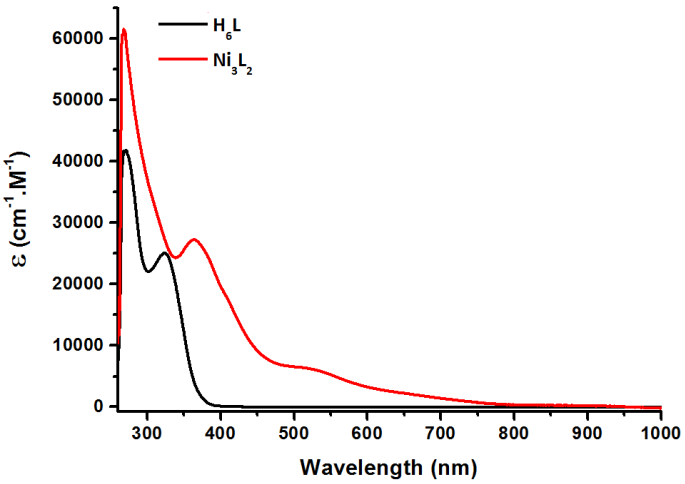

Figure 6. *Electronic absorption spectra for the H_6L ligand and the Ni_3L_2 complex, concentration of 0.05 mM in DMF.*

For the nickel complex, the absorption bands present at high energy (268 and 363 nm) have been previously attributed to (metal-ligand) to (metal-ligand) transitions[1,2] while the low-energy features are compatible with d-d transitions. These results were also supported by computations performed on Ni_3L_2 in the singlet state (S= 0) considering no bound DMSO molecules. The predicted spectroscopic data provided a calculated spectrum that compares reasonably well with the experimental observations (Figure 7). The computed UV-vis spectrum thus supports the dissociation of the solvent molecules from the complex once solubilized, with preference for a singlet state in solution.

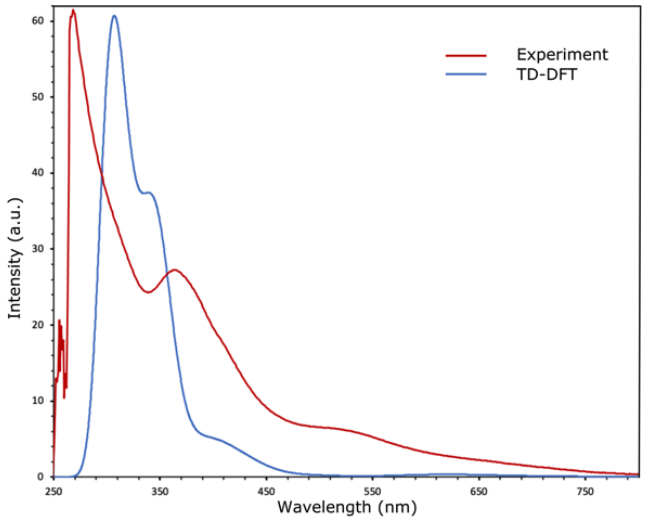

Figure 7. *Comparison between experimental and calculated UV-Vis spectra for Ni_3L_2 in DMF. Calculations performed on the neutral complex in a closed-shell singlet state (B3LYP/def2-TZVP).*

Table 1. *Main features of the electronic transitions from the UV-vis spectra of H_6L and Ni_3L_2 in DMF.*

Compound	λ (nm)	ε ($M^{-1}cm^{-1}$)
H_6L	270	22829.63
	325	13616.20
Ni_3L_2	268	55638.60
	363	19165.52
	518	4203.65
	895	1391.34

4.2.2 Electrochemical Investigation

The redox behavior of both the ligand and the complex was investigated by cyclic voltammetry at room temperature. A solution containing 0.1 M of NBu_4PF_6 as a supporting electrolyte, DMF as the solvent and 1 mM of either the complex or the ligand in an inert atmosphere was prepared. The electrochemical response was recorded in the potential range between 0 and -2.5 V vs. $Fc^{+/0}$ using a glassy carbon working electrode (Figure 8).

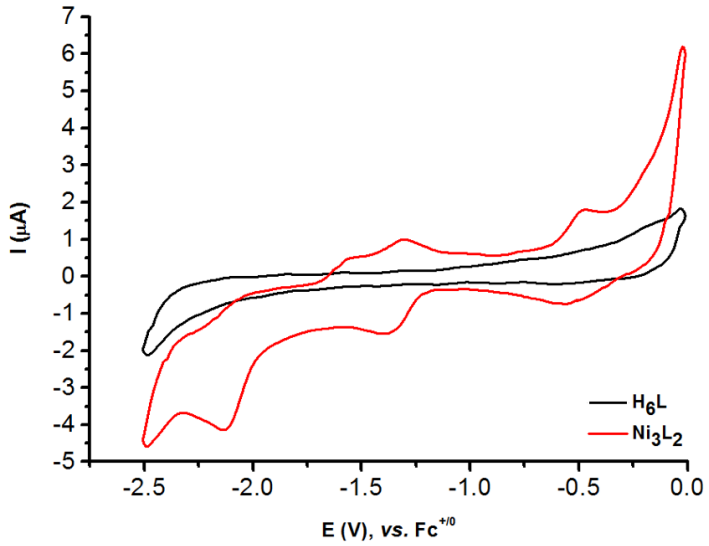

Figure 8. *Cyclic voltammograms of 1 mM solutions of H_6L and Ni_3L_2 in DMF solvent recorded at stationary glassy carbon electrode in DMF at 500 mV/s. Potentials referenced to the $Fc^{+/0}$.*

The cyclic voltammogram of H_6L is featureless over the scanned potential range whereas the complex shows two distinct reduction peaks in the cathodic region. A quasi-reversible wave is observed at -1.35 V $\left(0.5\left(E_{pc}^{*}+E_{pa}^{*}\right),\ \Delta E_p = 45\ \mathrm{mV}\right)$ and another irreversible at -2.1 V vs. $Fc^{+/0}$. The plot of the peak current versus the square root of the scan rate for the quasi-reversible cathodic wave was found to be linear, indicating that it is a diffusion-controlled process (Figure 9). In the anodic direction, the CV revealed a process with a quasi-reversible wave observed at -0.46 V vs. $Fc^{+/0}$. The redox behavior of Ni_3L_2 in the cathodic region is reminiscent of another trinuclear nickel complex previously reported in the laboratory[3] (for which the reduction events were ascribed as successive metal-based processes). These assignments will be further validated using complementary techniques that will be presented in the next sections of the chapter.

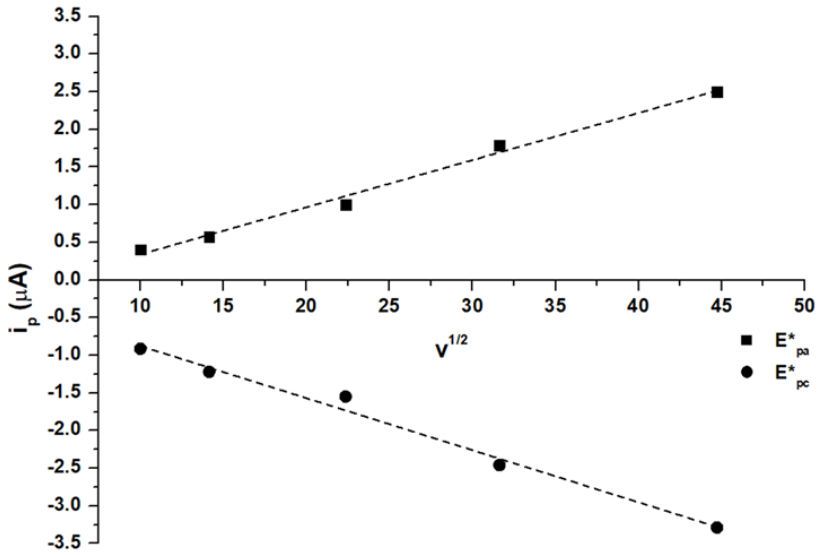

Figure 9. *Linear plot of the peak current i_p vs. the square root of the scan rate $v^{1/2}$ for anodic and cathodic waves of the first redox process of Ni_3L_2 ($0.5\left(E_{pc}^{*}+E_{pa}^{*}\right)$ = -1.35 V vs. $Fc^{+/0}$).*

To determine how many electrons are involved in each redox process, we performed chronoamperometry measurements. Using a glassy carbon working electrode we applied a standard potential over an extended period of time and through the current response, we measured the amounts of electrons absorbed in every process by our complex. For the first process, a potential of -1.5 V vs. $Fc^{+/0}$ was applied and the collected data indicated that the first process corresponds to a one-electron reduction. For the second reduction peak, a potential of -2.25 V vs. $Fc^{+/0}$ was applied and the results of this experiment showed that the second reduction is compatible with a two-electron process (Figure 10).

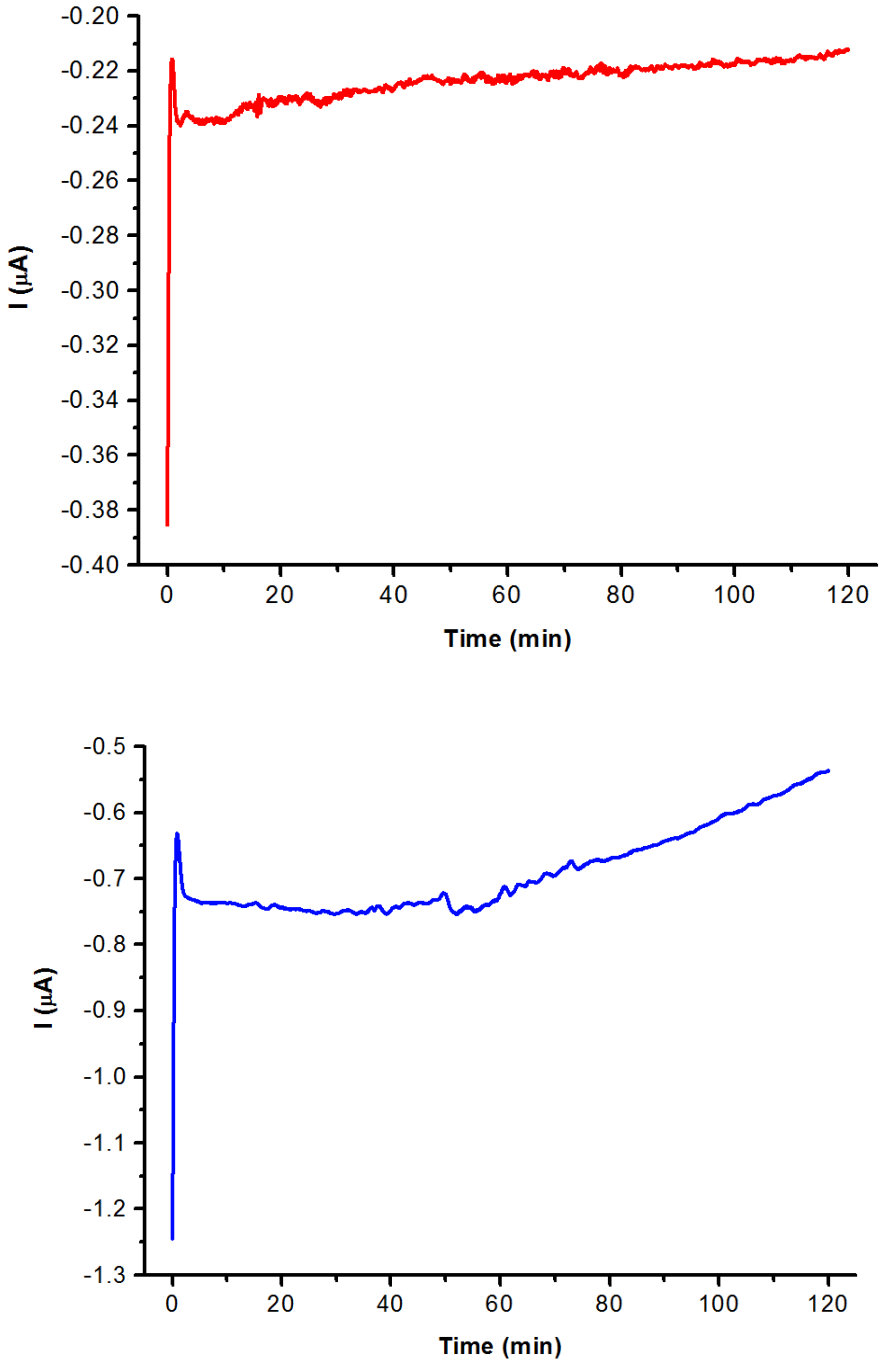

Figure 10. *Chronoamperogram of a 1 mM solution of Ni_3L_2 in DMF recorded at -1.5 V (top) and -2.25 V vs. $Fc^{+/0}$ (bottom) using a 1 mm glassy carbon electrode.*

After performing the first electrolysis at -1.5 V, a sample of the reduced complex was collected and frozen in liquid nitrogen for analysis by Electron Paramagnetic Resonance (EPR) spectroscopy. The EPR spectrum was recorded on a continuous wave spectrometer and resulted in an axial signal (Figure 11). A set of g-values of 2.012, 2.010 and 2.114 was obtained

from simulation with the Easyspin program package and was found to be compatible with the presence of a single paramagnetic center that was tentatively ascribed to a Ni^{I} center.

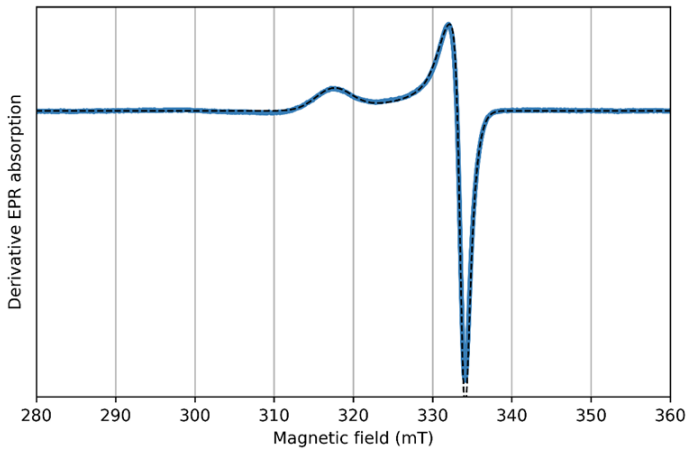

Figure 11. *Simulated and experimental cw X-band EPR spectra of a 1mM solution of Ni_3L_2 in DMF at T=50K recorded upon chronoamperometry at -1.5 V vs. $Fc^{+/0}$ at glassy carbon working electrode.*

These data were further confronted with computations performed on the one-electron reduced form of Ni_3L_2 considering a doublet state (S= 1/2) and no bound DMSO molecules. The predicted spectroscopic data provided a set of g-values of 2.052, 2.055 and 2.113 that are in fair agreement with the experimental ones. The electronic structure of the computed structure shows that the orbital occupied by the unpaired electron is centered on the central nickel and the spin density is distributed on the same site (Figure 12). We can thus conclude that the first reduction of the complex is a metal-based process and is attributed to a reduction of the central nickel center going from Ni^{II} to Ni^{I}, possibly due to stereochemical reasons.

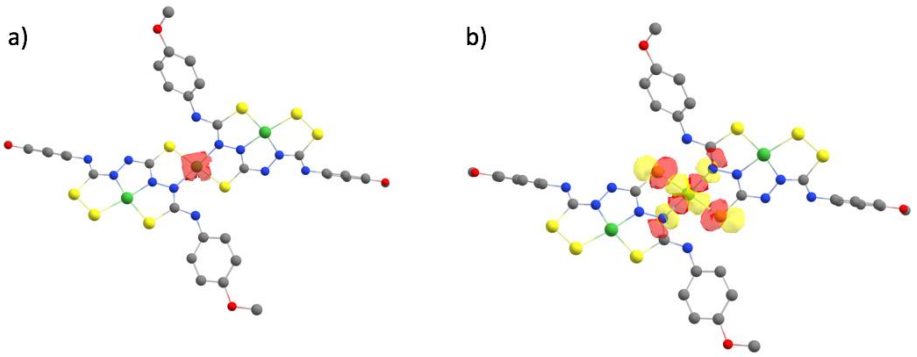

Figure 12. *a) Spin density distribution and b) Localized Singly Occupied Molecular Orbital (SOMO) for Ni_3L_2 after the first one-electron reduction.*

4.2.3 Electrocatalytic proton reduction

To explore the electrocatalytic capabilities of Ni_3L_2 for proton conversion into hydrogen, we recorded its electrochemical response with a glassy carbon electrode in DMF under argon in the presence of a proton source using the trifluoro acetic acid (TFA, pKa = 6.00 ± 0.3 in DMF).[4] The addition of increasing amounts of acid triggers the appearance of two peak-shaped waves with potentials starting at about -1.1 V vs. $Fc^{+/0}$, suggesting potential-dependent mechanisms (Figure 13). The current response of the two waves is proportional to the concentration of protons in the electrolyte solution. While the peak potential of the more negative process is shifting to slightly more negative potential values, the first process potential remains unaffected.

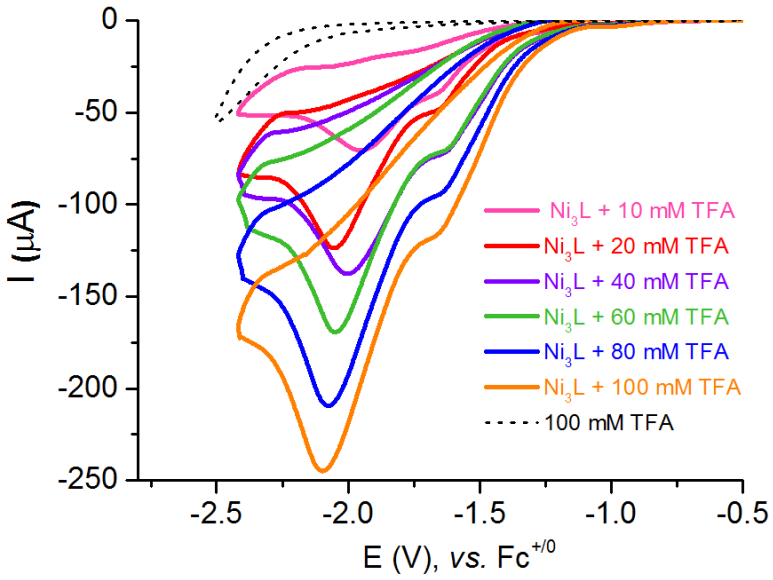

Figure 13. *Successive cyclic voltammograms of a 1 mM solution of Ni_3L_2 in DMF (0.1 M NBu_4PF_6) recorded at a glassy carbon electrode with increasing amounts of TFA at 500 mV/s. Potential referenced to the $Fc^{+/0}$.*

We only investigated the process occurring at the more positive potential with a mid-wave potential of -1.55 V vs. $Fc^{+/0}$. The peak current increases with the acid concentration until a plateau being is reached for a concentration of 60 mM of TFA and for a scan rate of 2 V/s (Figure 14).

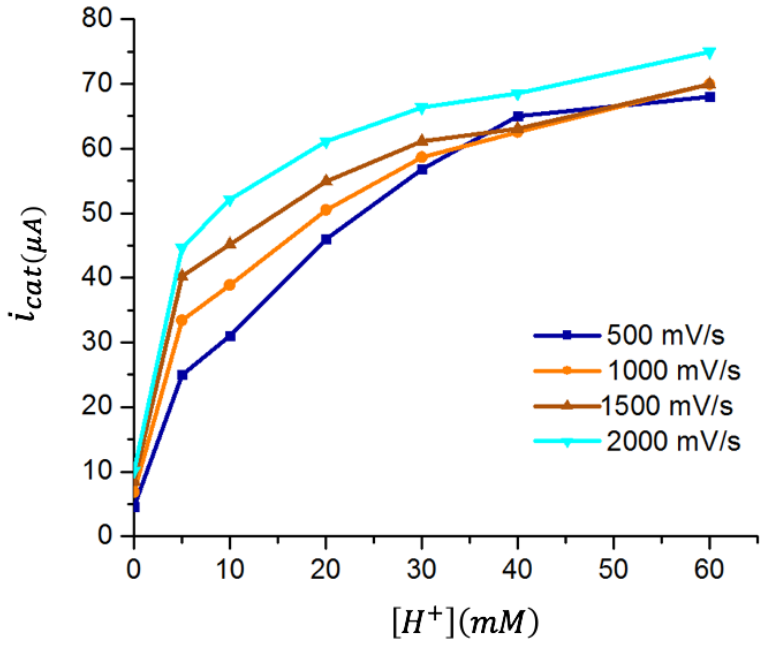

Figure 14. *Plot of i_{cat} of Ni_3L_2 for increasing concentrations of TFA at different scan rates.*

Control experiments were performed in the absence of the complex and the resulting CV clearly indicates the role played by Ni_3L_2 in the observed current enhancement (Figure 13, black dotted line). To verify that the observed catalytic signal does not correspond to species being absorbed onto the surface of the working electrode, we performed a series of dip and rinse tests. After each measurement, the working electrode was removed from the solution and dipped into a fresh solution of DMF, containing electrolyte. Only the residual background signal was recorded. Upon the addition of 100 mM TFA, sweeping the potential again in the cathodic region provided only the response of the acid blank (Figure 15, blue line). These control experiments proved that no absorbed species are formed onto the glassy carbon electrode during electrocatalytic measurements. This indicates that the signal is due to the dissolved trinuclear complex and therefore, we are investigating a homogenous catalytic system.

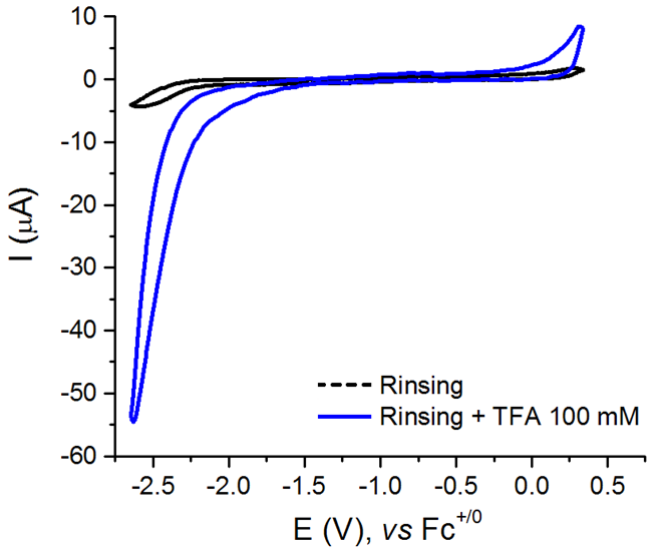

Figure 15. *Cyclic voltammograms recorded after electrocatalysis of Ni_3L_2 upon washing the working electrode and immersion into a fresh solution of dry DMF (0.1 M NBu_4PF_6, black dashed line) and in the presence of 100 mM of TFA (blue line). Scan rate 500 mV/s. Potential referenced to the $Fc^{+/0}$.*

To verify that the ligand in its free base form is also not responsible for the catalytic signal obtained in the presence of a proton source, the cyclic voltammogram of H_6L was recorded in the absence and the presence of 100 mM of TFA (Figure 16). Sweeping the potential in the cathodic region in these conditions did not reveal any catalytic activity. These data confirm that the ligand itself cannot mediate catalytic proton reduction.

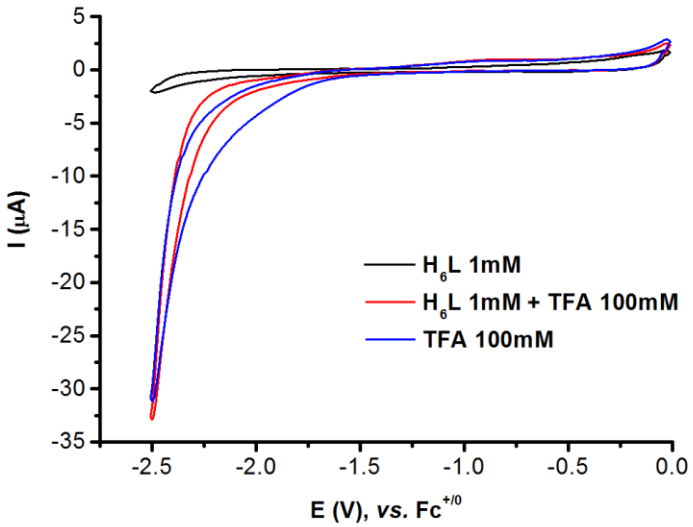

Figure 16. *Cyclic voltammogram of a 1 mM solution of H_6L (black line) in DMF recorded at a stationary glassy carbon with 0.1 M NBu_4PF_6 as supporting electrolyte. The cyclic voltammogram of a 100 mM of TFA solution in the absence (blue line) and in the presence (red line) of 1mM H_6L are also shown. Scan rate: 500 mV/s. Potential referenced to the $Fc^{+/0}$.*

To confirm that the recorded current response upon the addition of the acid corresponds to hydrogen production, bulk electrolysis experiments were performed and gas products were monitored by continuous in-line GC analysis. A solution of 8 ml DMF (0.1 M NBu_4PF_6) containing 1 mM of Ni_3L_2 and 100 mM of TFA was prepared. We applied a constant potential of -1.7 V vs. $Fc^{+/0}$ to the working electrode for 4 hours. We used a mercury pool-working electrode to make certain that any nickel nanoparticles produced will be absorbed into mercury keeping the homogeneous nature of our catalytic system.

During the 4 hour-period, Ni_3L_2 mediated hydrogen evolution with an 82% faradaic efficiency and a turnover number (TON) of 31 (Figure 17). In similar conditions, our reference catalyst NiTSC-OCH_3 produced hydrogen during 16 hours with 80% faradaic efficiency and a TON of 21.[1] These data first indicate that the trinuclear catalyst is probably less stable than the parent catalyst and likely point to degradation of the complex during catalysis. Nevertheless, the trinuclear complex is able to produce more hydrogen on a shorter timescale when compared to its mononuclear counterpart, which would support that nuclearity is playing a role in partially enhancing the catalytic activity of nickel thiosemicarbazone complexes.

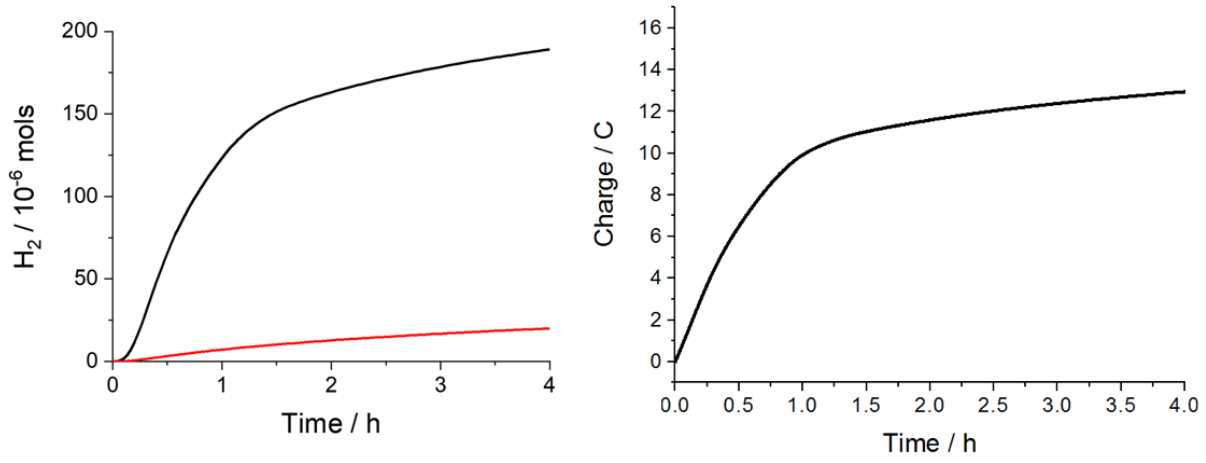

Figure 17. *Electrocatalytic data vs. time, by applying -1.7 V vs. $Fc^{+/0}$ to a pool mercury working electrode in 0.1 M NBu_4PF_6 solution of DMF. Left: Hydrogen production of the solutions containing 100 mM of TFA in the absence of catalyst (red line) and for a solution of 1 mM of Ni_3L_2 with 100 mM of TFA (black line). Right: Coulometry during bulk electrolysis of a solution containing 100 mM TFA and 1 mM of Ni_3L_2.*

As we can observe by looking at the data from Figure 17, the catalysis almost stops after 4 hours. To further investigate if this behavior can be attributed to the consumption of the proton source or the decomposition of the catalyst, we performed spectroelectrochemistry measurements. We monitored the UV-vis spectral evolution during catalysis and we observed

that upon two hours of reaction, the electronic absorption of the complex is reduced to almost half of its initial intensity, suggesting that the complex likely degrades in the course of catalysis (Figure 18).

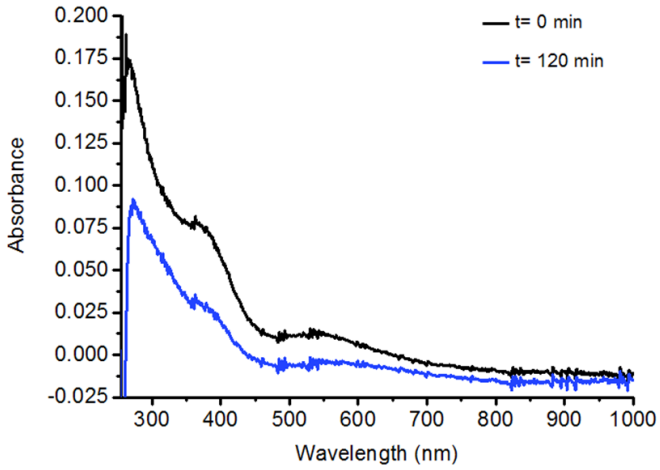

Figure 18. *Electronic absorption spectra for the Ni_3L_2 complex (black line), and upon chronoamperometry (-1.7 V vs. $Fc^{+/0}$ with 100 mM of TFA, blue line).*

4.2.4 Mechanistic investigations

To get insight into the sequence of electrochemical (reduction) and chemical (protonation) events leading to hydrogen evolution with our series of complexes, we perform complementary experiments. To start with, UV-vis spectra were recorded in the absence and presence of different concentrations of TFA (Figure 19). After successive additions of the proton source, the new spectra show almost identical features indicating that the structure of the complex is unaffected by the presence of protons. Since TFA is a strong acid, we can conclude that the complex is not getting protonated in the non-reduced state.

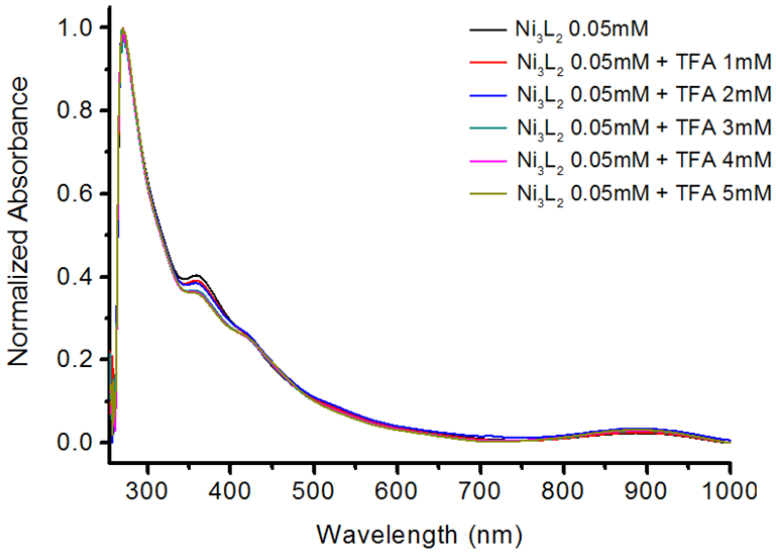

Figure 19. *Electronic absorption spectra of 0.05 mM Ni_3L_2 in DMF in the absence and the presence of different concentrations of TFA.*

These findings coupled with the information obtained from the EPR experiments give us some insight into the catalytic mechanism involving Ni_3L_2. Thus, we can propose that the mechanism is not initiated by a chemical event like a protonation but is likely triggered by an electrochemical one in the form of a reduction process likely occurring at the central nickel of the complex.

To further corroborate the above findings, DFT calculations were performed by our group and indicate that the first reduction occurs at the central nickel of the trinuclear complex with a computed redox potential of -1.06 V (Figure 12). The second reduction which was probed by electrolysis corresponds to a two-electron process, which is further supported by DFT calculations, showing that the two electrons are located on the side nickel centers (Figure 20) with a computed redox potential of -1.97 V. Comparison of the experimental values for the two reductions (-1.35 and -2.1 V vs. $Fc^{+/0}$) with the theoretical ones obtained from DFT calculations (-1.06 and -1.97 V vs. Fc+/0) shows that these two sets of values are in fair agreement and therefore, we can validate our previous assignments of the redox events. These results indicate that the ligand plays no part in the electrochemical behavior of the complex, as it facilitates no electron upon reduction, unlike its mononuclear counterpart.[1]

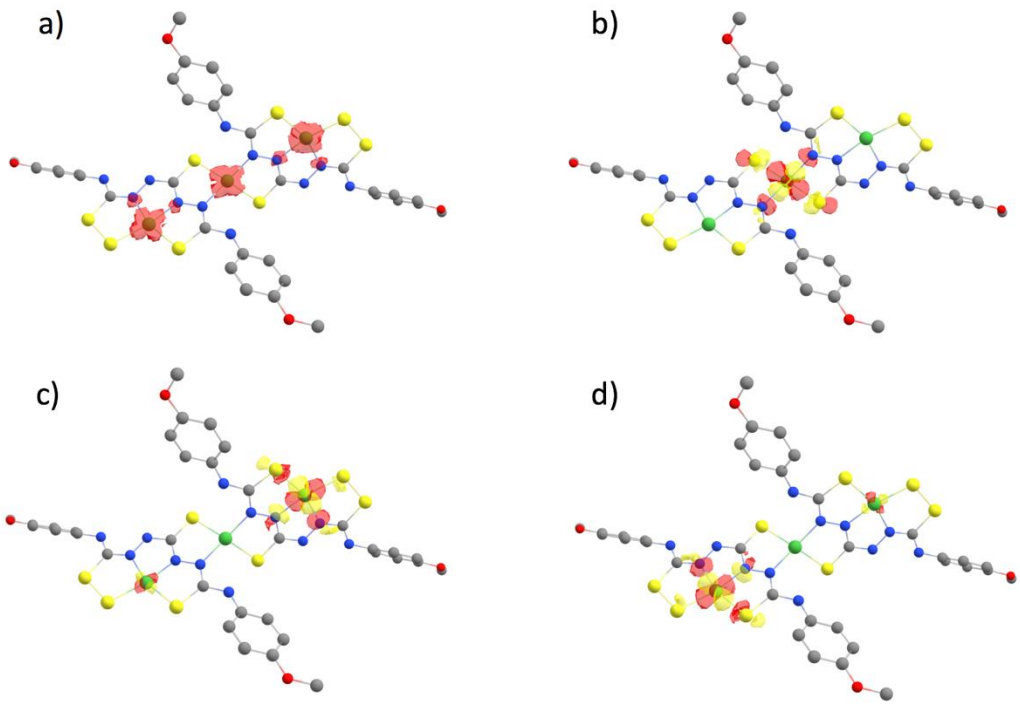

Figure 20. *a) Spin density distribution and b,c,d) Localized Singly Occupied Molecular Orbitals (SOMO) for Ni_3L_2 after the second two-electron reduction.*

From the computations of redox potentials and pK_a values DFT calculations identified two possible reaction mechanisms converting protons into hydrogen and probably occurring parallel to each other. In both cases, the reactivity is metal-centered and only involves the central nickel center, as opposed to the DFT findings about the mononuclear catalyst NiTSC-OCH_3 for which the reactivity was identified as ligand-assisted metal-centered. The first reaction pathway involves an EECC mechanism starting with two successive electron transfers (reductions) happening followed by two further chemical processes (protonations) of the trinuclear complex to release hydrogen and close the cycle (Figure 21).

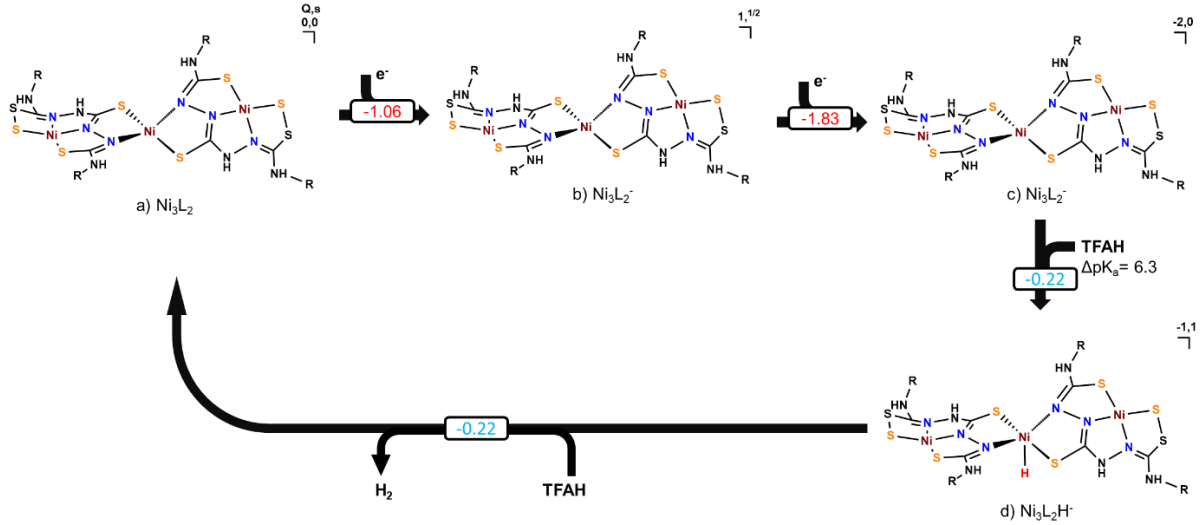

Figure 21. *Proposed EECC catalytic cycle performed by Ni_3L_2. Numbers in red correspond to redox potentials (in V vs $Fc^{+/0}$), whereas those in blue are free energy differences for proton transfer events, in eV. ΔpK_a displayed for the first proton transfer event corresponds to the difference in pK_as between Ni_3L_2H and TFAH.*

The second possible reaction pathway obtained from DFT calculations is an EECEC mechanism starting with the first three processes: two successive reduction steps and a first protonation event. Then the pathway deviates from the EECC one, with the complex facilitating a third electron transfer together with a second proton transfer. Upon the release of hydrogen, this mechanism cycles back to the one-electron reduced species (Figure 22) unlike the EECC reaction pathway.

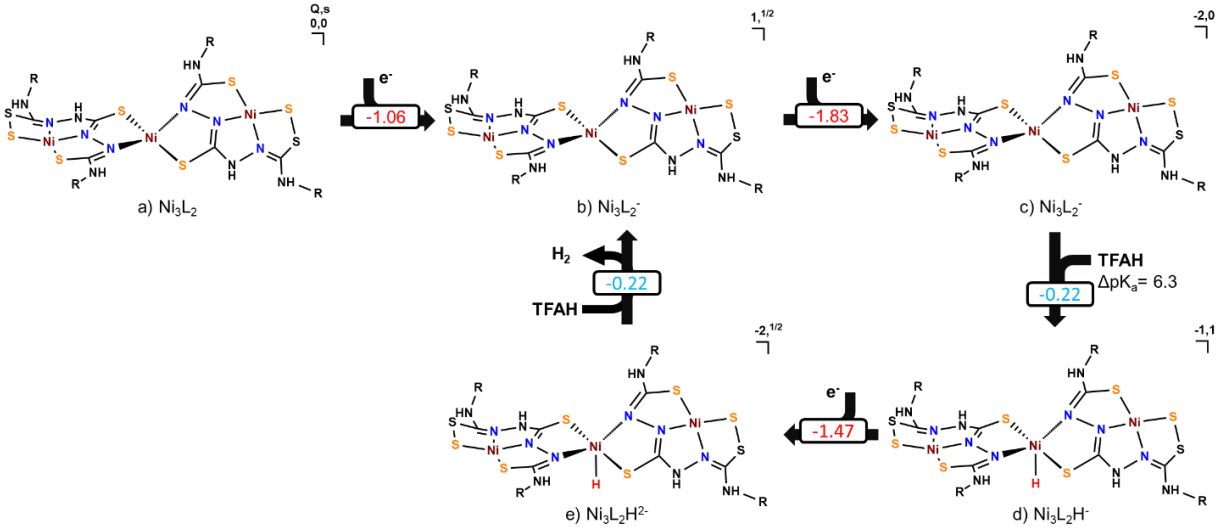

Figure 22. *Proposed EECEC catalytic cycle of Ni_3L_2. Numbers in red correspond to redox potentials (in V vs $Fc^{+/0}$), whereas those in blue are free energy differences for proton transfer events, in eV. ΔpK_a displayed for the first proton transfer event correspond to the difference in pK_as between Ni_3L_2H and TFAH. Note that the mechanism would cycle back to species b) once H_2 is formed, since two electrons and two protons would be gone, leaving one unpaired electron in the complex.*

4.2.5 Benchmarking of performances

A value of 0.564 V was calculated for the overpotential requirement, η, of Ni_3L_2 for proton reduction in the presence of TFA in DMF.[5] The rates and the performance of the catalyst during the hydrogen evolution reaction were quantified. The turnover frequency (TOF) value of Ni_3L_2 was evaluated using the catalytic cyclic voltammograms recorded in DMF at different scan rates (v = 0.5, 1, 1.5 and 2 V/s) for various amounts of TFA (5, 10, 20, 30,40 and 60 mM). The TOF value can be calculated from the ratio between the peak current of the catalyst in the absence (i_p) and presence of substrate (i_{cat}) as given by Equation 1:[6]

$$TOF_{max} = 1.938 \times \nu \times \left({i_{cat}}/{i_p}\right)^2$$

In the case of Ni_3L_2, the ratio $\left({i_{cat}}/{i_p}\right)$ varies linearly with the inverse of the square root of the scan rate ($v^{1/2}$) which confirms the validity of the above equation (Figure 23). Using this approach and considering a first order reaction in acid (Figure 24a) and in catalyst (Figure 24b), a maximum TOF value of 291 s^{-1} was obtained in the presence of 60 mM TFA.

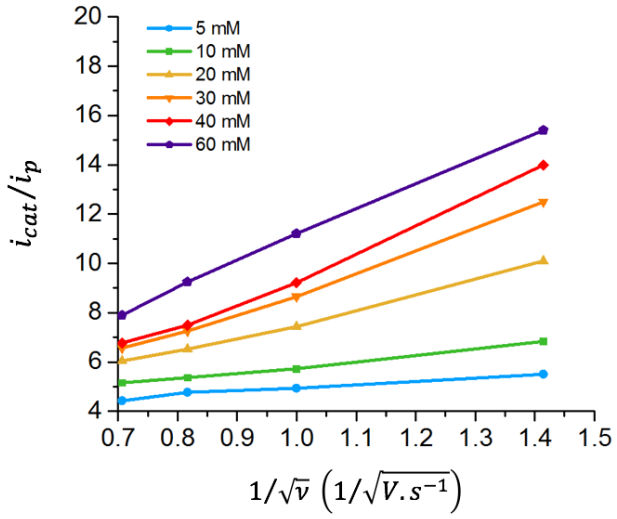

Figure 23. Plot of ${i_{cat}}/{i_p}$ versus inverse of the square root of the scan rate ($1/\sqrt{\nu}$) for Ni_3L_2 in DMF in the presence of different amounts of TFA. The plots were derived from the voltammograms recorded at different scan rates in the absence and presence of proton source.

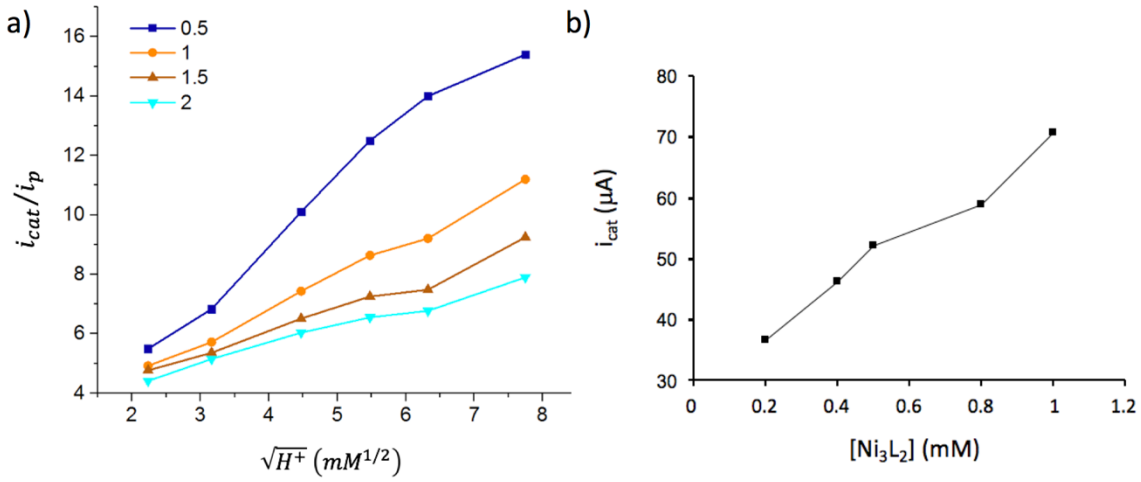

Figure 24. a*) Plot of* i_{cat}/i_p *versus the square root of the acid concentration (*$\sqrt{[H^+]}$ *) for Ni₃L₂ in DMF at different scan rates. The plots were derived from the voltammograms recorded at different scan rates in the absence and presence of proton source. b) Plot of* i_{cat} *versus the [Ni₃L₂] concentration in DMF in the presence of 60 mM TFA at 500 mV/s.*

Calculating a mid-wave potential $E_{1/2}^{cat}$ of -1.55 V vs. $Fc^{+/0}$ and an apparent equilibrium potential of the H^+/H_2 couple (-0.986 V vs $Fc^{+/0}$)[4] at 1M TFA concentration, we could derive catalytic Tafel plots correlating the turnover frequency (TOF) to the overpotential (η) related to H_2 evolution under the conditions used (Figure 25).[7] Comparing the Ni_3L_2 (purple trace) with other benchmarked catalysts from the literature, we observe that this complex displays a significant catalytic activity (log(TOF) > 2) for moderate overpotential values. While it does not surpass catalysts like cobaloximes (blue trace) or nickel bisdiphosphine catalysts (orange trace), it performs better than the parent thiosemicarbazone complex NiTSC-OCH_3 (green trace) as far as the turnover frequency is concerned.

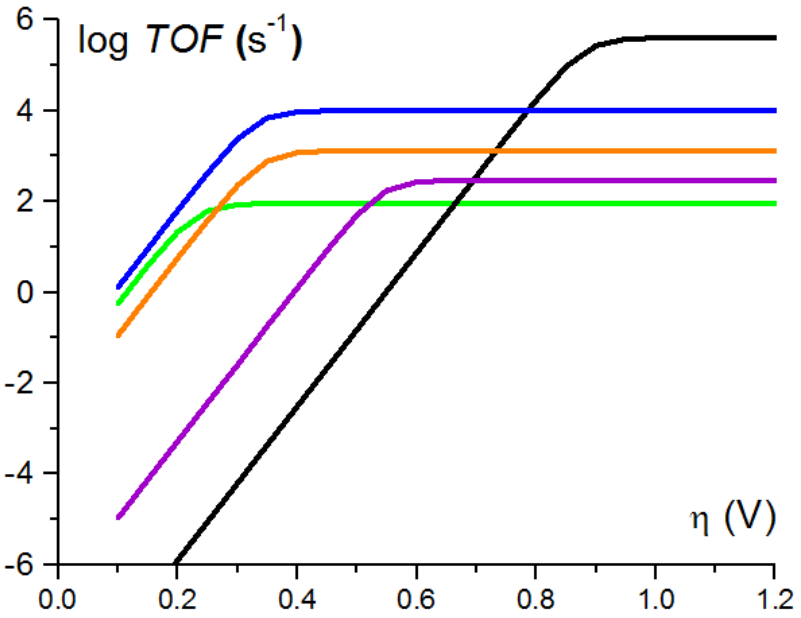

Figure 25. *Catalytic Tafel plots: comparison of performances for HER catalysed by Ni_3L_2 in DMF in the presence of 1M TFA (purple line) and NiTSC-OCH_3 in DMF in the presence of 1M TFA (green line)*[1] *with other catalysts reported in the literature. Black: Fe^{II}TPP, DMF, Et_3NH^+,*[8] *blue: $[Co^{II}(dmgH)_2py]$, DMF, Et_3NH^+,*[7,9] *orange: $[Ni^{II}(P_2PhN_2C_6H_4X)_2]^{2+}$, X = $CH_2P(O)(OEt)_2$, MeCN, DMFH.*[7,10]

When comparing our reference catalyst NiTSC-OCH_3 with the new trinuclear complex Ni_3L_2, we can observe that they differ in their catalytic performances while having both only one single nickel center involved in the conversion of protons into hydrogen as pointed out by the DFT computations of their reaction mechanisms. Even though their faradaic yields are of similar magnitude (80% and 82% for the NiTSC-OCH_3 and Ni_3L_2, respectively), the trinuclear catalyst displays a greater turnover number as opposed to the smaller value obtained for the mononuclear nickel compound over a longer time of reaction. A comparison of their TOF also shows how much more efficient Ni_3L_2 is with a value of 291 s^{-1} versus the 90 s^{-1} TOF value for NiTSC-OCH_3. However, these improved catalytic performances come at a cost of a greater overpotential requirement (0.564 V for Ni_3L_2 versus 0.344 V for NiTSC-OCH_3) and a reduced stability (4 hours for Ni_3L_2 versus 16 hours for NiTSC-OCH_3).

4.3 Conclusions

We reported on the synthesis and characterization of a new trinuclear complex (Ni_3L_2) based on a thiocarbohydrazide ligand (H_6L). The complex was tested and evaluated as a HER electrocatalyst, exhibiting a good performance. Interestingly, when compared with its mononuclear analog NiTSC-OCH_3, Ni_3L_2 surpassed its TON and TOF values on a shorter timescale with an almost identical faradaic yield. The trinuclear complex is a faster catalyst but this comes with the cost of a larger overpotential and a worse catalytic stability. These results support the fact that nuclearity influences the electronic and redox properties of the catalyst, which affects its performance even if in the present case, the two-peripheral metal centers do not play any specific role in the hydrogen evolution reaction that is mediated only by the central nickel ion of the complex.

Possible replacement of the two catalytically-inactive nickels with electronically richer and redox-innocent metal ions, like zinc, might improve the catalytic performance of the system by diminishing the overpotential requirements. Another important question to be addressed is whether a metal-centered reactivity is indeed responsible for better turnover rates. A good comparison example is the Co-based thiosemicarbazone complex, which has been shown to be an efficient HER catalyst requiring smaller overpotentials than its Ni counterpart does. Should synthesizing a trinuclear cobalt complex be possible, we could further probe how focusing density on the metal center actually assists in the catalytic turnover rates, as well as how it can impact the electrochemical properties of the system.

4.4 Experimental section and supplementary data

4.4.1 Synthesis and Characterization

Synthesis of H_6L

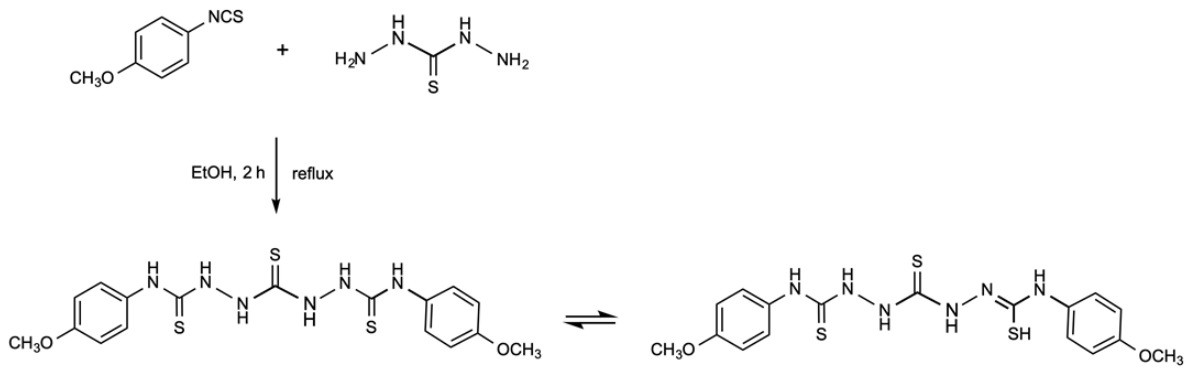

The thiocarbohydrazide (2.5 mmol 0.265g) was dissolved in 20 ml of ethanol, and 10 ml of 1-isothiocyanato-4-methoxy-benzene (5 mmol, 0.825g) solution in 10 mL ethanol was added dropwise. The mixture was refluxed for 2 h. After the reaction mixture was cooled to room temperature, the white product was filtered and washed twice with ethanol. The crude product was used in the next step without further purification. Yield 95%.

^{1}H NMR (400 MHz, DMSO-d6, 298K, TMS), δ: 10.36-9.17 (m, 6H, NH), 7.33 (d, 2J = 8.5 Hz, 4H, o-CH), 6.9 (d, 2J = 9 Hz, 4H, p-CH), 3.75 ppm (s, 6H, O-CH3).

HR ESI-MS $[M-H]^-$ for $C_{17}H_{20}N_6O_2S_3$: Calculated: 435.0737, found: 435.0741.

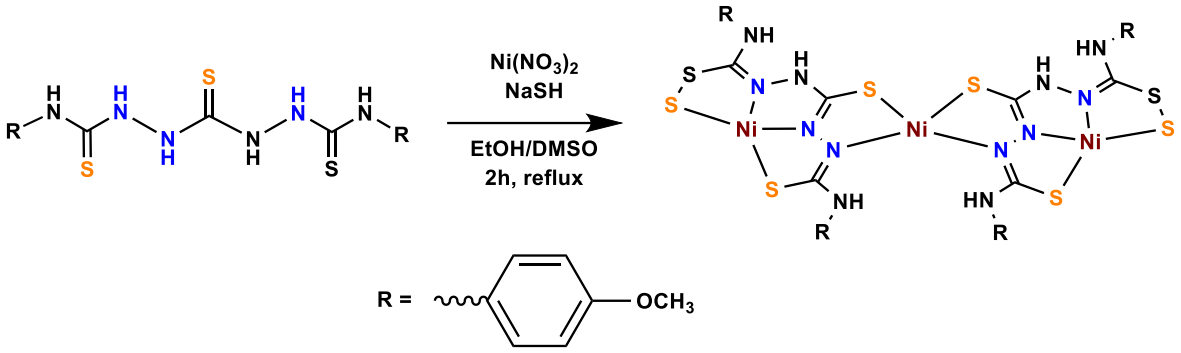

To the suspension of H_6L (0.225 mmol, 0.1 g) in 5 ml of methanol was added solid sodium hydrosulfide (0.112 mmol, 0.0062 g). The $Ni(NO3)_2$ (0.337 mmol, 0.098 g) dissolved in 5 ml of methanol was added dropwise to this solution. DMSO was added to fully dissolve the suspension the solution was stirred at reflux for 2 hours. Slow evaporation from this solution gave single crystals suitable for crystallographic analysis with a 70 % yield.

^{1}H NMR (600 MHz, DMSO-d6, 298K, TMS), δ: 8.75 (s broad, 6H, NH), 7.07-6.83 (s, 16H, ph-H), 3.85 (s, 6H, -OCH3) 3.70 ppm (s, 6H, -OCH3).

HR ESI-MS $[M-H]^-$ for $C_{34}H_{34}N_{12}O_4S_8Ni_3$: Calculated: 1104.8542, found: 1104.8548.

Table 2. *Crystal data and details of data collection for Ni_3L_2.*

Empirical formula	$C_{41.33}H_{57.33}Ni_3N_{12}O_{8.33}S_{11.67}$
Fw	1405.82
space group	*C2/c*
a [Å]	33.688(4)
b [Å]	30.5050(13)
c [Å]	24.913(3)
β [°]	132.81(2)
V [Å^3]	18781(6)
Z	12
λ [Å]	0.71073
ρ_{calcd} [g cm^{-3}]	1.492
crystal size [mm]	0.50 × 0.15 × 0.04
T [K]	293(2)
μ [mm^{-1}]	1.338
R_1[a]	0.0624
wR_2[b]	0.1169
GOF[c]	0.818
CCDC No.	2104371

[a] $R_1 = \Sigma||F_o| - |F_c||/\Sigma|F_o|$. [b] $wR_2 = \{\Sigma[w(F_o^2 - F_c^2)^2]/\Sigma[w(F_o^2)^2]\}^{1/2}$. [c] GOF = $\{\Sigma[w(F_o^2 - F_c^2)^2]/(n - p)\}^{1/2}$, where *n* is the number of reflections and *p* is the total number of parameters refined.

Symmetry codes: [1)]2 – *x*, *y*, 1.5 – *z*.

4.4.2 Electrochemistry

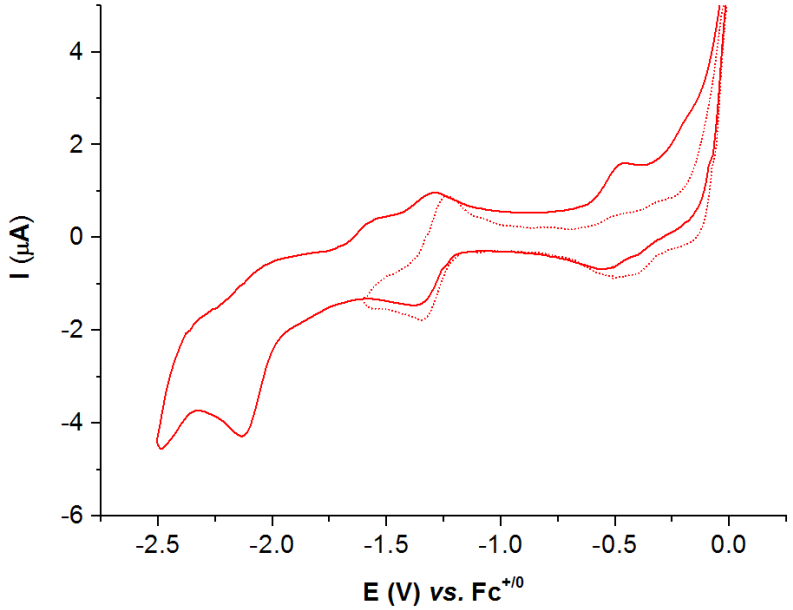

Figure 26. *Cyclic voltammogram of 1 mM solutions of Ni_3L_2 in DMF solvent recorded at stationary glassy carbon electrode in DMF at 500 mV/s (solid line) and focusing on the reversible redox process (dotted line). Potentials referenced to the $Fc^{+/0}$.*

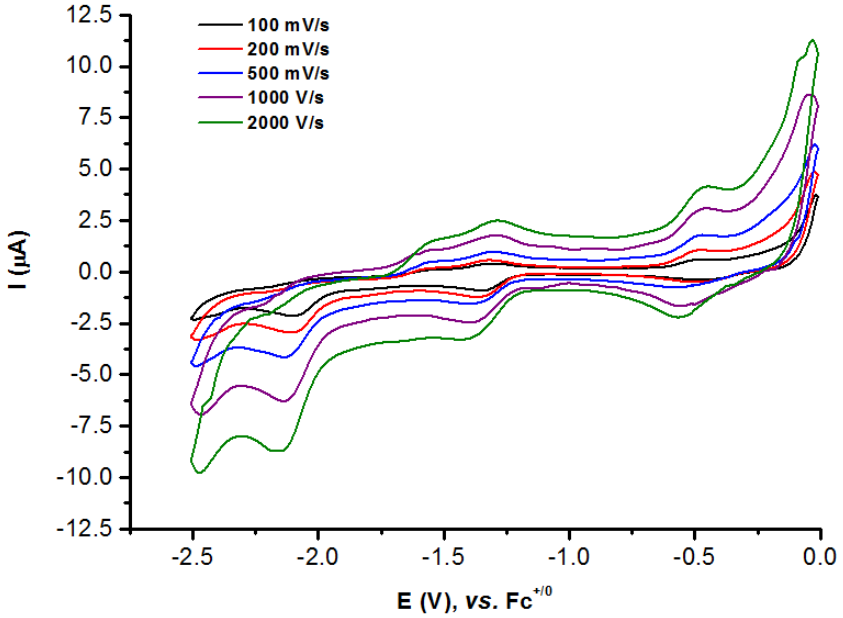

Figure 27. *Successive cyclic voltammogram of a 1 mM solution of Ni_3L_2 in DMF at a stationary glassy carbon electrode at different scan rates in DMF with 0.1 M NBu_4PF_6 as supporting electrolyte. Potentials referenced to the $Fc^{+/0}$.*

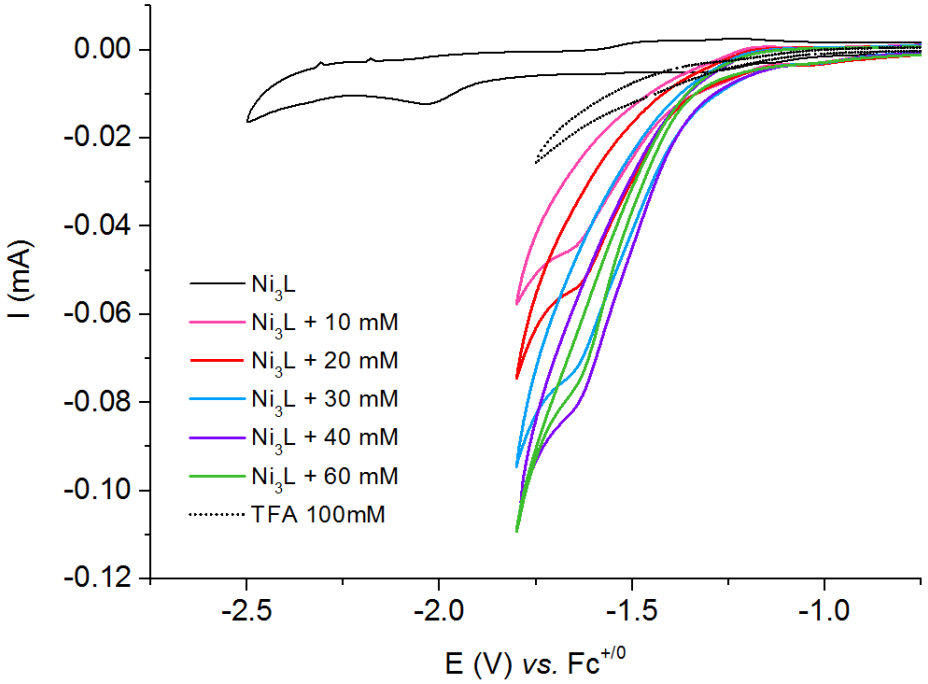

Figure 28. *Successive cyclic voltammograms of a 1 mM solution of Ni_3L_2 in DMF with increasing concentrations of TFA at a 500 mV/s scan rate.*

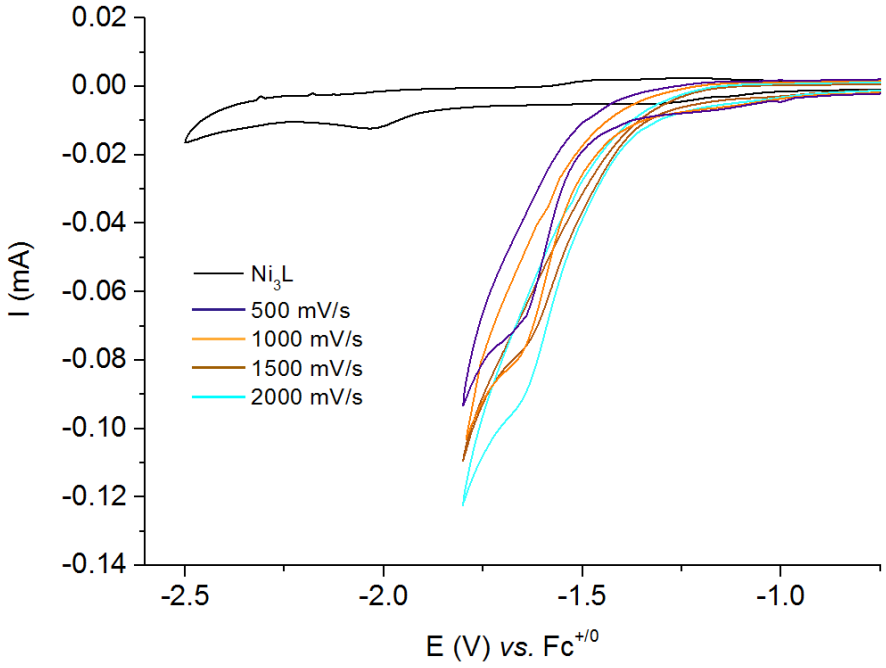

Figure 29. *Successive cyclic voltammograms of a 1 mM solution of Ni_3L_2 in DMF and 60 mM of TFA at 5 different scan rates.*

4.4.3 Overpotential calculations

The overpotential value for the trinuclear Ni_3L_2 complex was obtained following the same protocol that was presented in the previous chapters (see experimental section of Chapter 2 for the detailed analysis and formulas used).

4.4.4 Kinetic analysis

The turnover frequency (TOF) value of Ni_3L_2 was evaluated using the peak current of the catalyst in the absence (i_p) and presence of proton source (i_{cat}). Without substrate, the peak current is given by the Randles-Sevcik equation (1).

$$i_p = \left(0.4463 \times n_p FA[Cat]\right) \times \sqrt{F\nu D / RT} \quad (1)$$

In (1), n_p is the number of electrons transferred (n_p = 1), *F* is Faraday's constant, *A* is the active surface area of the working electrode, $[Cat]$ is the concentration of the catalyst, ν is the scan rate, D is the diffusion coefficient, *R* is the universal gas constant and *T* is temperature. In the presence of substrate, the peak current is given by the following equation:

$$i_{cat} = (n_{cat} FA[Cat]) \times \sqrt{D k_{H_2} [H^+]} \quad (2)$$

In (2), n_{cat} is the number of electrons required for the catalytic reaction (n_{cat}= 2), k_{H_2} is the rate constant of the catalytic reaction and $[H^+]$ is the acid concentration.[11] Thus, the ratio of i_{cat}/i_p is given by the following equation:

$$i_{cat}/i_p = \left(n_{cat}/0.4463 n_p\right) \times \sqrt{RT/F} \times \sqrt{k_{H_2}[H^+]/\nu} \quad (3)$$

Under pseudo first-order conditions where $k_{obs} = k_{H_2} \times [H^+]$, we obtain equation (4):[12]

$$i_{cat}/i_p = 4.484 \times \sqrt{RT/F} \times \sqrt{k_{obs}/\nu} \quad (4)$$

When at scan rate independent conditions, we can derive equation (5) to estimate the observed rate constant or the maximum TOF value:

$$TOF_{max} = k_{obs} = 1.938\, x\, v \left[{i_{cat}}/{i_p} \right]^2 \quad (5)$$

The above equations are used to estimate TOF values in the case of electrocatalysts under pure kinetic conditions where plateau current is easily observable and is scan rate independent. In the case of Ni_3L_2, the peak current i_{cat} plateaus for concentration of acid and scan rates higher than 60 mM and 2 V/s, respectively. In addition, the ratio $\left({i_{cat}}/{i_p} \right)$ varies linearly with the inverse of the square root of scan rate ($\sqrt{v}$) which confirms the validity of the approach.

References

1. Straistari, T. *et al.* A Thiosemicarbazone-Nickel(II) Complex as Efficient Electrocatalyst for Hydrogen Evolution. *ChemCatChem* **9**, 2262–2268 (2017).
2. Papadakis, M. *et al.* Ligand-based electronic effects on the electrocatalytic hydrogen production by thiosemicarbazone nickel complexes. *Dalton Trans.* **49**, 5064–5073 (2020).
3. Pieri, C. *et al.* Hydrogen evolution reaction mediated by an all-sulfur trinuclear nickel complex. *Chem. Commun.* **56**, 11106–11109 (2020).
4. Fourmond, V., Jacques, P.-A., Fontecave, M. & Artero, V. H_2 Evolution and Molecular Electrocatalysts: Determination of Overpotentials and Effect of Homoconjugation. *Inorg. Chem.* **49**, 10338–10347 (2010).
5. Fourmond, V. *et al.* A nickel–manganese catalyst as a biomimic of the active site of NiFe hydrogenases: a combined electrocatalytical and DFT mechanistic study. *Energy Environ. Sci.* **4**, 2417 (2011).
6. Roy, S. *et al.* Molecular Cobalt Complexes with Pendant Amines for Selective Electrocatalytic Reduction of Carbon Dioxide to Formic Acid. *J. Am. Chem. Soc.* **139**, 3685–3696 (2017).
7. Artero, V. & Saveant, J.-M. Toward the rational benchmarking of homogeneous H_2 -evolving catalysts. *Energy Environ. Sci.* **7**, 3808–3814 (2014).
8. Bhugun, I., Lexa, D. & Savéant, J.-M. Homogeneous Catalysis of Electrochemical Hydrogen Evolution by Iron(0) Porphyrins. *J. Am. Chem. Soc.* **118**, 3982–3983 (1996).
9. Coutard, N., Kaeffer, N. & Artero, V. Molecular engineered nanomaterials for catalytic hydrogen evolution and oxidation. *Chem. Commun.* **52**, 13728–13748 (2016).
10. Galan, B. R. *et al.* Electrocatalytic Oxidation of Formate by $[Ni(P^{R}_2N^{R'}_2)_2(CH_3CN)]^{2+}$ Complexes. *J. Am. Chem. Soc.* **133**, 12767–12779 (2011).
11. Wilson, A. D. *et al.* Hydrogen Oxidation and Production Using Nickel-Based Molecular Catalysts with Positioned Proton Relays. *J. Am. Chem. Soc.* **128**, 358–366 (2006).
12. Appel, A. M., DuBois, D. L. & Rakowski DuBois, M. Molybdenum−Sulfur Dimers as Electrocatalysts for the Production of Hydrogen at Low Overpotentials. *J. Am. Chem. Soc.* **127**, 12717–12726 (2005).

Chapter 5: Light-driven hydrogen evolution with thiosemicarbazone complexes

5.1 General Introduction

Electrocatalytic hydrogen production has been extensively discussed as an efficient way to produce hydrogen in the previous chapters. However, there is another alternative that has caught the interest of many researchers: the photochemical hydrogen production. By harvesting energy from the sun, an abundant energy source, hydrogen can be produced via water splitting. The first example of hydrogen being produced via solar energy was reported in 1972 using TiO_2 as a photocatalyst.[1] Until today many research groups have been working in this field with the aim to develop stable, robust and efficient solar driven systems able to produce hydrogen.[2]

There are two approaches to mediate light-driven hydrogen evolution with either a photoelectrochemical device (PEC) (Figure 1) or with a photochemical cell in which no external circuits are necessary for the water splitting process (Figure 2). For this Ph.D. work, we have been focusing on the latter process.

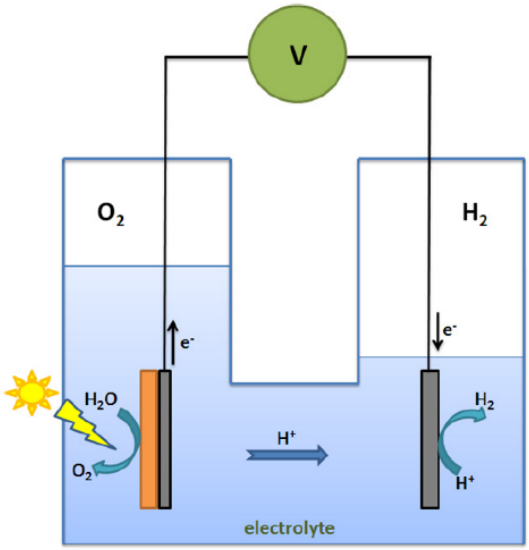

Figure 1. *Schematic representation of water splitting with a photoelectrochemical device.*[3]

In the case of the photochemical cell, the system uses sunlight to perform the redox reaction of water splitting into hydrogen and oxygen. The two reactions are performed in different spaces, connected by a membrane such as nafion, which allows the electrons and protons to freely move from one compartment to another. A target of these devices is the simultaneous production of H_2 and O_2, which is quite challenging.[4] A strategy to overcome this problem is to separate the two half-reactions by focusing on each single production process

individually. In order to render it possible, the correct charge has to be regenerated by using sacrificial agents.

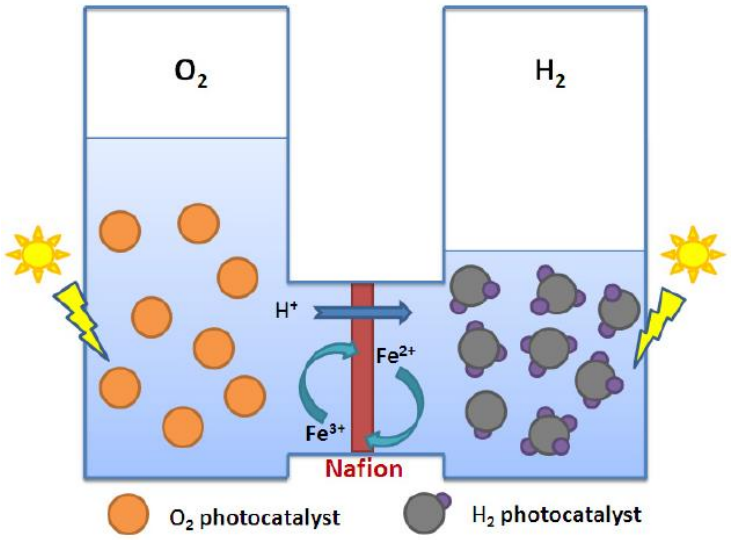

Figure 2. *Schematic representation of water splitting photochemical cell.*[3]

A simplified version of a photochemical hydrogen producing system contains three essential components:[5] a) a photosensitizer (or PS) able to absorb light irradiation and produce its corresponding excited species PS^* processing useful redox properties, b) a catalyst able to gather electrons and reduce protons into hydrogen and c) a sacrificial electron donor (or SED) that regenerates the electrons consumed during the hydrogen production process (Figure 3). All the individual parts of this system can exist in either solid state or can be dissolved in the reaction's medium, characterizing the system as either homogeneous or heterogeneous.

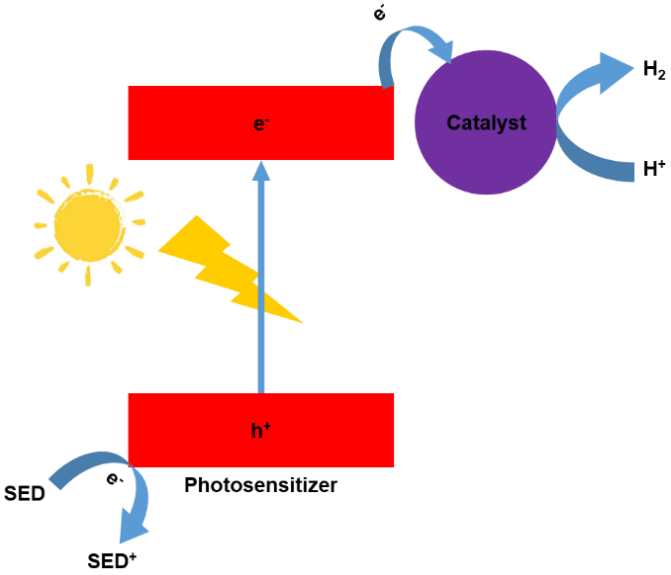

Figure 3. *Graphical representation of a three components photocatalytic system.*

Many inorganic compounds have been used and reported as photosensitizers in the literature. These compounds range usually from semiconductors like TiO_2[1] to metal-organic complexes deriving from iridium[6], ruthenium[7], zinc[8,9] and others metal centers.[10] Selected examples are provided in Figure 4.

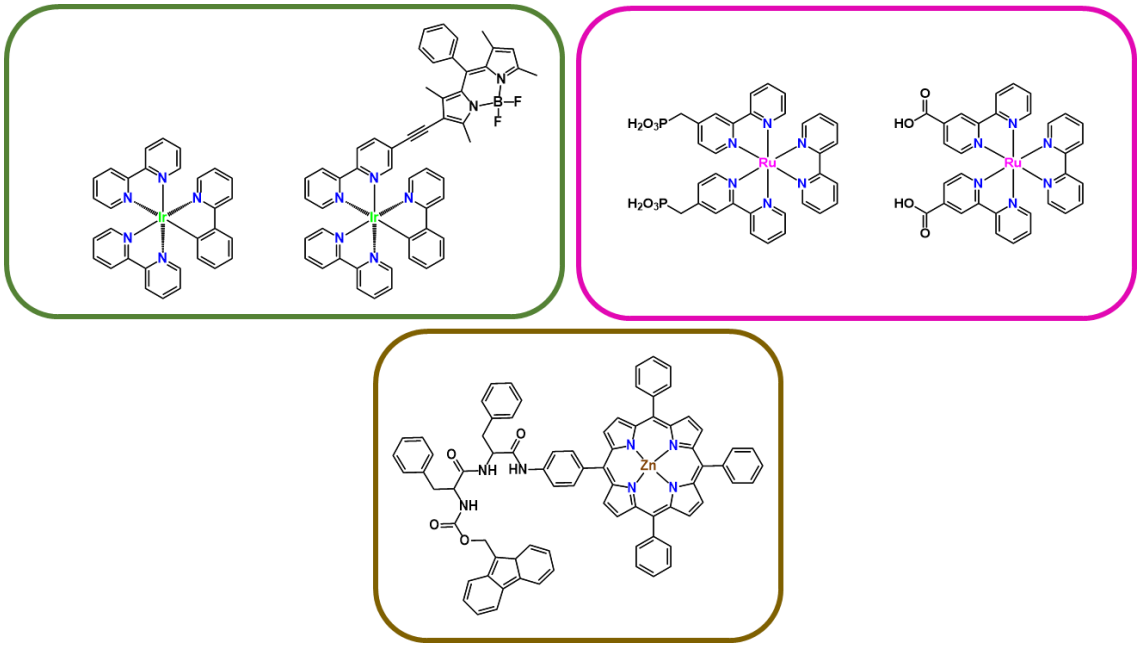

Figure 4. *Examples of iridium, ruthenium and zinc photosensitizers reported in the literature.*[6–8]

A plethora of inorganic compounds have been also used over the years as molecular catalysts in the context of photocatalytic hydrogen evolution and selected examples are shown in Figure 5. These compounds range from a wide range of metal-organic complexes with a great focus on cobalt.[10–15] Copper, nickel, iron, manganese and other metals have also been used as catalytic centers.[16,17]

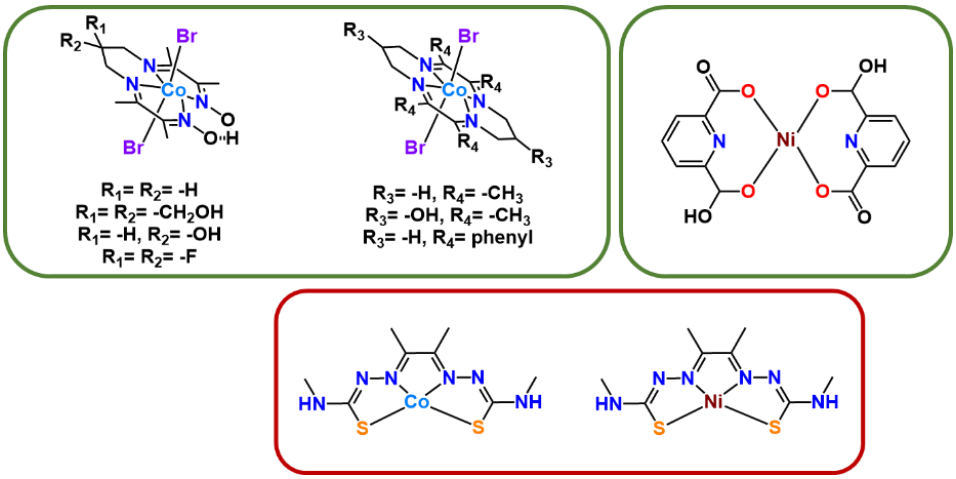

Figure 5. *Examples of cobalt and nickel catalysts used for photocatalytic hydrogen evolution reactions and reported in the literature.*[11–13,18,19]

Inspired by the use of nickel and cobalt thiosemicarbazone complexes as electrocatalysts for HER, our research group reported a first study using the parent nickel complex having methoxy groups on the para position of the phenyl rings, NiTSC-OCH_3, as a catalytic center in a photocatalytic system involving ruthenium and iridium polypyridine complexes as light harvesting systems.[20] This system was shown to be very efficient for hydrogen production but it had two disadvantages: (i) The system had a very short lifetime being able to evolve H_2 for only about 2 hours and (ii) due to the use of iridium, which gave the best results, the system is very cost-heavy as iridium is an expensive and rare metal on Earth.

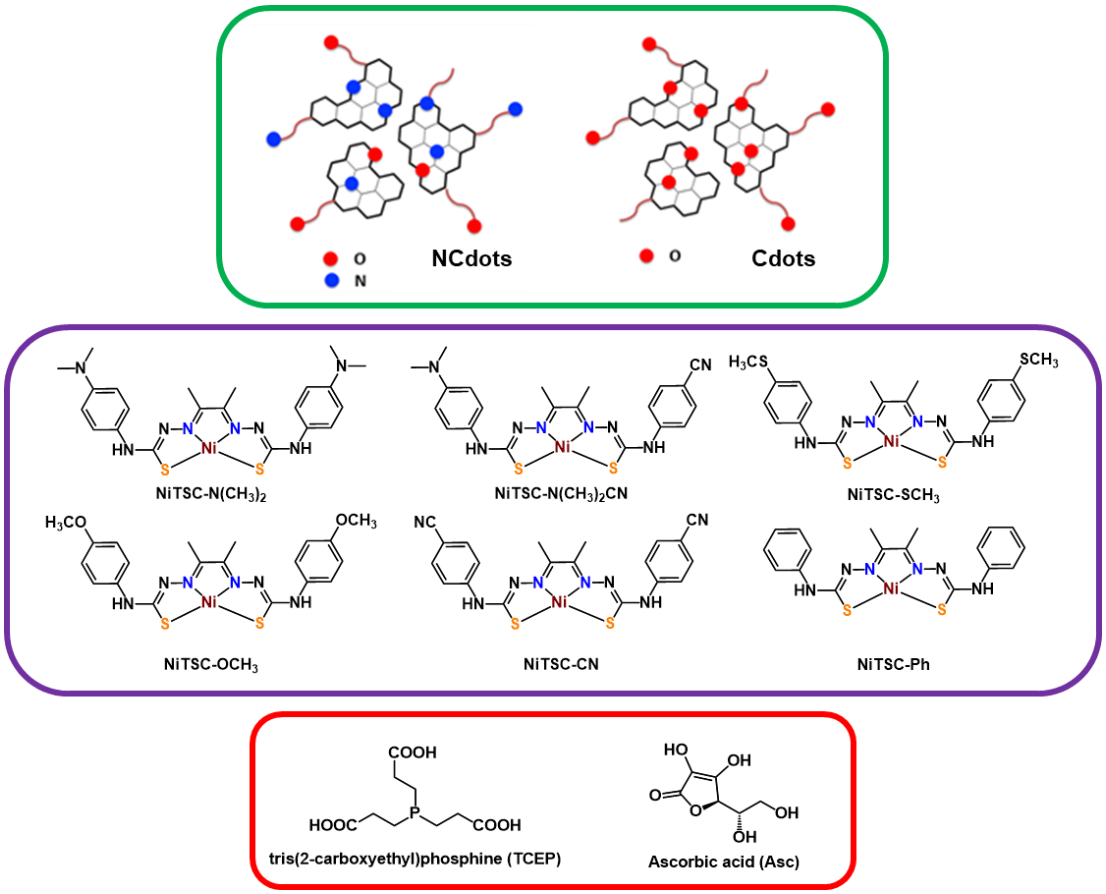

Figure 6. *Schematic representation of nitrogen-doped and carbon dots (green box), chemical structures of the series of nickel complexes (purple box) and selected sacrificial electron donors (red box).*

To overcome these drawbacks, we recently replaced the iridium polypyridine photosensitizer with noble metal-free photosensitizers, namely carbon dots or nitrogen-doped carbon dots.[21] For this new study, we included five additional complexes from our extended nickel thiosemicarbazone family (Figure 6) that were shown to mediate electrocatalytic hydrogen evolution. The new photocatalytic systems for HER were investigated in an aqueous solution with the use of two different sacrificial electron donors. The different parameters influencing the photoreactivity (photosensitizer, light source, catalyst, SED) were investigated and the systems were optimized to probe their maximum catalytic capability.

As a follow-up of this study, we have also tried to improve our system by replacing the nickel metallic center of the series with cobalt, a metal more widely used in literature for photocatalytic systems producing hydrogen (Figure 7).[11,13,14,16] Although this investigation is still ongoing, our preliminary results show great promise for the new cobalt-containing systems.

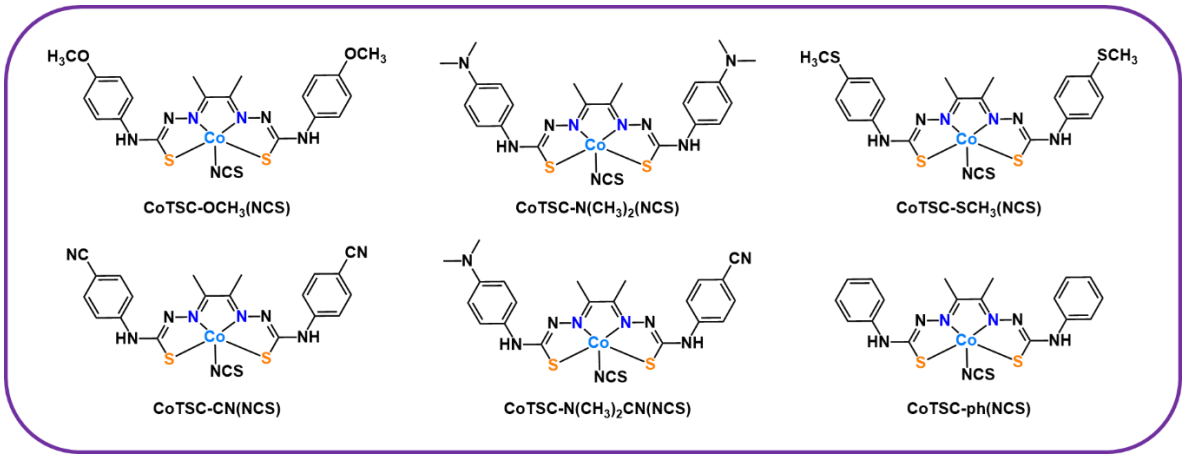

Figure 7. *Chemical structures of the series of cobalt complexes used in this work.*

5.2 Results and Discussion for the nickel series

5.2.1 Synthesis and Characterization

Carbon dots (Cdots) and nitrogen-doped carbon dots (NCdots) were synthesized by the group of our collaborator, Prof. A. G. Coutsolelos, following the previously reported synthetic protocols (Figure 8).[21] In both cases, citric acid was used as the precursor of these materials. For the preparation of CDots, citric acid was pyrolyzed at 180 ^{o}C for 5 days in an autoclave. The solution is then neutralized with NaOH to yield carbon dots bearing carboxylic groups. A similar process was used for the NCDots with the inclusion of ethylenediamine as a nitrogen source. The reaction was carried out in water for 8 hours and the crude powder was purified by the use of dialysis bags of 1kDa for 24 hours.

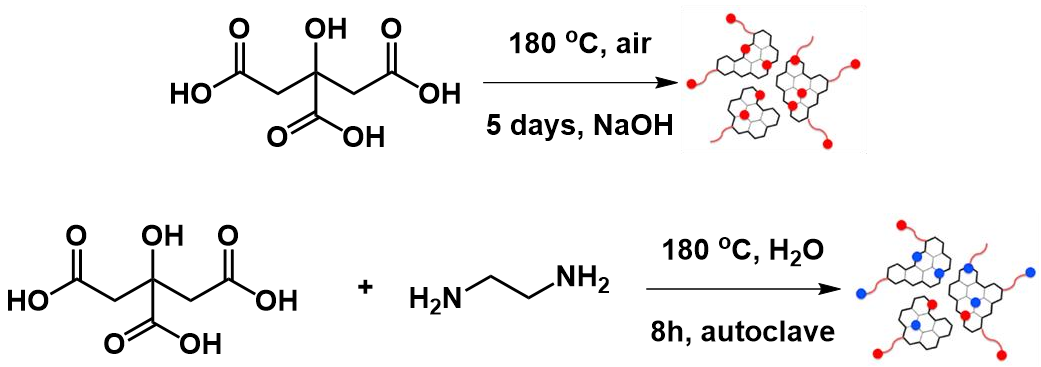

Figure 8. *Synthetic scheme to generate carbon dots and nitrogen-doped carbon dots.*[17]

The nickel complexes were synthesized as reported in the previous chapters: The synthetic protocols of NiTSC-SCH_3; NiTSC-CN; NiTSC-$N(CH_3)_2$ and NiTSC-$N(CH_3)_2CN$ were presented in Chapter 2 while the protocol leading to NiTSC-ph is provided in Chapter 3. The parent complex NiTSC-OCH_3 was synthesized according to literature.[22]

5.2.2 Photocatalytic hydrogen production

For a thorough evaluation of the experimental parameters (photosensitizer, light source, catalyst, concentration, SED) and to further optimize the best performing photocatalytic systems, a series of test experiments were performed.

We first investigated which of the two materials, Cdots and NCdots, was the best photosensitizer in this specific system. Following the previous study done by our collaborators, 10 mg of each photosensitizer were employed for the first photocatalytic experiments.[17] Combining Cdots with the nickel thiosemicarbazone complexes yielded no hydrogen evolution in aqueous solution with the use of a sacrificial electron donor (SED), tris(2-carboxyethyl)phosphine/ascorbic acid (TCEP/Asc) in 1:1 ratio at a pH = 5 under white led irradiation. On the other hand, NCdots were able to jumpstart the system's catalytic properties when introduced into the solution. From these results, all other test experiments were then performed with NCdots as photosensitizer.

Having two possible light sources, a UV led and a white led lights, we then investigated which one was adapted for our photocatalytic reaction. The first light source did not produce any photo-evolved hydrogen. On further investigation, it was obvious that this irradiation source lead to the decomposition of the catalysts (Figure 9). We, therefore, opted for a white led light as the irradiation source.

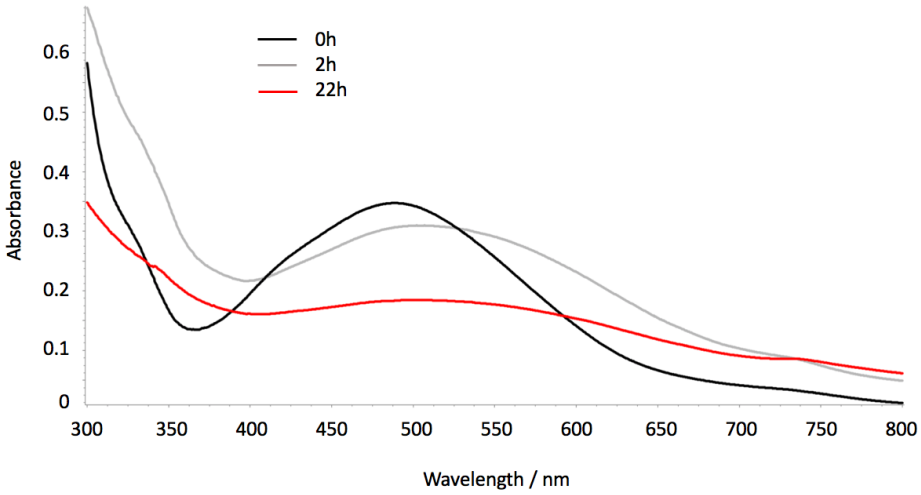

Figure 9. *UV-vis spectral evolution of the NiTSC-N(CH$_3$)$_2$ catalyst under UV led irradiation upon 0, 2 and 22 hours of exposure.*

We then performed a series of photocatalytic experiments on the whole set of catalysts using TCEP/Asc in 1:1 ratio as SED in aqueous solution at a pH = 5 under white led irradiation. Our results pointed at the nickel complex with dimethylamino groups, NiTSC-N$(CH_3)_2$, as the best performing catalytic center, by far. It largely surpasses the second best catalyst having cyano and dimethylamino groups, NiTSC-N$(CH_3)_2$CN (Figure 10). Indeed, the NiTSC-N$(CH_3)_2$ complex displays a turnover number (TON) value versus the catalyst that is twice larger than that of NiTSC-N$(CH_3)_2$CN with TON_{cat} = 148 for the former and 72 for the latter. The worst performing catalyst was identified as the NiTSC-ph one reaching a TON_{cat} of 26 and thus providing evidence that the para substituent on the phenyl ring of the ligand does influence the photocatalytic performance of the nickel complexes. This finding is further strengthened by the fact that the two best performing catalysts bear the most electron-donating group of the series, *i.e.* the dimethylamino,-N$(CH_3)_2$.

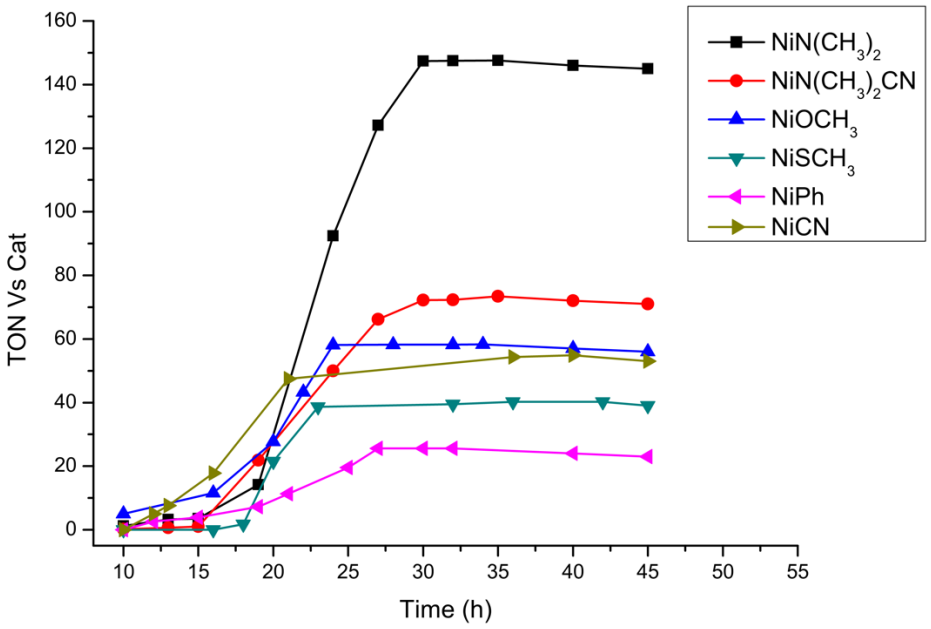

Figure 10. *Photocatalytic hydrogen production plots of 10 mg NCdots with 50 nmol nickel catalysts: NiTSC-N$(CH_3)_2$; NiTSC-N$(CH_3)_2$CN; NiTSC-SCH_3; NiTSC-OCH_3; NiTSC-CN; NiTSC-ph. All photocatalytic experiments were performed in aqueous TCEP/Asc (1:1) 0.1 M each at pH = 5. All the results presented in the hydrogen production plots are the average values of three independent measurements (within 5-10% error).*

The relative catalytic activity of the series comes down to the following TON_{cat} ranking: NiTSC-N$(CH_3)_2$ > NiTSC-N$(CH_3)_2$CN > NiTSC-OCH_3 > NiTSC-CN > NiTSC-SCH_3 > NiTSC-ph (Table 1); with the catalysis plateauing at around 30 hours (Figure 10).

Table 1. *Photocatalytic performances of the NiTSC-R series of catalysts. All the results presented are the average values of three independent measurements (within 5-10% error).*

Catalyst	TON_{cat}
NiTSC-N(CH₃)₂	148
NiTSC-N(CH₃)₂CN	72
NiTSC-OCH₃	58
NiTSC-CN	55
NiTSC-SCH₃	40
NiTSC-ph	26

The catalyst concentration was the next parameter that was probed in our test experiments. For that purpose, three different quantities of nickel complex, *i.e.* 20, 50, and 100 nmol of catalyst were used to investigate what was the optimal value for photocatalysis. Upon mixing the NiTSC-$N(CH_3)_2$ complex with NCdots, the best performances were obtained when using a 50 nmol quantity of catalyst, as illustrated in Figure 11 comparing the resulting TON_{cat} values in the different experimental conditions.

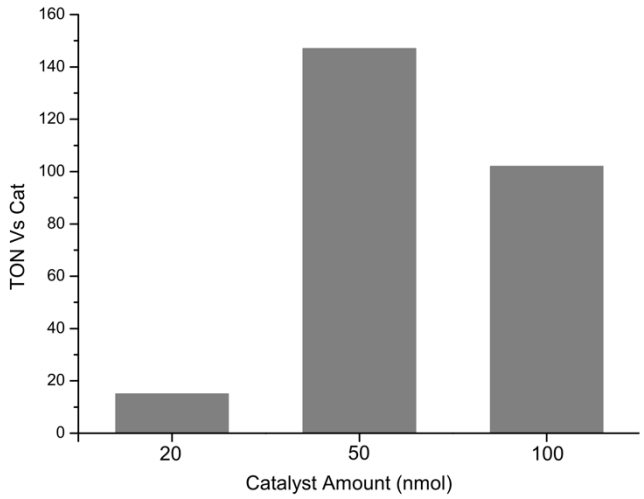

Figure 11. *Photocatalytic hydrogen production plots of 10 mg NCdots in three different amounts of the catalyst NiTSC-N(CH₃)₂: 20, 50 and 100 nmol. The photocatalytic experiments were conducted in aqueous TCEP/Asc (1:1) 0.1 M each at pH = 5. All the results presented in the hydrogen production plots are the average values of three independent measurements (within 5-10% error).*

Further test experiments were carried out to investigate the most adapted sacrificial electron donor for photocatalysis. When using ethylenediaminetetraacetic acid (EDTA), no hydrogen production was observed. A very low H_2 evolution was reached when also using only ascorbic acid as SED. When mixing tris(2-carboxyethyl)phosphine (TCEP) with ascorbic acid (Asc) in a 1:1 ratio, our photocatalytic systems were able to evolve H_2.

All of these findings brought forth the best performing hydrogen production systems which combine 10 mg of NCdots as the photosensitizer, 50 nmol of NiTSC-N$(CH_3)_2$ as the catalyst and a 1:1 ratio of TCEP/Asc as SED in an aqueous solution of pH= 5 in white led light irradiation. The hydrogen production using the series of catalysts in the above conditions is graphically presented in Figure 12.

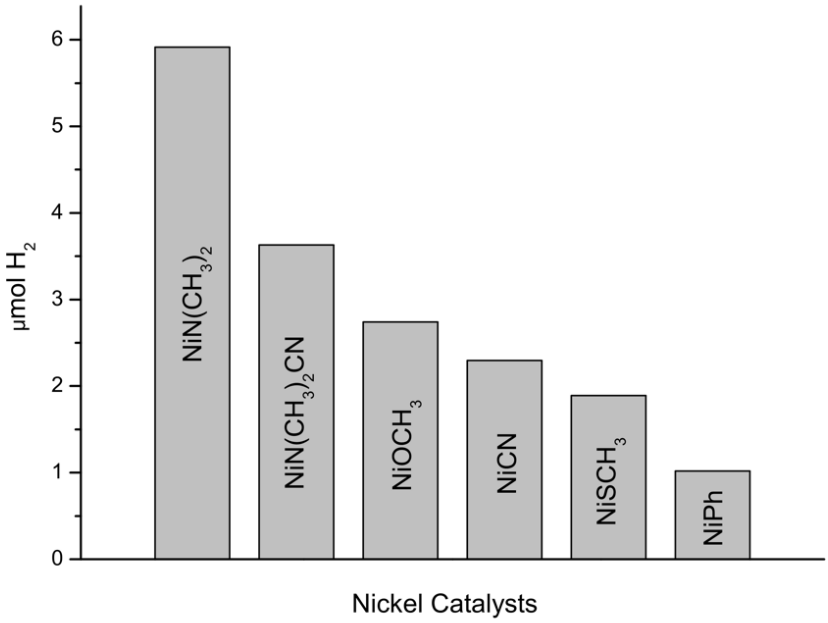

Figure 12. *Photocatalytic hydrogen production (µmol H_2) upon irradiation of 10 mg NCdots in the presence of 50 nmol of the NiTSC-R series in aqueous TCEP/Asc (1:1) 0.1 M each at pH = 5. All the results presented in the hydrogen production plots are the average values of three independent measurements (within 5-10% error).*

Additional control experiments were performed to validate the importance of every component of the photocatalytic system and were conducted in the absence of either the NCdots, the nickel catalysts, the SED or light with samples being stored under dark conditions for the latter case. In all scenarios, no hydrogen production was observed proving that all the parts of the system are essential for the photoreaction. Going forward to evaluate the importance of the nickel complexes, two more control experiments were considered. Firstly, we replaced the nickel catalyst with 50 nmol of $NiCl_2$ salt to use it as an alternate catalytic

center and no catalytic activity was observed in these conditions. A small amount of mercury (Hg) was also added to one sample to prove if hydrogen evolution was due to the formation of nanoparticles formed during the photo-irradiation process or if it was the molecular catalyst doing. The presence of Hg hardly affected the H_2 produced with our best photocatalytic system with TON_{cat} values of 135 and 148 with and without Hg, respectively. As a result, we can confirm that catalysis occurs in homogeneous conditions and is related with the presence of the molecular nickel catalysts.

Regeneration experiments were also performed to see which components might be unstable during catalysis and thus limit the lifetime of our system. When the plateau of the reaction was reached, more nickel complex or SED mixture was added to the reaction container but did not result in any increase in hydrogen production. However, upon regeneration of the photosensitizer, we started to detect more hydrogen being evolved. These results show that the bottleneck of the reaction is the photo-bleaching of the light harvester that limits the longevity of the system, while neither an excess of SED or an excess of catalyst did make any noticeable difference.

It is interesting to observe from Figure 10 that hydrogen production is being detected after approximately 13 hours of irradiation. Since this observation was similar for all the nickel complexes, this delay was attributed to the nitrogen-doped carbon dots. To verify this behavior, we irradiated 10 mg of NCdots in the presence of SED for 13 hours and we measured the quantum yield (QY) which was found to be 16% compared to the initial material with QY = 26%. TEM images before and after irradiation were collected and presented in Figure 13. The material retained its spherical morphology, but the diameter of some particles became much larger compared with the NCdots before irradiation. Consequently, the morphology of the material changes over time upon irradiation, and possibly must obtain a specific form to start producing H_2.

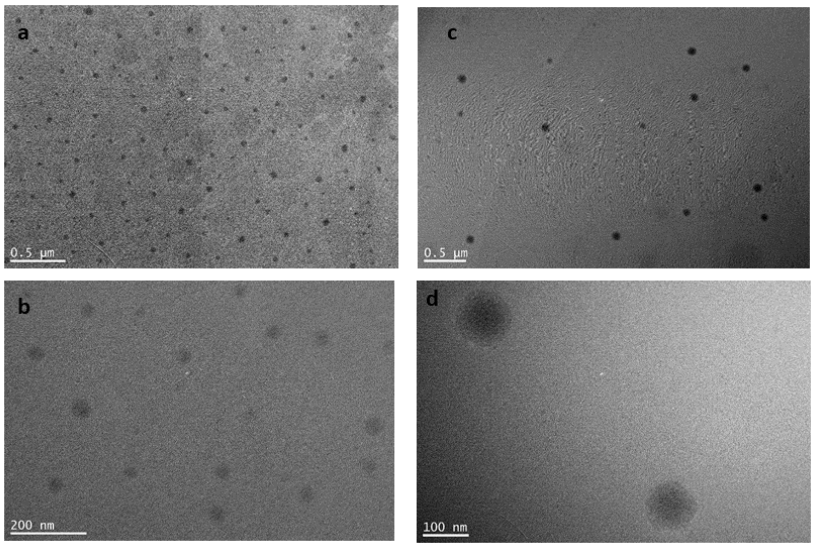

Figure 13 *TEM images of NCdots before light irradiation (a and b) and after 13 hours of white led irradiation (c and d).*

To prove that this transformation is done upon light irradiation, we stirred all components of our best photocatalytic system in the dark overnight. Afterward, the system was irradiated using a white light source. Once again, the system started producing hydrogen after about 10 hours with a TON_{cat} of 132 for about 30 hours of catalysis. Therefore, the photosensitizer transformation happens upon light irradiation and it is essential to jumpstart the hydrogen photoproduction. In order to better investigate this delay, a mixture of the NCdots and SED was irradiated for 13 hours and the NiTSC-N$(CH_3)_2$ catalyst was then added. After 5 hours of irradiation, our system started producing hydrogen and reached a plateau with a TON_{cat} of 135 after 20 hours which fairly compares to the 30 hours of reaction initially observed. These data prove that the photocatalytic system works faster if we pre-irradiate just the photosensitizer and then add the nickel complexes. Further investigation is being carried out to shine light on what kind of transformation is happening to the NCdots that render them efficient for photocatalysis.

5.2.3 Mechanistic Investigation

To get insight into the reaction mechanism involving our photocatalytic systems, we evaluated the thermodynamic ability for photochemical hydrogen evolution from the redox potentials of the nickel complexes and the NCDots (Table 2). The valence band (VB) and conduction band (CB) of the nitrogen-doped carbon dots were obtained from literature[21] while

the reduction potentials of the nickel complexes were previously reported (Chapters 2 and 3). Based on these values, the ΔG (PS/Cat) was calculated for both reduction events of the nickel complexes. As all the values were found to be negative, an electron can be thus transferred from the NCdots to the catalysts rendering hydrogen production thermodynamically allowed with all nickel complexes.

Table 2. *Redox potentials (eV vs. NHE) of the photosensitizer and catalysts with the thermodynamic driving forces of electron transfer processes ΔG_1 (PS/Cat) and ΔG_2 (PS/Cat) (eV). a) Oxidation potentials measured by cyclic voltammetry and referenced to NHE. b) Values calculated as the difference of the oxidation potentials and the optical band gap energy E_{00}, calculated in eV. c) E_{00} values calculated from the intersection between the normalized absorption and emission spectra. d) Reduction potentials measured by cyclic voltammetry and referenced to NHE.*

Compound	**E_{VB}[a]**	**E_{CB}[b]**	**E_{00}[c]**	
NCDots	1.01	-2.13	3.14	
	E_{red1}[d]	**E_{red2}[d]**	**ΔG_1 (PS/Cat)**	**ΔG_2 (PS/Cat)**
NiTSC-N(CH$_3$)$_2$	-0.99	-1.48	-1.14	-0.65
NiTSC-N(CH$_3$)$_2$CN	-0.85	-1.46	-1.28	-0.67
NiTSC-SCH$_3$	-0.87	-1.50	-1.26	-0.63
NiTSC-OCH$_3$	-0.94	-1.57	-1.19	-0.56
NiTSC-CN	-0.77	-1.36	-1.36	-0.77
NiTSC-ph	-0.99	-1.67	-1.14	-0.46

Furthermore, photoluminescence experiments were performed to investigate the mechanism of the catalytic reaction. Using a constant amount of NCdots in the presence of increasing amounts of the nickel catalysts, the emission spectra were recorded in an aqueous solution (Figure 14).

All catalysts were dissolved in DMSO to obtain concentrated solutions and various amounts of these solutions were then added to aqueous solutions containing NCdots. The emission spectra were recorded upon excitation of the solutions at 340 nm. Every consecutive addition of the complexes to the solutions leads to a significant decrease in the emission intensity with variations up to more than 90% of the initial signal intensity. Only the NiTSC-$N(CH_3)_2$ and NiTSC-OCH_3 catalysts showed a smaller quenching of about 85% and 75% respectively.

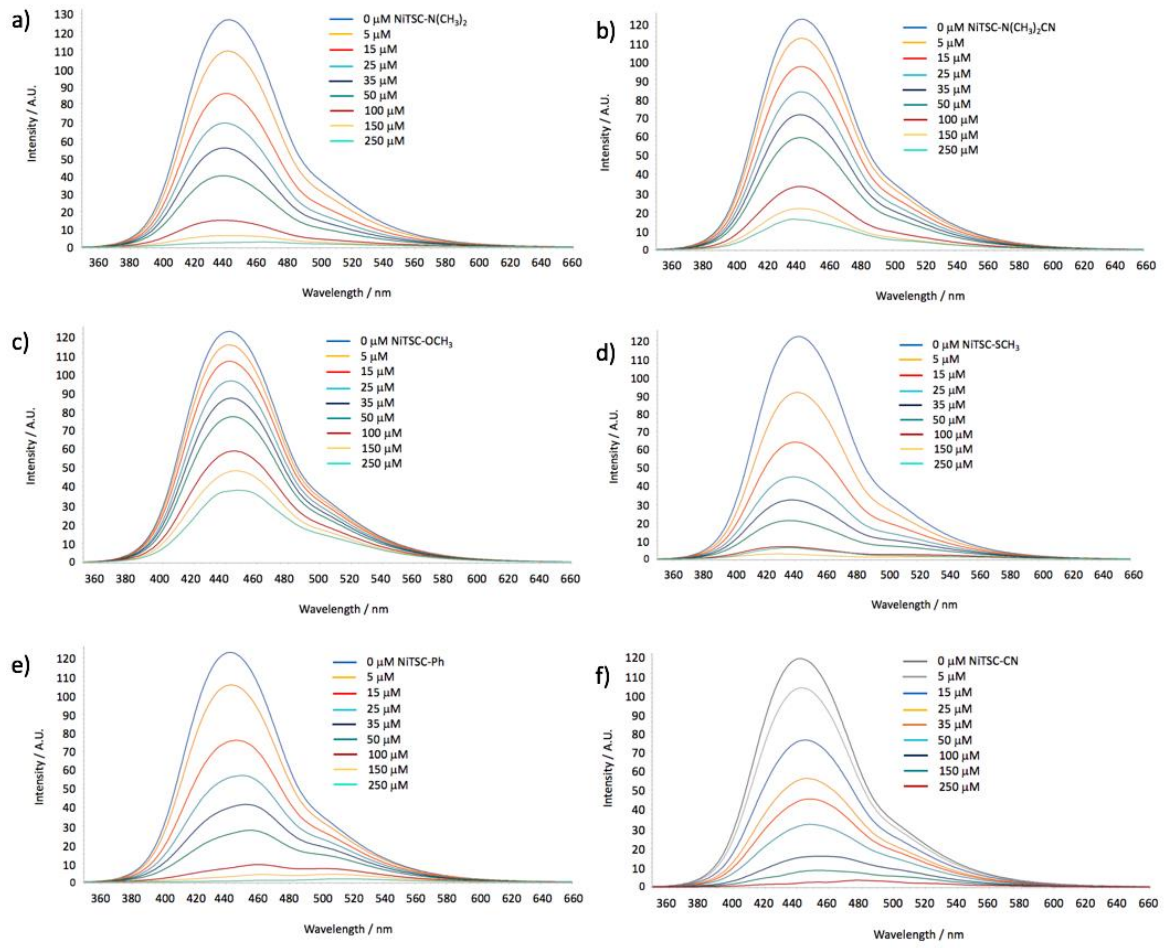

Figure 14. *Emission spectra of NCdDots in aqueous solution with increasing concentrations of: a) NiTSC-N(CH₃)₂, b) NiTSC-N(CH₃)₂CN, c) NITSC-OCH₃, d) NiTSC-SCH₃, e) NiTSC-CN, f) NiTSC-ph.*

Stern-Volmer (K_{SV}) and emission quenching constants (K_Q) were calculated for all the complexes according to literature (Table 3) and fitting curves were generated (Figure 10).[21] The calculated K_{sv} values for all the nickel complexes are much larger when compared to that of ascorbic acid (SED). A similar observation can be made for the calculated quenching constants. Under white light irradiation using 0.1 M of SED and 16 μM of each catalyst, the quenching is more intense in the case of ascorbic acid. Consequently, electrons flow from ascorbic acid towards the conduction band (CB) of NCDots through a reductive quenching process, since the SED concentration is larger than that of the catalysts.

Table 3. *Stern-Volmer constants, K_{sv} and quenching constants, K_Q, of the series of nickel catalysts.*

Compound	K_{sv} (M^{-1})	$K_Q = K_{SV}/t$ ($M^{-1}s^{-1}$)
NiTSC-N(CH₃)₂	43574	$4.1 * 10^{12}$
NiTSC-N(CH₃)₂CN	21128	$2.0 * 10^{12}$
NiTSC-SCH₃	94414	$9.0 * 10^{12}$
NiTSC-OCH₃	11726	$1.1 * 10^{12}$
NiTSC-CN	52555	$5.0 * 10^{12}$
NiTSC-ph	63313	$6.0 * 10^{12}$
Ascorbic Acid	13.8	$1.3 * 10^{12}$

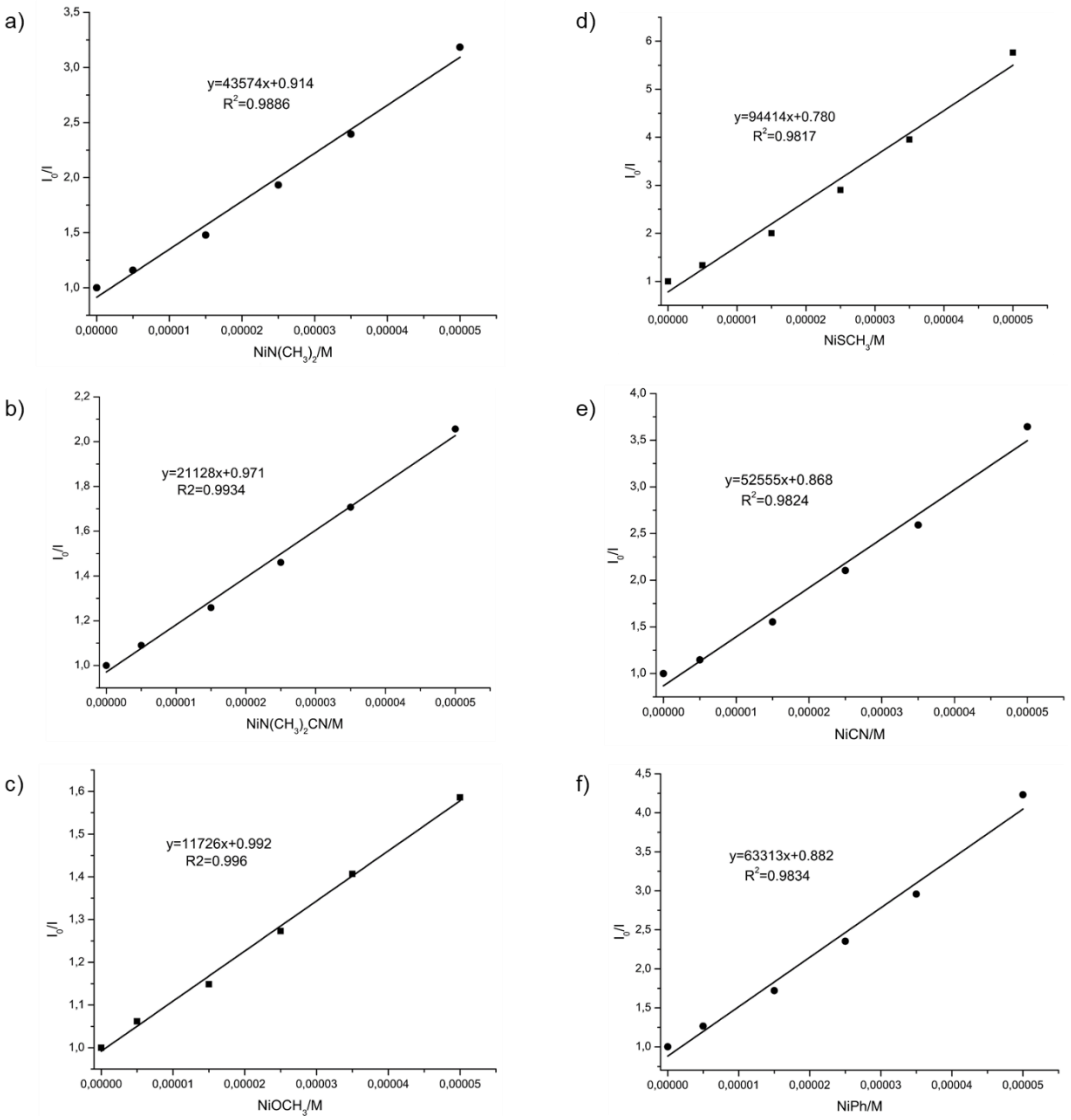

Figure 15. *Stern-Volmer plots of NCdot emission quenching with: a) NiTSC-N(CH₃)₂, b) NiTSC-N(CH₃)₂CN, c) NiTSC-OCH₃, d) NiTSC-SCH₃, e) NiTSC-CN, f) NiTSC-ph catalysts.*

All these information allowed us to propose a reaction mechanism leading to photoinduced hydrogen evolution with our noble metal-free photocatalytic system. A schematic representation of the reaction pathway is presented in Figure 16. Photo-excitation of the nitrogen-doped carbon dots by visible light irradiation initiates the catalytic cycle. Electrons are transferred from the valence band (VB) to the conduction band (CB) of the NCdots. The electron hole created in the NCdot VB is filled by an electron transfer from the sacrificial electron donor (SED) via a reductive quenching process. The photo-generated electrons are then transferred to the nickel catalysts, which are subjected to subsequent protonation and reduction steps. From there, hydrogen is formed through a ligand-assisted metal-centered pathway and its release closes the cycle and the metal complex is regenerated.

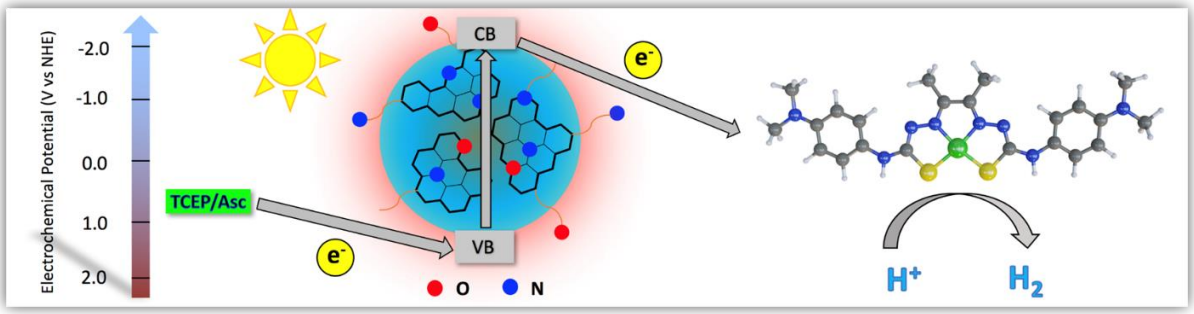

Figure 16. *Photocatalytic mechanism for H_2 evolution using nitrogen-doped carbon dots as photosensitizer, TCEP/Asc as sacrificial electron donor and nickel complexes as catalysts.*

5.3 Results and Discussion for the cobalt series

5.3.1 Synthesis and characterization

Since cobalt has been widely used in many photocatalytic studies,[11,13,14,17] we replaced the nickel metallic center with cobalt in our series of molecular catalysts to investigate how our photocatalytic system is going to be affected (Figure 17). The synthesis of these compounds was done following a modified protocol similar to that of the parent complex, CoTSC-OCH_3(NCS), which was previously reported by our group.[23] All complexes were prepared and characterized by HRMS ESI, electrochemistry, UV-vis spectroscopy. They were also studied in solid state by superconducting quantum interference device (SQUID).

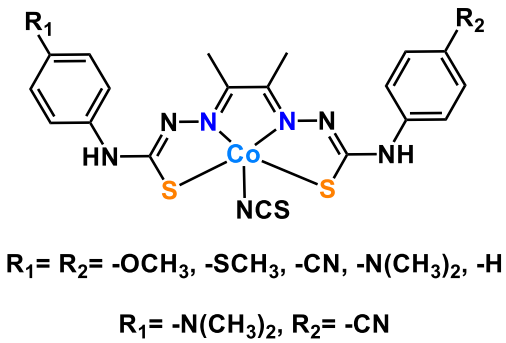

Figure 17. *Schematic representation of the series of cobalt complexes used in this work.*

To address the question of the spin configuration of the cobalt ion, the magnetic properties of the complexes were investigated in the solid state using the SQUID technique. These measurements were performed for the entire series to determine the cobalt oxidation state with exception of the unsubstituted complex, NiTSC-ph which measurements are still ongoing. Figure 18 shows the temperature dependence of the product between the susceptibility with the temperature, χT (blue lines). Considering the solid-state structure of the CoTSC-OCH_3 catalyst was previously reported as a dimer,[23] all complexes were treated as binuclear species. The green line represents the best fit for a paramagnetic system S= 3/2 having one low-spin Co^{III} center (S= 0) and one high-spin Co^{II} center (S= 3/2). In this case, χT is 1.875 $cm^3.K.mol^{-1}$ and is temperature independent. The orange line represents the best fit for a diamagnetic system S= 0 having two low-spin Co^{III} centers (S= 0). All complexes present

a similar behavior with the magnetic susceptibility curves being consistent with the presence of the cobalt ions being mostly diamagnetic low-spin Co^{III} centers. The deviation of the curves from the best fit for a diamagnetic system (orange line) is attributed to contamination from paramagnetic high-spin Co^{II}.The contribution from the latter contamination was estimated to be 17%, 4%, 0.5%, 9% and 1% for CoTSC-$N(CH_3)_2CN(NCS)$, CoTSC-$OCH_3(NCS)$, CoTSC-CN(NCS) and CoTSC-$N(CH_3)_2(NCS)$, CoTSC-$SCH_3(NCS)$ respectively. These results are thus in agreement with the electronic structure previously reported for the parents complex which was found to be a diamagnetic Co^{III} dimer.

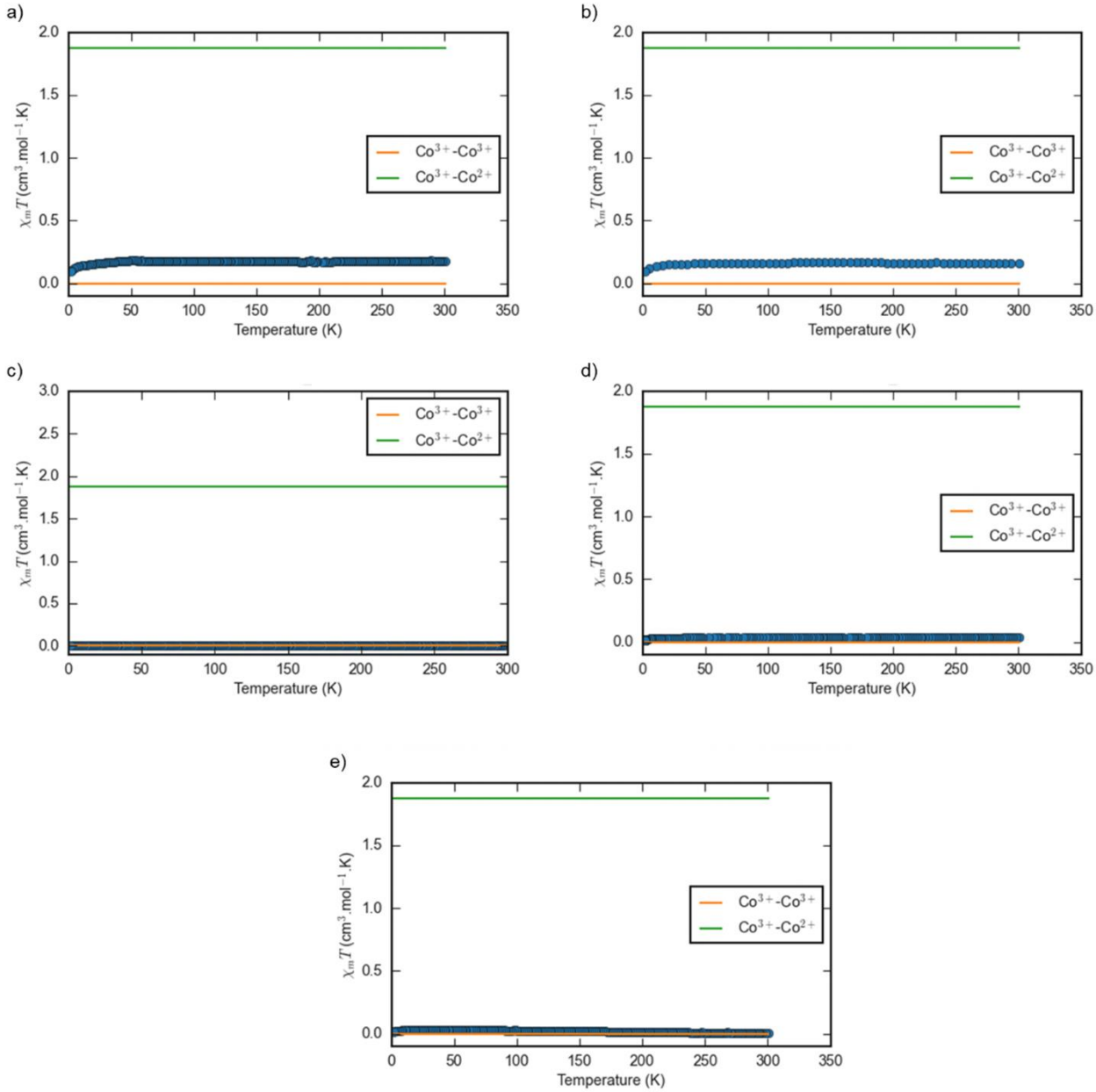

Figure 18. *Temperature dependence of the magnetic susceptibility for a) COTSC-$N(CH_3)_2CN(NCS)$, b) CoTSC-$OCH_3(NCS)$, c) CoTSC-CN(NCS), d) CoTSC-$N(CH_3)_2(NCS)$ and e) CoTSC-$SCH_3(NCS)$.*

The UV-vis spectra of the complexes were recorded to examine the electronic properties of the complexes. The UV-vis spectra display a main absorption band ranging between 336 and 550 nm (Table 4). There is also a second absorption band detected for all complexes between 271 to 287 nm which is reminiscent of the ligand. Interestingly, the CoTSC-N(CH_3)$_2$CN(NCS) complex bears two shoulder-like absorptions at 449 and 550 nm, due to its asymmetrical nature that affects the electron density distribution within the ligand as observed in the case with its nickel counterpart. Overall, the spectral features of the cobalt complexes are similar to those from the nickel series and the observed shifts of the main absorption band are also attributed to the different electronic donating properties of the phenyl ring substituents (Figure 19).

Table 4. *Selected spectral features from the electronic absorption spectra of CoTSC-R(NCS) series in DMF.*

Catalyst	λ (nm)	ε ($M^{-1}*cm^{-1}$)
CoTSC-N(CH_3)$_2$CN(NCS)	281	29617
	449	10140
	550	7587
CoTSC-N(CH_3)$_2$(NCS)	275	32967
	448	8482
CoTSC-CN(NCS)	287	30807
	336	24220
CoTSC-OCH_3(NCS)	271	35651
	426	15776
CoTSC-ph(NCS)	269	29649
	412	13598
CoTSC-SCH_3 (NCS)	278	33496
	421	12716

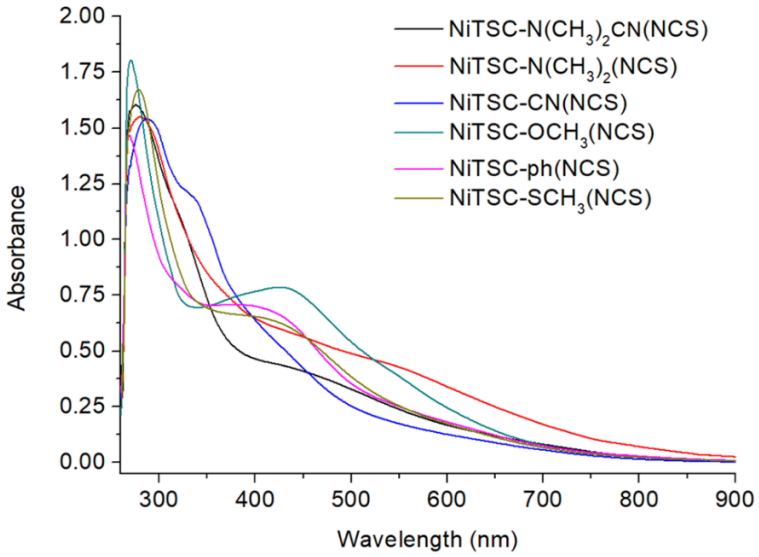

Figure 19. *UV-vis spectra of the CoTSC-R(NCS) series.*

Cyclic voltammograms of the series of complexes were recorded on solutions containing tetrabutylammonium hexafluorophosphate (NBu_4PF_6) as a supporting electrolyte in DMF and an inert atmosphere at room temperature. A three-electrode system was used with the working electrode being a glassy carbon electrode. The redox behaviors of the complexes were investigated between +0.5 and -2.65 V vs $Fc^{+/0}$. In the cathodic region, CoTSC-OCH_3 displays a quasi-reversible system at $^1/_2\,(E_{pc} + E_{pa})$ = -0.60 V, a reversible process at $^1/_2\,(E_{pc} + E_{pa})$ = -1.50 V and an irreversible process at -2.43 V (Table 5 and Figure 20). These data are consistent with those previously reported by our group.

Table 5. *Electrochemical data of NiTSC-R series (V vs. $Fc^{+/0}$).*

Catalyst	CoTSC-R / $[CoTSC\text{-}R]^-$	$[CoTSC\text{-}R]^-$ / $[CoTSC\text{-}R]^{2-}$	$[CoTSC\text{-}R]^{2-}$ / $[CoTSC\text{-}R]^{3-}$
CoTSC-OCH₃(NCS)	-0.60	-1.53	-2.43
CoTSC-SCH₃(NCS)	-0.63	-1.59	-2.46
CoTSC-ph(NCS)	-0.60	-1.47	-2.41

Looking at CoTSC-SCH_3 and CoTSC-ph catalysts, their cyclic voltammograms are fairly similar to that of CoTSC-OCH_3 but are less defined. However, we can still observe the presence of the reversible system at potentials close to that for CoTSC-OCH_3. For the parent complex, this

process, assigned as ligand-based and providing a Co^{II}-ligand radical species, was shown to be the initiation step for electrocatalytic hydrogen production by CoTSC-OCH_3. Such analysis thus stands in the case of CoTSC-SCH_3 and CoTSC-ph. The situation regarding the other complexes is somewhat different as their cyclic voltammogram are ill-defined due to solubility issues. Further work is currently under progress in the laboratory to overcome this issue and confirm that the whole series of catalysts does feature similar redox characteristics.

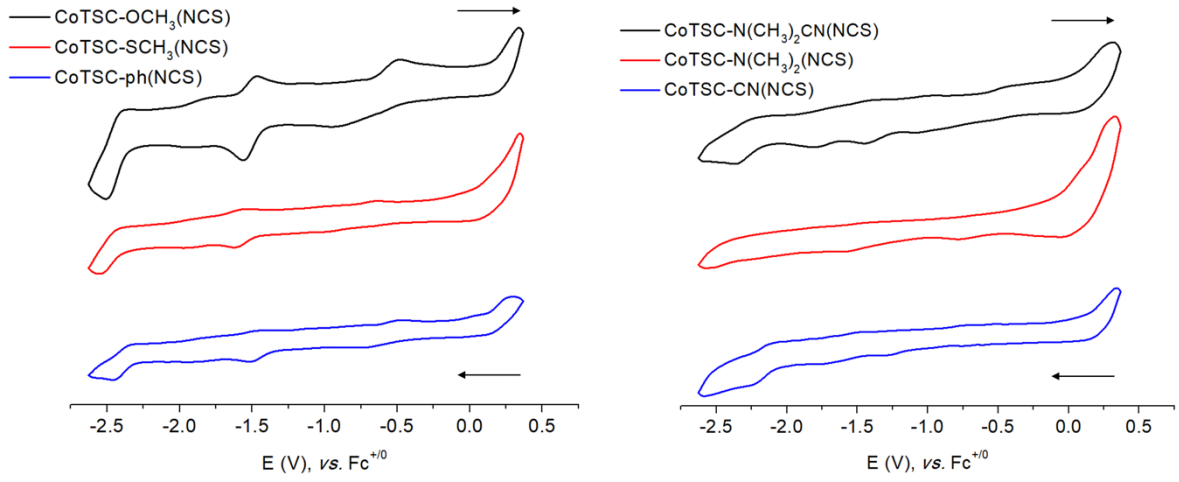

Figure 20. *Cyclic voltammograms of CoTSC-R series (V vs. $Fc^{+/0}$). Conditions: concentration 1 mM at a stationary 1.5 mm glassy carbon electrode in DMF + 0.1 M NBu_4PF_6 using a 500 mV s^{-1} scan rate.*

5.3.2 Photocatalytic hydrogen production

As a follow-up to our photocatalytic investigation with the series of nickel complexes, we investigate the cobalt-based complexes under the same conditions. We prepared aqueous solutions containing a 1:1 ratio of TCEP/ Asc as SED at pH= 5. Carbon dots were first tested as photosensitizers and combined with the cobalt complexes as catalytic centers but none of the resulting photocatalytic systems led to significant hydrogen production upon white led irradiation. When using the NCdots with the cobalt catalysts, subsequent hydrogen production was detected upon photo-irradiation of the solutions (Figure 21).

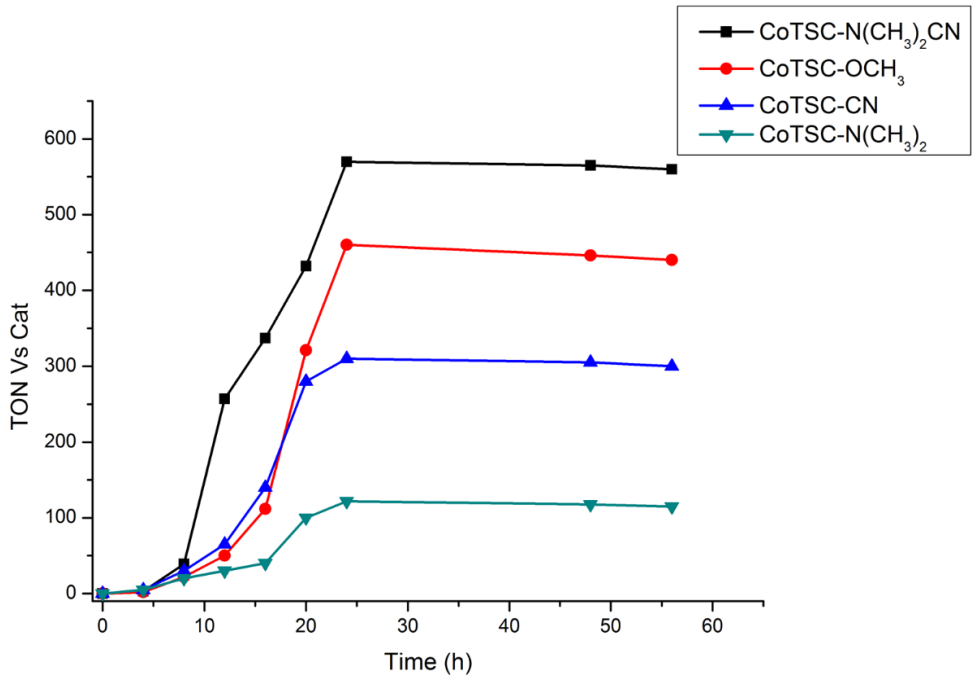

Figure 21. *Photocatalytic hydrogen production plots of 10 mg NCdot with 100 nmol cobalt catalysts: CoTSC-N(CH₃)₂CN(NCS); CoTSC-OCH₃(NCS); CoTSC- CN(NCS); CoTSC-N(CH₃)₂(NCS). All photocatalytic experiments were performed in aqueous TCEP/Asc (1:1) 0.1 M each at pH = 5. All the results presented in the hydrogen production plots are the average values of three independent measurements (within 5-10% error).*

To determine the optimum quantity of complex to be used in the new photocatalytic systems, we used five different concentrations to prepare our samples. For solutions containing 20 nmol of complex, no photo-evolved H_2 was detected. When we increased the quantity of catalyst to 50 nmol, an adequate amount of hydrogen was produced in these conditions. We further increased the catalyst quantity to 100 nmol which drastically improved the turnover number value versus the catalyst, TON_{cat}. Successive increase in catalyst quantity to 150 and 200 nmol did not further improve the total TON_{cat} values (Figure 22). For these reasons, the following photocatalytic experiments were performed using 100 nmol of each cobalt complex.

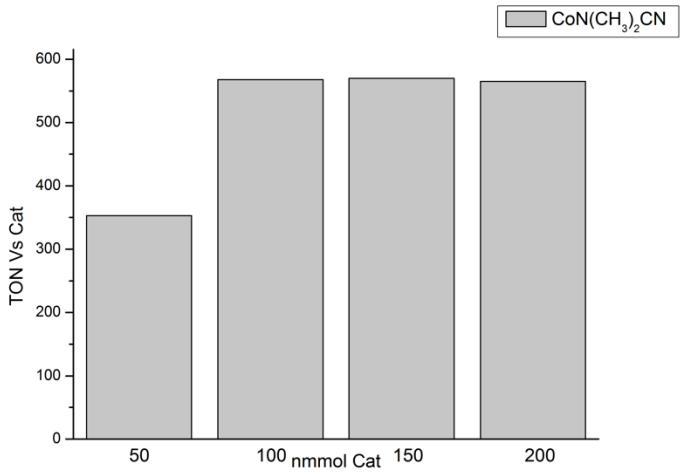

Figure 22. *Photocatalytic hydrogen production plots of 10 mg NCdots in three different amounts of the catalyst CoTSC-N(CH₃)₂CN(NCS): 50, 100, 150 and 200 nmol. The photocatalytic experiments were conducted in aqueous TCEP/Asc (1:1) 0.1 M each at pH = 5. All the results presented in the hydrogen production plots are the average values of three independent measurements (within 5-10% error).*

For the cobalt series, the best catalyst of the group was found to be the asymmetrical complex bearing dimethylamino and cyano groups, CoTSC-N(CH_3)$_2$CN(NCS) (Figure 21). The system reached a plateau at about 24 hours, in a faster manner compared to the average 30 hours needed for the nickel series. The results of the optimised photocatalytic experiments using all cobalt complexes are given in Table 6 and Figure 23. The best noble metal-free photocatalytic system contained 10 mg of NCdots, 0.1 M of TCEP / Asc in a 1:1 ratio and 100 nmol of CoTSC-N(CH_3)$_2$CN(NCS) in an aqueous solution at pH=5 under white led irradiation.

Table 6. *Photocatalytic performances of CoTSC-R(NCS) series of catalysts. All the results presented are the average values of three independent measurements (within 5-10% error).*

Catalyst	TON_{cat}
CoTSC-N(CH₃)₂CN(NCS)	570
CoTSC-OCH₃(NCS)	460
CoTSC-CN(NCS)	310
CoTSC-N(CH₃)₂(NCS)	122

Looking at the TON_{cat} values, the relative photocatalytic activity of the cobalt series is the following: CoTSC-N(CH_3)$_2$CN)NCS) > CoTSC-OCH_3(NCS) > CoTSC-CN(NCS) > CoTSC-N(CH_3)$_2$(NCS). Focusing on the ligand nature, the cobalt series performs in the same way as

the nickel family but displays increased hydrogen production with exception of the dimethylamino containing ligand. Even though it was found to be the best performing catalyst as a nickel complex, it is the worst performing one in the cobalt series with TON_{cat} = 122 and 148 for CoTSC-N$(CH_3)_2$(NCS) and NiTSC-N$(CH_3)_2$, respectively.

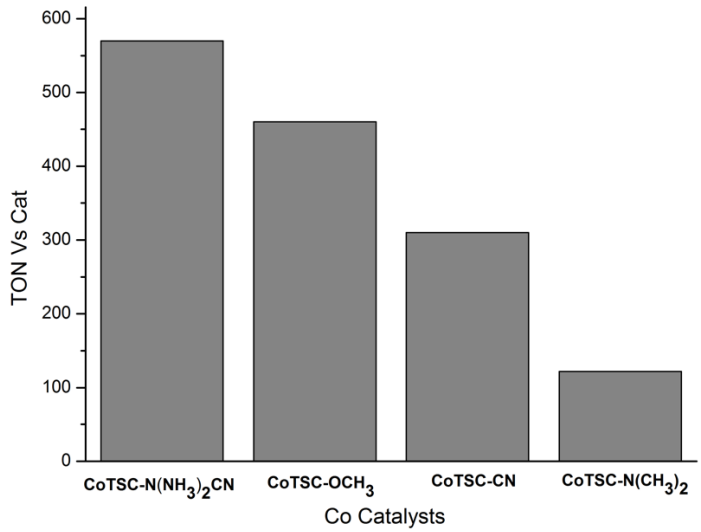

Figure 23. *Turnover number vs catalyst upon irradiation of 10 mg NCdots in the presence of 100 nmol of the CoTSC-R(NCS) series in aqueous TCEP/Asc (1:1) 0.1 M each at pH = 5. All the results presented in the hydrogen production plots are the average values of three independent measurements (within 5-10% error).*

When comparing the two series, it becomes obvious that the cobalt series greatly improved the catalytic performances with respect to the nickel series. The asymmetrical and the methoxy complexes display catalytic performances 8 times larger when transitioning from a nickel center to a cobalt one, whereas the performances of the cyano one is about 6 times larger.

As for the nickel complexes, we also performed control experiments with the cobalt series. Mercury was introduced in the system to provide proof that the catalysis is a result of the molecular complexes and not due to the formation of any nanoparticles. Upon the addition of a few Hg drops, no change in hydrogen production was observed. Lastly, replacing the cobalt complexes for $Co(NCS)_2$ did not provide any H_2 photo-evolution.

This study is still ongoing as we need to investigate the photocatalytic properties of CoTSC-ph(NCS) and CoTSC-SCH_3(NCS) and to get insight into the reaction mechanism and to better understand how the inclusion of cobalt helped our system to produce hydrogen with improved rates.

5.4 Conclusions

In the present study, we tested the hydrogen production capabilities of a new photocatalytic system composed of carbon dot materials with a series of noble metal-free complexes based on bisthiosemicarbazone ligands. The complex series differ in the para substituent of the phenyl ring, with a wide range of electron donating groups being employed. We evaluated their catalytic capabilities and investigated how the system can optimize its production by considering different sacrificial electron donors, photosensitizers and light sources. Nitrogen-doped carbon dots as light harvesters combined with the NiTSC-N$(CH_3)_2$ as the catalytic center in an aqueous solution at pH= 5 using TCEP/Asc as SED in a 1:1 ratio for 30 hours of reaction yielded a TON_{cat} of 148 and was identified as the best performing photocatalytic system. Our results indicated that the chemical nature of the substituent in the para position of the ligand indeed influences the photocatalytic behavior of the systems and their hydrogen evolution performances. However, consistently with our previous study on the electrocatalytic performances[24] of these complexes, it remains difficult to find a clear rationale between the catalysis parameters, i.e. the TON values, and the electron donating ability of the substituents (-N$(CH_3)_2$ > -N$(CH_3)_2$CN > -OCH_3 > -SCH_3 > -ph > -CN).

On the other hand, the cobalt series crowned a new complex as a component of the best photocatalytic system and the CoTSC-N$(CH_3)_2$(NCS) outshined the rest of the series with a TON_{cat} of 570 in about 24 hours of catalysis. Two complexes have yet to be tested for their photocatalytic capabilities to conclude on the role of the metal of the catalytic center with respect to photocatalysis. Further investigation on the cobalt series will likely provide us with better information on how we can improve our noble metal-free catalytic system towards even more efficient light-induced hydrogen production.

5.5 Experimental section and supplementary data

5.5.1 Synthesis and Characterization

General synthetic protocol of cobalt complexes:

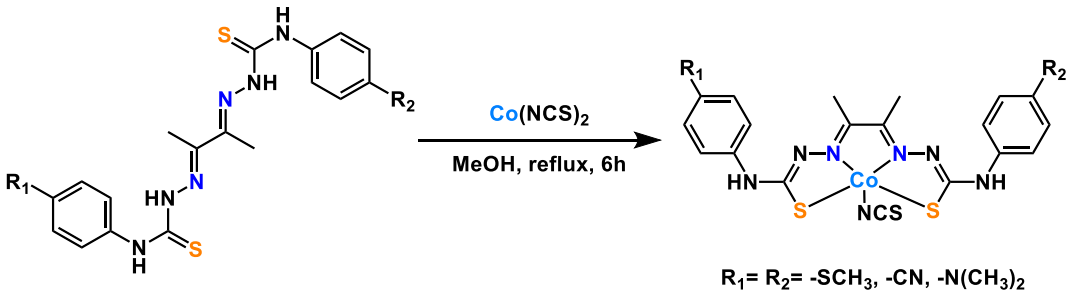

In a solution of methanol, 1 equivalent of the corresponding ligand is added with 1.5 equivalents of $CO(NCS)_2$. The mixture is refluxed. After 6 hours, the reaction is cooled to 0°C with a water bath and water is added. The mixture is filtered and washed with cold water and cold methanol. A neutral alumina (Al_2O_3) liquid chromatography column is prepared to purify the desired compound. CoTSC-OCH_3 was synthesized according to literature.[23]

*2,3-di(4-(dimethylaminophenylthiosemicarbazone) butane cobalt (*CoTSC-$N(CH_3)_2$(NCS))

From 2,3-di(4-(dimethylaminophenylthiosemicarbazone) butane (0.085 mmol, 40 mg) in 3 ml methanol and $Co(NCS)_2$ (0.102 mmol, 18 mg) in solution in 2 ml methanol. Alumina column with dichloromethane/trimethylamine 1%. A dark brown solid (21 mg, 43 %) was obtained after filtration and washing with two portions of methanol.

HR ESI-MS: $[M\text{-}NCS^-]^+$ calculated for $C_{22}H_{28}N_8S_2Co$: 527.1205, observed: 527.1216.

2,3-di(4-(cyanophenylthiosemicarbazone) butane cobalt (CoTSC-CN(NCS))

From 2,3-di(4-(cyanophenylthiosemicarbazone) butane (0.092 mmol, 40 mg) in 3 ml methanol and $Co(NCS)_2$ (0.105 mmol, 20 mg) in solution in 2 ml methanol. Alumina column with dichloromethane/methanol 2%. A dark brown solid (18 mg, 37 %) was obtained after filtration and washing with two portions of methanol.

HR ESI-MS: $[M\text{-}NCS^-]^+$ calculated for $C_{20}H_{16}N_8S_2Co$: 491.0266, observed: 491.0263.

2-(4-(dimethylaminophenylthiosemicarbazone), 3-(4-(cyanophenylthiosemicarbazone) butane nickel (II) (CoTSC-$(N(CH_3)_2)$CN(NCS))

From 2-(4-(dimethylaminophenylthiosemicarbazone), 3-(4-(cyanophenylthiosemicarbazone) butane (0.088 mmol, 40 mg) in 3 ml methanol and $Co(NCS)_2$ (0.106 mmol, 19 mg) in solution in 2 ml methanol. Alumina column with dichloromethane/ethanol/triethylamine 97:2:1. A dark brown solid (13 mg, 26 %) was obtained after filtration and washing with two portions of methanol.

HR ESI-MS: $[M\text{-}NCS^-]^+$ calculated for $C_{21}H_{22}N_8S_2Co$: 509.0735, observed: 509.0740.

2,3-di(phenylthiosemicarbazone) butane cobalt (CoTSC-ph(NCS))

From 2,3-di(phenylthiosemicarbazone) butane (0.104 mmol, 40 mg) in 3 ml methanol and $Co(NCS)_2$ (0.125 mmol, 22 mg) in solution in 2 ml methanol. Alumina column with dichloromethane/ethanol 2%. A dark brown solid (26 mg, 51 %) was obtained after filtration and washing with two portions of methanol.

HR ESI-MS: $[M + (M\text{-}NCS^-]^+$ calculated for $C_{37}H_{36}N_{13}S_5Co_2$: 940.479, observed: 940.0473.

2,3-di(4-(methylmercaptophenylthiosemicarbazone) butane cobalt (CoTSC-SCH_3(NCS))

From 2,3-di(4-(methylmercaptophenylthiosemicarbazone) butane (0.084 mmol, 40 mg) in 3 ml methanol and $Co(NCS)_2$ (0.101 mmol, 18 mg) in solution in 2 ml methanol. Alumina column with dichloromethane/methanol 1%. A dark brown solid (24 mg, 48 %) was obtained after filtration and washing with two portions of methanol.

HR ESI-MS: $[M\text{-}NCS^-]^+$ calculated for $C_{20}H_{22}N_6S_4Co$: 533.0115, observed: 533.0118.

2,3-di(4-(methoxyphenylthiosemicarbazone) butane cobalt (CoTSC-OCH_3(NCS))

From 2,3-di(4-(methoxyphenylthiosemicarbazone) butane (0.090 mmol, 40 mg) in 3 ml methanol and $Co(NCS)_2$ (0.107 mmol, 19 mg) in solution in 2 ml methanol. Alumina column with dichloromethane/ethanol 3%. A dark brown solid (27 mg, 53 %) was obtained after filtration and washing with two portions of methanol.

HR ESI-MS: $[M + (M\text{-}NCS)^-]^+$ calculated for $C_{41}H_{44}N_{13}S_5Co_2$: 1060.0901, observed: 1060.0897.

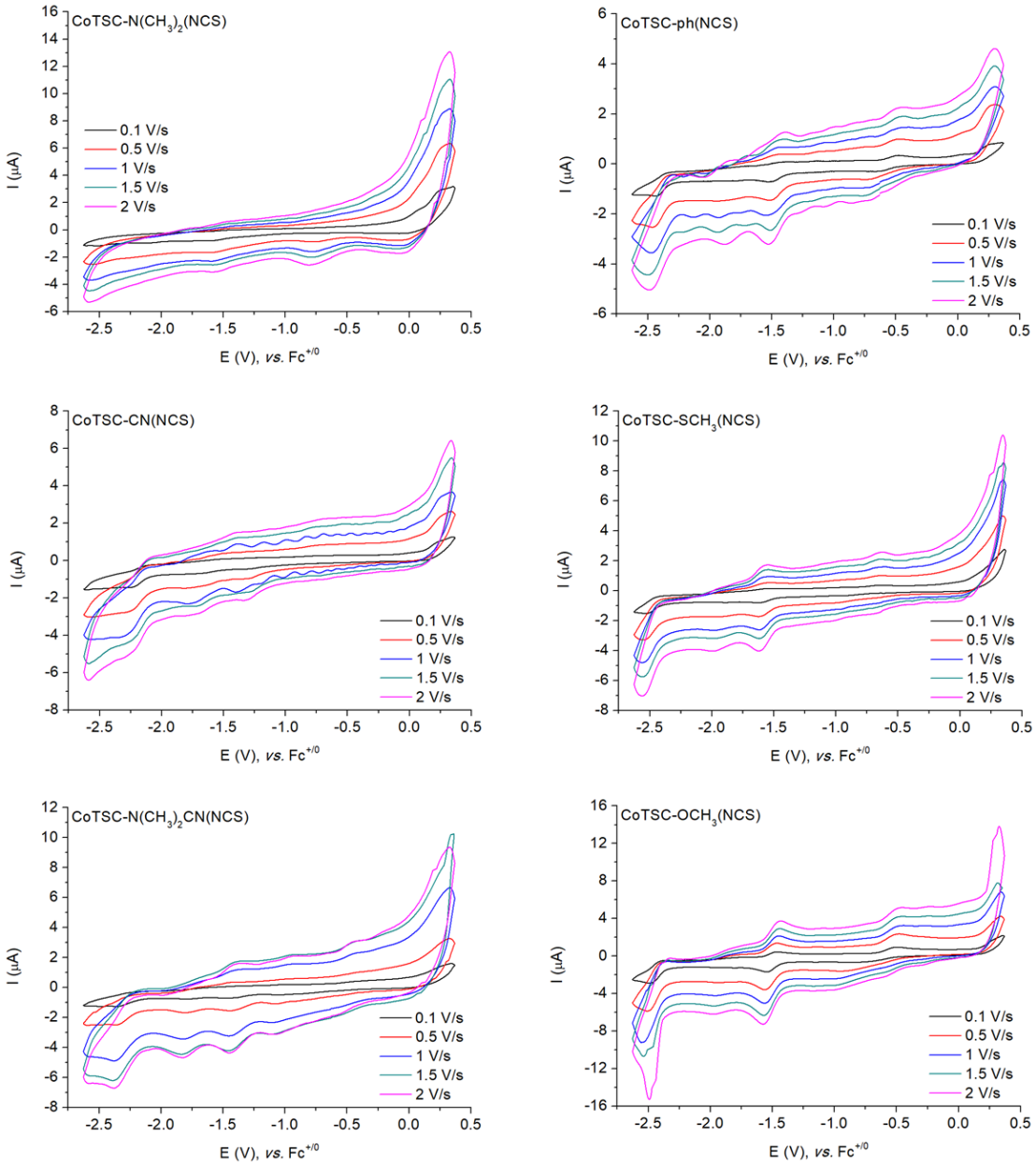

Figure 24. *Cyclic voltammograms of CoTSC-R(NCS) series (V vs. $Fc^{+/0}$). Conditions: concentration 1 mM at a stationary 1 mm glassy carbon electrode in DMF with 0.1 M NBu_4PF_6.*

5.5.2 Photocatalytic HER and Photophysical Measurements

The photocatalytic reactions were performed in a 3 ml aqueous solution of TCEP/Asc (1:1) 0.1 M each at pH 5.0. The TCEP and Asc are both serving as reversible sacrificial electron donors. In all experiments 10 mg of the photosensitizer was used. The appropriate amount of catalyst was added in the reaction vessel from a stock solution of each nickel catalyst dissolved in DMSO. A 10 ml flask was used with a rubber septum where the mixture was purged with nitrogen for 15 min in order to remove oxygen. The reaction mixture was continuously stirred with irradiated with a 100 W white led emitting lamp. At certain time intervals 100 μl was removed from the headspace of the flask and was analyzed by Shimadzu GC 2010 plus chromatograph with a TCD detector and a molecular sieve 5 Å column (30 m - 0.53 mm) in order to measure the amount of hydrogen that was produced. The H_2 amount produced was quantified using a calibration curve and in all cases, the reported H_2 production and the turnover number (TON) is the average of three independent experiments.

The UV-vis absorption spectra of all compounds in solution were obtained using a Shimadzu UV-1700 spectrophotometer in quartz cuvettes of 1 cm path-length. The emission spectra of all derivatives in solution were measured on a JASCO FP-6500 fluorescence spectrophotometer equipped with a red-sensitive WRE-343 photomultiplier tube (wavelength range: 200-850 nm).

References

1. Fujishima, A. & Honda, K. Electrochemical Photolysis of Water at a Semiconductor Electrode. *Nature* **238**, 37–38 (1972).
2. Ahmad, H., Kamarudin, S. K., Minggu, L. J. & Kassim, M. Hydrogen from photo-catalytic water splitting process: A review. *Renewable and Sustainable Energy Reviews* **43**, 599–610 (2015).
3. Liao, C.-H., Huang, C.-W. & Wu, J. C. S. Hydrogen Production from Semiconductor-based Photocatalysis via Water Splitting. *Catalysts* **2**, 490–516 (2012).
4. Lewis, N. S. & Nocera, D. G. Powering the planet: Chemical challenges in solar energy utilization. *Proc. Natl. Acad. Sci. U.S.A.* **103**, 15729–15735 (2006).
5. Ladomenou, K. *et al.* Photochemical hydrogen generation with porphyrin-based systems. *Coordination Chemistry Reviews* **304–305**, 38–54 (2015).
6. Wang, Y. *et al.* Development of solid-state electrolytes for sodium-ion battery–A short review. *Nano Materials Science* **1**, 91–100 (2019).
7. Watanabe, M. Dye-sensitized photocatalyst for effective water splitting catalyst. *Science and Technology of Advanced Materials* **18**, 705–723 (2017).
8. Nikolaou, V., Charalambidis, G. & Coutsolelos, A. G. Photocatalytic hydrogen production of porphyrin nanostructures: spheres *vs.* fibrils, a case study. *Chem. Commun.* **57**, 4055–4058 (2021).
9. Balzani, V., Credi, A. & Venturi, M. Photochemical Conversion of Solar Energy. *ChemSusChem* **1**, 26–58 (2008).
10. Eckenhoff, W. T. & Eisenberg, R. Molecular systems for light driven hydrogen production. *Dalton Trans.* **41**, 13004 (2012).
11. Probst, B., Guttentag, M., Rodenberg, A., Hamm, P. & Alberto, R. Photocatalytic H_2 Production from Water with Rhenium and Cobalt Complexes. *Inorg. Chem.* **50**, 3404–3412 (2011).
12. Lo, W. K. C. *et al.* Synthesis, Characterization, and Photocatalytic H_2 -Evolving Activity of a Family of $[Co(N4Py)(X)]^{n+}$ Complexes in Aqueous Solution. *Inorg. Chem.* **55**, 4564–4581 (2016).
13. Zhang, H. *et al.* A novel dinuclear cobalt-bis(thiosemicarbazone) complex as a cocatalyst to enhance visible-light-driven H2 evolution on CdS nanorods and a mechanism discussion. *Journal of Photochemistry and Photobiology A: Chemistry* **426**, 113771 (2022).
14. Droghetti, F., Lucarini, F., Molinari, A., Ruggi, A. & Natali, M. Recent findings and future directions in photosynthetic hydrogen evolution using polypyridine cobalt complexes. *Dalton Trans.* **51**, 10658–10673 (2022).
15. Han, Z. & Eisenberg, R. Fuel from Water: The Photochemical Generation of Hydrogen from Water. *Acc. Chem. Res.* **47**, 2537–2544 (2014).
16. Dalle, K. E. *et al.* Electro- and Solar-Driven Fuel Synthesis with First Row Transition Metal Complexes. *Chem. Rev.* **119**, 2752–2875 (2019).
17. Du, P. & Eisenberg, R. Catalysts made of earth-abundant elements (Co, Ni, Fe) for water splitting: Recent progress and future challenges. *Energy Environ. Sci.* **5**, 6012 (2012).

18. Jiang, W.-X., Xie, Z.-L. & Zhan, S.-Z. A photocatalytic system with a bis(thiosemicarbazonato)-nickel over CdS nanorods for hydrogen evolution from water under visible light. *Inorganic Chemistry Communications* **102**, 5–9 (2019).
19. Du, J., Yang, H., Wang, C.-L. & Zhan, S.-Z. A nickel(II) complex of 2,6-pyridinedicarboxylic acid ion, an efficient electro-catalyst for both hydrogen evolution and oxidation. *Molecular Catalysis* **516**, 111947 (2021).
20. Panagiotakis, S. *et al.* Efficient Light-Driven Hydrogen Evolution Using a Thiosemicarbazone-Nickel (II) Complex. *Front. Chem.* **7**, 405 (2019).
21. Ladomenou, K., Landrou, G., Charalambidis, G., Nikoloudakis, E. & Coutsolelos, A. G. Carbon dots for photocatalytic H_2 production in aqueous media with molecular Co catalysts. *Sustainable Energy Fuels* **5**, 449–458 (2021).
22. Straistari, T. *et al.* A Thiosemicarbazone-Nickel(II) Complex as Efficient Electrocatalyst for Hydrogen Evolution. *ChemCatChem* **9**, 2262–2268 (2017).
23. Straistari, T. *et al.* Hydrogen Evolution Reactions Catalyzed by a Bis(thiosemicarbazone) Cobalt Complex: An Experimental and Theoretical Study. *Chem. Eur. J.* **24**, 8779–8786 (2018).
24. Papadakis, M. *et al.* Ligand-based electronic effects on the electrocatalytic hydrogen production by thiosemicarbazone nickel complexes. *Dalton Trans.* **49**, 5064–5073 (2020).

Chapter 6: General conclusions and perspectives

This doctoral dissertation aimed to validate the use of metal-organic complexes based on redox-active thiosemicarbazone ligands as catalysts for hydrogen evolution reactions. Inspired by our previous work on a nickel thiosemicarbazone complex bearing a methoxy group, we tried to enhance its catalytic performances by tailoring the complex in different aspects.

In Chapter 2, we investigated the replacement of the methoxy group by three other chemical groups possessing different electron donating abilities ranging from a very strong electron donor, the dimethylamino group, to the electron withdrawing abilities of the cyano group. This investigation gave rise to four new compounds that were compared with the original complex for electrocatalytic hydrogen evolution. One of these new nickel catalysts, bearing a thiomethyl moiety, took the spotlight by significantly improving the capabilities of the system almost doubling the total hydrogen production and enhancing the catalysis rate of the targeted reaction. Detailed analysis and benchmarking of the performances of the thiomethyl-based complex compared against other well know electrocatalysts from the literature, showed great promise in regard to its overpotential requirements.

As a continuation of our work, in Chapter 3 we investigated the importance of the position of the methoxy substituent on the bisthiosemicarbazone ligand. Our investigation lead us to synthesize and test a new family of compounds with the methoxy moiety existing in different positions on the phenyl ring. Our results clearly show an improved hydrogen production together with larger TOF values. Three of the six new complexes gave very interesting results outperforming both the parent nickel compound and the best catalyst in our previous study. Our results highlighted the complex having the methoxy substituent in ortho position as the best system for electrocatalytic hydrogen evolution reaction.

Another angle on our pursuit of an optimum electrocatalyst for hydrogen evolution was adopted in Chapter 4 and brought us to use a trinuclear complex with a ligand structurally very similar to our reference complex having para methoxy substituents. In this study, we investigated the influence of having more than one possible catalytic centers and how their implementation changed the overall performance of the complex toward hydrogen production. Although the compound started showing great promise with an increased total production and catalysis rate, further investigation showed that it only involves one catalytic center with the other two metals taking the role of electron reservoirs. Moreover, two main drawbacks were identified as our idea resulted in the increase of the driving force of the reaction together with the a decreased stability in catalytic conditions.

Lastly, we tested in Chapter 5 the capabilities of our new nickel catalysts to behave as catalytic centers in a new photocatalytic system employing metal-free photosensitizers in the

form of carbon dots. Upon testing many different experimental parameters, we optimized the working conditions and our system was able to produce hydrogen when light-irradiated. Our results identified the complex having para dimethylamino substituents as the best performing catalyst within the group of studied compounds. As this idea proved to be valid, we tried to further improve our system by replacing nickel with cobalt, a more widely used metal in the field of photocatalysis. Although this investigation is still ongoing, our preliminary results show great promise with most cobalt-based photocatalytic systems outperforming the entire nickel series.

As a general conclusion, it becomes clear that complexes based on thiosemicarbazone ligands have the ability to work as both electro- and photo-catalysts for hydrogen evolution. Our endeavors on improving the system by tuning the electronic properties of the ligand through chemical or structural tailoring gave fruitful results as we managed to boost our performances. However, can we go beyond the results presented in this manuscript? Did we reach the full capabilities of our systems and can we consider that we have reached optimum catalysis? The answer is definitively no as there is still a plethora of possibilities that lie ahead of us. Up to now, we have been mostly dealing with changes to the outer part of our ligands. There are countless chemical changes we can perform to modify our ligands and regulate the electronic properties of the resulting complexes. The complete substitution of the whole phenyl ring is one of many possibilities that can affect our catalysis. However, the most interesting alteration might relate with the first coordination sphere of our complexes. All our compounds have two nitrogen and two sulphur coordinating with the metal centers. What would happen if one sulphur is replaced by one oxygen or if all four moieties become nitrogen-based while keeping the rest of the ligand structure intact? Nevertheless, the possibilities do not stop at a molecular level. Since our complexes are active in both photo- and electro-catalysis, why not combine the best of both domains by implementing them into a photoelectrochemical system? Lastly, as the lifetime of a catalytic system is one of the most important characteristics, employing a different strategy and shifting from a homogeneous system to a heterogeneous one could lengthen the life of our reactions. We could think of designing devices that could result in molecular hydrogen evolution for an extended period when in presence of a proton source. These are just some of the perspectives of this work and some of them will definitively be considered in the group to move forward with this hot topic.

Appendix

Materials

- ^{1}H NMR spectra were recorded on Bruker 400 and 300 MHz Avance III nanobay. Chemical shifts for ^{1}H NMR spectra refer to TMS or the residual protonated solvent.

- 2D DOSY experiments were acquired on a BRUKER AVANCE III 600MHz NMR spectrometer with a Double Resonance Broad Band Probe (BBFO) at 300K, using a pulse sequence that incorporated bipolar gradient pulses and a longitudinal eddy current delay (LED). A total of 32 gradient values were lineary sampled from 6% to 95%. 32 scans were acquired with 32k data points, for a total acquisition time of ca. 60 min. The gradient pulse duration ($\partial/2$) and the diffusion time (Δ) were set to 1.8 ms and 150 ms, respectively, with a gradient recovery delay of 0.1 ms and a LED of 5 ms. The DOSY spectra were simply obtained by using the single-exponential fitting routine of the EDDOSY feature of the TopSpin software from Bruker

- ESI-MS analyses were performed using a SYNAPT G2 HDMS (Waters) spectrometer equipped with a pneumatically assisted Atmospheric Pressure Ionization (API) source. Samples were ionized by positive electrospray mode as follows: ion-spray voltage: 2.8 kV; sampling cone: 20 V; nitrogen flux (nebulization): 100 L h−1. High resolution mass spectra (HRMS) were performed on a QStar Elite (Applied Biosystems SCIEX) spectrometer equipped with atmospheric pression ionization source (API) pneumatically assisted. The samples were placed in a methanol/3 mM ammonium acetate. The results were validated by three measurements.

- Continuous wave-EPR measurements were performed using a conventional Bruker EMX spectrometer operating in X-band with microwave frequencies of about 9.624 GHz. This spectrometer is equipped with a He-flow cryostat (ESR900) and a cryogen-free cooler (Bruker Stinger). The measurements were performed at 50K, a microwave power of 20 mW and modulation amplitude of 6.7G. A particular attention has been done to avoid the saturation of the signal while keeping a good signal noise ratio. The EPR spectrum simulations have been performed using Matlab program package Easyspin.

- UV-Vis spectra were recorded on a Varian Cary 50 spectrophotometer.

- Suitable crystals for the compounds were measured on a Rigaku Oxford Diffraction SuperNova diffractometer at room temperature at the CuKα radiation (λ=1.54184 Å). Data collection reduction and multiscan ABSPACK correction were performed with CrysAlisPro (Rigaku Oxford

Diffraction). Using Olex21 the structures were solved by direct methods with SHELXT2 and SHELXL3 was used for full matrix least squares refinement. All H-atoms were found experimentally and refined as riding atoms with Uiso parameters constrainted to 1.5Ueq (parent atoms) for the methyl groups and to 1.2Ueq (parent atom) for the other carbons and the amines.

- Magnetic characterization has been performed using a conventional SQUID magnetometer MPMS-XL from Quantum Design working at a magnetic field up to 5 T and temperature down to 2 K. The samples (powder) are filled in polypropylene sleeves then sealed in order to remove the maximum of dioxygen, which give the signal around 50 K (antiferromagnetic transition). Diamagnetic contribution of the sample holder was removed. To avoid field dependent effects (like ferromagnetic impurities), the temperature dependence of the susceptibility was recorder for three magnetic field: 0.1, 1 and 4T. Considering a non-interacting inter trimer paramagnetic centres, we fitted χT by $1/8.S(S+1).giso^2$ in CGS units.

- Cyclic voltammetry experiments were performed using a BioLogic SP300 potentiostat and a three-electrode set-up consisting of a glassy carbon working electrode, a platinum wire counter electrode and a Leakless (Ag/AgCl) reference electrode. Controlled potential electrolysis experiments were carried out in two-compartment cell. The working electrode used was a pool of mercury, separated from the coiled platinum wire counter electrode by a porous frit. Bulk electrolysis solutions were purged witch N_2 gas for at least 20 min prior to electrolysis and stirred throughout bulk electrolysis experiment. During the experiment, the cell was continuously purged with nitrogen (5 ml/min) and the output gas was analyzed at two minute intervals in a PerkinElmer Clarus 500 (Chapter 2 and 4) or a Shimadzu GC-2010 pro (Chapter 3) gas chromatographer using a previously described setup.

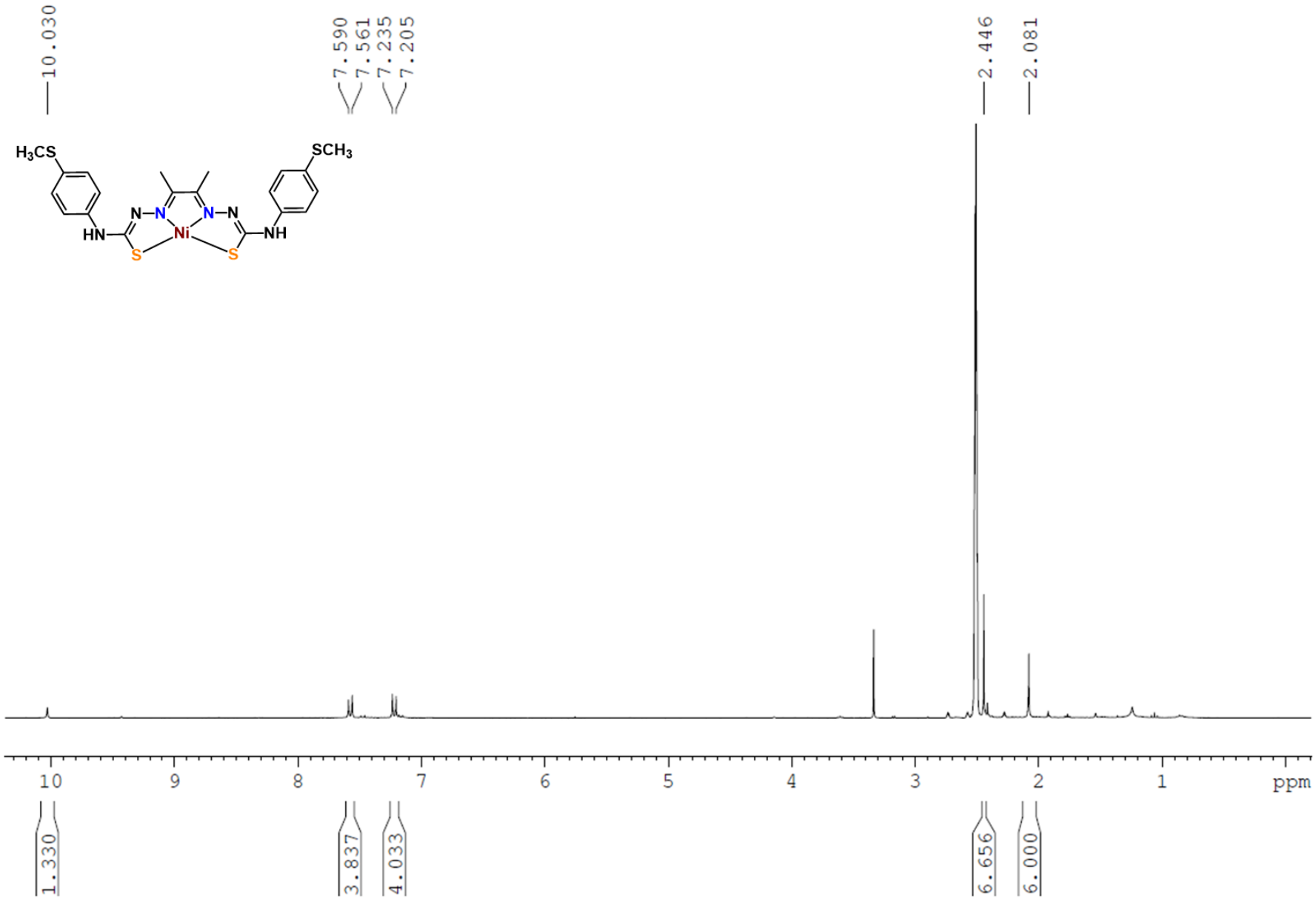
10.030
7.590
7.561
7.235
7.205
2.446
2.081
H3CS
SCH3
HN
NH
N
Ni
S
10
9
8
7
6
5
4
3
2
1
ppm
1.330
3.837
4.033
6.656
6.000

9.745
7.445
7.423
6.682
6.659
2.847
2.043
1.678
3.635
3.929
11.428
6.000
ppm

10.416
7.779
7.756
7.746
7.723
2.118
6.000
8.557
1.957
ppm
1
2
3
4
5
6
7
8
9
10
CN
NH
N
Ni
S
NC

ppm
1
2
3
4
5
6
7
8
9
10
1.067
1.066
4.049
2.219
2.164
6.156
2.909
3.000
2.853
2.107
2.051
10.296
9.916
7.784
7.762
7.741
7.719
7.434
7.421
6.684
6.661
CN
NH
N
S
Ni

ppm
1
2
3
4
5
6
7
8
9
10
6.000
5.933
2.046
1.938
2.059
1.918
2.017
1.993
3.827
8.651
7.711
7.691
7.108
7.104
7.087
7.069
7.065
7.035
7.032
7.015
6.941
6.938
6.921
6.903
6.900
OCH3
NH
N
N
Ni
S
S
N
N
HN
H3CO

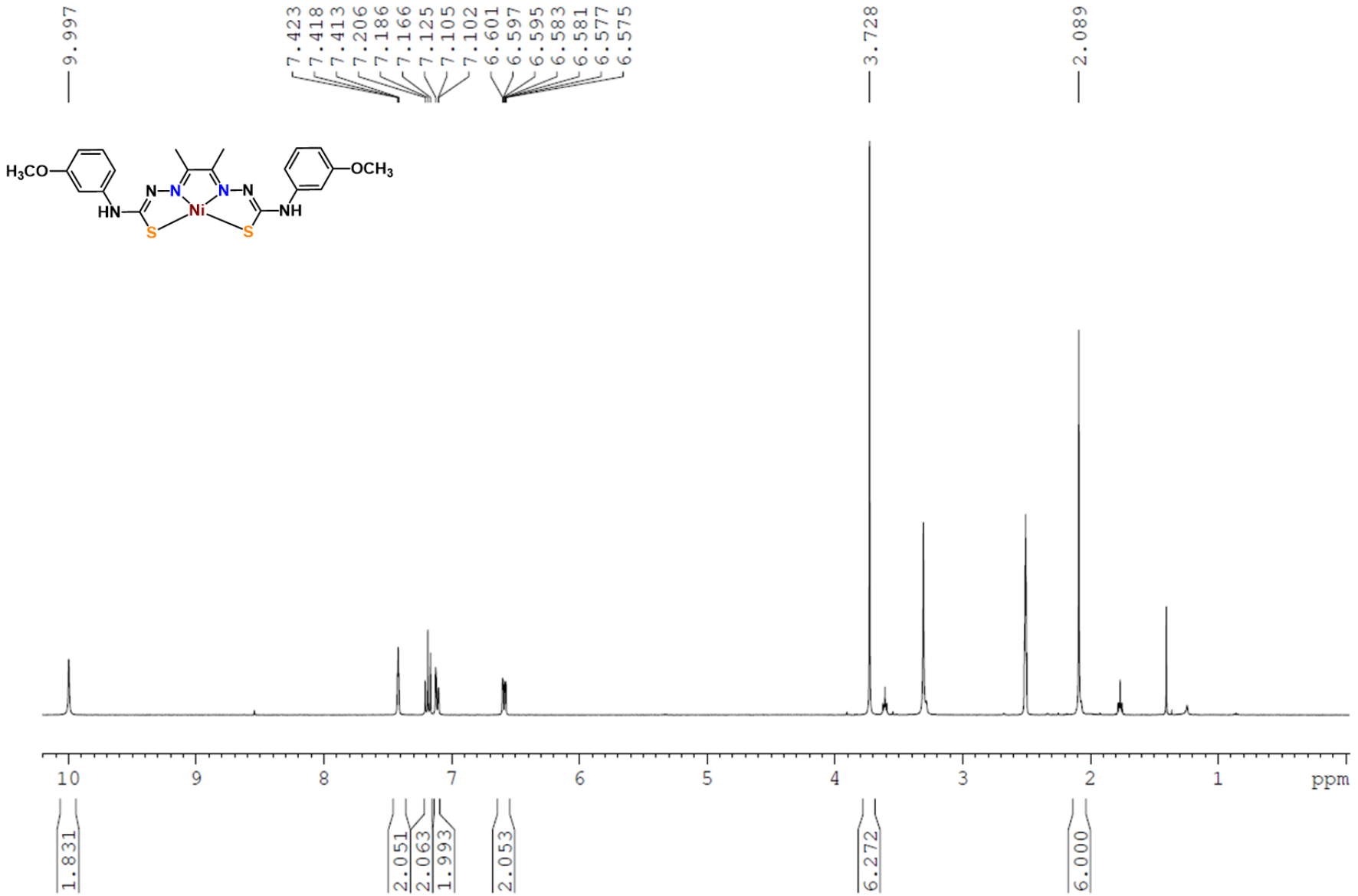
9.997
7.423
7.418
7.413
7.206
7.186
7.166
7.125
7.105
7.102
6.601
6.597
6.595
6.583
6.581
6.577
6.575
3.728
2.089
H3CO
OCH3
HN
NH
N
Ni
S
10
9
8
7
6
5
4
3
2
1
ppm
1.831
2.051
2.063
1.993
2.053
6.272
6.000

ppm
1
2
3
4
5
6
7
8
9
10
5.995
6.324
6.029
2.095
2.063
1.942
1.903
2.081
3.726
3.713
9.880
7.496
7.492
7.066
7.060
7.044
7.038
6.886
6.864
OCH3
OCH3
NH
N
N
Ni
S
S
N
N
HN
H3CO
H3CO

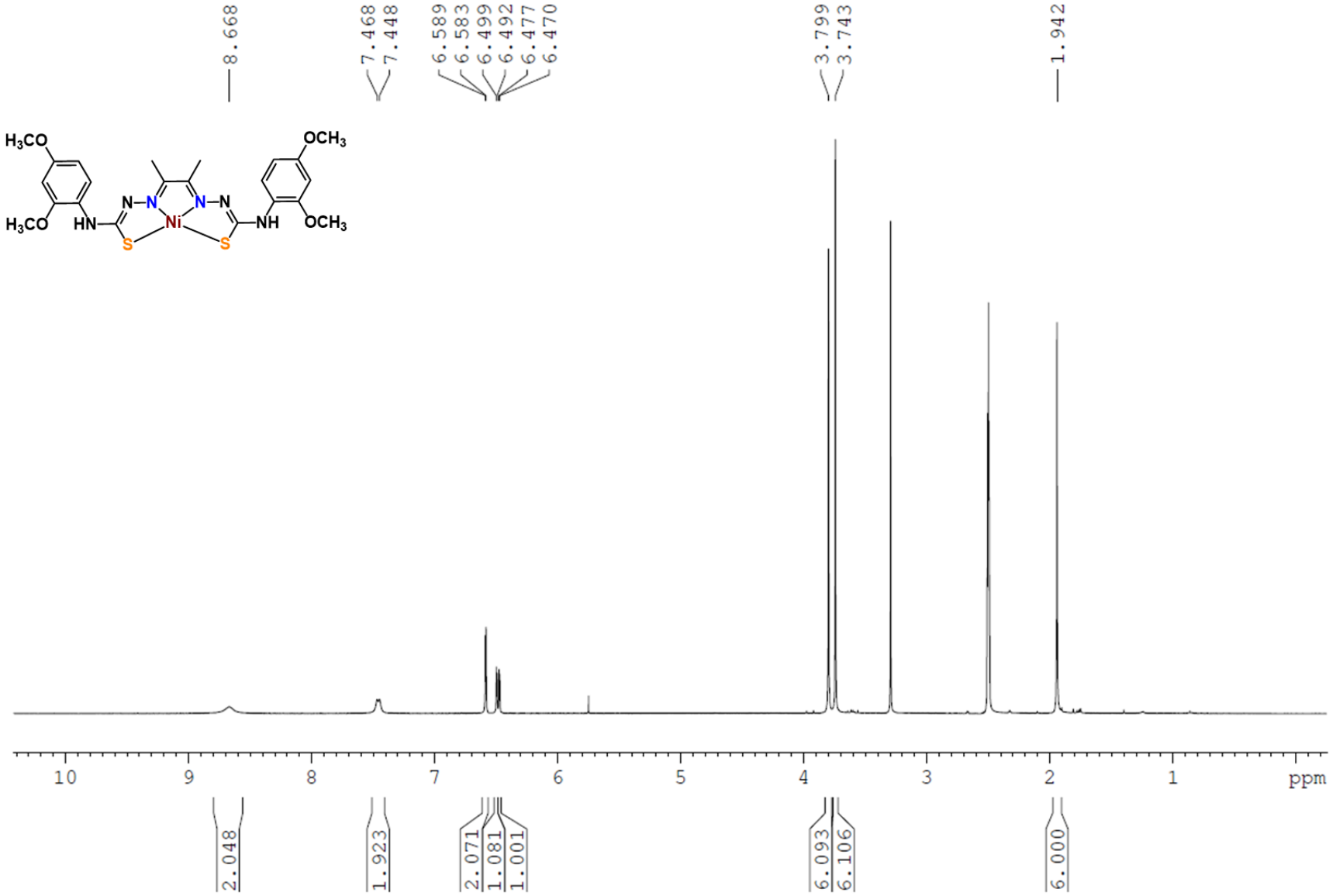
8.668
7.468
7.448
6.589
6.583
6.499
6.492
6.477
6.470
3.799
3.743
1.942
H3CO
OCH3
H3CO
HN
N–N
Ni
N–N
NH
OCH3
S
S
10
9
8
7
6
5
4
3
2
1
ppm
2.048
1.923
2.071
1.081
1.001
6.093
6.106
6.000

2.120
3.724
3.597
7.079
9.878
6.001
6.202
12.577
4.124
1.948
ppm
10.0
9.5
9.0
8.5
8.0
7.5
7.0
6.5
6.0
5.5
5.0
4.5
4.0
3.5
3.0
2.5
OCH3
OCH3
H3CO
H3CO
NH
HN
N
N
N
N
Ni
S
S

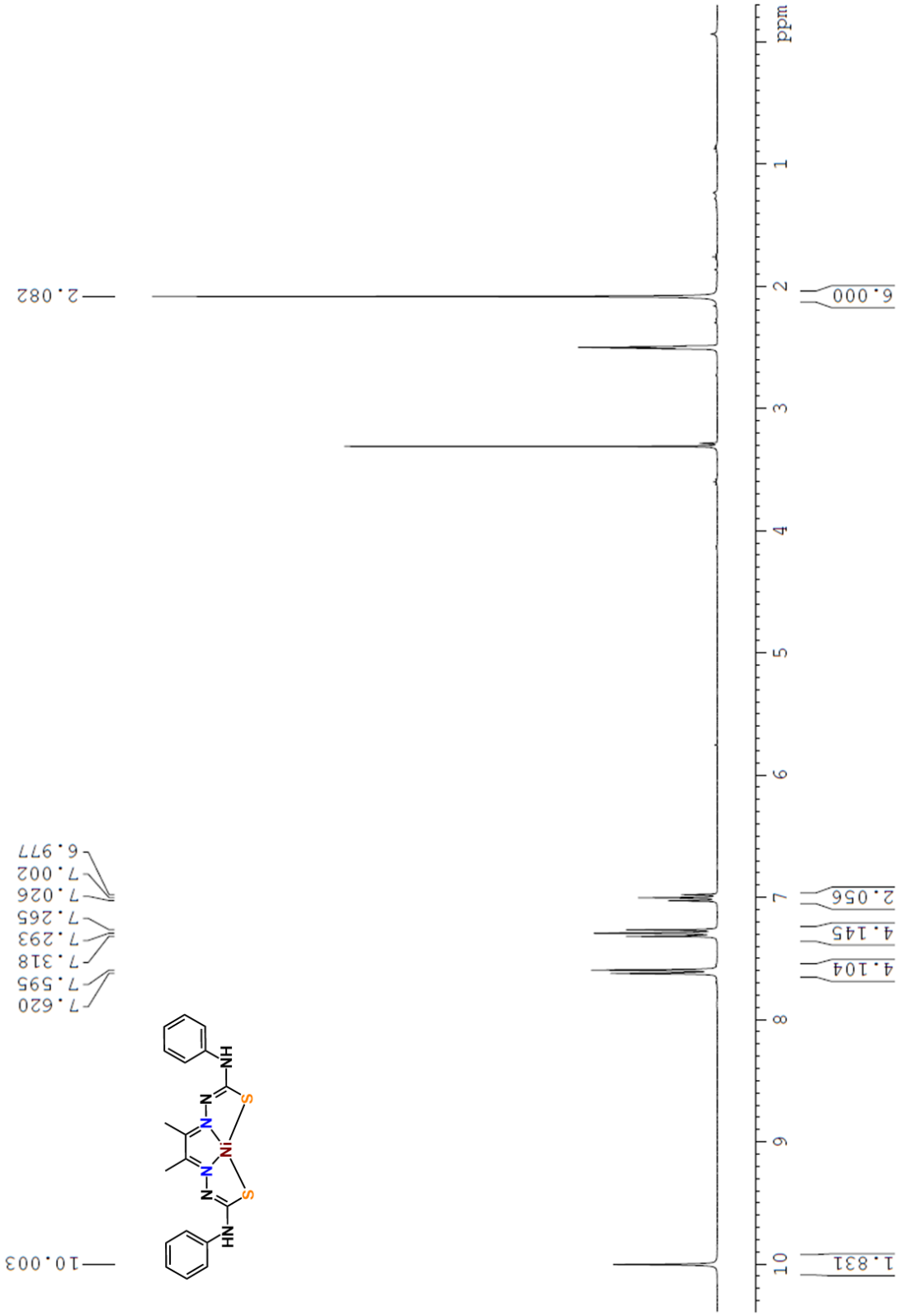
ppm
1
2
3
4
5
6
7
8
9
10
6.000
2.082
2.056
4.145
4.104
1.831
10.003
7.620
7.595
7.318
7.293
7.265
7.026
7.002
6.977
NH
N
N
Ni
N
N
S
S
NH

10.369
9.934
9.694
9.489
9.186
7.345
7.324
6.912
6.890
3.745
6.205
3.771
3.950
6.000
ppm
0
1
2
3
4
5
6
7
8
9
10
H3CO
OCH3

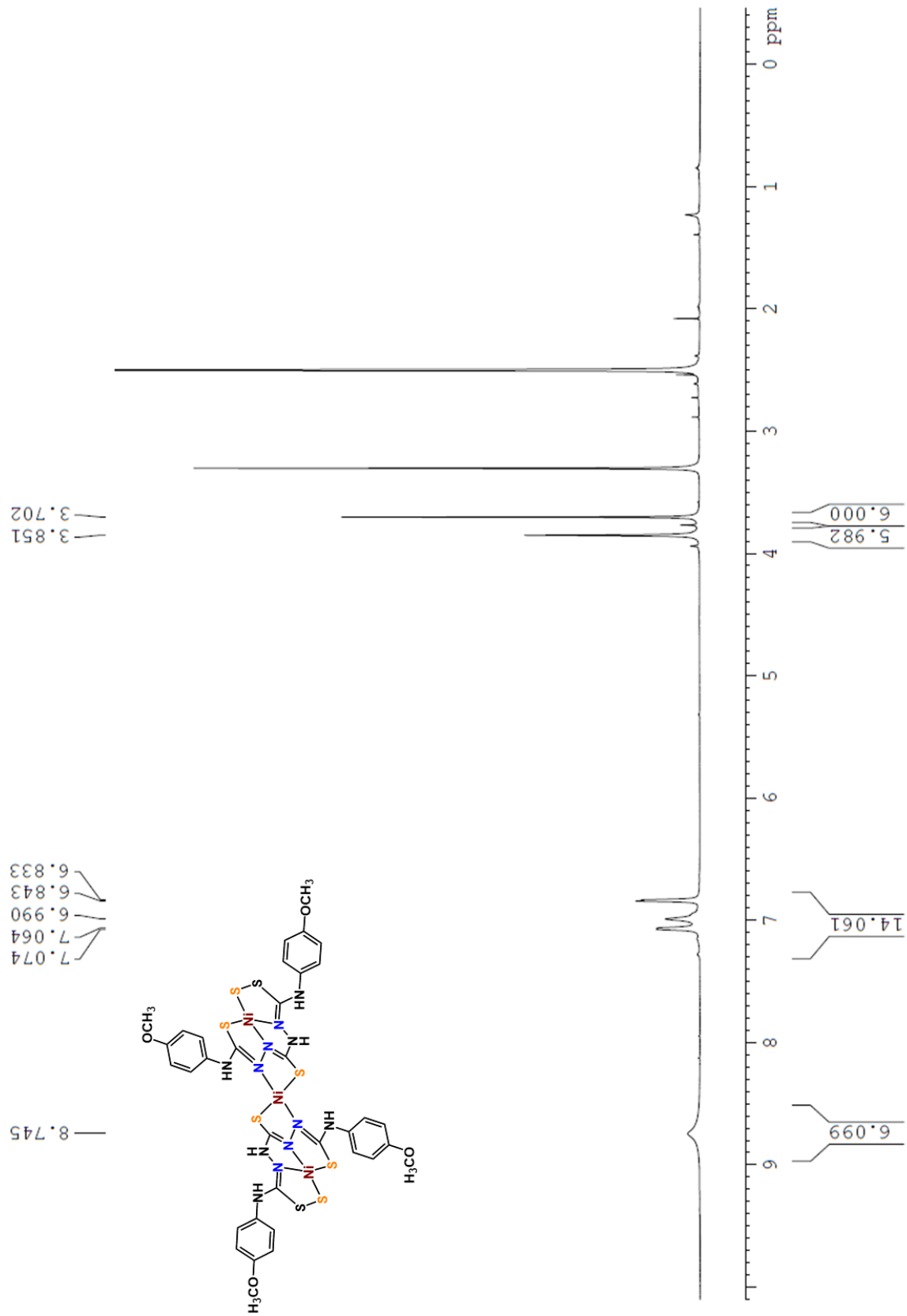

ppm
0
1
2
3
4
5
6
7
8
9
3.702
3.851
6.000
5.982
6.833
6.843
6.990
7.064
7.074
14.061
8.745
6.099

List of figures

Chapter 1: Introduction

Figure 1. Global electricity generation mix 2019.

Page 21

Figure 2. Example of alkaline water electrolysis cell.

Page 22

Figure 3. Schematic views of the active sites of [NiFe] (left), [FeFe] (middle) and [Fe]-only (left) hydrogenases.

Page 23

Figure 4. Graphical representation of hydrogen splitting and production catalyzed at the metallic active sites of [NiFe] and [FeFe] hydrogenase.

Page 24

Figure 5. The proposed catalytic mechanism for reversible hydrogen oxidation by the [NiFe] hydrogenase with the three proposed structures for the Ni-R state (red for Ni-H2 and blue for Fe-H2 binding).

Page 25

Figure 6. Examples of structural mimics of the [NiFe] hydrogenase active site, with the [Ni(μ-SR)$_2$Fe] cores highlighted in red.

Page 27

Figure 7. Examples of structural mimics of the [NiFe] hydrogenase active site, with the Ni(II) and Ru(II) metallic centers.

Page 27

Figure 8. Examples of catalytically active complexes containing nickel and iron as mimics of [NiFe] hydrogenase active site.

Page 28

Figure 9. Nickel and manganese containing complexes as mimics of [NiFe] hydrogenase active site.

Page 29

Figure 10. [NiFe] hydrogenase mimic in both unprotonated and protonated forms (highlighted in red).

Page 29

Figure 11. Nickel iron complexes coordinating phosphorus-containing ligands to the iron center in their intermediate hydride form (hydride highlighted in red).

Page 30

Figure 12. Structure of Manor and Rauchfuss models without and with the bridging hydride.

Page 30

Figure 13. Structure of the Duboc catalyst.

Page 31

Figure 14. Selected examples of iron porphyrin catalysts active for HER.

Page 32

Figure 15. Selected cobalt complexes reported as HER catalysts.

Page 33

Figure 16. Selected examples of copper catalysts active for HER.

Page 33

Figure 17. Macrocyclic nickel complexes reported as HER catalysts.

Page 34

Figure 18. Structures of complexes coordinating nickel with sulphur-containing ligands.

Page 35

Figure 19. Nickel complexes with phosphine ligands.

Page 35

Figure 20. Structure of the Dubois complex.

Page 36

Figure 21. First generation thiosemicarbazone-based catalysts for HER.

Page 37

Figure 22. Second-generation thiosemicarbazone-based catalystsfor HER.

Page 38

Figure 23. Structures of the nickel, cobalt and palladium bisthiosemicarbazone catalysts active for HER.

Page 38

Figure 24. Graphical representation of water electrolysis designed by International PtX Hub.

Page 39

Figure 25. a) Graphical representation of the electrochemical cell. b) Example of cyclic voltammogram of a given complex. c) Example of an electrocatalytic voltammogram for the same complex in the presence of a proton source.

Page 40

Figure 26. Example of earliest event and maximum current of catalytic wave highlighted with green arrows.

Page 41

Figure 27. a) Example of current recorded during electrolysis and converted into charge over time b) Example of evolved hydrogen measured over time by gas chromatography.

Page 41

Figure 28. Structure of complexes studied in this work.

Page 44

Chapter 2: Ligand chemical tailoring of thiosemicarbazone nickel complexes for electrocatalytic hydrogen production

Figure 1. Structures of NiTSC-R series derived from the parent NiTSC-OCH_3 complex.

Page 55

Figure 2. X-ray crystal structure of NiTSC-SCH_3 (top) and NiTSC-CN (bottom) complexes.

Page 56

Figure 3. UV-vis spectra of the NiTSC-R series including the NiTSC-OCH_3 reference complex.

Page 57

Figure 4. Cyclic voltammograms of NiTSC-R series (V vs. $Fc^{+/0}$). Conditions: concentration 1 mM at a stationary 1.5 mm glassy carbon electrode in DMF (0.1 M NBu_4PF_6) using a 500 mV/s scan rate.

Page 58

Figure 5. Successive cyclic voltammograms recorded at a glassy carbon as working electrode of a 1 mM solution of NiTSC-SCH_3 complex in DMF (0.1 M NBu_4PF_6) in the presence of increasing amounts of TFA. The black dotted curve shows the CV of 100 mM TFA in the absence of complex under the same conditions. Scan rate: 500 mV/s.

Page 61

Figure 6. Successive cyclic voltammograms recorded after electrocatalysis upon washing the glassy carbon electrode and immersion into a fresh solution of DMF (0.1 M NBu_4PF_6, black line) and in the presence of 60 mM of TFA (blue line). Scan rate: 500 mV/s.

Page 62

Figure 7. Coulometry of the NiTSC-R series during bulk electrolysis experiments at -1.70 V vs. $Fc^{+/0}$ using a pool mercury working electrode. The electrolytic solution contains 0.1M NBu_4PF_6 in DMF, 100 mM TFA and/or 1 mM of NiTSC-R.

Page 63

Figure 8. UV-vis spectra of a) NiTSC-SCH_3, b) NiTSC-CN, c) NiTSC-$N(CH_3)_2$, d) NiTSC-$(CN)(N(CH_3)_2)$ in the absence and upon the addition of TFA.

Page 64

Figure 9. UV-vis spectra of a) NiTSC-$N(CH_3)_2$, b) NiTSC-$(CN)(N(CH_3)_2)$ upon acidification and neutralization of the solution.

Page 65

Figure 10. Proposed DFT-computed catalytic mechanisms for hydrogen evolution with the NiTSC-R series.

Page 66

Figure 11. Catalytic Tafel plots: Comparison of performances for HER catalyzed by the series of NiTSC-R complexes in DMF in presence of 1 M TFA.

Page 69

Figure 12. Catalytic Tafel plots: comparison of performances for HER catalysed by NiTSC-SCH_3 in DMF in the presence of 1 M TFA (red line) and NiTSC-OCH_3 in DMF in the presence of 1 M TFA (green line) with other catalysts reported in the literature. Black: $Fe^{II}TPP$, DMF, Et_3NH^+, blue: $[Co^{II}(dmgH)_2py]$, DMF, Et_3NH^+, orange: $[Ni^{II}(P_2PhN_2C_6H_4X)_2]^{2+}$, X = $CH_2P(O)(OEt)_2$, MeCN, $DMFH^+$.

Page 70

Figure 13. Electronic absorption spectra of each ligand and NiTSC-R complex in DMF.

Page 76

Figure 14. Cyclic voltammograms of 1 mM of ligand (red line) recorded at a stationary glassy carbon electrode in DMF with 0.1 M NBu_4PF_6 as supporting electrolyte. The cyclic voltammograms of 40 mM of TFA solution in the absence (dotted black line) and in the presence of 1 mM ligand (blue line) are also shown. Scan rate: 500 mV/s.

Page 79

Figure 15. Cyclic voltammograms of NiTSC-R at a stationary glassy carbon electrode at different scan rates (v) in DMF with 0.1 M NBu_4PF_6 as supporting electrolyte (left) and linear plot of ip vs. $v^{1/2}$ for anodic and cathodic waves of both processes (right).

Page 80

Figure 16. Successive cyclic voltammograms recorded at a glassy carbon as working electrode of a 1 mM solution of NiTSC-R complex in DMF (0.1 M NBu_4PF_6) in the presence of increasing amounts of TFA. The black dotted curve shows the CV of 100 mM TFA in the absence of complex under the same conditions. Scan rate: 500 mV/s.

Page 81

Figure 17. Successive cyclic voltammograms recorded at a glassy carbon as working electrode of a 1 mM solution of NiTSC-R series in DMF (0.1 M NBu_4PF_6) with 60 mM TFA at five different scan rates (left) and increasing concentration of TFA at 500 mV/s scan rates (right).

Page 82

Figure 18. Log(k_1) values obtained through FOWA for NiTSC-R complexes.

Page 84

Chapter 3: Ligand stereochemical tailoring of thiosemicarbazone nickel complexes for electrocatalytic hydrogen production

Figure 1. Structures of NiTSC-(x)-OCH_3 and NiTSC-ph series derived from the parent complex NiTSC-OCH_3.

Page 93

Figure 2. X-ray crystal structures of nickel complexes: a) NiTSC-(o)-OCH_3 b) NiTSC-(m)-OCH_3 c) NiTSC-(m,p)-$2OCH_3$ d) NiTSC-(o,p)-$2OCH_3$ e) NiTSC-(m,m,p)-$3OCH_3$ f) NiTSC-ph.

Page 94

Figure 3. UV-vis spectra of the the NiTSC-(x)-OCH_3 series in DMF.

Page 95

Figure 4. Cyclic voltammograms of NiTSC-(x)-OCH_3 series. Conditions: concentration 1 mM at a stationary 1 mm glassy carbon electrode in DMF (0.1 M NBu_4PF_6) using a 500 mV/s scan rate.

Page 97

Figure 5. Successive cyclic voltammograms recorded at a glassy carbon as working electrode of a 1 mM solution of NiTSC-(x)-OCH_3 series in DMF (0.1 M NBu_4PF_6) with increasing concentration of TFA at 500 mV/s scan rates (left) and 60 mM TFA at five different scan rates (right).

Page 99-100

Figure 6. Successive cyclic voltammograms recorded after electrocatalysis upon washing the glassy carbon electrode and immersion into a fresh solution of DMF (0.1 M NBu_4PF_6, black line) and in the presence of 100 mM of TFA (blue line) of: a) NiTSC-(o)-OCH_3 b) NiTSC-(m)-OCH_3 c) NiTSC-(m,p)-$2OCH_3$ d) NiTSC-(o,p)-$2OCH_3$ e) NiTSC-(m,m,p)-$3OCH_3$ f) NiTSC-ph. Scan rate: 500 mV/s.

Page 101

Figure 7. a) Coulometry and b) total H_2 production of the NiTSC-(x)-OCH_3 series during bulk electrolysis experiments at -1.70 V vs. $Fc^{+/0}$ using a pool mercury working electrode. The electrolytic solution contains 0.1 M NBu_4PF_6 in DMF, 100 mM TFA and 1 mM of NiTSC-(x)-OCH_3.

Page 103

Figure 8. UV-vis spectra of: a) NiTSC-(o)-OCH_3 b) NiTSC-(m)-OCH_3 c) NiTSC-(m,p)-$2OCH_3$ d) NiTSC-(o,p)-$2OCH_3$ e) NiTSC-(m,m,p)-$3OCH_3$ f) NiTSC-ph, in the absence and upon the addition of TFA.

Page 104

Figure 9. Catalytic Tafel plots: comparison of performances for HER catalyzed by NiTSC-(x)-OCH_3 series in DMF in presence of 1 M TFA.

Page 107

Figure 10. Catalytic Tafel plots: comparison of performances for HER catalysed by NiTSC-(o)-OCH_3, NiTSC-(m)-OCH_3 and NiTSC-(m,m,p)-$3OCH_3$ in DMF in the presence of 1 M TFA (red, purple and brown line respectively) and NiTSC-OCH_3 in DMF in the presence of 1 M TFA (green line) with other catalysts reported in the literature. Black: $Fe^{II}TPP$, DMF, Et_3NH^+, blue: $[Co^{II}(dmgH)_2py]$, DMF, Et_3NH^+, orange: $[Ni^{II}(P_2PhN_2C_6H_4X)_2]^{2+}$, X = $CH_2P(O)(OEt)_2$, MeCN, $DMFH^+$.

Page 108

Figure 11. Cyclic voltammograms of: a) NiTSC-(o)-OCH_3, b) NiTSC-(m)-OCH_3, c) NiTSC-(m,p)-$2OCH_3$, d) NiTSC-(o,p)-$2OCH_3$, a) NiTSC-(m,m,p)-$3OCH_3$ and a) NiTSC-ph at a stationary glassy carbon electrode at different scan rates (v) in DMF with 0.1 M NBu_4PF_6 as supporting electrolyte (left) and linear plots of ip vs. $v^{1/2}$ for anodic and cathodic waves of both processes (right).

Page 119-120

Figure 12. Successive cyclic voltammograms recorded at a glassy carbon as working electrode of a DMF solution (0.1 M NBu_4PF_6) with 1 mM of: a) NiTSC-(o)-OCH_3 b) NiTSC-(m)-OCH_3 c) NiTSC-(m,p)-$2OCH_3$ d) NiTSC-(o,p)-$2OCH_3$ e) NiTSC-(m,m,p)-$3OCH_3$ f) NiTSC-ph in the presence of increasing amounts of TFA. Scan rate: 500 mV/s.

Page 121

Chapter 4: Nuclearity influence on hydrogen evolution reaction with thiocarbohydrazone nickel complexes

Figure 1. Structure of the trinuclear nickel thiocarbohydrazone complex (Ni_3L_2).

Page 127

Figure 2. Schematic representation of the synthetic protocol yielding Ni_3L_2.

Page 128

Figure 3. 2D DOSY Spectrum for Ni_3L_2 in DMF at 298 K processed using DOSY Toolbox.

Page 129

Figure 4. X-ray molecular structure of **Ni_3L_2** with selected atom labelling and thermal ellipsoids at 40% level. Non-relevant H-atoms are omitted for clarity. Symmetry code: [i] [1]2 – x, y, 1.5 – z. Selected bonds (Å) and angles (°): Ni4-S13 2.133(3), Ni4-S14 2.145(3), Ni4-N15 1.843(8), Ni4-N17 1.786(9), Ni5-S11 2.392(3), Ni5-O9 2.131(6), Ni5-N14 2.137(9); N15-Ni4-S13 85.7(3), N17-Ni4-S14 92.8(3), N15-Ni4-S14 176.5(4), N17-Ni4-S13 1···69.7(3), N14-Ni5-S11 85.2(3), N14-Ni5-O9 90.4(3), $O9^1$-Ni5-O9 85.0(4), O9-Ni5-S11 172.1(2). H bond parameters: N13-H···O9 [N13-H 0.86 Å, H···O9 2.02 Å, N13···O9 2.73(1) Å, ∠N13HO9 138.7°.

Page 129

Figure 5. Temperature dependence of the magnetic susceptibility for Ni_3L_2. The inset is the temperature dependence of the susceptibility in log scale showing the expected Curie behavior for any field at T>10K.

Page 130

Figure 6. Electronic absorption spectra for the H_6L ligand and the Ni_3L_2 complex, concentration of 0.05 mM in DMF.

Page 131

Figure 7. Comparison between experimental and calculated UV-Vis spectra for Ni_3L_2 in DMF. Calculations performed on the neutral complex in a closed-shell singlet state (B3LYP/def2-TZVP).

Page 131

Figure 8. Cyclic voltammograms of 1 mM solutions of H_6L and Ni_3L_2 in DMF solvent recorded at stationary glassy carbon electrode in DMF at 500 mV/s. Potentials referenced to the $Fc^{+/0}$.

Page 132

Figure 9. Linear plot of the peak current i_p vs. the square root of the scan rate $v^{1/2}$ for anodic and cathodic waves of the first redox process of Ni_3L_2 ($0.5\left(E_{pc}^{*} + E_{pa}^{*}\right)$ = -1.35 V vs. $Fc^{+/0}$).

Page 133

Figure 10. Chronoamperogram of a 1 mM solution of Ni_3L_2 in DMF recorded at -1.5 V (top) and -2.25 V vs. $Fc^{+/0}$ (bottom) using a 1 mm glassy carbon electrode.

Page 134

Figure 11. Simulated and experimental cw X-band EPR spectra of a 1mM solution of Ni_3L_2 in DMF at T=50K recorded upon chronoamperometry at -1.5 V vs. $Fc^{+/0}$ at glassy carbon working electrode.

Page 135

Figure 12. a) Spin density distribution and b) Localized Singly Occupied Molecular Orbital (SOMO) for Ni_3L_2 after the first one-electron reduction.

Page 135

Figure 13. Successive cyclic voltammograms of a 1 mM solution of Ni_3L_2 in DMF (0.1 M NBu_4PF_6) recorded at a glassy carbon electrode with increasing amounts of TFA at 500 mV/s. Potential referenced to the $Fc^{+/0}$.

Page 136

Figure 14. Plot of i_{cat} of Ni_3L_2 for increasing concentrations of TFA at different scan rates.

Page 137

Figure 15. Cyclic voltammograms recorded after electrocatalysis of Ni_3L_2 upon washing the working electrode and immersion into a fresh solution of dry DMF (0.1 M NBu_4PF_6, black dashed line) and in the presence of 100 mM of TFA (blue line). Scan rate 500 mV/s. Potential referenced to the $Fc^{+/0}$.

Page 138

Figure 16. Cyclic voltammogram of a 1 mM solution of H_6L (black line) in DMF recorded at a stationary glassy carbon with 0.1 M NBu_4PF_6 as supporting electrolyte. The cyclic voltammogram of a 100 mM of TFA solution in the absence (blue line) and in the presence (red line) of 1mM H_6L are also shown. Scan rate: 500 mV/s. Potential referenced to the $Fc^{+/0}$.

Page 138

Figure 17. Electrocatalytic data vs. time, by applying -1.7 V vs. $Fc^{+/0}$ to a pool mercury working electrode in 0.1 M NBu_4PF_6 solution of DMF. Left: Hydrogen production of the solutions containing 100 mM of TFA in the absence of catalyst (red line) and for a solution of 1 mM of Ni_3L_2 with 100 mM of TFA (black line). Right: Coulometry during bulk electrolysis of a solution containing 100 mM TFA and 1 mM of Ni_3L_2.

Page 139

Figure 18. Electronic absorption spectra for the Ni_3L_2 complex (black line), and upon chronoamperometry (-1.7 V vs. $Fc^{+/0}$ with 100 mM of TFA, blue line).

Page 140

Figure 19. Electronic absorption spectra of 0.05 mM Ni_3L_2 in DMF in the absence and the presence of different concentrations of TFA.

Page 141

Figure 20. a) Spin density distribution and b,c,d) Localized Singly Occupied Molecular Orbitals (SOMO) for Ni_3L_2 after the second two-electron reduction.

Page 142

Figure 21. Proposed EECC catalytic cycle performed by Ni_3L_2. Numbers in red correspond to redox potentials (in V vs $Fc^{+/0}$), whereas those in blue are free energy differences for proton transfer events, in eV. ΔpK_a displayed for the first proton transfer event corresponds to the difference in pK_as between Ni_3L_2H and TFAH.

Page 143

Figure 22. Proposed EECEC catalytic cycle of Ni_3L_2. Numbers in red correspond to redox potentials (in V vs $Fc^{+/0}$), whereas those in blue are free energy differences for proton transfer events, in eV. ΔpK_a displayed for the first proton transfer event correspond to the difference in pK_as between Ni_3L_2H and TFAH. Note that the mechanism would cycle back to species b) once H_2 is formed, since two electrons and two protons would be gone, leaving one unpaired electron in the complex.

Page 143

Figure 23. Plot of i_{cat}/i_p versus inverse of the square root of the scan rate ($1/\sqrt{v}$) for Ni_3L_2 in DMF in the presence of different amounts of TFA. The plots were derived from the voltammograms recorded at different scan rates in the absence and presence of proton source.

Page 144

Figure 24. a) Plot of i_{cat}/i_p versus the square root of the acid concentration ($\sqrt{[H^+]}$) for Ni_3L_2 in DMF at different scan rates. The plots were derived from the voltammograms recorded at different scan rates in the absence and presence of proton source. b) Plot of i_{cat} versus the [Ni_3L_2] concentration in DMF in the presence of 60 mM TFA at 500 mV/s.

Page 145

Figure 25. Catalytic Tafel plots: comparison of performances for HER catalysed by Ni_3L_2 in DMF in the presence of 1M TFA (purple line) and NiTSC-OCH_3 in DMF in the presence of 1M TFA (green line) with other catalysts reported in the literature. Black: $Fe^{II}TPP$, DMF, Et_3NH^+, blue: [$Co^{II}(dmgH)_2py$], DMF, Et_3NH^+, orange: $[Ni^{II}(P_2PhN_2C_6H_4X)_2]^{2+}$, X = $CH_2P(O)(OEt)_2$, MeCN, DMFH.

Page 146

Figure 26. Cyclic voltammogram of 1 mM solutions of Ni_3L_2 in DMF solvent recorded at stationary glassy carbon electrode in DMF at 500 mV/s (solid line) and focusing on the reversible redox process (dotted line). Potentials referenced to the $Fc^{+/0}$.

Page 151

Figure 27. Successive cyclic voltammogram of a 1 mM solution of Ni_3L_2 in DMF at a stationary glassy carbon electrode at different scan rates in DMF with 0.1 M NBu_4PF_6 as supporting electrolyte. Potentials referenced to the $Fc^{+/0}$.

Page 151

Figure 28. Successive cyclic voltammograms of a 1 mM solution of Ni_3L_2 in DMF with increasing concentrations of TFA at a 500 mV/s scan rate.

Page 152

Figure 29. Successive cyclic voltammograms of a 1 mM solution of Ni_3L_2 in DMF and 60 mM of TFA at 5 different scan rates.

Page 152

Chapter 5: Light-driven hydrogen evolution with thiosemicarbazone complexes.

Figure 1. Schematic representation of water splitting with a photoelectrochemical device.

Page 159

Figure 2. Schematic representation of water splitting photochemical cell.

Page 160

Figure 3. Graphical representation of a three components photocatalytic system.

Page 161

Figure 4. Examples of iridium, ruthenium and zinc photosensitizers reported in the literature.

Page 161

Figure 5. Examples of cobalt and nickel catalysts used for photocatalytic hydrogen evolution reactions and reported in the literature.

Page 162

Figure 6. Schematic representation of nitrogen-doped and carbon dots (green box), chemical structures of the series of nickel complexes (purple box) and selected sacrificial electron donors (red box).

Page 163

Figure 7. Chemical structures of the series of cobalt complexes used in this work.

Page 164

Figure 8. Synthetic scheme to generate carbon dots and nitrogen-doped carbon dots.

Page 165

Figure 9. UV-vis spectral evolution of the NiTSC-N$(CH_3)_2$ catalyst under UV led irradiation upon 0, 2 and 22 hours of exposure.

Page 166

Figure 10. Photocatalytic hydrogen production plots of 10 mg NCdots with 50 nmol nickel catalysts: NiTSC-N$(CH_3)_2$; NiTSC-N$(CH_3)_2$CN; NiTSC-SCH_3; NiTSC-OCH_3; NiTSC-CN; NiTSC-ph. All photocatalytic experiments were performed in aqueous TCEP/Asc (1:1) 0.1 M each at pH = 5. All the results presented in the hydrogen production plots are the average values of three independent measurements (within 5-10% error).

Page 167

Figure 11. Photocatalytic hydrogen production plots of 10 mg NCdots in three different amounts of the catalyst NiTSC-N$(CH_3)_2$: 20, 50 and 100 nmol. The photocatalytic experiments were conducted in aqueous TCEP/Asc (1:1) 0.1 M each at pH = 5. All the results presented in the hydrogen production plots are the average values of three independent measurements (within 5-10% error).

Page 168

Figure 12. Photocatalytic hydrogen production (µmol H_2) upon irradiation of 10 mg NCdots in the presence of 50 nmol of the NiTSC-R series in aqueous TCEP/Asc (1:1) 0.1 M each at pH = 5. All the results presented in the hydrogen production plots are the average values of three independent measurements (within 5-10% error).

Page 169

Figure 13 TEM images of NCdots before light irradiation (a and b) and after 13 hours of white led irradiation (c and d).

Page 171

Figure 14. Emission spectra of NCdDots in aqueous solution with increasing concentrations of: a) NiTSC-N$(CH_3)_2$, b) NiTSC-N$(CH_3)_2$CN, c) NITSC-OCH_3, d) NiTSC-SCH_3, e) NiTSC-CN, f) NiTSC-ph.

Page 173

Figure 15. Stern-Volmer plots of NCdot emission quenching with: a) NiTSC-N$(CH_3)_2$, b) NiTSC-N$(CH_3)_2$CN, c) NiTSC-OCH_3, d) NiTSC-SCH_3, e) NiTSC-CN, f) NiTSC-ph catalysts.

Page 174

Figure 16. Photocatalytic mechanism for H_2 evolution using nitrogen-doped carbon dots as photosensitizer, TCEP/Asc as sacrificial electron donor and nickel complexes as catalysts.

Page 175

Figure 17. Schematic representation of the series of cobalt complexes used in this work.

Page 176

Figure 18. Temperature dependence of the magnetic susceptibility for a) COTSC-N(CH_3)$_2$CN(NCS), b) CoTSC-OCH_3(NCS), c) CoTSC-CN(NCS), d) CoTSC-N(CH_3)$_2$(NCS) and e) CoTSC-SCH_3(NCS).

Page 177

Figure 19. UV-vis spectra of the CoTSC-R(NCS) series.

Page 179

Figure 20. Cyclic voltammograms of CoTSC-R series (V vs. $Fc^{+/0}$). Conditions: concentration 1 mM at a stationary 1.5 mm glassy carbon electrode in DMF + 0.1 M NBu_4PF_6 using a 500 mV s^{-1} scan rate.

Page 180

Figure 21. Photocatalytic hydrogen production plots of 10 mg NCdot with 100 nmol cobalt catalysts: CoTSC-N(CH_3)$_2$CN(NCS); CoTSC-OCH_3(NCS); CoTSC- CN(NCS); CoTSC-N(CH_3)$_2$(NCS). All photocatalytic experiments were performed in aqueous TCEP/Asc (1:1) 0.1 M each at pH = 5. All the results presented in the hydrogen production plots are the average values of three independent measurements (within 5-10% error).

Page 181

Figure 22. Photocatalytic hydrogen production plots of 10 mg NCdots in three different amounts of the catalyst CoTSC-N(CH_3)$_2$CN(NCS): 50, 100, 150 and 200 nmol. The photocatalytic experiments were conducted in aqueous TCEP/Asc (1:1) 0.1 M each at pH = 5. All the results presented in the hydrogen production plots are the average values of three independent measurements (within 5-10% error).

Page 182

Figure 23. Turnover number vs catalyst upon irradiation of 10 mg NCdots in the presence of 100 nmol of the CoTSC-R(NCS) series in aqueous TCEP/Asc (1:1) 0.1 M each at pH = 5. All the results presented in the hydrogen production plots are the average values of three independent measurements (within 5-10% error).

Page 183

Figure 24. Cyclic voltammograms of CoTSC-R(NCS) series (V vs. $Fc^{+/0}$). Conditions: concentration 1 mM at a stationary 1 mm glassy carbon electrode in DMF with 0.1 M NBu_4PF_6.

Page 187

List of Tables

Chapter 2: Ligand chemical tailoring of thiosemicarbazone nickel complexes for electrocatalytic hydrogen production

Table 1. Selected spectral features from the electronic absorption spectra of NiTSC-R series in DMF.

Page 57

Table 2. Electrochemical data of NiTSC-R series (V vs. $Fc^{+/0}$).

Page 58

Table 3. Calculated redox potentials of NiTSC-R series (V vs. $Fc^{+/0}$).

Page 59

Table 4. HER parameters of the NiTSC-R series.

Page 63

Table 5. Calculated TOF values for the NiTSC-R series.

Page 67

Table 6. Calculated mid-wave potentials and overpotentials (V vs. $Fc^{+/0}$) for NiTSC-R series.

Page 68

Table 7. Crystallographic data, details of data collection and structure refinement parameters for NiTSC-SCH_3.

Page 77

Table 8. Crystallographic data, details of data collection and structure refinement parameters for NiTSC-CN.

Page 78

Table 9. k_1 calculations using different concentrations of TFA at 4 different scan rates.

Page 85

Chapter 3: Ligand stereochemical tailoring of thiosemicarbazone nickel complexes for electrocatalytic hydrogen production

Table 1. Selected spectral features from the electronic absorption spectra of NiTSC-(x)-OCH_3 series in DMF.

Page 95

Table 2. Electrochemical data of NiTSC-(x)-OCH_3 series (V vs. $Fc^{+/0}$) including the parent complex NiTSC-OCH_3.

Page 96

Table 3. Calculated redox potentials of NiTSC-(x)-OCH_3 series (V vs. $Fc^{+/0}$).

Page 98

Table 4. HER parameters of the NiTSC-(x)-OCH_3 series.

Page 102

Table 5. Calculated TOF values for the NiTSC-(x)-OCH_3 complex family.

Page 106

Table 6. Calculated mid-wave potential and overpotential (V vs. $Fc^{+/0}$) for the NiTSC-(x)-OCH_3 family.

Page 106

Table 7. Crystallographic data, details of data collection and structure refinement parameters for NiTSC-(o)-OCH_3.

Page 113

Table 8. Crystallographic data, details of data collection and structure refinement parameters for NiTSC-(m)-OCH_3.

Page 114

Table 9. Crystallographic data, details of data collection and structure refinement parameters for NiTSC-(m,p)-$2OCH_3$.

Page 115

Table 10. Crystallographic data, details of data collection and structure refinement parameters for NiTSC-(o,p)-$2OCH_3$.

Page 116

Table 11. Crystallographic data, details of data collection and structure refinement parameters for NiTSC-(m,m,p)-$3OCH_3$.

Page 117

Table 12. Crystallographic data, details of data collection and structure refinement parameters for NiTSC-ph.

Page 118

Chapter 4: Nuclearity influence on hydrogen evolution reaction with thiocarbohydrazone nickel complexes

Table 1. Main features of the electronic transitions from the UV-vis spectra of H_6L and Ni_3L_2 in DMF.

Page 132

Table 2. Crystal data and details of data collection for Ni_3L_2.

Page 150

Chapter 5: Light-driven hydrogen evolution with thiosemicarbazone complexes.

Table 1. Photocatalytic performances of the NiTSC-R series of catalysts. All the results presented are the average values of three independent measurements (within 5-10% error).

Page 168

Table 2. Redox potentials (eV vs. NHE) of the photosensitizer and catalysts with the thermodynamic driving forces of electron transfer processes ΔG_1 (PS/Cat) and ΔG_2 (PS/Cat) (eV). a) Oxidation potentials measured by cyclic voltammetry and referenced to NHE. b) Values calculated as the difference of the oxidation potentials and the optical band gap energy E_{00}, calculated in eV. c) E_{00} values calculated from the intersection between the normalized absorption and emission spectra. d) Reduction potentials measured by cyclic voltammetry and referenced to NHE.

Page 172

Table 3. Stern-Volmer constants, K_{sv} and quenching constants, K_Q, of the series of nickel catalysts.

Page 174

Table 4. Selected spectral features from the electronic absorption spectra of CoTSC-R(NCS) series in DMF.

Page 178

Table 5. Electrochemical data of NiTSC-R series (V vs. $Fc^{+/0}$).

Page 179

Table 6. Photocatalytic performances of CoTSC-R(NCS) series of catalysts. All the results presented are the average values of three independent measurements (within 5-10% error).

Page 182

Abstract

For the past two centuries, the consumption of fossil fuels has increased dramatically, leaving their reserves depleted. These problems have turned our interest towards developing catalytic systems that produce environmentally friendly fuel sources. Hydrogen is abundant and is considered an “ideal” fuel since its combustion only releases water vapors into the environment. In recent years, efforts have been made in developing new methods to generate hydrogen from renewable and sustainable resources, such as electrocatalytic and photocatalytic hydrogen evolution reactions (HER). Hydrogenases, the biological systems that naturally produce hydrogen, are a great inspiration for the design of metal-organic complexes that mimic their catalytic abilities.

In this work, we have synthesized, characterized and tested different series of nickel complexes based on thiocarbazone ligands for their ability to produce hydrogen from two different catalytic processes. The first part of this Ph.D. work describes the use of two new families based on bis-thiosemicarbazone ligands and investigates how appropriate ligand-tailoring can affect electrocatalytic performance for HER. The second part describes the use of a polynuclear nickel complex and how the incorporation of several metallic centers can affect electrocatalysis. In the last part of the manuscript, new photocatalytic systems were developed using carbon nanodots as light harvesters and the series of nickel-thiosemicarbazone complexes as catalytic centers for photo-producing hydrogen.

Résumé

Au cours des deux derniers siècles, la consommation de combustibles fossiles a augmenté de façon spectaculaire contribuant à l’épuisement de leurs réserves. Ces problèmes nous ont amené à développer des systèmes catalytiques qui produisent des sources d’énergie respectueuses de l'environnement. L'hydrogène est abondant et est considéré comme un vecteur d’énergie idéal puisque sa combustion ne libère que des vapeurs d'eau dans l'environnement. Ces dernières années, de nombreux efforts ont été déployés pour mettre au point de nouvelles méthodes de production d'hydrogène à partir de ressources renouvelables et durables, telles que les réactions de production d'hydrogène par voies électrocatalytique et photocatalytique. Les hydrogénases, les systèmes biologiques produisant naturellement de hydrogène, sont une grande source d'inspiration pour la conception de complexes métallo-organiques imitant leur activité catalytique.

Dans ce travail, nous avons synthétisé, caractérisé et testé différentes séries de complexes de nickel basés sur des ligands thiocarbazone pour leur capacité à produire de l’hydrogène à partir de deux processus catalytiques différents. La première partie de ce travail de thèse décrit l'utilisation de deux nouvelles familles basées sur des ligands bis-thiosemicarbazone et étudie comment une modulation appropriée du ligand peut affecter les performances électrocatalytiques pour la production d’hydrogène. La deuxième partie décrit l'utilisation d'un complexe de nickel polynucléaire et comment l'incorporation de plusieurs centres métalliques peut affecter l'activité électrocatalitique du système. Dans la dernière partie du manuscrit, de nouveaux systèmes photocatalytiques ont été développés en utilisant des nanoparticules de carbone comme capteurs de lumière et la série de complexes nickel à ligands thiosemicarbazones comme centres catalytiques pour photoproduire de l’hydrogène.

Abstract

For the past two centuries, the consumption of fossil fuels has increased dramatically, leaving their reserves depleted. These problems have turned our interest towards developing catalytic systems that produce environmentally friendly fuel sources. Hydrogen is abundant and is considered an “ideal” fuel since its combustion only releases water vapors into the environment. In recent years, efforts have been made in developing new methods to generate hydrogen from renewable and sustainable resources, such as electrocatalytic and photocatalytic hydrogen evolution reactions (HER). Hydrogenases, the biological systems that naturally produce hydrogen, are a great inspiration for the design of metal-organic complexes that mimic their catalytic abilities.

In this work, we have synthesized, characterized and tested different series of nickel complexes based on thiocarbazone ligands for their ability to produce hydrogen from two different catalytic processes. The first part of this Ph.D. work describes the use of two new families based on bis-thiosemicarbazone ligands and investigates how appropriate ligand-tailoring can affect electrocatalytic performance for HER. The second part describes the use of a polynuclear nickel complex and how the incorporation of several metallic centers can affect electrocatalysis. In the last part of the manuscript, new photocatalytic systems were developed using carbon nanodots as light harvesters and the series of nickel-thiosemicarbazone complexes as catalytic centers for photo-producing hydrogen.

Résumé

Au cours des deux derniers siècles, la consommation de combustibles fossiles a augmenté de façon spectaculaire contribuant à l’épuisement de leurs réserves. Ces problèmes nous ont amené à développer des systèmes catalytiques qui produisent des sources d’énergie respectueuses de l'environnement. L'hydrogène est abondant et est considéré comme un vecteur d’énergie idéal puisque sa combustion ne libère que des vapeurs d'eau dans l'environnement. Ces dernières années, de nombreux efforts ont été déployés pour mettre au point de nouvelles méthodes de production d'hydrogène à partir de ressources renouvelables et durables, telles que les réactions de production d'hydrogène par voies électrocatalytique et photocatalytique. Les hydrogénases, les systèmes biologiques produisant naturellement de hydrogène, sont une grande source d'inspiration pour la conception de complexes métallo-organiques imitant leur activité catalytique.

Dans ce travail, nous avons synthétisé, caractérisé et testé différentes séries de complexes de nickel basés sur des ligands thiocarbazone pour leur capacité à produire de l’hydrogène à partir de deux processus catalytiques différents. La première partie de ce travail de thèse décrit l'utilisation de deux nouvelles familles basées sur des ligands bis-thiosemicarbazone et étudie comment une modulation appropriée du ligand peut affecter les performances électrocatalytiques pour la production d’hydrogène. La deuxième partie décrit l'utilisation d'un complexe de nickel polynucléaire et comment l'incorporation de plusieurs centres métalliques peut affecter l'activité électrocatalitique du système. Dans la dernière partie du manuscrit, de nouveaux systèmes photocatalytiques ont été développés en utilisant des nanoparticules de carbone comme capteurs de lumière et la série de complexes nickel à ligands thiosemicarbazones comme centres catalytiques pour photoproduire de l’hydrogène.